Model of the western Laurentide Ice Sheet, North America

Evan James Gowan

A thesis submitted for the degree of

Doctor of Philosophy

The Australian National University

April, 2014

Declaration

This thesis is an account of research undertaken between July 2010 and April 2014 at the Research School of Earth Science, ANU College of Physical & Mathematical Sciences, The Australian National University, Canberra, Australia.

Except where acknowledged in the customary manner, the material presented in this thesis is, to the best of my knowledge, original and has not been submitted in whole or part for a degree in any university.

Evan J. Gowan

April, 2014

Acknowledgements

I would like to thank my supervisor, Paul Tregoning, for giving me the opportunity to do this project, and giving me support during the past four years.

I thank my supervisory panel of Tony Purcell, Kurt Lambeck and Tom James, who have helped me with the many questions I had while working on this project.

Much of the data used in this study were compiled by geological surveys in Canada. I thank Art Dyke at the Geological Survey of Canada for sending me an updated version of his 2003 database of radiocarbon dates relevant to deglaciation, which had a few samples that I did not find in my own literature searches. Tom James at the Geological Survey Canada provided an unpublished compilation of sea level indicators. I thank Michelle Trommelen at the Manitoba Geological Survey for providing me with her preliminary compilation of glacial landforms of Manitoba.

I would like to thank Stewart Fallon and Rachel Wood at the ANU radiocarbon laboratory, who have aided me on all questions related to radiocarbon dating.

I have appreciated many discussions with Nick Scroxton and Claire Krause on paleo-climate change. I also enjoyed many conversations with Malte Willmes and Rachel Wood on archaeology.

Jean-Philippe Montillet did the MCMC analysis of the lake gauge data for me. I also thank him for helping me with various questions on data analysis.

Discussions with Achraf Koulali, Simon McClusky, and Michael Moore were instrumental in developing my think on interpreting the GPS data.

Herb McQueen provided assistance on computing issues. Computing resources were provided by Terrawulf (Sambridge et al., 2009).

I shared an office with Bianca Kallenberg and Janosch Hoffmann for the duration

of my PHD. The provided help and relief from many long days in the office.

I'd like to thank all the staff and students at RSES. Their friendship and support from the people in this department has led to a pleasant experience at the ANU.

I'd like to thank all my friends at Burgmann College, especially Emma-Kate Potter, who provided many insights of her past experience in doing a PHD in RSES.

Finally, I would like to thank my partner, Yasuko Honda, who has provided me with love and support for the past three years. I love you.

Abstract

The Laurentide Ice Sheet reached its maximum extent at the Last Glacial Maximum, 26 500-19 000 years before present. It is responsible for a large portion of the approximately 130 m of eustatic sea level fall since that time. During its retreat, meltwater from the Laurentide Ice Sheet caused rapid changes in sea level, and affected global climate by changing ocean circulation. However, previous estimates of the absolute volume of the Laurentide Ice Sheet through time have been limited due to deficiencies in the chronology of margin retreat and information on glacial-isostatic adjustment (GIA). In this study, I present a new numerical ice sheet model of the western portion of the Laurentide ice sheet. I constrain the model using GIA indicators, including the tilts of well dated glacial lake strandlines, tilt rates of contemporary modern lakes, uplift rates from GPS, and relative sea level indicators. I also present a new margin history based on the minimum timing of retreat. All data used in the modelling exercise are carefully assessed to ensure they are reliable.

At the Last Glacial Maximum, the ice sheet model has a broad dome that extended from the Cordillera to the area west of Great Slave Lake, Northwest Territories. The southern portion of the ice sheet is modelled to have a shallow gradient, with thickness values less than 2000 m south of 56 degrees north. This is in contrast to previous ice sheet models of the Laurentide Ice Sheet based on GIA modelling, such as ICE-5G (Peltier, 2004), that have over 5000 m of ice in this region. During deglaciation, the largest decrease in volume happened between 16,000 and 13,000 years before present, coinciding with margin retreat in Alberta and Northwest Territories. From 13 000 to 11 500 years before present, ice sheet retreat slowed, corresponding to Younger Dryas cooling. After 11 500 years before present, ice sheet

retreat was more rapid, and by 6500 years before present, no ice remained in the study area. Glacial lake tilt observations support a thick elastic lithosphere, with values greater than 120 km providing the best fit to the data. A wide range of mantle viscosity values were investigated, and the calculated GIA matched observations within the range of 3-5$\times 10^{20}$ Pa s for the upper mantle and $> 5 \times 10^{21}$ Pa s for the lower mantle for the majority of observations.

Contents

List of Figures

List of Tables

Chapter 1

Introduction

1.1 Overview

During the Quaternary (2.6 million years ago to present), high latitude areas of the Earth have periodically been covered in thick, extensive sheets of ice (Imbrie et al., 1992; Lambeck et al., 2002). These ice sheets had a profound impact on global sea-level, as water transferred between the oceans and continental regions. The weight of the ice sheets deformed the Earth, causing areas in the centre of the ice sheets to subside, and areas on the periphery of the ice sheets to uplift (Farrell and Clark, 1976). Due to the viscous rheology of the mantle, uplift continues today in areas that were once covered in ice. This phenomenon is called glacial-isostatic adjustment (GIA).

Globally, the ice sheets reached their maximum extent at the Last Glacial Maximum (LGM) between 26 000 and 19 000 years before present (yr BP) (Fig. 1.1, Clark et al., 2009). The glaciation caused global (eustatic) sea level to fall by approximately 120-135 m during that time (*i.e.* Fairbanks, 1989; Yokoyama et al., 2000; Lambeck and Chappell, 2001; Jansen et al., 2007). At 5000-7000 yr BP, the continental ice sheets had either completely retreated or attained levels similar to present. By 3000 yr BP, global sea level stabilised to within a metre of present levels. At present, the areas that were covered by ice sheets continue to impact global sea level due to ongoing rebound as the mantle flows back towards centres of glaciation (*i.e.*

Mitrovica and Milne, 2002; Bindoff et al., 2007). The changing mass distribution within the Earth due to GIA and on the surface due to changes in the distribution of water mass affects the gravitational field and rotation of the Earth.

There are great challenges to reconstructing the thickness and extent of ice sheets that have fully retreated. The chronology of retreat is often constrained using radiocarbon dates, which provide the age of organic material. This only gives a minimum timing of retreat, as there is an unknown amount of time between when an ice sheet melted and when plants and animals could repopulate the area. The chronological data is also spatially variable. High resolution estimates of thickness of ice sheets based on GIA are usually determined using local (relative) sea level measurements, which only exist in coastal regions. Another problem is that past sea level is dependent on the amount of ice that is present in global ice sheets, so all ice sheets must be included to estimate it. The global distribution of ice through time is uncertain. Geodetic data (*i.e.* measurements of the change in shape and distribution of mass of the Earth), such as vertical velocity rates from Global Positioning System (GPS) may be useful to determine the duration of ice cover and past ice volume in formerly glaciated regions. These measurements are less affected by uncertainties in global ice volume, and can be used to assess GIA in areas far from the coast. Due to the relatively recent development of this technique, these data have been underutilised in reconstructing ice sheets (though the recently published model ICE-6G (Peltier et al., 2015) has used these data).

The Laurentide ice sheet was the largest of the great ice sheets that existed during the LGM and subsequently retreated. It covered most of Canada and parts of the northern United States. Despite its importance in contributing to global sea level change during the last glaciation (accounting for 40–55 m of equivalent global sea level at the LGM, Licciardi et al., 1998), uncertainties remain in the configuration and thickness of the ice sheet through time. There have been recent

attempts to create glaciological reconstructions of the ice sheet (*e.g.* Gregoire et al., 2012; Tarasov et al., 2012; Abe-Ouchi et al., 2013; Kleman et al., 2013), but these are driven by climate forcing, which have great uncertainties the further back in time you go. The last attempt at a model independent of climatic assumptions was ICE-5G (Peltier, 2004). Since then, advances in computing power and the addition of new geodetic techniques provide new means of assessing size of the ice sheet through time. Peltier et al. (2015) published an update of this model that utilises these data, called ICE-6G, though this came out after the original submission of this thesis (April 2014), and is not considered in subsequent chapters.

1.2 The North American Ice Sheet Complex

1.2.1 Reconstruction of the ice sheet complex

The North American Ice Sheet Complex consisted of three independent ice sheets that converged and covered most of Canada and parts of the northern United States and Alaska (Dyke et al., 2002; Dyke, 2004). The ice complex reached its maximum extent at the Last Glacial Maximum between 18 000-24 000 yr BP (Fig. 1.2). Reconstructions of the ice sheet that covered North America have been attempted since the 1870s (see Prest, 1990 for a review of studies prior to 1990). The complex includes the Cordilleran Ice Sheet, centred over the Cordillera of western North America, the Laurentide Ice Sheet, with centre of flow surrounding Hudson Bay, and the Innuitian Ice Sheet, centred over the northern Arctic Archipelago (Dyke et al., 2002; England et al., 2006). At the LGM, there was a confluence of these three ice sheets.

Much work has been accomplished since the publication of ice margin maps by Dyke (2004) to try to improve the chronology of the timing of deglaciation for the North American ice sheet complex (*i.e.* Briner et al., 2009; Carlson et al., 2007;

Curry and Petras, 2011; England et al., 2006, 2009; Fisher et al., 2009; Jackson et al., 2011; Lowell et al., 2009; Ross et al., 2012). The focus of many of these studies has been to constrain the timing of drainage routes of glacial Lake Agassiz to determine if its drainage was responsible for sudden climate change events. Other studies have focused on the glacial history of the Canadian Arctic, which was previously poorly constrained. These new data, along with improved calibrations and modelling constraints, have led to the need to revise the margin reconstructions of the ice sheets (*i.e.* Tarasov et al., 2012).

Many models exist for the North American ice sheet complex (*e.g.* Licciardi et al., 1998; Marshall et al., 2002; Peltier, 2004; Tarasov et al., 2012). Though many groups have worked on this problem, there are still uncertainties on the volume of ice, timing of deglaciation, and misfits to relative sea level and geodetic observations (Argus and Peltier, 2010; Carlson et al., 2012; Tarasov et al., 2012). These analyses make it clear that there is a need to assess these data and use them to produce a new ice sheet history. Lambeck et al. (2010) presented a systematic way to reconstruct ice sheets using margin constraints, relative sea level data and inversions of the Earth response. This will serve as the basis to reconstruct the history of the North American ice sheet complex. An overview of some previous numerical ice sheet models follows.

1.2.2 Models by Peltier and colleagues

Tushingham and Peltier (1991) presented the ICE-3G model, which used finite element disc loads to simulate the ice sheets and ocean. The resolution of the elements is $2^\circ \times 2^\circ$ in most areas, with smaller elements where relative sea level data are abundant. Ice volume in ICE-3G was constrained by fitting calculated relative sea level to observed relative sea level and fitting radiocarbon constraints on deglaciation based on the work of Dyke and Prest (1987). They used an Earth model with a 120 km

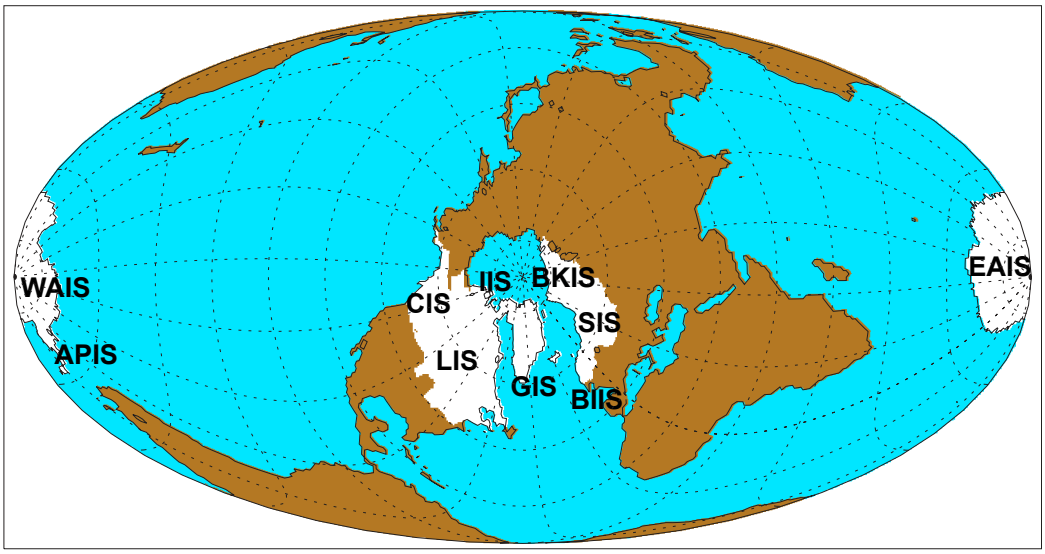

Figure 1.1: Extent of ice cover during the Last Glacial Maximum (Clark et al., 2009). EAIS - East Antarctic Ice Sheet; SIS - Scandinavian Ice Sheet; BKIS - Barents-Kara Sea Ice Sheet; BIIS - British Isles Ice Sheet; GIS - Greenland Ice Sheet; IIS - Innuitian Ice Sheet; CIS - Cordilleran Ice Sheet; LIS - Laurentide Ice Sheet; WAIS - Wast Antarctic Ice Sheet; APIS - Antarctic Peninsula Ice Sheet

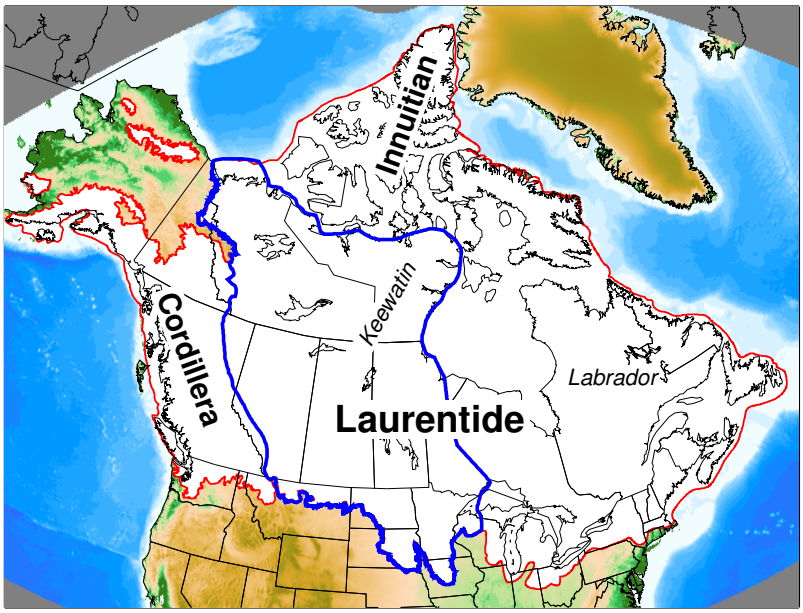

Figure 1.2: Maximum extent of the North American Ice Sheet Complex during the last glaciation. The extent for most of the ice sheet is from Dyke (2004), except for areas in the western Arctic, which is derived from England et al. (2009). The blue outline is the area of the western Laurentide Ice Sheet that is the focus of this study. Also shown are the locations of the Keewatin and Labrador sectors of the Laurentide Ice Sheet.

thick elastic lithosphere, a viscosity of 10^{21} Pa s for the upper mantle and a viscosity of 2.4×10^{21} Pa s for the lower mantle. This Earth model was inferred from previous forward modelling experiments (Peltier and Andrews, 1976; Wu and Peltier, 1983). The maximum thickness at the centre of the ice sheet was less than that proposed by Denton and Hughes (1981). The volume of ice in the North American portion of the model at the LGM was equivalent to lowering eustatic sea level by 55 m.

ICE-4G is a refinement of ICE-3G to account for changes in eustatic sea level found in Barbados (Peltier, 1994). In addition, a major change in methodology saw the use of spherical harmonic expansion of the ice sheet and ocean functions, rather than using finite element disc loads (Mitrovica and Peltier, 1991). The major modification of the Laurentide Ice Sheet in this model was to significantly reduce the amount of ice prior to the Younger Dryas (a period of cool climate conditions that lasted about 1300 years beginning about 12 900 yr BP), and to slow the rate of deglaciation at subsequent times.

ICE-5G was developed primarily by adjusting ice loads to fit relative sea-level, geodetic observations in North America and geological constraints on glaciation (Peltier, 2004). Peltier (2002) describes the development of the model of the North American glaciation in ICE-5G. The Earth model used in the modelling process (VM2) has a lithospheric thickness of 90 km, and a mantle viscosity that was found using an iterative Bayesian inversion post-glacial sea level change in Scandinavia and North America (Peltier, 1996). At each iteration, the ice sheet model was adjusted to better fit the sea level observations. The North American portion of the ICE-5G model differs significantly from ICE-4G, primarily by adding much more ice south of Hudson Bay (Fig. 1.3, Peltier, 2004). He included this extra ice to account for the change in gravity rate found by Lambert et al. (2001) at six absolute gravity stations extending from Hudson Bay to Iowa. Argus and Peltier (2010) note that the ice added to the Laurentide ice sheet in ICE-5G was too great, and that vertical

velocities measured using GPS are inconsistent with such a large load. In addition, the large jumps in ice thickness, such as the 3000 m thick element in North Dakota (Fig. 1.3) are glaciologically implausible. ICE-6G addresses these issues (Peltier et al., 2015), but since it was published after the majority of the work in this thesis was completed prior to its publication, it is not considered

1.2.3 Models by Tarasov and colleagues

Perhaps the most prolific work on numerical modelling of the North American Ice Sheet Complex in the past fifteen years is from the models created by L. Tarasov and colleagues (Tarasov and Peltier, 1997, 1999, 2000, 2004; Tarasov et al., 2012; Stokes et al., 2012). Their suite of models incorporate a variety of parameters, such GIA, relative sea level, orbital variability, atmospheric conditions, precipitation, basal ice flow parameters and basal heat flux. Tarasov and Peltier (1999, 2004) explain the modelling method in detail. It incorporates coupling between more parameters than used in previous numerical ice sheet reconstructions, though they acknowledge that many remain largely unconstrained. The flow of the ice sheet in their models is governed by Glen's Flow Law, which is dependent on temperature conditions within the ice sheet, ice sheet thickness and basal topography. Temperature in the model is controlled by latitude and albedo.

The latest model by Tarasov et al. (2012) incorporates 39 model parameters, the majority of which are climatologically related. They used a simplified version of the margin chronology by Dyke (2004) as a starting point in their analysis. The data used to assess the modelled ice sheets include ice margin constraints, marine limits, relative sea level, modern uplift rates and lake strandlines. Their simulation use a Monte Carlo method for selecting these data to validate the models (with the exception of marine limits), with weights on data density. The model parameters were varied in over 50,000 runs, and an ensemble mean of 10,000 runs was used in their

final model. The conclusion of this study was that there are still large uncertainties in creating a model of North American ice sheets. In particular, the uncertainty in ice sheet margin chronology has not been assessed and may be the largest source of error. They also acknowledge that many of the parameters, such as basal ice velocity and temperature are only indirectly resolved by geological and geophysical data. Their model does have correspondence to observed sea level rise events, such as meltwater pulse 1A, with the greatest uncertainties on the contribution from the western Laurentide Ice Sheet. Their model at the LGM (Fig. 1.4) shows a dome located west of Hudson Bay with a maximum elevation of 3000 m, a secondary dome south of Hudson Bay maximum elevation of 2700 m, and a dome east of Hudson Bay with maximum elevation of 2600 m.

1.2.4 Oregon State University model

Clark (1994) began to investigate the Laurentide ice sheet and how deformation of soft sediments at the base of the ice sheet may have shaped its evolution. The results of this investigation suggested that, when ice covered soft deformable sediments, the ice sheet was highly lobate and was prone to fluctuations. When the ice covered rigid bedded regions, such as the Canadian Shield, the ice sheet was far less dynamic and retreated at a steady rate. He also suggests that some of the major fluctuations during retreat could not be explained purely by climate change because they were asynchronous along the margin. Tests of till from the Lake Michigan lobe indicated that sediment velocities could reach up to 500 m/a depending on saturation conditions (Jenson et al., 1995).

The Oregon State University ice model incorporates ice and sediment deformation, heat flow, accumulation and ablation of ice, and isostatic adjustment of basal topography (Jenson et al., 1996). The Jenson *et al* study focused primarily on the Lake Michigan lobe, which had a dynamic history that involved soft sediment de-

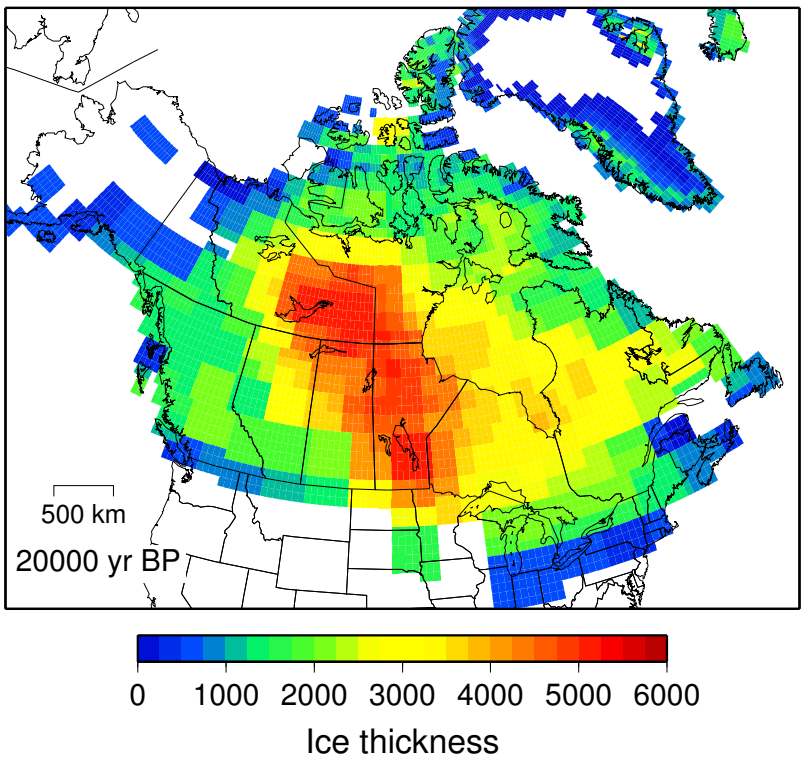

Figure 1.3: Ice thickness for the ICE-5G model at 20 000 yr BP, relative to present day.

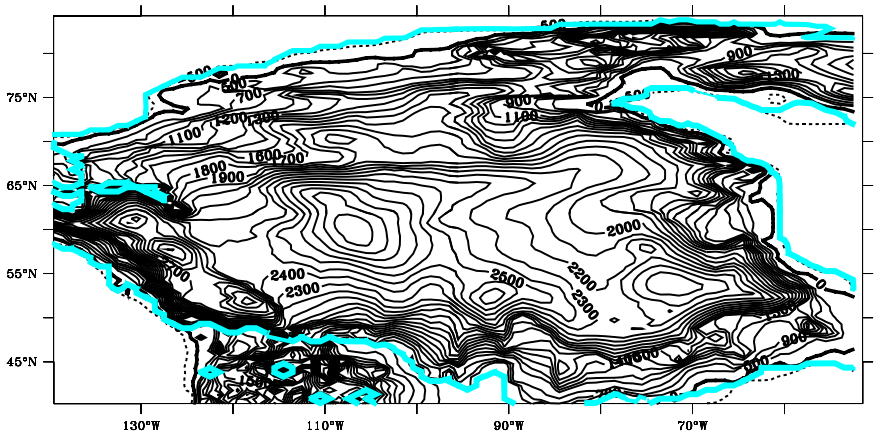

Figure 1.4: Ensemble mean ice sheet model from Tarasov et al. (2012) at 20 000 yr BP. Contour interval is 100 m, and the cyan line is the ice extent limit.

formation. They found that increasing the viscosity of the base of the ice sheet when the flowline reached the Canadian Shield significantly increased the surface slope of the ice sheet. They also found that simulations using low viscosity basal sediment were more sensitive to changes in precipitation and temperature. Clark et al. (1996) and Licciardi et al. (1998) expanded this analysis to reconstruct the Laurentide Ice Sheet (Fig. 1.5). The ice model featured three ice flow centres at the LGM, located in Keewatin, northern Quebec, and northwestern Ontario (Clark et al., 1996). Licciardi et al. (1998) tested the modelling method using a variety of sediment viscosity, temperature and ice accumulation values. The surface slope of the ice sheet was most sensitive to changes in sediment viscosity. They created minimum and maximum ice volume models, which used different sediment viscosity values in the Hudson Bay and Hudson Strait regions. Their minimum and maximum models had a total equivalent eustatic sea level equivalent of 40 m and 49 m, respectively. They found that their models were similar to that of Fisher et al. (1985), who reconstructed the Laurentide ice sheet using changes to basal shear stress as the sole variable parameter. The models contained a similar volume of ice to that of ICE-4G. This model was not tested against GIA constraints, and used a simple exponential relationship to calculate deformation due to loading (Jenson et al., 1996).

1.2.5 Modelling by Marshall *et al.*

Marshall et al. (2002) created a model of the North American ice sheet complex using a coupled glaciological and geodynamic model, similar to the Tarasov models. The parameters used included basal deformability, paleoclimate, and isostatic response to loading. A suite of models were able to achieve the approximate southern limit of glaciation at the Last Glacial Maximum, except when the climate parameters were cold and dry or when basal shear stress was too extreme (Fig. 1.6). The

most sensitive parameter in their simulations was the relationship between ice sheet elevation and precipitation. Their model predicts a greater contribution to eustatic sea level than other models such as ICE-4G (78-88 m), but they cautioned that the volume of ice at the Last Glacial Maximum is ambiguous due to a lack of observational evidence. These models were unable to reproduce the lobate structure of the southern part of the ice sheet, due to the lack of deformable beds in the model.

1.2.6 Model by Gregoire *et al.*

Gregoire et al. (2012) presented a model of the North American ice sheet complex that was developed using a glacial systems model (Fig. 1.7). The variables used in this model include basal sliding, climate and sea-level. The reconstruction used the ICE-5G model to reconstruct climate forcing and eustatic sea level change. The main conclusion of their study was that the collapse of an ice saddle that connected the Laurentide Ice Sheet and Cordilleran Ice Sheet was responsible for Meltwater Pulse 1A, a rapid rise in eustatic sea level that happened between 14 000 and 15 000 yr BP. However, they were unable to replicate the timing of the collapse of the saddle, as their model predicted it happening between 12 000 and 11 000 yr BP.

1.2.7 ANU model

The ANU ice sheet model is a suite of semi-independently determined models of regional ice sheets. Published descriptions of the development of these ice sheet models have been made for the British Isles (Lambeck, 1993a,b; Lambeck et al., 1996), Barents Sea (Lambeck, 1995, 1996) Scandinavia (Lambeck et al., 1998a, 2006, 2010), and Greenland (Fleming and Lambeck, 2004). The methodology to develop the ANU ice sheet models is described in detail in Lambeck et al. (2010). First, a map of the margin history, generally from radiocarbon constraints, outlines when and where ice can exist in the different parts of the ice sheet. Second, relative sea level

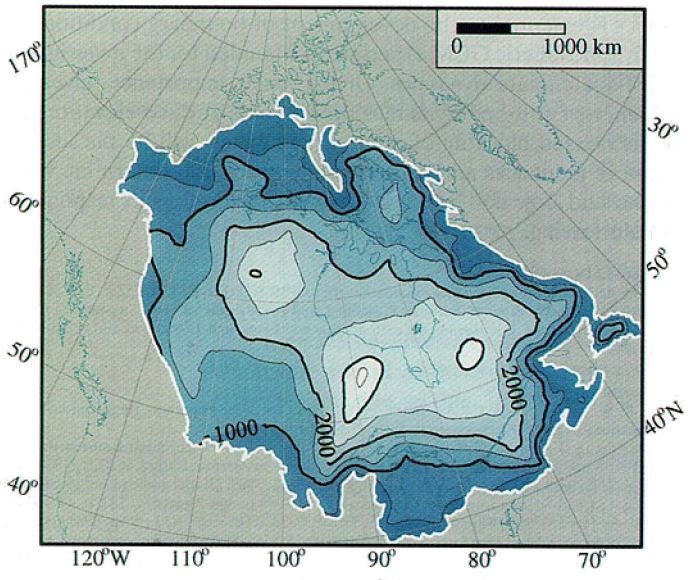

Figure 1.5: The "maximum" Oregon State University reconstruction of the Laurentide Ice Sheet at the LGM, with high viscosity till in Hudson Bay (Clark et al., 1996; Licciardi et al., 1998). Contour interval is 500 m.

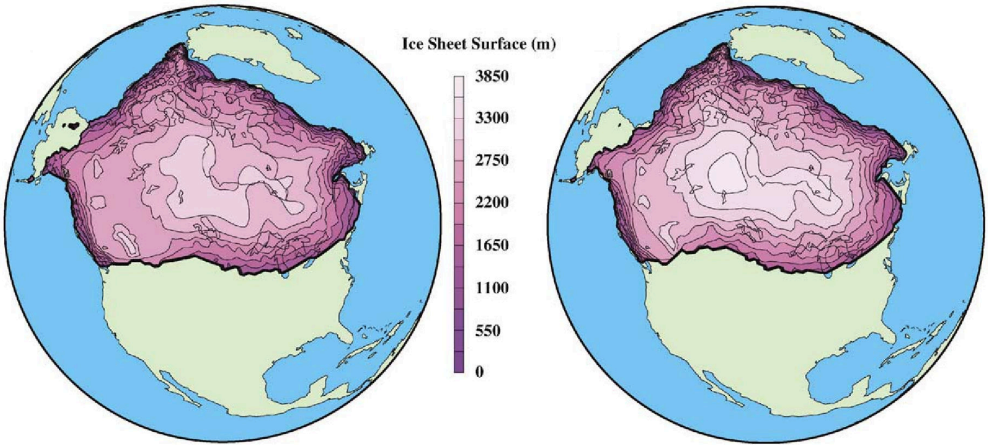

Figure 1.6: Examples of the Marshall et al. (2002) models at LGM conditions.

indicators are compiled to determine the pattern of deformation due to ice sheet loading. Finally, the ice model was adjusted to fit these constraints using a range of Earth model parameters. The Earth models used to calculate the response to loading have three variables - lithospheric thickness, upper mantle viscosity (defined to extend down to the 670 km discontinuity), and lower mantle viscosity. Density and bulk and shear moduli of the Earth are taken from the PREM model (Dziewonski and Anderson, 1981).

The ANU model of the North American ice sheet complex is presently unpublished, though some of the details on its construction are as follows (K. Lambeck and A. Purcell, *pers. comm.* 2011). The initial ice model for North America is a convergence of the Denton and Hughes (Denton and Hughes, 1981) and Oregon State University (Clark et al., 1996; Licciardi et al., 1998) ice models, using the margin data chronology determined by Dyke (2004). The Denton and Hughes models are based on basal sliding and internal ice deformation mechanics, while the Oregon State University models include basal sediment deformation mechanics. These two models were selected a priori because they were constructed independent of assumptions on Earth rheology. Relative sea level data was inverted to find the optimal Earth and ice sheet models. The ice thickness was varied based on the fit to the observations. Finally, the model was smoothed to make the elevation gradients of the ice topography smaller and more realistic. The ANU model of the Laurentide Ice Sheet is divided into 56 time steps from 240 000 to 6800 yr BP, to encompass both the Wisconsin and penultimate (Illinoian) glaciations and the interglacial period that separated them. At 6800 yr BP, the model reaches modern ice distribution. The ice model uses a latitudinal grid spacing of 0.5 degrees and a longitudinal spacing of 0.25 degrees. At 20 000 yr BP, there is substantial ice thickness in the region surrounding Hudson Bay (Fig. 1.8). This ice sheet model is not realistic in many areas, such as southwestern Hudson Bay, where there is an area of thin (<1000 m)

ice, surrounded by areas where peak ice thickness is in excess of 4000 m. There are also artefacts where ice thickness exceeds 6000 m.

1.3 Motivation

Despite the many attempts in previous studies to create models of the Laurentide Ice Sheet, there is still room for improvement. Ice sheet models that are based on climate simulations have not been successful at simulating the geometry of the ice sheet, due to the large uncertainties in climatic conditions during the last glacial cycle. ICE-5G and the ANU model are reconstructions of ice sheets that are independent of climatic parameters, developed primarily to fit observations of GIA and relative sea level. However, these models are geologically and glaciologically unrealistic, and the ice volume away from coastal areas is highly uncertain.

The contribution of the Laurentide ice sheet to global sea level rise, especially rapid events like Meltwater Pulse 1A are currently amongst the most hotly debated topics in paleoclimate (Carlson and Clark, 2012). The source of much of Meltwater Pulse 1A has been attributed to the western Laurentide Ice Sheet, generally assumed to have been due to catastrophic drainage of Lake Agassiz eastward through the St. Laurence valley (Carlson and Clark, 2012) or northwards through the Mackenzie River (Murton et al., 2010). One motivation of this study is to determine if GIA modelling alone can constrain the contribution of the ice sheet to global sea level rise through time. Separating the contributions of the Laurentide ice sheet to eustatic sea level from the less well constrained Antarctic Ice Sheet will help improve estimates the source of eustatic sea level rise. Providing a better model of the Laurentide Ice Sheet therefore will make it easier to estimate past ice volume in Antarctica (*i.e.* Lambeck and Chappell, 2001).

Another factor motivating the reconstruction of ice sheets is to use as input of climate models. Many paleoclimate models use the geographical reconstructions

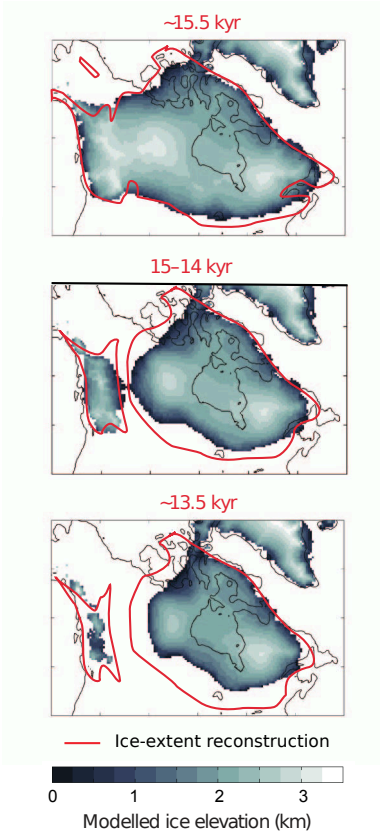

Figure 1.7: The evolution of the Gregoire et al. (2012) model through the Meltwater Pulse 1A event. The red line is the margin reconstruction used by Peltier (2004). Note that the actual timing of the separation of the Laurentide and Cordilleran ice sheets in their model was between 12 000 and 11 000 yr BP.

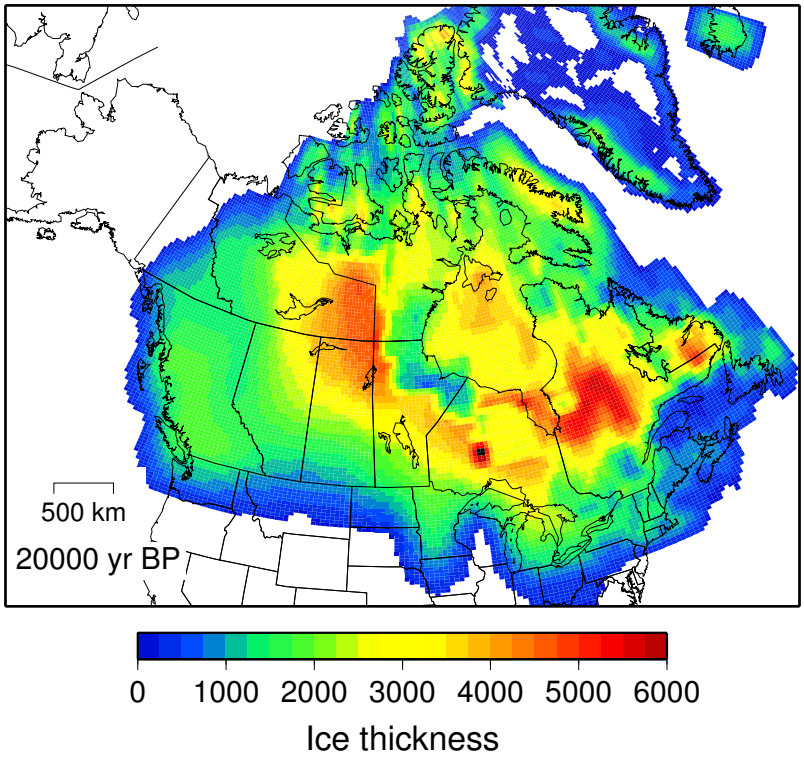

Figure 1.8: Ice thickness for the ANU model at 20 000 yr BP.

as input to determine past climate (*e.g.* He et al., 2013; Taylor et al., 2012). The choice of ice sheet model will affect the resulting distribution of precipitation, air temperature, ocean temperature and circulation, among other parameters. If the reconstructions are in error (such as incorrect ice sheet topography or extent), it will bias the resulting modelled climate.

Accurate reconstruction of past ice sheets also is important for assessing current and future global sea level rise and past climate change. Assessing contemporary global sea level rise requires a correction for GIA in order to remove that component from climatic and oceanic induced changes (Church et al., 2004). The choice of ice sheet and Earth model will factor into the accuracy of these assessments. This is important for determining places where global sea level rise will be faster or slower than the global average. The ice sheet also influences climate by changing the Earth's albedo, weather patterns, vegetation distribution, ocean circulation and surface temperature (Clark et al., 1999).

The approach taken in this study is to reconstruct the Laurentide Ice Sheet using a simple glaciological technique, using observations of GIA to assess the volume, height and extent of the ice sheet. A specific focus is to improve ice volume estimates in areas away from the coast. One possible source of information for GIA away from the coast is from large proglacial lakes. Recently, there have been efforts to find the age and extent of strandlines of Glacial Lake Agassiz, a large proglacial lake that existed along the southern margin of the Laurentide Ice Sheet (Fisher, 2005; Lepper et al., 2007, 2011, 2013; Rayburn and Teller, 2007; Weller and Fisher, 2009; Yang and Teller, 2012). Since their formation, differential uplift has caused the portion of the strandline (beaches, scarps and ridges associated with the shore of a lake) closest to the ice margin to be 10s to 100s of m higher than the portion furthest away. The largest of these strandlines is the Upper Campbell, which has approximately 160 m of differential uplift. A comparison of the calculated tilt of

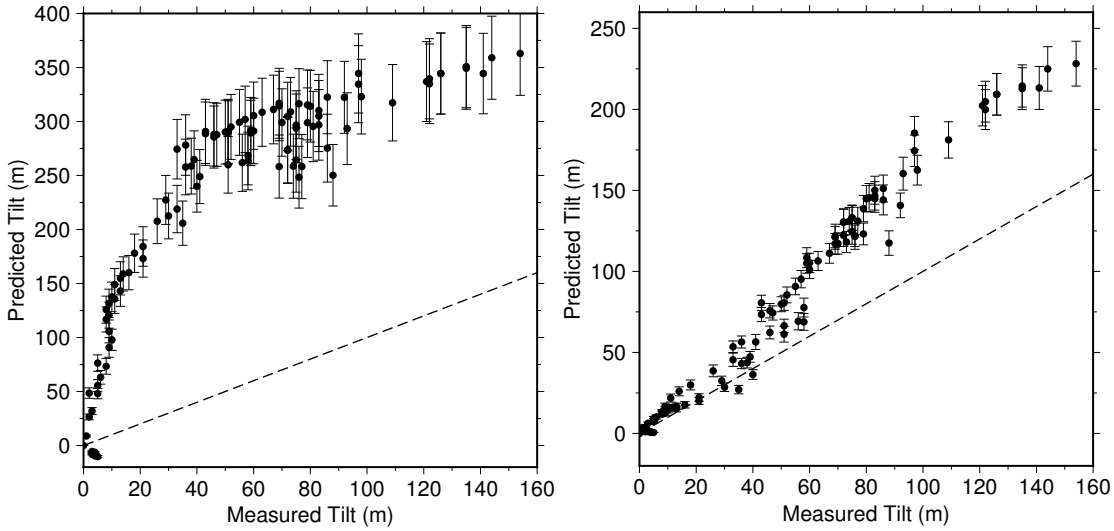

Figure 1.9: Comparison of the observed and calculated tilt of the Upper Campbell strandline for (a) ICE-5G and (b) the ANU model

ICE-5G and the ANU model is shown on Fig. 1.9. The results show that the ANU model over-predicts the amount of tilt by about 100 m, while ICE-5G exceeds the observations by over 150 m. Since these models did not use constraints such as these in their development, there is an opportunity to make an improved ice sheet model incorporating them.

Another factor that motivates the creation of a new ice sheet model is ice sheet geometry. Fig. 1.10 shows a comparison of ICE-5G and the ANU model at 20 000 yr BP. ICE-5G has a very coarse resolution, and, at some locations, there are abrupt changes in thickness of 2-3 km. The ANU model is much smoother, but it too has abrupt changes in ice thickness which are unlikely to be glaciologically reasonable. These models are also at odds with glaciologically based reconstructions such as Fisher et al. (1985), which predict relatively thin ice cover in the southern Laurentide Ice Sheet.

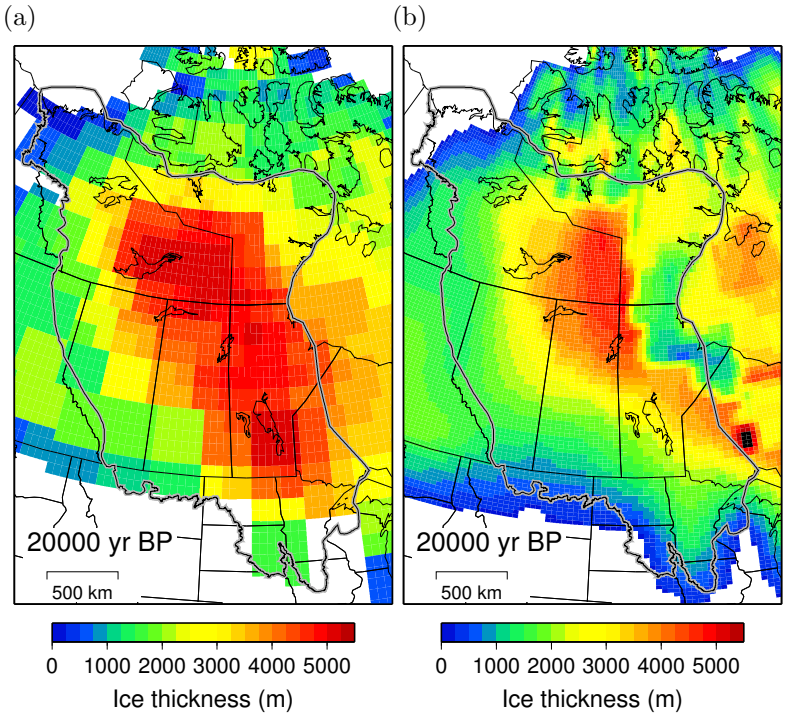

Figure 1.10: Comparison of the ice sheet models at 20 000 yr BP. (a) ICE-5G (b) ANU Model.

1.4 Outline

The goal of this project is to reconstruct the western Laurentide Ice Sheet (see Fig. 1.2 for an outline of the region of interest). It was decided that, due to the large size of the North American Ice Sheet Complex, focusing on a portion of it was necessary for timely completion of the project. A vital component of reconstructing the ice sheet is to refine the location of the ice sheet margins using radiocarbon, cosmogenic and optical dating methods that limit the extent of the ice sheet. Pre-LGM margin reconstructions of the entire Laurentide Ice Sheet, based on sparse chronological and geomorphological data, are shown in Chapter 2. Chapter 3 shows the result of a model of the minimum timing of retreat of the western Laurentide Ice Sheet. This chapter was published in Quaternary Science Reviews by Gowan (2013). To create this model, there is assessment of all chronological information on the timing of retreat, and determination of the probable direction of retreat.

The maximum plausible extent of the ice sheet from the minimum timing of retreat models serves as the starting point for ice sheet modelling. The study area was chosen because it was poorly constrained by observations of GIA. This has changed due to recent acquisition of vertical velocity rates from Global Positioning Satellites (GPS), contemporary lake tilt and glacial strandline tilt. In addition, there have been additional relative sea level data in the northern part of this study area that have been published recently (*e.g* Dyke et al., 2011; Ross et al., 2012; Savelle et al., 2012). Details on the observations related to GIA are shown in chapters 4–6. All data are scrutinised for quality and reliability.

A goal of the modelling project is to ensure that the reconstruction is glaciologically plausible. The technique used to reconstruct the ice sheets involves glacial flowline reconstruction, which was originally used by Reeh (1982) and Fisher et al. (1985). This allows for the reconstruction of ice sheets using only two variables: margin location and basal shear stress. The intention is to produce a realistic ice sheet model, without introducing many climatic and ice physics parameters. Climatic parameters have a complicated influence on the dynamics of the ice sheet, and are largely unconstrained. The ice sheet modelling technique and tests of modelling parameters are described in Chapter 7. Chapter 8 provides an overview of the resulting ice sheet model, modelled GIA, comparison with observations and comparison with ICE-5G and the ANU model.

1.5 Map of locations

This thesis encompasses a large geographical area. Fig 1.11 shows the location of places discussed in the text.

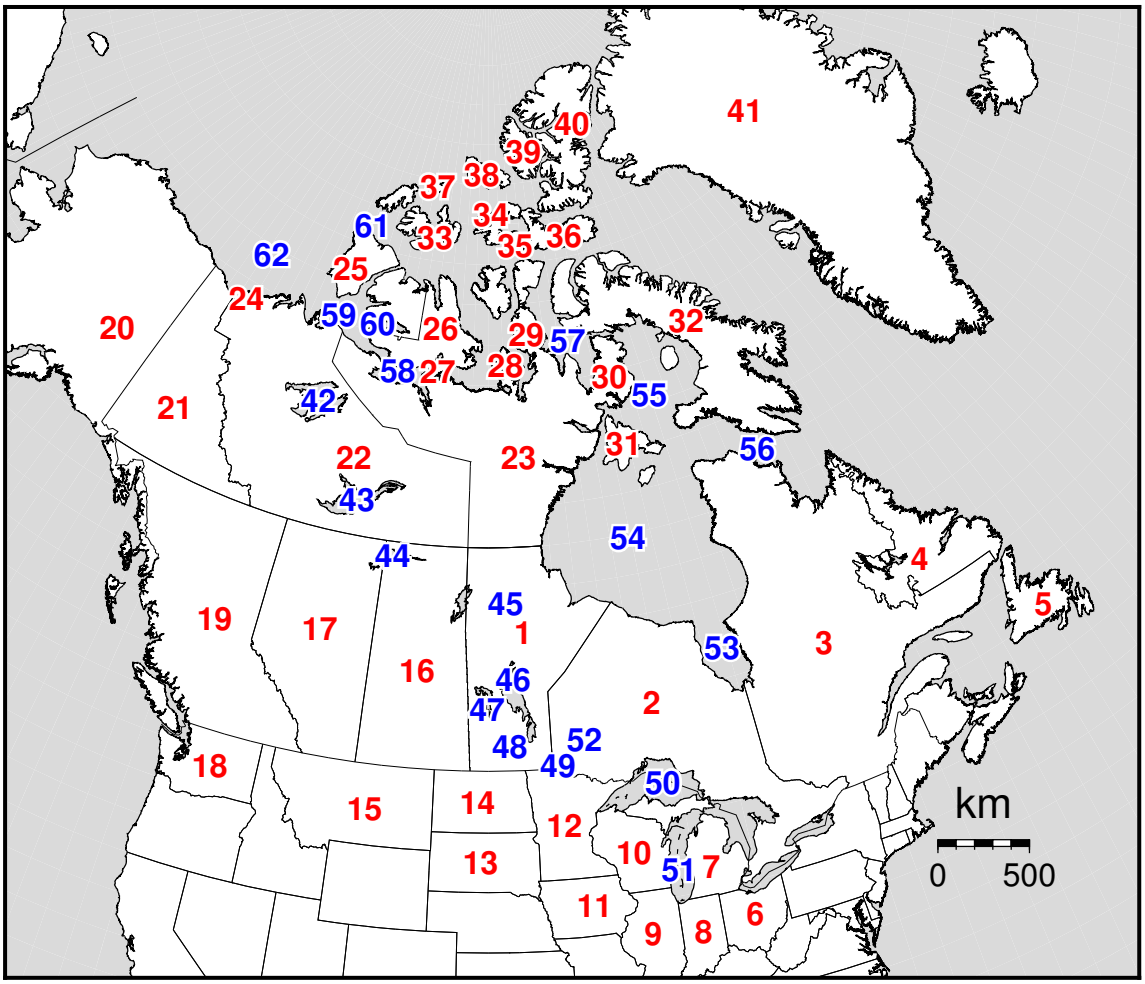

Figure 1.11: Location of places discussed in the text. Red numbers indicate the names of states, provinces, territories and islands, while blue numbers are water bodies. 1 - Manitoba, 2 - Ontario, 3 - Quebec, 4 - Labrador, 5 - Newfoundland, 6 - Ohio, 7 - Michigan, 8 - Indiana, 9 - Illinois, 10 - Wisconsin, 11 - Iowa, 12 - Minnesota, 13 - South Dakota, 14 - North Dakota, 15 - Montana, 16 - Saskatchewan, 17 - Alberta, 18 - Washington, 19 - British Columbia, 20 - Alaska, 21 - Yukon, 22 - Northwest Territories, 23 - Mainland Nunavut/Keewatin/Kivalliq, 24 - Mackenzie Delta/Tuktoyuktak Coastlands, 25 - Banks Island, 26 - Victoria Island, 27 - Kent Peninsula/ Bathurst Inlet, 28 - King William Island, 29 - Boothia Peninsula, 30 - Melville Peninsula, 31 - Southampton Island, 32 - Baffin Island, 33 - Melville Island, 34 - Bathurst Island, 35 - Cornwallis Island, 36 - Devon Island, 37 - Mackenzie King Islands, 38 - Ellef Ringnes Island, 39 - Axel Heiberg Island, 40 - Ellesmere Island, 41 - Greenland, 42 - Great Bear Lake, 43 - Great Slave Lake, 44 - Lake Athabasca, 45 - Southern Indian Lake, 46 - Lake Winnipeg, 47 - Lake Winnipegosis, 48 - Lake Manitoba, 49 - Lake of the Woods, 50 - Lake Superior, 51 - Lake Michigan, 52 - Lac Seul, 53 - James Bay, 54 - Hudson Bay, 55 - Foxe Basin, 56 - Hudson Strait, 57 - Gulf of Boothia, 58 - Coronation Gulf, 59 - Amundsen Gulf, 60 - Prince Albert Sound, 61 - McClure Strait, 62 - Beaufort Sea,

Chapter 2

Ice sheet margin reconstructions

2.1 Introduction

One of the largest sources of uncertainty in reconstructions of ice sheets is margin chronology (*e.g.* Tarasov et al., 2012). The most recent synthesis of margin reconstructions of the Laurentide Ice Sheet since the Last Glacial Maximum (LGM) was by Dyke (2004), with time intervals of 500 ^{14}C years. These reconstructions were based on a suite of uncalibrated, reservoir-corrected radiocarbon ages and geomorphic features that formed during the deglacial period. Geological-based reconstructions leading up to the LGM have not been attempted in such detail. Kleman et al. (2010) presented relative ages of major flow features that were likely produced prior to the LGM, with ages based on relatively few absolute age constraints. Numerical modelling of the Laurentide Ice Sheet depends on having adequate estimates on the duration and extent of ice coverage. Duration of ice cover controls how much time there is for the mantle to flow away from the ice load, while the extent of the ice sheet will determine the depth into the Earth that is affected by the load.

The chronological information for margin reconstruction comes from a variety of sources. Here, radiocarbon dates are denoted "^{14}C yr BP" for uncalibrated ages, and "cal yr BP" for calibrated ages. All radiocarbon dates were calibrated using OxCal 4.1 (Bronk Ramsey, 2009), with age ranges reported at the 95% confidence limit. For marine organisms, the reservoir corrections determined by Coulthard

et al. (2010) are used, unless otherwise noted. Luminescence (optical and infrared), cosmogenic and U/Th dates are reported as "yr BP" and assumed to correspond to calendar years before present.

This chapter provides a summary of the ice sheet margin reconstructions used for the Laurentide Ice Sheet model. The post-LGM period for the western Laurentide Ice Sheet is covered in Gowan (2013), which follows this chapter. In that study, the minimum timing of retreat is modelled, using existing radiocarbon and optical dates and an inferred direction of retreat based on deglacial landforms. The pre-LGM configuration will be discussed in detail in this chapter, as well as the post-LGM history for areas outside of the western Laurentide Ice Sheet.

2.2 Pre-Last Glacial Maximum reconstructions

2.2.1 Penultimate (Illinoian) glaciation and last interglacial

The Illinoian Glaciation, which reached a maximum about 138 000 yr BP (Carlson and Winsor, 2012), is not rigorously investigated in this study, but is included as it was similar in dimensions to the Wisconsin glaciation and was recent enough that it may be manifest in recent GIA. The timing of the Illinoian maximum is set to 140 000 yr BP, based on the timing of the eustatic sea level minimum (*e.g.* Thomas et al., 2009). Labrador-centred ice reached its largest late Pleistocene extent into the United States during the this glaciation, covering most of the state of Illinois (Curry et al., 2011). Investigations of glacial deposits in Alberta (*i.e.* Jackson et al., 2011) and the Banks Island (*i.e.* Lakeman and England, 2012) indicate that, in the Keewatin sector, the Illinoian glaciation was not as extensive as the Wisconsin. The Cordilleran Ice Sheet was more extensive than the late Wisconsin glaciation during the penultimate glaciation (Demuro et al., 2012). The margin reconstruction takes into account these constraints (Fig. 2.1).

The ice sheet history after the Illinoian maximum is not well defined. Global mean sea level peaked at about 5.5-9 m above present at 120 000 yr BP (Dutton and Lambeck, 2012). The extent of ice at this time is set to be the same as present. Sea level fluctuated by 10s of metres during oxygen isotope stage 5 (130 000–80 000 yr BP), likely reflecting growth and retreat of various ice sheets, including the Laurentide (Lambeck and Chappell, 2001). U/Th dates from wood and infrared-stimulated luminescence dates of interglacial sediments located south of Hudson Bay indicate that Hudson Bay was likely ice free until after 95 000 yr BP (Allard et al., 2012). The Keewatin and Labrador sectors were set to have ice cover at 110 000 yr BP, and Hudson Bay is set to be ice covered at 90 000 yr BP.

2.2.2 Early to middle Wisconsin

The basis for the ice margin reconstructions for the early and middle Wisconsin glaciation comes from inferences of landform swarm directions that predate the final deglaciation of the Laurentide Ice Sheet (Kleman et al., 2010). The period between the start of the Wisconsin glaciation (80 000 yr BP) and 30 000 cal yr BP is split into 10 000 year intervals. This study uses the preferred chronology of Kleman et al. (2010), where major landform swarms they identified are inferred to have formed between 80 000 and 30 000 yr BP. The margin reconstructions are shown on Fig. 2.2.

The early Wisconsin glaciation is largely undated, as it is beyond the limits of radiocarbon dating and the sedimentary record is fragmented. In eastern Canada, the ice sheet advanced east of the present-day coastline during the early Wisconsin (Stea et al., 2011). Stea et al. suggested that the age of this advance was between 75 000 and 50 000 yr BP, based on bracketing ages from the penultimate interglacial and subsequent mid-Wisconsin retreat. They interpreted this advance to be from an ice centre east of the Labrador-centred Laurentide Ice Sheet, due to the lack of eastward oriented striae in eastern Quebec and the lack of Canadian Shield-derived

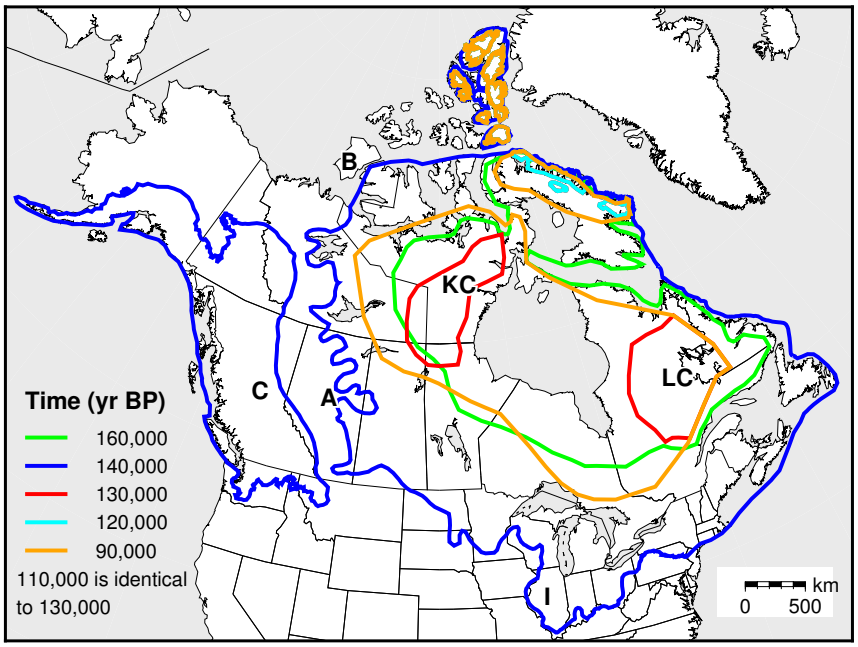

Figure 2.1: Margin reconstructions for the penultimate glaciation and interglacial period. KC - Keewatin centre, LC - Labrador centre, C - Cordillera centre, A - Alberta, I - Illinois, B -Banks Island

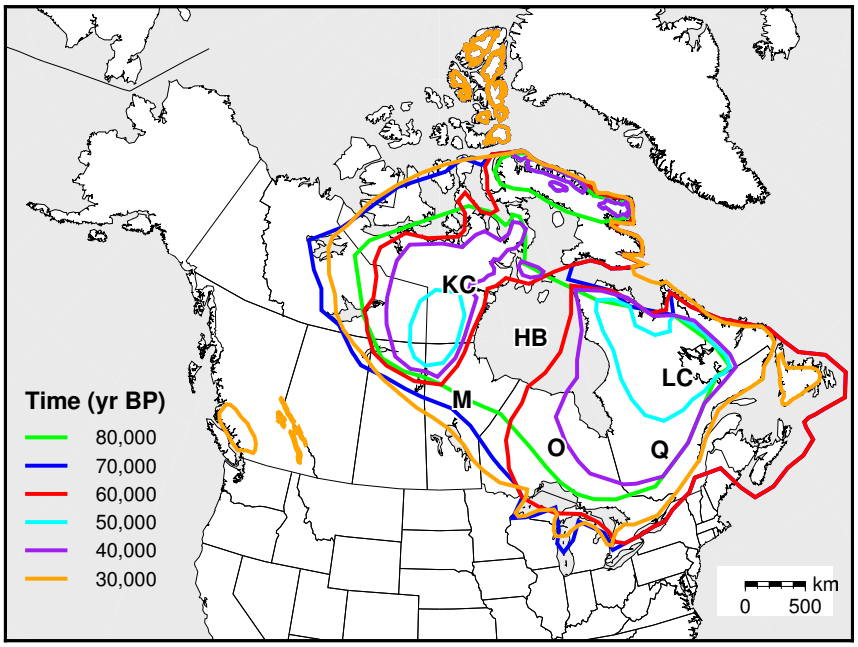

Figure 2.2: Margin reconstructions early and mid-Wisconsin glaciation, 80 000 to 30 000 yr BP. KC - Keewatin centre, LC - Labrador centre, M - Manitoba, O - Ontario, Q - Quebec

erratics in glacial sediments. The margin reconstructions used in this study has the margin on the shelf of eastern Canada at 70 000 and 60 000 yr BP. This also corresponds to the timing of the Caledonia and Fundy swarm identified by Kleman et al. (2010). Kleman et al. correlated the Rocksand swarms in eastern Quebec and northern Ontario with the Fundy swarm. The configuration leading to the Rocksand swarms is set to be at 60 000 yr BP. The Garry swarm located west of Hudson Bay was also assigned to be the same age. For the time periods prior to 60 000 yr BP, the ice margin reconstruction is simplistic, with the Keewatin and Labrador sectors merged within Hudson Bay. This was done due to the lack of non-glacial sediments dating to younger than 90 000 yr BP and older than 50 000 yr BP in southern Hudson Bay.

At 50 000 yr BP, there was an interstadial event where Hudson Bay may have become ice free, with only fragmentary ice in areas surrounding the bay. In the configuration presented here, ice covers much of northern Quebec and Labrador, and a smaller ice cap is present in the Keewatin region. The sea that formed during this time is known as the Prest Sea. An exact age of this phase is still debated, and may be early Wisconsin, in age even though Kleman et al. (2010) assigned an age of around 50 000 yr BP. McMartin et al. (2013) reported pre-LGM shells from till deposits northwest of Hudson Bay, with minimum and maximum uncorrected ages of 34 400–35 400 and 41 900–43 200 cal yr BP (31 660±210 and 39 190±460 ^{14}C yr BP). This may indicate that Hudson Bay remained ice free until after 40 000 cal yr BP. Thorleifson et al. (1992) also reported finite radiocarbon dates from southern Hudson Bay, but suggested the samples may have been contaminated. They assigned the Prest Sea to MIS 5a (80 000 yr BP). Berger and Nielsen (1991) reported four thermoluminescence dates from non-glacial sediments in northern Manitoba pre-dating the LGM, with ages between 32 000 and 46 000 yr BP. Dubé-Loubert et al. (2012) stated anomalous fading maybe have caused these ages to appear young.

Ice sheet surface temperature reconstructions based on oxygen isotope ratios from ice cores in Greenland indicate that there were rapid oscillations between warm and cold periods between 60 000 and 30 000 yr BP (Fig 2.3, Johnsen et al., 2001). Millennial scale oscillations are related to changes in ocean circulation in the Atlantic. Longer lasting cool periods are caused by a shutdown of north Atlantic deep water circulation due to rapid influxes of ice and water into the north Atlantic by the Laurentide Ice Sheet (*i.e.* Heinrich Events, Clark et al., 1999). Heinrich Events may be caused by a collapse of the ice sheet when it advanced on the soft-bedded Hudson Bay (MacAyeal, 1993). There were three Heinrich Events between 50 000 and 30 000 yr BP, indicating Hudson Bay did periodically contain ice. Kirby and Andrews (1999) suggested that the period between 35 000 and 45 000 yr BP was a time of ice sheet build-up, culminating with a major collapse of the ice sheet in Hudson Strait that corresponds with the Heinrich Event at 35 000 yr BP.

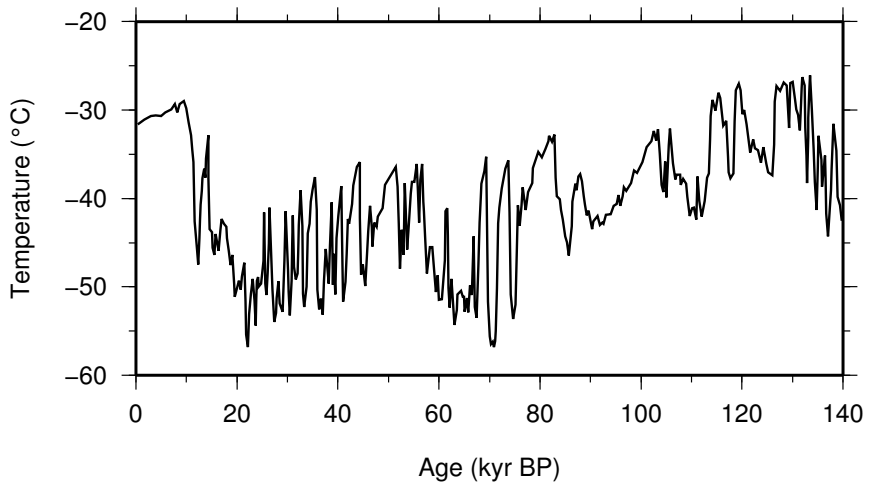

Figure 2.3: Surface air temperature reconstructions from a composite of ice cores in Greenland (Johnsen et al., 2001).

The 10 000 year interval of margin reconstructions used prior to 30 000 yr BP is insufficient to capture the probable rapid fluctuations of the ice sheet. The lack of chronological and geological information from this time does not justify highly detailed reconstructions for the purposes of post-LGM ice sheet modelling. Hudson

Bay is considered to be largely ice free in the margin model at 50 000 and 40 000 years. This is justified by the largely warm interstadial conditions present in Greenland through this period and the presence of marine organisms in northwestern Hudson Bay. The ice extent is shown to grow in both the Labrador and Keewatin ice centres in this period. The 30 000 yr BP margin is described in further detail in the next section. The implication of this reconstruction is that the Sachigo and Aberdeen swarms (Kleman et al., 2010) are assumed to have happened 40 000 and 30 000 yr BP.

2.2.3 Lead-up to the Last Glacial Maximum

The advance of the Laurentide Ice Sheet after 30 000 yr BP was determined using radiocarbon dates from sediments that underlay or are within late Wisconsin till. Dyke et al. (2002) showed the limit of the ice sheet at about 34 000–31 000 cal yr BP (27 000–30 000 ^{14}C yr BP), when the ice sheet was restricted to the Canadian Shield. This margin location is the basis of the reconstruction at 30 000 cal yr BP for this model. The evolution of the ice sheet between 30 000 and 20 000 cal yr BP is split into 2000 year time intervals. The explanation of the timing of advance to the maximum limit is given in this section (Fig. 2.4).

Previous ice margin reconstructions of the northwestern Laurentide Ice Sheet left most of Banks Island ice free during the late Wisconsin and the maximum glacial extent was from a pre-Wisconsin glaciation (*i.e.* Dyke and Prest, 1987; Dyke, 2004). This position was challenged by England et al. (2009) using a suite of finite-aged radiocarbon dates from shells within glacial sediment from the most extensive glacial advance. The youngest age for the western Arctic Archipelago was from a shell fragment on Melville Island with an uncorrected age of 28 400–29 400 cal yr BP (TO-10626, 25 520±200 ^{14}C yr BP), which indicates that the strait north of Banks Island was likely ice free prior to 30 000 cal yr BP. The youngest pre-glacial shell from

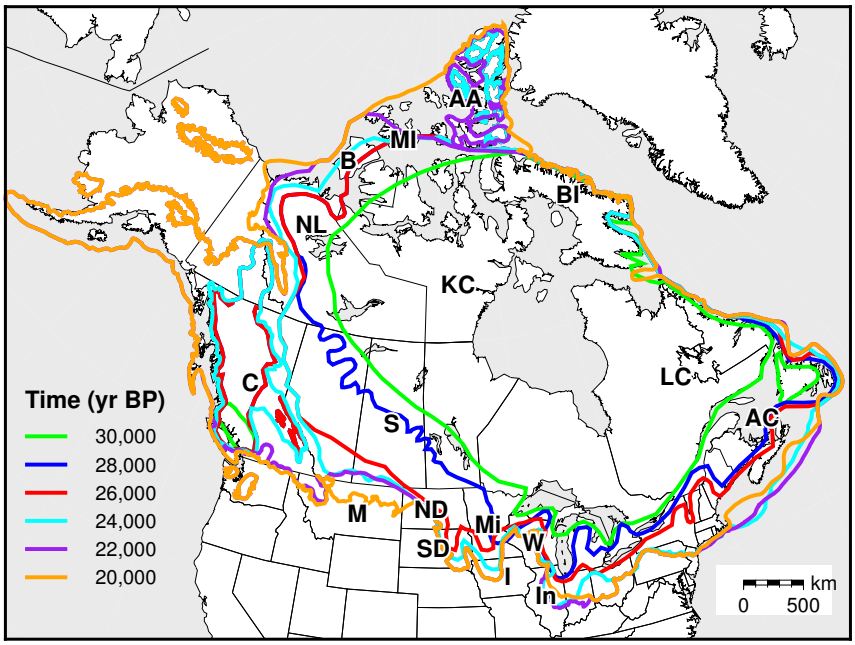

Figure 2.4: Margin reconstructions from 30 000 to 20 000 yr BP. KC - Keewatin centre, LC - Labrador centre, C - Cordilleran centre, NL - Northeastern Laurentide, B - Banks Island, MI - Melville Island, AA - Arctic Archipelago, BI - Baffin Island, M - Montana, S - Saskatchewan, ND - North Dakota, SD - South Dakota, Mi - Minnesota, I - Iowa, W - Wisconsin, In - Indiana, AC - Atlantic Canada

the west coast of Banks Island has an uncorrected age of 33 700–34 400 cal yr BP (NOSAMS-79536, 30 700±140 ^{14}C yr BP, Lakeman and England, 2013). This is the maximum age of the ice sheet overriding Banks Island. The margin reconstructions in this study give a steady advance of the ice sheet over Banks Island after 30 000 cal yr BP, with the margin off the west coast of the island at 22 000 cal yr BP.

The southwestern Laurentide Ice Sheet did not advance past the approximate limits of the Canadian Shield until after 30 000 cal yr BP (Dyke et al., 2002). Forests persisted north of 54.5°N in Saskatchewan until at least 27 000–26 200 cal yr BP (SacA 27174, 22 330±130 ^{14}C yr BP, Bélanger et al., 2014). Numerous radiocarbon dates from southwestern Alberta indicate that the Laurentide Ice Sheet did not reach the Rocky Mountains until close to the LGM (Jackson et al., 2011). The youngest date from Alberta has an age of 24 800–26 400 cal yr BP (AECV-1664c, 21 330±340 ^{14}C yr BP, Young et al., 1994). Luminescence and cosmogenic dates

from glacial lakes in Montana indicate that the maximum extent did not happen until after 22 000 yr BP (Davis et al., 2006; Hill and Feathers, 2002). The margin of the ice sheet is shown to gradually reach the LGM limit from the Canadian Shield between 30 000 and 20 000 yr BP.

The advance of the northwestern mainland Laurentide Ice Sheet probably happened close to the LGM (Kennedy et al., 2010; Lacelle et al., 2013; Murton et al., 2007). Redeposited wood located southwest of Great Bear Lake indicates that the ice sheet did not reach the Mackenzie Mountains until after 30 800–31 500 cal yr BP (TO-1192, 27 170±250 ^{14}C yr BP, Smith, 1992). The maximum extent at the Richardson Mountains post-dates 20 000 cal yr BP (Kennedy et al., 2010; Lacelle et al., 2013). Murton et al. (2007) collected luminescence dates on pre-glacial aeolian sand from Tuktoyuktak Coastlands (located adjacent to the Beaufort Sea), which indicate that the advance of the ice sheet to the coast did not happen until after 22 000 yr BP. The exact timing of advance in areas further southeast of the maximum limits is less certain. In the reconstructions presented here, an ice lobe extends northwest of Great Bear Lake at 28 000 yr BP, and steadily expands until reaching near-maximum extent at 20 000 yr BP.

The advance of the ice sheet into the northern United States was highly diachronous with rapid fluctuations. The first major advance of the Des Moines and James Lobes, located largely in Minnesota, and North and South Dakota, happened about 24 000 cal yr BP (Clayton and Moran, 1982). The age maximum extent of the Superior Lobe in Minnesota and Wisconsin is poorly determined (Patterson and Johnson, 2004; Syverson and Colgan, 2011), but the maximum age of the first late Wisconsin advance from wood underlying glacial deposits is 31 800–33 300 (28 580±220 ^{14}C yr BP, Meyer and Stefanova, 2009). Optical dates from loess deposits indicate that the ice margin advanced into northern Wisconsin by 23 800 yr BP (Schaetzl et al., 2014). The Lake Michigan Lobe reached its maximum extent

about 23 000 cal yr BP, with a less extensive advance about 28 500 cal yr BP (Curry et al., 2011). The maximum extent of the Erie Lobe in Indiana and Ohio was attained at around 23 300 cal yr BP (Glover et al., 2011). The margin chronology used in this study for this region largely follows the chronology laid out by the preceding studies.

The margin reconstruction for Atlantic Canada follows Stea et al. (2011). A Maritime-based ice dome operated during the lead-up to the LGM, and the ice margin was likely on the continental shelf by 24 000 yr BP. The margin from this time until 20 000 yr BP is placed at the edge of the continental shelf.

For northeastern Canada, the ice margin was located near the current shoreline position on Labrador and Baffin Island at 30 000 yr BP. There are several radiocarbon dates that postdate 30 000 ^{14}C yr BP ($<$ 34 000 cal yr BP, Dyke et al., 2002), which indicates that advance off the present coast happened after that. The reconstructions after 30 000 yr BP have a gradual advance to fill fjords and straits before reaching the continental shelf break. The build-up of the Innuitian Ice Sheet in the northern Arctic Archipelago follows England et al. (2006), who state that advance of ice caps beyond their modern limit did not begin until about 22 000 yr BP.

Reconstruction of the build-up of the Cordilleran Ice Sheet follows Clague and Ward (2011). The southwestern Coast Mountains had substantial ice volume by 28 000 cal yr BP, indicated by high relative sea level at that time (Clague et al., 2005). The maximum extent of the western Cordilleran Ice Sheet was not attained until after 20 000 yr BP, but was extensive enough to merge with the Laurentide ice sheet in Alberta by that time.

2.3 Post-Last Glacial Maximum configuration

2.3.1 Innuitian Ice Sheet

The glacial history of the Innuitian Ice Sheet in the Canadian Arctic Archipelago went through a major revision by England et al. (2006), which serves as the basis for the margin chronology for this region. The ice sheet featured a complex set of ice divides and domes, centred over modern islands. It converged with the Greenland Ice Sheet in the strait east of Ellesmere Island. It converged with the Laurentide Ice Sheet along the southern boundary of Devon, Cornwallis, Bathurst and Melville islands. The glacial limit at the LGM is currently speculative, although it probably lay on the continental shelf. The reconstruction used in this study is at the continental shelf break, similar to the position proposed by England et al. (2006). The isochrones by England et al. (2006) were reported as ^{14}C yr BP, using a reservoir correction of 410 years (*i.e.* ΔR=0). A more appropriate correction for this area was reported by Coulthard et al. (2010) as ΔR=335±85 years. The majority of the radiocarbon dates used to constrain ice sheet history in this region are marine shells, so it is appropriate to use the larger reservoir correction while converting these isochrones to calendar years.

In the reconstruction used in this study (Fig. 2.5), the Innuitian ice sheet is set to remain at the continental shelf edge and merged with the Greenland and Laurentide Ice Sheets until 14 000 yr BP. At 13 000 yr BP, the ice sheet had retreated off the western shelf, with the margin at the Ellef Ringnes and Mackenzie King islands. There was further retreat at 12 000 yr BP, with the margin laying off the coast of Bathurst Island, and retreat within the straits to the north and south of Devon Island. At 10 000 yr BP, the Innuitian ice sheet was no longer connected to the Laurentide Ice Sheet, although it still extended off the west side of Ellesmere Island to between Ellef Ringnes and Bathurst islands. At 9000 yr BP, the ice sheet

had broken up, and ice caps were restricted to Devon, Axel Heiberg and Ellesmere islands. By 8000 yr BP, the ice caps were not much more extensive than at present.

2.3.2 Northwestern Laurentide Ice Sheet

Margin reconstructions for the northwestern Laurentide ice sheet on Banks and western Victoria Island is based on the isochrones by Lakeman and England (2012) (Fig. 2.5). At the LGM, the margin is located at the continental shelf break, off the west coast of Banks Island. By 14 000 cal yr BP, the ice margin retreated to central Banks Island. At 13 000 cal yr BP, the McClure Strait between Banks Island and Melville Island was ice free, and most of Banks Island was ice free. At 12 000 cal yr BP, the ice margin lay near the modern border between the Northwest Territories and Nunavut on Victoria Island. The margin configuration after 12 000 yr BP uses isochrones based on the reconstructions by Dyke (2004).

2.3.3 Eastern Laurentide Ice Sheet

The margin history of the eastern Laurentide Ice Sheet is based on the reconstructions of Dyke (2004) (Fig. 2.6). Occhietti et al. (2011) proposed a revision to this chronology for much of this region, though it is not significantly different from Dyke's model, so the older model is used for consistency over the whole region. The isochrones in Dyke's reconstruction were based on intervals of 500 ^{14}C years. These were converted to calendar years by assigning a 1-sigma error of 250 years (half the 500 year interval), and calibrating them with OxCal. The median of the calibrated probability distribution was taken to be the representative age of the isochrone (Table 2.1). To match the 500-1000 year time interval used in the modelling the isochrones were rounded to the nearest 500 years.

2.3.4 Cordillera Ice Sheet

The margins of the Cordillera Ice Sheet follow the isochrones of Dyke (2004). The configuration in the interior of this ice sheet is highly uncertain, near present-day glacial extent was attained between 12,000 and 13 000 cal yr BP. The latest review of the glacial history of British Columbia (Menounos et al., 2009) confirms this value. During the LGM, the Cordillera Ice Sheet and the western Laurentide Ice Sheet merged from the Canada-US border in Alberta to as far north as the Yukon-British Columbia border (Clague, 1989). Cosmogenic ages suggest this confluence may have persisted until 12 000–18 000 yr BP (Jackson et al., 1999).

Table 2.1: Conversion of radiocarbon ages to calendar years

Radiocarbon age (^{14}C yr BP)	Calendar Age (cal yr BP)	Radiocarbon age (^{14}C yr BP)	Calendar Age (cal yr BP)
18000	21500	10250	12000
17500	20800	10000	11600
17000	20200	9600	10900
16500	19700	9500	10800
16000	19200	9000	10100
15500	18700	8500	9500
15000	18200	8000	8900
14500	17600	7800	8700
14000	17100	7700	8600
13500	16500	7600	8400
13000	15700	7200	8000
12500	14700	7000	7900
12000	13900	6500	7400
11500	13400	6000	6900
11000	12900	5500	6300
10500	12300	5000	5800

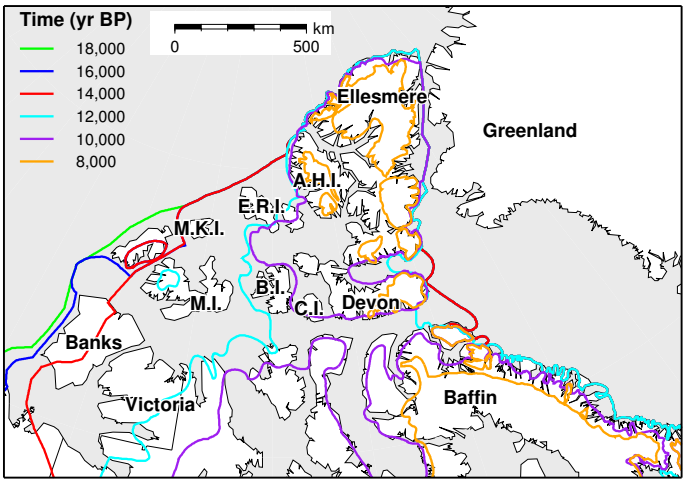

Figure 2.5: Margin reconstruction of the northern Laurentide Ice Sheet (based on Dyke (2004) and Lakeman and England (2012)) and the Innuitian ice sheet (based on England et al. (2006)) at 2000 year intervals.. Abbreviations for islands mentioned in the text: B.I. – Bathurst Island, E.R.I. – Ellef Ringnes Island, A.H.I. – Axel Heiberg Island, M.K.I. – Mackenzie King Islands, M.I. – Melville Island, C.I. – Cornwallis Island

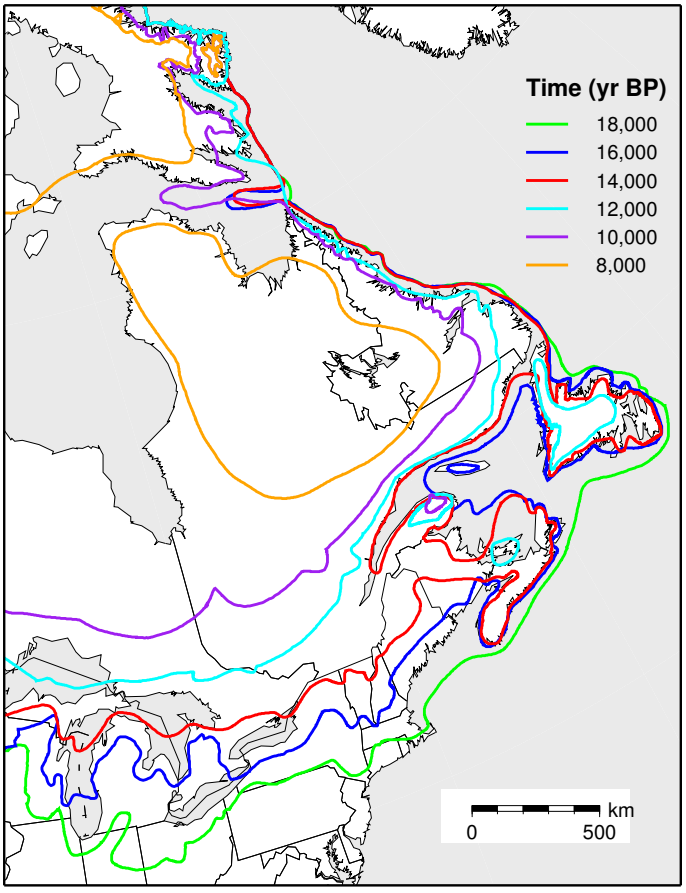

Figure 2.6: Margin reconstruction of the eastern Laurentide Ice Sheet (based on Dyke (2004)) at 2000 year intervals.

Chapter 3

An assessment of the minimum timing of ice free conditions of the western Laurentide Ice Sheet

Preamble

Since the focus of this study is to produce a model of the western Laurentide Ice Sheet since the LGM, the history of retreat in that area was subjected to a more thorough investigation. This chapter was published in Quaternary Science Reviews, volume 75, pp. 100–113 Gowan (2013). In this study, the focus was not on attempting to determine the exact location of the ice margin through time, as had been done in studies such as Dyke (2004), but to determine the certainty that areas had been deglaciated. All chronological constraints from the study area were carefully assessed for quality. The direction of margin retreat was also needed to determine the area confirmed to be ice free. A map of the direction of retreat was produced using geomorphic features that formed during deglaciation, derived from previously published surficial geology maps. The list of chronological constraints and the direction of retreat map are included as electronic supplements.

Abstract

This study presents an investigation of the minimum timing of retreat of the western Laurentide Ice Sheet, which covered parts of Canada and the northern United States. The retreat of the ice sheet is poorly constrained due to low spatial resolution of chronological data that indicate ice free conditions. A limitation of radiocarbon and luminescence dating methods is that it is only possible to determine the time when it is certain that ice is absent from a region, which may differ substantially from the true date of ice margin retreat. The minimum timing of ice free conditions is determined using a model of ice sheet retreat, inferred from landforms that formed during the late stages of glaciation, and extrapolating the calibrated probability distribution of chronological data in the opposite direction. The analysis excludes radiocarbon samples from materials that have been shown to give artificially old ages, such as bulk sediments. The results of the analysis identify 55 dates that have the most impact on the model. The retreat of the western Laurentide Ice Sheet commenced by at least 15 000 cal yr BP, while the minimum timing of ice free conditions between the Laurentide Ice Sheet and the Cordillera is after 11 000 cal yr BP. A lack of data in the Keewatin sector prevents the determination of a precise timing of ice free conditions in the last vestiges of the Laurentide Ice Sheet. The model provides a guide to where additional samples could improve chronological control on ice margin location.

3.1 Introduction

The Laurentide Ice Sheet covered most of Canada and parts of the northern United States, reaching a maximum extent at the Last Glacial Maximum, between 26.5-19 ka (Clark et al., 2009). The ice sheet retreated over a period of 14 000-16 000 years, affecting global climate and sea level. Dyke and Prest (1987) and Dyke (2004) pre-

sented a reconstruction of the margins of the retreat of the Laurentide Ice Sheet, based on median ages of uncalibrated radiocarbon dates (Dyke et al., 2003), glacial geomorphological features (*i.e.* moraines, ice contact deltas, meltwater channels), and glacial flow features that indicate the most likely direction of ice retreat. Uncertainties in margin position are one of the largest potential sources of error in ice sheet reconstructions and models (*i.e.* Tarasov et al., 2012). In this paper, I create a model of the minimum timing of ice free conditions in the western Laurentide Ice Sheet. The model is developed using techniques similar to those applied by past workers such as Dyke and Prest (1987) and Dyke (2004) though, instead of determining a model of margin positions, chronological data are extrapolated in the direction opposite of retreat to determine the minimum timing of retreat. These results can be used as constraints for ice sheet models, by determining the region certain to be ice free for any time period. The model also serves as a basis for determining where more data would best improve temporal controls of ice margin reconstructions.

The western Laurentide Ice Sheet includes the region of ice that flowed from the Keewatin sector (Fig. 3.1). It converged with the Cordillera Ice Sheet to the west, and extended into northern midwestern United States (Dyke, 2004). The easternmost boundary of this sector lay in northwestern Ontario and Manitoba, where ice from northeastern sectors also influenced the direction of flow. The retreat of ice in this region has implications for major climatic events (*i.e.* Tarasov and Peltier, 2005; Broecker, 2006; Gregoire et al., 2012), the drainage of glacial lakes (*i.e.* Fisher et al., 2002; Teller et al., 2002; Teller and Leverington, 2004; Broecker, 2006; Fisher et al., 2009; Fisher and Lowell, 2012), and the migration of mammals in deglacial and post-glacial North America (*i.e.* Meltzer, 2003; Burns, 2010).

It is important to recognise that radiocarbon dates only provide a minimum timing of retreat. There is an unknown period of time between when ice retreated

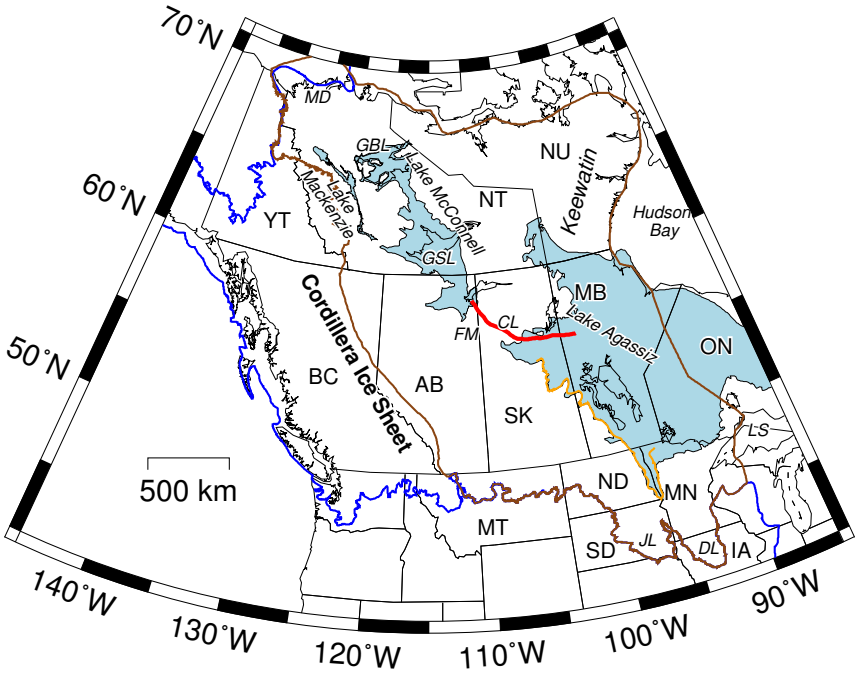

Figure 3.1: Map of the western Laurentide Ice Sheet and adjacent areas. The maximum extent of late Wisconsin ice is shown by the blue line, based on maps by Dyke (2004), and the "Illinoian" maximum extent by Fullerton et al. (1995, 2004, 2007), Hallberg et al. (1994) and Swinehart et al. (1994), which is now suspected to date to the late Wisconsin (Jackson et al., 2011). The brown outline is the area investigated in this study, which is bounded on the west by the convergence zone of the Laurentide and Cordillera ice sheets. The area covered by glacial lakes Mackenzie (Smith, 1992), McConnell (Smith, 1994) and Agassiz (Leverington and Teller, 2003) are shown in lightblue. The Upper Campbell Beach, the most extensive beach of Lake Agassiz, is shown in orange (Fisher and Lowell, 2012). The location of the Cree Lake Moraine (CL) is shown with a red line (Fulton, 1995). Locations mentioned in this paper: MT - Montana; ND - North Dakota; SD - South Dakota; MN - Minnesota; IA - Iowa; BC - British Columbia; AB - Alberta; SK - Saskatchewan; MB - Manitoba; ON - Ontario; YT - Yukon; NT - Northwest Territories; NU - Nunavut; JL - James Lobe; DL - Des Moines Lobe; GSL - Great Slave Lake; GBL - Great Bear Lake; LS - Lake Superior; MD - Mackenzie Delta; FM - Fort McMurray region

from a region and when organisms reoccupied it. The full suite of available radiocarbon dates also represent results from a wide variety of studies, many that were not attempting to constrain the precise timing of retreat. These data nevertheless provide estimates of the minimum timing of ice free conditions. During the past 20 years, researchers have also started to use surface exposure and luminescence dating methods to constrain the retreat of the Laurentide Ice Sheet (*i.e.* Duk-Rodkin et al., 1996; Jackson et al., 1997, 1999, 2011; Wolfe et al., 2004, 2007; Davis et al., 2006; Lepper et al., 2007; Murton et al., 2007; Munyikwa et al., 2011). These methods provide an independent means of determining the timing of ice sheet retreat from radiocarbon dating, and they do not require the presence of organic material to determine that ice is absent.

Dates in key locations provide the minimum timing of ice free conditions for their location and deglaciated regions in the direction opposite of retreat. The direction of retreat can be inferred directly using marginal features such as end moraines or, when absent, from ice flow indicators and eskers, which is the basis for margin reconstructions (*e.g.* Dyke, 2004). The continuity of ice free areas laterally from the sample may be less certain and the confidence should be down-weighted.

In this paper, I determine the minimum timing of ice free conditions of the area covered by the western Laurentide Ice Sheet. This involves assessing the currently available chronological data that indicate ice free conditions, and rejecting samples that may be affected by contamination and give anomalously old ages. I produce a spatial and temporal model of the minimum timing of retreat using the calibrated age of these data.

3.2 Dating methods

3.2.1 Radiocarbon dating

Temporal control on the retreat of the western Laurentide Ice Sheet comes primarily from radiocarbon dates. An updated version of the compilation by Dyke et al. (2003) (A.S. Dyke, pers. comm. 2010) was the source of the majority of radiocarbon dates used in this study. These are supplemented by samples from recent studies that have focused on the chronology of strandlines and drainage routes of glacial Lake Agassiz (*e.g.* Lowell et al., 2005, 2009; Teller et al., 2005; Yansa and Ashworth, 2005; Boyd, 2007; Fisher, 2007; Lepper et al., 2007; Fisher et al., 2009; Anderson, 2012; Fisher and Lowell, 2012), other studies focusing on ice sheet retreat, glacial geology and other glacial lakes (*e.g.* Fulton et al., 2004; Dredge and McMartin, 2005; Bateman and Murton, 2006; Little, 2006; Couch and Eyles, 2008; Huntley et al., 2008; Yu et al., 2010; Breckenridge et al., 2012) plus other studies that did not have a particular focus on the retreat of the Laurentide Ice Sheet but nonetheless provide evidence of ice free conditions (a compilation of samples used in this study is available as an electronic supplement).

Radiocarbon dates need to be calibrated to account for changes in the concentration of ^{14}C in the atmosphere. OxCal 4.1 (Bronk Ramsey, 2009) is used to calibrate dates in this study. Terrestrial samples were calibrated using the IntCal09 curve, while marine samples used the Marine09 curve (Reimer et al., 2009). Calibrated radiocarbon dates are denoted as "cal yr BP", while uncalibrated dates are denoted as "^{14}C yr BP". Ages reported in this paper are at the 95% confidence interval, rounded to the nearest hundred years, though the full calibrated distribution is used in the modelling.

Organisms that grew in marine environments have measured ages that are older than their true age due to the delay in incorporation of atmospheric ^{14}C into the

water, the upwelling of ^{14}C deficient waters by currents, and the influx of glacial meltwater into the ocean (Hutchinson et al., 2004; Coulthard et al., 2010; Vickers et al., 2010). An estimation of the deficiency of ^{14}C in a modern reservoir is made by finding the difference between the true and apparent ages of pre-bomb molluscs of known age (*i.e.* McNeely et al., 2006). Subtracting that value from the apparent age of the samples gives an improved estimate of its true age. Coulthard et al. (2010) made an estimation of modern reservoir age by comparing the ages of molluscs of known age with their measured radiocarbon ages. The difference between the local reservoir age and the globally averaged value (ΔR) is subtracted before calibration. For samples from northern mainland Northwest Territories and Nunavut, the modern reservoir correction of $\Delta R = 335 \pm 85$ is used (Coulthard et al., 2010). Deposit feeding molluscs, such as *Portlandia arctica*, can have a larger, unpredictable reservoir age compared to suspension feeder molluscs from the same region (England et al., 2013). Due to this, these species, along with samples where species identification are not provided, are excluded from the main analysis in this study.

The magnitude of the marine reservoir effect varied through time in glaciated regions (Barber et al., 1999; Kovanen and Easterbrook, 2002; Hutchinson et al., 2004; McNeely et al., 2006; Coulthard et al., 2010; Vickers et al., 2010), so the modern value may not be appropriate. For instance, Vickers et al. (2010) found that the postglacial reservoir offset in Hudson Strait was $\Delta R = 615 \pm 15$, which is 375±25 years larger than the modern value of $\Delta R = 240 \pm 15$ (McNeely et al., 2006). Southampton Island, located at the northern end of Hudson Bay has a postglacial reservoir offset of $\Delta R = 263 \pm 48$ (Ross et al., 2012). The island is situated at the boundary of two oceanographic subdivisions used by Coulthard et al. (2010). The postglacial reservoir age in that location is greater than the modern value for Hudson Bay ($\Delta R = 110 \pm 65$) and lower than the modern value of the Foxe Basin ($\Delta R = 310 \pm 90$), and $\Delta R = 352 \pm 52$ years lower than the early postglacial offset

in Hudson Strait (Vickers et al., 2010). Ross et al. (2012) attributed the lower postglacial reservoir offset on Southampton Island relative to Hudson Strait to the presence of non-calcareous Precambrian bedrock. Coulthard et al. (2010) separated Hudson Bay and James Bay into two regions, finding offsets of $\Delta R = 110 \pm 65$ and $\Delta R = 395 \pm 115$, respectively. Barber et al. (1999) found a modern marine reservoir offset of $\Delta R = 310 \pm 50$ for southeastern Hudson Bay and James Bay. They stated that modern correction in the Hudson Bay region would be conservative compared to early postglacial time due to increased runoff from retreating ice sheets, and the abundance of freshly glacially eroded carbonate bedrock.

The apparent age of marine samples from southwestern Hudson Bay after deglaciation provide evidence that the reservoir age is greater than the modern value. The age of marine organisms found in southwestern Hudson Bay must postdate the 8.2 ka event, a climate change event associated with the drainage of lakes Agassiz and Ojibway into the northern Atlantic Ocean, which happened between 8490–8040 cal yr BP (Lewis et al., 2012). The final drainage event may correspond to when Hudson Bay became ice free (Barber et al., 1999), though initial drainage may have been subglacial (Roy et al., 2011). Regardless, the calibrated age of marine organisms in this region must postdate this drainage event, as ice within Hudson Bay would have blocked the incursion of marine water. An estimate of the timing of marine inundation into southwestern Hudson Bay was made using OxCal's "boundary" functionality (Fig. 3.2, Bronk Ramsey, 2009). A total of 18 marine shell samples dating between 8200 and 7000 ^{14}C yr BP from northern Manitoba, derived from Morlan et al. (2000), were used to model the beginning of marine inundation into Manitoba. The timing of the event was tested using using no additional marine reservoir correction ($\Delta R = 0$), the modern value ($\Delta R = 110 \pm 65$, Coulthard et al., 2010), and the sum of the modern correction and the additional offset of 375±25 found in the Hudson Strait (Vickers et al. 2010, $\Delta R = 470 \pm 100$). The modelled

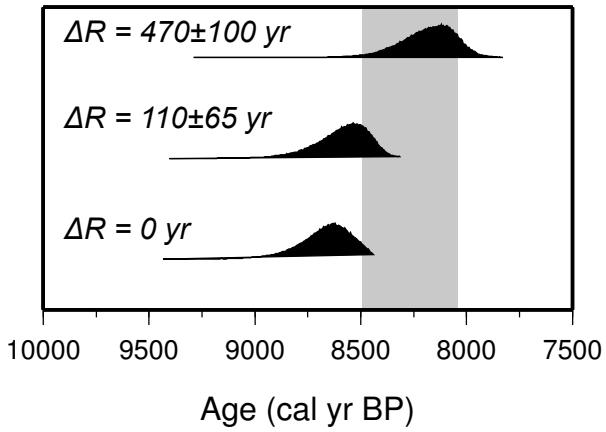

Figure 3.2: Probability distributions for the timing of the initial inundation northern Manitoba by the Tyrrell Sea. The grey bar is the approximate timing of the 8.2 ka event (Lewis et al., 2012). The distributions correspond to models using the given ΔR values.

age of marine inundation for northern Manitoba is older than the inferred timing of the 8.2 ka event using the modern reservoir correction (Table 3.1, Fig. 3.2). The modelled age of marine inundation falls within the 8.2 ka event using the larger value ($\Delta R = 470 \pm 100$) (Table 3.1). This ΔR value is used to correct marine samples from the Hudson Bay region. This correction is only a minimum value if the 8.2 ka event was caused by subglacial drainage of the lakes (*i.e.* Lajeunesse and St-Onge, 2008), rather than the complete deglaciation of Hudson Bay that would have allowed sea water to enter the region.

Table 3.1: Modelled age of the initial inundation of northern Manitoba by sea water

ΔR	95% probability range	median age	mode age
0	8895–8470	8655	8630
110 ± 65	8920–8385	8575	8535
470 ± 100	8520–7960	8175	8120

The incorporation of pre-glacial organic material, lignite, hydrocarbons, carbonate rocks, and hardwater effects can cause radiocarbon dates on bulk sediments to appear older than their true age (*i.e.* Deevey et al., 1954; Ogden, 1977; Nam-

budiri et al., 1980; MacDonald et al., 1991; Shore et al., 1995). In regions previously glaciated by the western Laurentide Ice Sheet, measurements of bulk sediment can be several hundred to over 1000 years older than contemporaneously deposited terrestrial macrofossils (MacDonald et al., 1991; Grimm et al., 2009). The heterogeneous composition of sediments and peat can cause variability in the apparent age of material taken from the same horizon (*e.g.* Brock et al., 2010, 2011). Abbott and Stafford (1996) have also showed that anomalously old ages can occur in lakes in the Arctic, even when the local bedrock geology does not contain carbonates. The age of such sediments may be influenced by the input of old material from around the basin (Bertrand et al., 2012). Before the advent of accelerator mass spectrometry (AMS) dating methods that allowed the measurement of small samples, bulk sediment, peat and gyttja were used often to constrain the timing of ice sheet retreat. It may be appropriate to use bulk sediment or peat samples if it is clear that the material is predominately terrestrial plant material (*i.e.* Nilsson et al., 2001), but often this information is not reported or known. Dyke et al. (2003) rejected most samples that were most likely affected by recycled carbon and hardwater effects, but kept samples where it was less clear. Other studies of the retreat of the western Laurentide Ice Sheet (*e.g.* Clayton and Moran, 1982; Teller, 1989; Arnold, 2002; Fisher, 2007; Fisher et al., 2009) have rejected samples where the material sampled could be contaminated. In this study, where the purpose is determining the minimum timing of deglaciation, samples that may give anomalously old ages, such as bulk sediments and peat, are rejected. A comparison of the minimum timing of retreat with and without these samples is presented as an electronic supplement.

3.2.2 Surface exposure and luminescence

Surface exposure and luminescence methods are alternative dating methods that have been used to provide estimates on when regions became ice free, and avoids the

problem with the unknown duration of time between deglaciation and the colonisation of plants and animals (*e.g.* Jackson et al., 1997, 1999; Wolfe et al., 2004; Munyikwa et al., 2011). Surface exposure dating involves the measurement of the relative abundance of elements formed by cosmogenic radiation bombarding exposed rock (Zreda and Phillips, 2000; Gosse and Phillips, 2001). This method requires estimates of the erosion rate and how shielded the rock is from the direct exposure (*i.e.* snow cover, topographical relief). The studies that presented surface exposure dates concluded that these effects were small (*e.g.* Jackson et al., 1997, 1999; Davis et al., 2006; Bednarski and Smith, 2007). There also is the possibility that the rock was exposed prior to glaciation, which increases the apparent age of exposure (*e.g.* Jackson et al., 1997), or that the samples first became exposed after eroding out of glacial deposits, giving an age that post-dates deglaciation (*e.g.* Jackson et al., 1999). Due to these uncertainties, surface exposure dates are not used in the main analysis of the minimum timing of retreat. Luminescence dates provide the timing of deposition and burial of silicate minerals such as quartz and feldspar (Forman et al., 2000). To acquire an accurate date, the minerals must be sufficiently exposed to light prior to burial to reset the signal. Dates from aeolian deposits are likely to have been fully exposed, and accurately record the timing of burial (*e.g.* Wolfe et al., 2004; Munyikwa et al., 2011; Bateman and Murton, 2006). Murton et al. (2010) collected samples from fluvial sediments, that are less likely to have been fully exposed to light. Since the material from that study was derived from post-glacial aeolian deposits, the dates should be reliable for the purposes of finding the minimum timing of retreat. Samples from studies dating strandlines were from the littoral zone of beaches (i.e. Lepper et al., 2007, 2011), maximising the likelihood of material being exposed prior to burial. Ages from these two methods are reported in this paper as "ka" with 1σ error ranges. Luminescence and surface exposure ages are reported relative to the year the sample was measured, so in the modelling they

are adjusted to be relative to 1950 A.D. for consistency with calibrated radiocarbon dates ages.

3.3 Chronological constraints on the minimum timing of retreat of the western Laurentide Ice Sheet

3.3.1 Radiocarbon dates

There are 604 radiocarbon dates available in the study region, most derived from an updated version of the compilation by Dyke et al. (2003) (A.S. Dyke *pers. comm.* 2010). A literature search was completed to find additional relevant radiocarbon samples from the study area.[1] The distribution of samples is biased to areas in the southern part of the study area and areas along the northern mainland coast (Fig. 3.3). There are few samples in the interior of mainland Northwest Territories and Nunavut, as well as northern Manitoba and Saskatchewan. For the analysis of the minimum timing of retreat, the radiocarbon dates were grouped into four different classes. There are 313 samples that are terrestrial materials, such as wood, charcoal, terrestrial plants and mammal fossils. These samples are regarded as having reliable dates. There are 49 samples of suspension feeding marine molluscs, and are deemed to be reliable after reservoir correction. There are 225 samples of sediment, peat, soil, marl, gyttja and aquatic plants and animals that have the potential of being affected by hardwater effects and old carbon, and were excluded from the main analysis. There are 17 samples that are deposit feeding marine molluscs, or where the species are not stated, which are excluded from the main analysis.

[1] A list of samples used in this study is included as an electronic supplement.

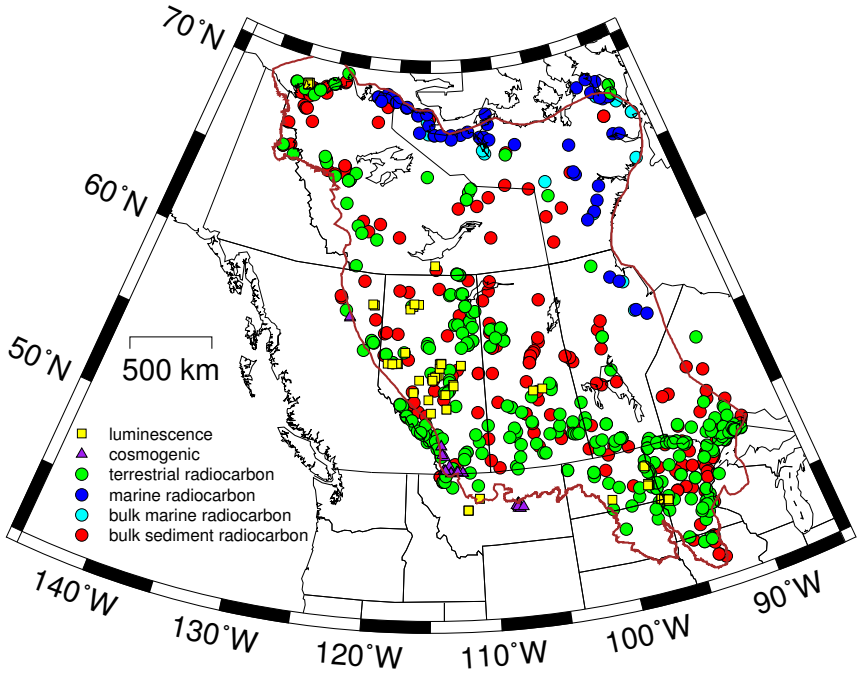

Figure 3.3: Map showing the location of chronological constraints relevant to the minimum timing of the retreat of the western Laurentide Ice Sheet. The brown outline is the area investigated in this study.

3.3.2 Luminescence dates

There are 84 luminescence dates that are relevant for determining the minimum timing of retreat in the study area. These data were collected for dating post-glacial sand dune formation (Wolfe et al., 2004, 2006, 2007; Munyikwa et al., 2011), the age of strandlines of glacial Lake Agassiz (Fisher et al., 2008; Lepper and Sager, 2000; Lepper et al., 2007, 2011, 2013) and late glacial events in the Mackenzie Delta (Bateman and Murton, 2006; Murton et al., 2007, 2010). In cases where a strandline can be traced to the contemporaneous ice margin, they provide a minimum timing of retreat for the entire length (*i.e.* Fisher and Lowell, 2012). Though not done in the main analysis, the Herman and Norcross strandlines impact the model from the period between 14,000 to 13 000 cal yr BP, while the Campbell strandline (Fig. 3.1) has a more limited impact from 11 000 to 10 000 cal yr BP.[2]

[2]Models including strandlines are included as an electronic supplement.

3.3.3 Surface exposure dates

There are 38 surface exposure dates relevant to deglaciation of the western Laurentide Ice Sheet. Most of these are ^{36}Cl dates that come from locations near the convergence zone of the Laurentide and Cordilleran ice sheets (Bednarski and Smith, 2007; Jackson et al., 1997, 1999, 2011). The ages of the samples are variable (20-10 ka), and depend in part on the determination of an appropriate erosion rate.

3.4 Direction of ice margin retreat

The determination of the direction of retreat assumes time transgressive formation of landforms, such as moraines, streamlined landforms and eskers. This methodology has been used in prior margin models (*i.e.* Bryson et al., 1969; Prest, 1969; Boulton et al., 1985; Dyke and Prest, 1987; Dyke, 2004). End and recessional moraines and crevasse-fill ridges formed roughly parallel to the recessional ice margin, while flutings, drumlins and other streamlined landforms that formed in the recessional phase are roughly perpendicular to the margin. Eskers and meltwater channels are other features that can form perpendicular to the direction of late stage ice retreat (Clark and Walder, 1994; Kleman and Borgström, 1996). In the Keewatin sector, the final retreat may have been by downwasting of an inactive ice sheet (Aylsworth and Shilts, 1989a), and eskers may better reflect the direction of retreat than flutings. Landforms inferred to have formed prior to deglaciation and had been overridden were excluded from the model.

Glacial landforms used to infer the direction of margin retreat are derived from a variety of published surficial geology maps, with scales ranging between 1:50 000 to 1:5 000 000. Retreat features for the northern United States and adjacent regions of Canada are sourced from USGS 1:1 000 000 Quaternary Geological Atlas of the United States maps (Goebel et al., 1983; Hallberg et al., 1994; Swinehart et al., 1994;

Sado et al., 1995; Fullerton et al., 1995, 2000, 2007). A map of glacial limits by Fullerton et al. (2004) is used to determine the inferred direction of retreat in Montana. Features for northern and central Manitoba come from a preliminary map of glacial features (McMartin et al., 2011,Trommelen and Ross, 2010, Trommelen et al., 2012, 2013, M. Trommelen *pers. comm*, 2012). Glacial features for Saskatchewan come from the Geological Atlas of Saskatchewan (McMartin et al., 2010; Hanson et al., 2011; Slimmon, 2011). In most of Alberta, recent interpretations of glacial features by Evans et al. (2008) are used. Features for much of mainland Northwest Territories are derived from Brown et al. (2011). Features for the Keewatin sector are predominantly derived from Aylsworth and Shilts (1989b). These sources are complemented by smaller scale maps in Alberta, British Columbia, Yukon, Northwest Territories and mainland Nunavut (a full list of sources is included as an electronic supplement). In regions without coverage, the 1:5 000 000 surficial materials map of Canada by Fulton (1995) is used. Maps that explicitly stated the relative chronology of glacial features were used as a guide to interpret the rest of the area (*e.g.* Little and Ferbey, 2003; McMartin and Dredge, 2005; Smith et al., 2007; Fisher et al., 2009; Trommelen and Ross, 2010; Bednarski, 2008; Brown, 2012).

A database of retreat direction vectors was compiled using ArcGIS 10.1 (ESRI, 2012) based on glacial and surficial geology maps. The vectors are perpendicular to margin normal features, such as recessional moraines, and parallel to flutings. The vectors are parallel to the trend of eskers that were used as constraints, with consideration of regional retreat patterns. Since the density of features is variable, the map of inferred direction of retreat was converted to a regular grid using a triangulated irregular network and linear interpolation of the vectors. The vectors were first interpolated onto a 1 km grid, and then averaged onto a 20 km grid. This size was chosen as a balance between the low resolution of landforms in some areas, and to be high enough to capture lobate ice margins and where significant changes

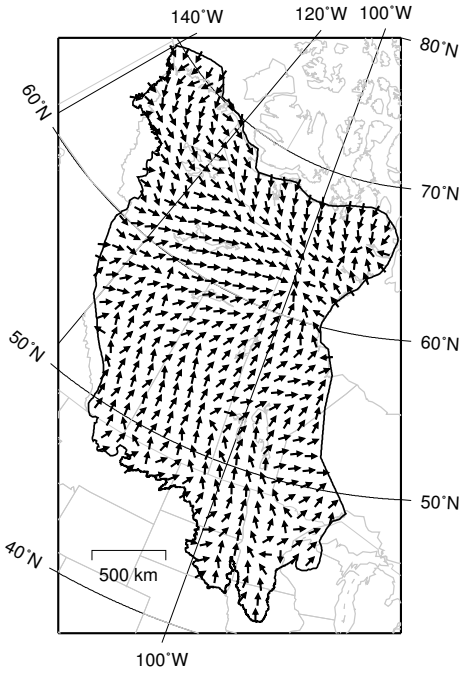

Figure 3.4: Map showing the direction of retreat on a 100 km grid. The black outline shows the region investigated in this study.

in the direction of retreat occurred. Fig. 3.4 shows a map of the direction of retreat at a grid resolution of 100 km[3].

3.5 Modelling the minimum timing of ice free conditions

A program was created in order to assess the minimum timing of retreat. The program extrapolates the probability distribution of the age of a dated sample in the direction opposite of retreat, using the assumption that the margin retreated in a time transgressive fashion (*i.e.* the margin retreated progressively from the Last Glacial Maximum limit to the Keewatin region). Instead of using the probability distribution to pinpoint an exact age of the sample, it is used to express increased confidence that the sample is older than a given date. For instance, if a sample has a normally distributed age of 9000±50 yr BP, then at 9000 yr BP there is 50%

[3]A map with the 20 km grid is included as an electronic supplement

confidence the sample is older than than that, while at 9100 yr BP the confidence is 97.8%. Note that the calibrated probability distribution is generally not normally distributed, so the sum of the area under the probability curve up to the desired age is used. The probability is scaled directionally using an azimuthal cos^2 function until it reaches zero in the direction normal to deglaciation. This function ensures that the maximum influence of the sample is in the direction directly opposite of retreat, and does not influence areas perpendicular to retreat. The scaling function changes direction at every grid point (20 km) defined by the retreat map. This allows the scaling function to be broader in areas where the direction of retreat is concave (such as lobate regions). The program imposes a tolerance to stop the extrapolation if the direction of retreat changes by more than 25° in adjacent grid points. This prevents extrapolation to areas glaciated by different sectors, such as the boundary between the Cordillera and Laurentide ice sheets. After extrapolation, the program stores the scaling factor on a 20 km grid. An example of the scaling function is shown on Fig. 3.5. The probability at each grid point is the sum of the age distribution of the sample up to the time of interest, multiplied by the scaling factor. For radiocarbon dates, the calibrated distribution determined by OxCal was used, while a scaled error function was used to calculated the probability of surface exposure and luminescence samples. At each grid point, the maximum value for all samples is taken as the confidence of ice free conditions.

3.6 Comparison of the model with bulk dates

Fig. 3.6 shows a comparison of the results with and without using bulk sediment and peat samples at 12 000 cal yr BP, corresponding to a period within the Younger Dryas. Drainage of glacial lakes located in the western Laurentide ice sheet has been suggested as being one of the factors for causing and maintaining this cold period (*e.g.* Tarasov and Peltier, 2005; Condron and Winsor, 2012; Not and Hillaire-Marcel,

2012). Murton et al. (2010) suggested that Lake Agassiz could be a possible source of this water, though investigations of the northwestern outlet by Fisher et al. (2009) and Fisher and Lowell (2012) cast doubt that the it was available before the late Younger Dryas. A sample of lake sediment northwest of Great Slave Lake (GSC-3524, 12 600-12 100 cal yr BP, MacDonald, 1987) has a large impact on the model and, if accepted, indicates that it is certain the area between the Laurentide Ice Sheet and the Cordillera is ice free at this time. As previously discussed, lake sediment samples can be contaminated by hardwater effects and old carbon, and could potentially give an age that is older than the true age. If this sample is rejected on this basis, the oldest dates from this region include a bison bone with an age of 11 300-10 300 cal yr BP (I-9997, Harington, 2003), and wood with an age of 10 400-9300 cal yr BP (AECV-915C, Smith, 1992), both of which postdate the Younger Dryas. Though there have been recently published dates related to the opening of the northwest outlet of Lake Agassiz (*i.e.* Fisher et al., 2009), there are still few constraints between the outlet and the Arctic Ocean, even with the inclusion of bulk dates. This is especially true in areas where the density of data is low, such as the area north of 60°N.[4] The minimum timing of retreat of the region between the northwestern outlet of Lake Agassiz and the Arctic Ocean significantly postdates the start of the Younger Dryas when bulk sediment dates are excluded, and less so when they are included.

3.7 Minimum timing of ice free conditions

Maps of the modelled minimum timing of retreat are shown for the time intervals used by Dyke (2004) to compare the certainty of ice free conditions with the inferred margin position (Fig. 3.7-3.9). Dyke (2004) used 500 year intervals in radiocarbon

[4]See electronic supplement for maps comparing models with and without bulk dates at 500 year intervals.

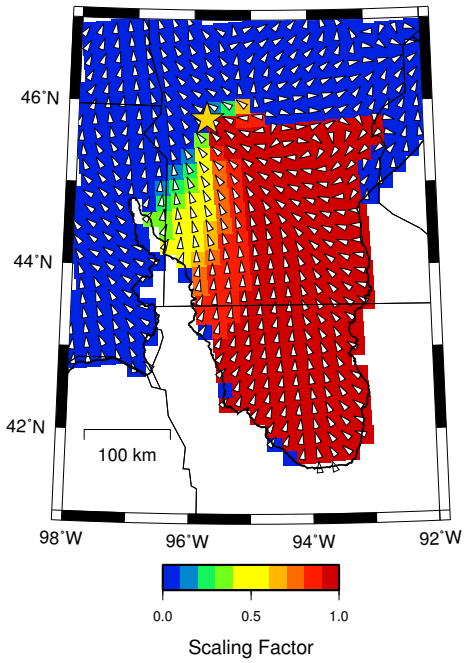

Figure 3.5: Example of the scaling factor applied to a sample located at 45.789°N 95.763°W (gold star, ETH-32331, Lepper et al., 2007) at the northern end of the Des Moines lobe. The white arrows are the inferred direction of retreat at a grid resolution of 20 km. The scaling factor is close to one in areas in the opposite direction of retreat, but is zero in areas glaciated by the Superior Lobe (Goebel et al., 1983).

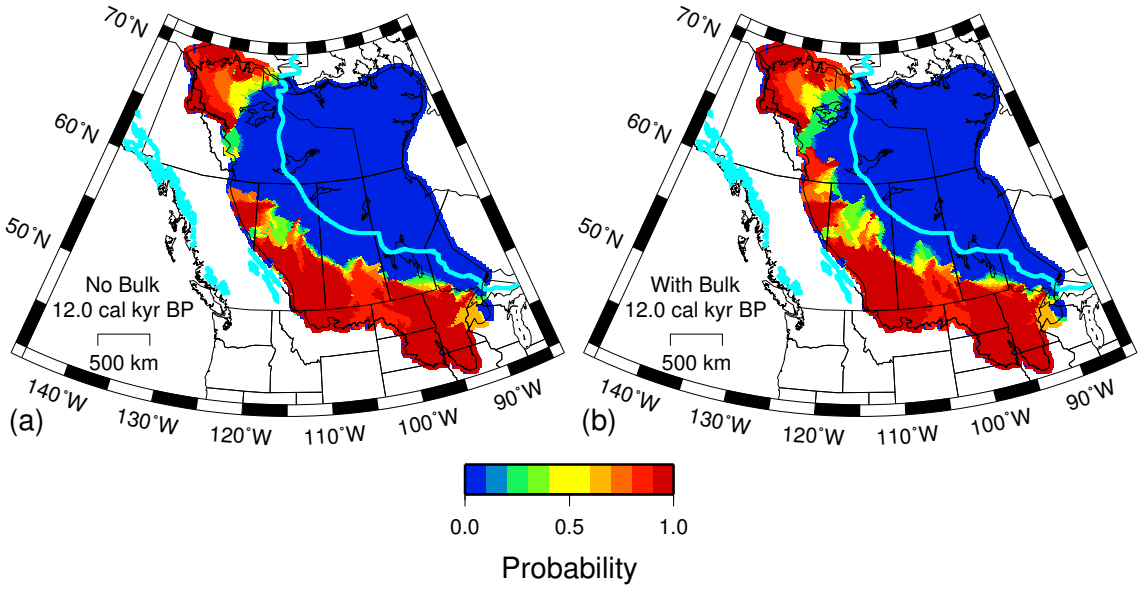

Figure 3.6: A comparison of the chronological constraints at 12,000 cal yr BP (a) without bulk sediment and peat samples (b) with bulk sediment and peat samples. The light blue line is the corresponding margin reconstruction by Dyke (2004) at 10.25 ^{14}C kyr BP.

years before present, and the actual timing in calendar years can be variable depending on how they are calibrated. To convert the margin model to calendar years, an error of 250 years at 1σ (half of the 500 year interval) is applied before calibration. The age used in the maps is the median calibrated age, rounded to the nearest 100 years. The following section highlights specific samples that have the most impact on the model.

3.7.1 Oldest dates constraining the minimum timing of retreat

The southwestern margin of the Laurentide ice sheet was marked by convergence with the Cordillera ice sheet (Dyke and Prest, 1987; Dyke, 2004). The oldest radiocarbon date from terrestrial material that postdates deglaciation in southwestern Alberta is a sample of wood, which has an age of 21 700-17 100 cal yr BP (TO-5190, Beierle and Smith, 1998). This sample lies in an area covered by till of Cordilleran origin (Bayrock and Reimchen, 1980), and indicates the end of convergence between the Laurentide and Cordilleran ice sheets at this latitude. Several surface exposure ^{36}Cl dates from the Foothills erratics train, which is near the confluence of the Cordillera and Laurentide ice sheets, are older than 15 ka (Jackson et al., 1997, 1999, 2011). The large range in ages from these boulders (28-11 ka) makes it difficult to use these to constrain the minimum timing of deglaciation. The oldest radiocarbon date that overlies Laurentide deposits is a sample of wood from northeastern British Columbia (TO-2742, 17 600-16 800 cal yr BP, Catto et al., 1996).

In the Dakotas, Minnesota and Iowa, the maximum extent of the Laurentide Ice Sheet was attained by the James and Des Moines lobes (Fig. 3.1, Clayton and Moran, 1982). The glacial history of this region is complicated, reflecting the dynamic nature of the southern margin of the Laurentide Ice Sheet. The minimum timing of deglaciation of the Des Moines lobe from its maximum extent is from a wood

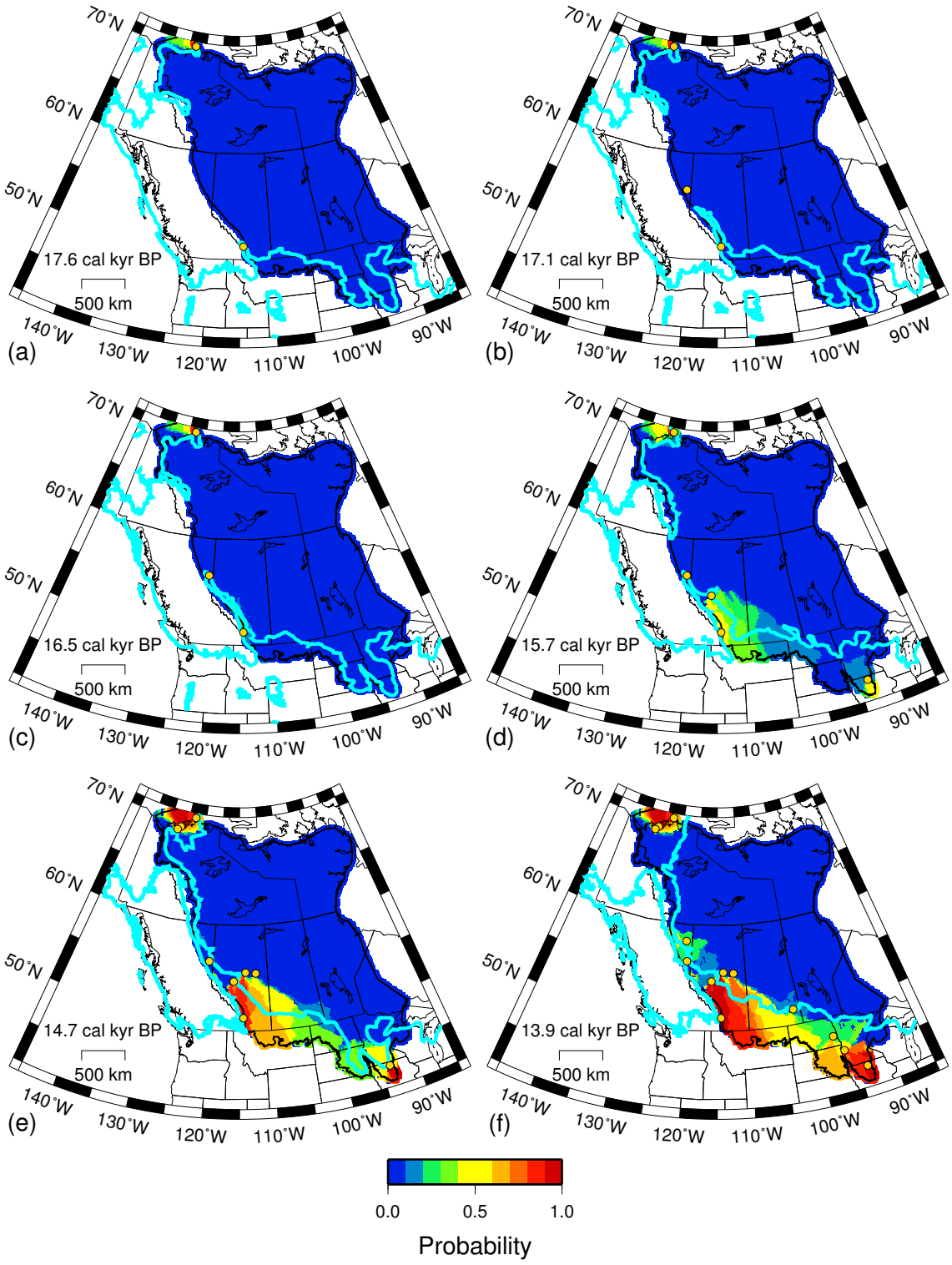

Figure 3.7: Minimum timing of retreat for early deglaciation of the western Laurentide Ice Sheet. The light blue line is the margin reconstruction by Dyke (2004). The yellow circles are the samples discussed in the text that have the most impact on the model. (a) 17.6 cal kyr BP (14.5 ^{14}C ky BP), (b) 17.1 cal kyr BP (14.0 ^{14}C ky BP), (c) 16.5 cal kyr BP (13.5 ^{14}C ky BP), (d) 15.7 cal kyr BP (13.0 ^{14}C ky BP), (e) 14.7 cal kyr BP (12.5 ^{14}C ky BP), (f) 13.9 cal kyr BP (12.0 ^{14}C ky BP)

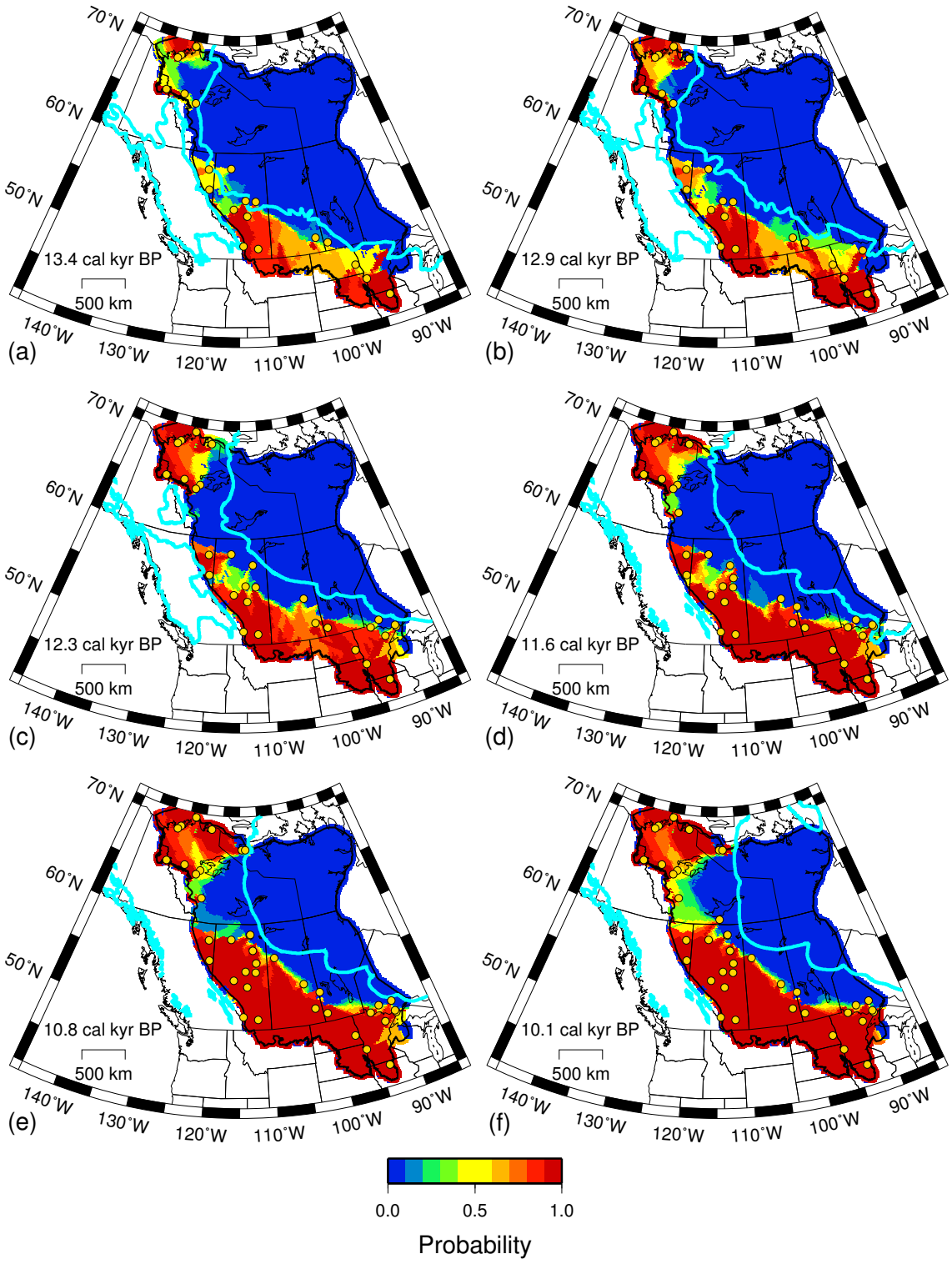

Figure 3.8: Minimum timing of retreat for deglaciation of the western Laurentide Ice Sheet in the late Pleistocene and early Holocene. The light blue line is the margin reconstruction by Dyke (2004). The yellow circles are the samples discussed in the text that have the most impact on the model. (a) 13.4 cal kyr BP (11.5 ^{14}C kyr BP), (b) 12.9 cal kyr BP (11.0 ^{14}C kyr BP), (c) 12.3 cal kyr BP (10.5 ^{14}C kyr BP), (d) 11.6 cal kyr BP (10 ^{14}C kyr BP), (e) 10.8 cal kyr BP (9.5 ^{14}C kyr BP), (f) 10.1 cal kyr BP (9.0 ^{14}C kyr BP)

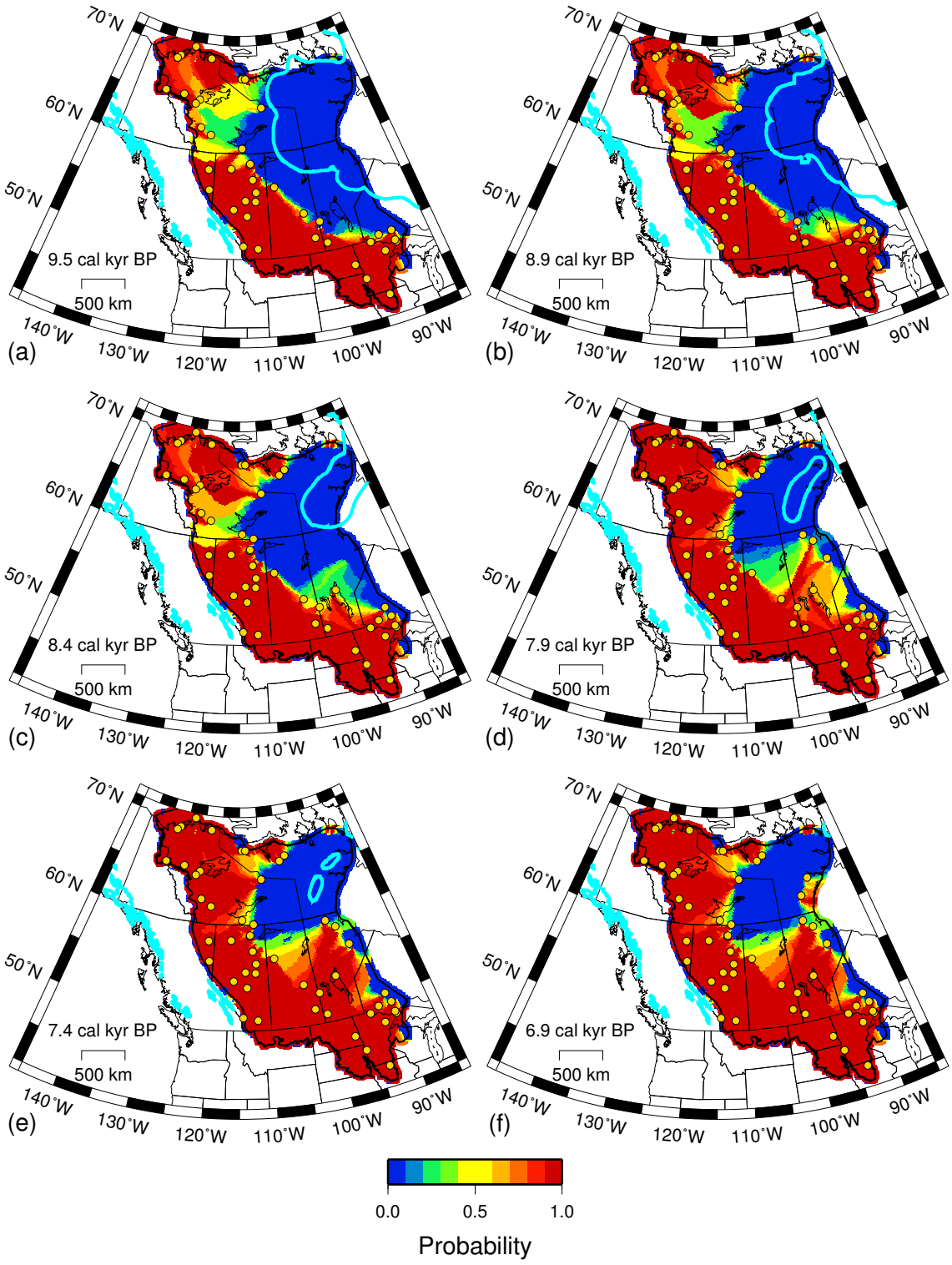

Figure 3.9: Minimum timing of retreat for deglaciation of the western Laurentide Ice Sheet in the early Holocene. The light blue line is the margin reconstruction by Dyke (2004). The yellow circles are the samples discussed in the text that have the most impact on the model. (a) 9.5 cal kyr BP (8.5 ^{14}C kyr BP), (b) 8.9 cal kyr BP (8.0 ^{14}C kyr BP), (c) 8.4 cal kyr BP (7.6 ^{14}C kyr BP), (d) 7.9 cal kyr BP (7.0 ^{14}C kyr BP), (e) 7.4 cal kyr BP (6.5 ^{14}C kyr BP), (f) 6.9 cal kyr BP (6.5 ^{14}C kyr BP)

sample, which has an age of 16 600-14 600 cal yr BP (W-626, Ruhe, 1969). There are no available deglacial terrestrial organic dates within the southern limits of the James Lobe, but a wood sample from below till near the southernmost extent has an age of 15 400-14 000 cal yr BP (Johnson and McCormick, 2005), indicating the maximum position may have been attained after the Des Moines Lobe.

In the northwestern Laurentide Ice Sheet, luminescence dates from sand that predates the last advance of the ice sheet have ages between 22 000 and 16 000 yr BP (Murton et al., 2007; Murton, 2009). A saiga antelope bone from the Mackenzie Lowlands region that has an age of 18 600-17 700 cal yr BP (Beta-25119, Harington and Cinq-Mars, 1995) may postdate glaciation, though the stratigraphic context of the sample was not clear. The next oldest dates are from grass samples in ice-proximal outwash, with ages of 16 400-15 200 and 16 200-15 100 cal yr BP (GSC-1995 and GSC-1784-2, Rampton, 1988).

3.7.2 Early retreat – 15 000 to 13 000 cal yr BP

By 15 000 cal yr BP, there is reasonable confidence that most of southern Alberta was free of ice, as indicated by luminescence dates from post-glacial sand dunes (Fig. 3.7, Wolfe et al., 2004; Munyikwa et al., 2011). Several dates from central Alberta have an impact on the model have ages of 15.7±1.6 ka (SFU-O-275, Wolfe et al., 2004), 15.4±1.1 ka (USU-524, Munyikwa et al., 2011) and 14.7±1.6 ka (USU-524, Munyikwa et al., 2011). The oldest radiocarbon dates from southern and central Alberta are from a bison bone with an age of 13 800-13 200 (AECV-1203C Burns, 1996) and a horse bone with an age of 13 800-13 200 (OxA-14273 Burns, 2010). Luminescence dates from northeastern British Columbia and northwestern Alberta indicate ice free conditions by about 13 000 cal yr BP (13.9±1.2 ka, SUV05309, and 13.4±1.2 ka, SAW05-01 Wolfe et al., 2007).

The Des Moines and James lobes are certain to have retreated north of the North

and South Dakota border by 14 000 cal yr BP (Fig. 3.7). Luminescence dates on sand from the Herman strandline of Lake Agassiz give an average age of 14.0±0.3 ka (Lepper et al., 2007, 2011). Radiocarbon dates on wood from this region (*e.g* ETH-32334, 14 500-13 800 cal yr BP, Lepper et al., 2011) support that areas south of 46°N were ice free. Terrestrial samples from southern Manitoba and Saskatchewan indicate ice free conditions existed north of the US-Canada border by 13 000 cal yr BP (GSC-1081, 13 900-13 100 cal yr BP Lowdon et al., 1971; S-553, 14 900-13 500 cal yr BP, Christiansen, 1979).

By 13 000 cal yr BP, northwestern mainland Northwest Territories and northern Yukon are certain to be ice free (Fig. 3.7). Terrestrial radiocarbon dates in Yukon near the maximum limit of glaciation indicate that retreat began before 13 800 to 13 400 cal yr BP. (GSC-2745, 13 800-13 400 cal yr BP, McNeely, 1989; OxA-18549, 13 800-13 500 cal yr BP, Zazula et al., 2009). There are several dates on wood from the Mackenzie River southwest of Fort Good Hope with ages greater than 13 000 cal yr BP, the oldest being 13 800-13 400 (TO-1190) and 13 800-13 100 (I-15020) (Smith, 1992). A sample of Hiatella arctica east of the Mackenzie Delta on the northern coast of mainland Northwest Territories has an age of 13 700-12 900 cal yr BP (AECV-643Cc, McNeely and Jorgensen, 1992).

3.7.3 Younger Dryas – 13 000 to 11 500 cal yr BP

Determining the chronology of potential northwest and eastern drainage routes of Lake Agassiz has been the focus of several recent studies (*i.e.* Teller et al., 2005; Lowell et al., 2005, 2009; Fisher et al., 2009), and several samples from these areas date to the Younger Dryas period (Fig. 3.8). The area near Lake Superior in northeastern Minnesota is certain to be ice free during the Younger Dryas, based on dates on wood (ETH-28939, 12 600-12 200 cal yr BP and ETH-31429, 12 600-11 800, Lowell et al., 2009; TO-1504, 13 200-12 100 cal yr BP, Bajc et al., 2000; W-827,

14 000-12 600 cal yr BP, Wright and Watts, 1969). Ice also had retreated north of the Minnesota-Ontario border, as indicated by a wood sample (ETH-32339, 12,600-12100 cal yr BP, Lowell et al., 2009). In the vicinity of the northwestern drainage route in Alberta, there are two terrestrial samples that provide a minimum timing of retreat during the Younger Dryas (ETH-30586, 12600-12100 cal yr BP and ETH-32165, 12400-11800 cal yr BP, Fisher et al., 2009). Other dates from this period in the Prairies include a bison bone from western Manitoba (BGS-617, 12 600-11 400, Nielsen et al., 1984) and wood from central Saskatchewan (S-3271, 13 500-11 500 cal yr BP, Christiansen et al., 1995). In the Northwest Territories, wood samples (AECV-917C, 12 600-11 400 cal yr BP, Smith, 1992; 13 000-12 600, GSC-6805, Dyke et al., 2003) indicate that much of the region occupied by glacial Lake Mackenzie was ice free during the Younger Dryas.

3.7.4 Early Holocene - 11 500 to 10 000 cal yr BP

There are a few samples that impact the minimum timing of retreat model in the early Holocene (Fig. 3.8). Several marine shell dates from northwestern mainland Nunavut are from this period, with the oldest ages of 11 500-10 800 cal yr BP (GSC-5999, McNeely, 2006) and 11 700-11 100 cal yr BP (GSC-6081, Dredge et al., 1999). A luminescence date south of Great Slave Lake has an age of 10.5±0.5 ka (SFU-O-159 Wolfe et al., 2004). There are several dates from northeastern Alberta that are early Holocene in age, but the samples that impact the model the most are two wood samples from a delta that formed in glacial Lake McConnell, with ages of 11 400-11 200 cal yr BP (WAT-2661 and WAT-2662, Smith, 1994). In western Saskatchewan the most significant date is a sample of plant macrofossils that has an age of 11 700-11 300 cal yr BP (UCIAMS-34698, Anderson, 2012). A sample of wood from northwest of Lake Superior with an age of 11 600-10 700 cal yr BP (ETH-31001, Lowell et al., 2009) impacts the model in the area north of the Ontario-Minnesota

border.

3.7.5 10 000–8000 cal yr BP

A few samples during the period between 10 000 and 8000 cal yr BP significantly increase the area constrained to be ice free (Fig. 3.9). Twigs from an ice contact deposit with an age of 10 000-9200 cal yr BP (TO-4241, Dredge et al., 1999) provide the minimum timing of retreat for a large region between Great Bear Lake and north of Great Slave Lake. A wood sample with an age 10 400-9300 cal yr BP (AECV-915C, Smith, 1992) indicates that southeastern glacial Lake Mackenzie was ice free. A twig (TO-7868, Seppä et al., 2003) and marine shell dates (GSC-110-2, Lowdon and Blake, 1968) indicate that the region southeast of Bathurst Inlet in Nunavut was ice free by 9000-8400 cal yr BP. Several wood samples from glacial Lake McConnell near the town of Fort Smith, Northwest Territories, date to this period, the oldest having an age of 9500-8700 cal yr BP (I-14568, Smith, 1994). Twigs from central Manitoba have an age of 8600-8400 cal yr BP (CAMS-32189 Morlan et al., 2000). Two marine shell samples with ages of 9000-7600 cal yr BP (BGS-813, Nielsen et al., 1986) and 8400-7900 cal yr BP (GSC-3070, Morlan et al., 2000) constrain the minimum timing of retreat to northern Manitoba. A charcoal sample from western Ontario has an age of 9400-8800 cal yr BP (Beta-111667, Dyke et al., 2003).

3.7.6 Final stages of glaciation - 8000–6000 cal yr BP

There are seven samples that are relevant to the minimum timing of retreat from 8000-6000 cal yr BP (Fig. 3.9). A woody scale from northern Manitoba has an age of 8200-7600 cal yr BP (CAMS-109288, Camill et al., 2012). Two marine shells from west of Hudson Bay in Nunavut have ages of 7400-6900 cal yr BP (GSC-5234, McNeely and Atkinson, 1995) and 7200-6700 cal yr BP (GSC-2042, McNeely and

Brennan, 2005). In northeastern mainland Nunavut, a marine shell date has an age of 6400-6000 (GSC-6839, Dredge and McMartin, 2005). There are three dates west of the Keewatin sector divide including marine shells with ages of 6800-6300 and 6500-6100 cal yr BP (GSC-693, Lowdon and Blake, 1968 and GSC-6857, McMartin et al., 2006) and a sample of Salix charcoal with an age of 6400-6100 cal yr BP (GSC-2152, McNeely, 1989). There are no samples that constrain the final timing of deglaciation for much of the Keewatin region of Nunavut.

3.8 Discussion

3.8.1 Comparison with margin reconstructions

Figures 3.7-3.9 show the inferred margin positions of Dyke (2004) along with this study's models of the minimum timing of deglaciation. In most cases, the minimum timing of deglaciation lags the ice free areas determined by Dyke (2004). The only exceptions are in Alberta, where recently published luminescence dates indicate earlier ice free conditions. There are a few causes for the lag between margin reconstructions and the minimum timing of deglaciation. During early deglacial times, the vegetation records indicate a tundra climate (Dyke et al., 2004), so there was likely limited production of plants that could be preserved for radiocarbon dating. The delay of recolonisation may not be present in all locations, as Fisher et al. (2009) suggested in the Fort McMurray area. Ice proximal lakes covered vast regions of the study area, and are often devoid of sufficient material suitable for radiocarbon dating (*e.g.* Risberg et al., 1999; Teller et al., 2000). Finally, the distribution of dates means that a single sample is often the only constraint on the timing of deglaciation over several hundred to thousands of km^2.

Of the several hundred radiocarbon and luminescence dates used to produce the models on Figures 3.7-3.9, only 55 have a significant impact on advancing the

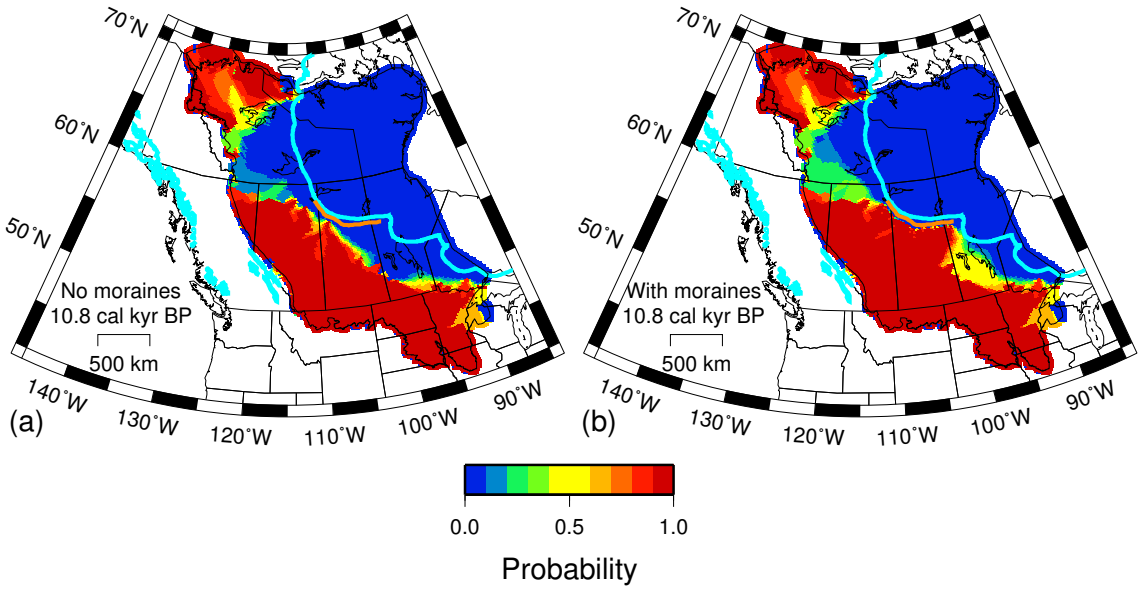

Figure 3.10: Probability of the minimum timing of retreat for deglaciation of the western Laurentide Ice Sheet at 10.8 cal kyr BP (a) without extrapolating the minimum age of the Cree Lake Moraine, and (b) extrapolating the age of the minimum age of 11 200-10 800 cal yr BP across the length of the moraine. Orange line is the location of the Cree Lake Moraine (Fulton, 1995). The light blue line is the margin reconstruction by Dyke (2004) at 10.8 cal kyr BP (9.5 ^{14}C kyr BP).

area constrained to be ice free based purely on absolute chronology. Additional constraints in key locations could greatly improve the model of the minimum timing of retreat. Extrapolation of constraints along broad moraines could provide the minimum timing of retreat over a wide area. For example, the Cree Lake Moraine in northern Saskatchewan (Fig. 3.1) has a minimum age of 11 200-10 800 cal yr BP (ETH-30175) according to Fisher et al. (2009). Fig. 3.10 shows the minimum timing of retreat when this age is extrapolated along its entire length at 10 800 cal yr BP. The reconstructed margin by Dyke (2004) at this time matches the boundary between where ice free conditions are certain and unknown in the model. Fig. 3.10 illustrates the sensitivity of the modelling technique, and how additional data would change the minimum timing of retreat. Acquisition of early dates in areas where there are few data would greatly reduce the uncertainty of the timing of deglaciation.

3.8.2 Northwest drainage route of Lake Agassiz

The timing of drainage of Lake Agassiz though northern Alberta has been the subject of many recent investigations (*i.e.* Lowell et al., 2005; Teller et al., 2005; Teller and Boyd, 2006; Fisher, 2007; Couch and Eyles, 2008; Fisher et al., 2009; Murton et al., 2010; Anderson, 2012; Fisher and Lowell, 2012). There is considerable debate as to when the northwest outlet was available to flow towards the Arctic Ocean, and if it was at the start, and possibly the cause of the Younger Dryas. The model of minimum timing of retreat (Fig. 3.9) shows that in the region between the Mackenzie Delta and the northwestern outlet of Lake Agassiz is only certain to be ice free during the early Holocene (section 3.7.4). Even when bulk dates are included (section 3.6), the minimum timing of retreat post-dates the start of the Younger Dryas. This does not completely eliminate the possibility that a glacial lake drained from the southwestern part of the ice sheet in the early Younger Dryas to account for the erosional event observed in the Mackenzie Delta by Murton et al. (2010), as there are few data between the two locations. The geomorphic and chronological evidence presented by Fisher et al. (2009) and Fisher and Lowell (2012) indicates that it was unlikely to be Lake Agassiz.

3.9 Conclusions

This study presents an assessment of the minimum timing of ice free conditions in the area covered by the western Laurentide Ice Sheet using previously published radiocarbon and luminescence dates. A map of the direction of retreat was constructed using geomorphic features, such as moraines, streamlined landforms and eskers. The direction of retreat was used to extrapolate chronological constraints to determine when areas were certain to be ice free. The model shows that there is a deficiency of data for large regions, with 55 samples identified as providing the greatest influence

on the model. In many areas, the margin chronology reconstructed by Dyke and Prest (1987) and Dyke (2004) is up to several hundred kilometres from the nearest constraint. This is most evident in areas north of 60°N, where there a single data point can be the only constraint over large regions. Some areas with a high density of significant dates include the area west of Lake Superior, central Alberta, and the glacial Lake Mackenzie basin. Excluding radiocarbon dates of questionable material makes the minimum timing of retreat over 1000 years younger in some locations. This has potential implications for ice sheet modelling, as early retreat from a region could cause ice volume to be underestimated, and impact the timing of meltwater when entered the ocean. Considering the contributions of the western Laurentide Ice Sheet to sea level change and the proposed impacts of its retreat on global climate during the late Pleistocene and early Holocene, there is a need for focused studies in areas identified by the model to improve understanding of retreat history.

3.10 Acknowledgements

Funding for this research was provided by ANU PhD and International Postgraduate Research scholarships. I thank my supervisor Paul Tregoning and my supervisory panel of Anthony Purcell, Kurt Lambeck and Thomas James for their support and feedback on this work. My gratitude goes to A.S. Dyke for sending me an updated version of his radiocarbon date database and Michelle Trommelen for sending me a preliminary database of glacial features for Manitoba. I appreciate discussions with Stewart Fallon and Rachel Wood on radiocarbon dating. Comments by Timothy Fisher, Rod Smith and an anonymous reviewer led to substantial improvements of this paper.

Chapter 4

Uplift rates determined from permanent GPS stations located in the area influenced by the western Laurentide Ice Sheet

4.1 Introduction

Vertical velocity estimates from Global Positioning System (GPS) observations have the potential to constrain GIA in North America (Calais et al., 2006; Sella et al., 2007; Argus and Peltier, 2010; Wu et al., 2010; Mazzotti et al., 2011). The present-day uplift rates measured in western Canada are amongst the highest in the world due to ongoing GIA. Recently networks of continuous and campaign GPS have been used for GIA studies for the Laurentide ice sheet (*i.e.* Sella et al., 2007; Argus and Peltier, 2010; Zhao, 2013; Peltier et al., 2015), with the purpose of determining Earth rheology. These measurements have also been used to remove the effects of GIA so that climatological information can be determined (*e.g.* Lambert et al., 2013). GPS measures deformation due to both GIA and hydrological effects (Tregoning et al., 2009b). If the hydrological effects are sufficiently large, it may not be possible to determine the GIA uplift rate accurately. This chapter gives an overview of the GPS

stations available in the study area, and investigates whether the calculated vertical velocity values are suitable for use in constraining the ice sheet model.

4.2 GPS data

4.2.1 Introduction

Eleven GPS stations with time series over eight years in duration were used for this study (Fig. 4.1). They were chosen based on their proximity to where effects of the GIA are likely to be observed (Wu et al., 2010). Since this study focuses on the western Laurentide Ice Sheet, only those stations in the area of influence of this region are considered. The raw uncorrected time series of height estimates are shown on Figs. 4.2 and 4.3.

The GPS time series are from a reanalysis of a global GNSS (global navigation satellite system) solution, provided by Michael Moore and Simon McClusky, known as the ANU/MIT (Australian National University and Massachusetts Institute of Technology) REPRO2 solution. The results of this reanalysis will be part of a new realisation of the international terrestrial reference frame (ITRF). The details of the reanalysis have yet to be published, but have been provided by M. Moore (pers. comm. 2014). The data are processed using GAMIT/GLOBK 10.5 (Herring et al., 2008), with corrections applied for atmospheric, oceanic, ionospheric and tidal effects, general relativity, and antenna and satellite phase centre variations. The resulting reference frame from the analysis is generally comparable with ITRF2008 (Altamimi et al., 2011).

In order to properly assess the true uplift rate and error, it is necessary to account for the fact that GPS data are affected by time-correlated noise sources. The time series were analysed using the Hector software, which uses the maximum likelihood estimation (MLE) method to assess the linear trend and noise parameters (Bos et al.,

2013). This software is designed to handle time series with significant gaps in measurements, which is beneficial as there are several time series with gaps of upwards of several years, such as Baker Lake (Fig. 4.2). Hector produces comparable results to the CATS software (Williams, 2008), which is commonly used to calculate trends in GPS data, but at a fraction of the computational time (differences in velocity determined by Bos et al. (2013) were less than 0.05 mm/yr). Prior to calculating the trend, outliers that exceeded a three-sigma criteria were excluded. The noise analysis included the determination of an annual component, and used power law and white noise models. Figures in the following sections show the modelled time series, as well as the residuals. The results of the analysis are shown in Table 4.1. The reported uncertainties throughout this study are one-sigma.

One potential problem with these data are changes in height that are unrelated to geophysical signals. If there is an offset due to problems with the station (*i.e.* equipment changes), this will affect the calculation of the linear rate. Information used in this study on the equipment and problems with the stations come from the International GNSS Service website (`http://igscb.jpl.nasa.gov/`). Receiver firmware changes prior to 2000 may also cause an offset in the data, because some receivers were unable to track the L2 phase properly (Tregoning et al., 2004). At stations where a sudden change in vertical position could be explained by equipment changes, an offset was calculated using Hector. Other undocumented equipment changes may cause offsets that can be detected in the residuals after subtracting the modelled linear and annual rates from the time series. In order to assess the impact of equipment changes, the rate at each site is first calculated with all equipment changes included as potential offset points (as well as any other visual offsets in the data). If a calculated offset was larger than zero at the two-sigma level, it was included in the final rate determination. The calculated offsets are shown in Table 4.2.

Table 4.1: Vertical velocity rates at GPS stations in the study area (in mm.yr^{-1}).

Location	Station	Latitude	Longitude	No changes	All changes	Selected changes
Baker Lake, Nunavut	BAKE	64.3178	-96.0023	13.04±0.39	12.00±0.53	12.56±0.43
Churchill, Manitoba	CHUR	58.7591	-94.0887	10.44±0.22	9.80±0.47	10.33±0.26
Lac Du Bonnet, Manitoba	DUBO	50.2588	-95.8662	0.14±0.28	1.42±0.39	1.17±0.31
Flin Flon, Manitoba	FLIN	54.7256	-101.9780	2.91±0.29	4.20±0.45	4.25±0.42
Ulukhaktok, Northwest Territories	HOLM	70.7363	-117.7612	2.77±0.30	2.62±0.44	2.70±0.33
Inuvik, Northwest Territories	INVK	68.1822	-133.3137	-2.98±0.46	-1.65±0.53	-1.28±0.46
North Liberty, Iowa	NLIB	41.7716	-91.5749	-1.44±0.27	-2.49±0.40	-2.24±0.30
Pickle Lake, Ontario	PICL	51.4798	-90.1620	5.03±0.57	6.28±0.72	5.68±0.62
Calgary, Alberta	PRDS	50.5216	-114.1736	-0.20±0.26	-0.58±0.38	-0.46±0.34
Saskatoon, Saskatchewan	SASK	52.1963	-106.3984	-0.32±0.31	-0.33±0.40	-0.32±0.31
Yellowknife, Northwest Territories	YELL	62.4809	-114.4807	5.88±0.24	6.41±0.31	6.45±0.25

Table 4.2: Calculated offsets at equipment changes

Date (yyyy-mm-dd)	Julian day	description	Offset (mm)
BAKE - all equipment changes			
2009-12-14	55179.5	antenna/receiver change	4.29±2.53
2011-11-16	55881.5	receiver change	5.32±1.67
2013-09-10	56545.5	receiver change	1.10±2.04
BAKE - two sigma			
2011-11-16	55881.5	receiver change	5.13±1.67
CHUR - all equipment changes			
1995-10-05	49995.5	firmware update	-1.69±1.79
1996-09-18	50344.5	receiver change	0.41±2.00
1996-12-14	50431.5	firmware update	-1.37±1.89
1997-12-18	50800.5	receiver change	2.02±1.88
1998-03-10	50882.5	receiver change	0.97±1.89
1999-02-22	51231.5	receiver change	1.91±1.84
1999-08-10	51400.5	receiver change	2.28±1.84

... Table 4.2 continued

Date (yyyy-mm-dd)	Julian day	description	Offset (mm)
2000-07-19	51744.5	antenna change	-4.26±1.89
2004-09-25	53273.5	antenna change	-1.22±1.87
2005-02-03	53404.5	antenna change	3.89±2.03
2008-03-10	54535.5	antenna/receiver change	1.36±2.40
2009-04-01	54922.5	antenna/receiver change	0.57±2.08
2010-09-02	55441.5	antenna/receiver change	-1.77±2.00
2011-02-02	55594.5	unknown	8.21±1.90
2011-06-08	55720.5	firmware update	-0.02±1.92
2011-08-26	55799.5	receiver change	0.50±1.89
		CHUR - two sigma	
2000-07-19	51744.5	antenna change	-3.72±1.84
2011-02-02	55594.5	unknown	7.25±1.73
		DUBO - all equipment changes	
1997-01-08	50456.5	antenna change	-18.96±1.92
1999-05-26	51324.5	firmware update	-1.58±1.89
1999-10-04	51455.5	antenna/receiver change	-19.52±2.54
2000-10-12	51829.5	receiver change	-2.44±1.84
2001-01-23	51932.5	receiver change	0.03±1.83
2004-11-26	53335.5	receiver change	-2.70±1.78
2009-08-27	55070.5	antenna/receiver change	6.42±1.76
2011-10-03	55837.5	receiver change	2.54±1.75
		DUBO - two sigma	
1997-01-08	50456.5	antenna change	-18.95±1.93
1999-10-04	51455.5	antenna/receiver change	-21.11±2.31
2009-08-27	55070.5	antenna/receiver change	6.98±1.76
		FLIN - all equipment changes	
1997-01-07	50455.5	antenna/receiver change	-9.05±2.03
1997-12-09	50791.5	receiver change	-0.59±2.00
1998-09-23	51079.5	receiver change	5.11±2.72
1998-12-10	51157.5	receiver change	3.21±2.13
1999-05-26	51324.5	firmware update	-5.69±2.07
1999-09-21	51442.5	antenna change	-11.52±2.03
2001-01-13	51922.5	receiver change	-0.29±1.96
2004-11-23	53332.5	unknown	-6.56±1.98
2009-05-13	54964.5	antenna/receiver change	-4.51±1.97
2010-12-21	55551.5	antenna/receiver change	5.78±1.96
		FLIN - two sigma	
1997-01-07	50455.5	antenna/receiver change	-8.83±2.05
1998-09-23	51079.5	receiver change	6.91±2.57
1999-05-26	51324.5	firmware update	-5.05±2.08

... Table 4.2 continued

Date (yyyy-mm-dd)	Julian day	description	Offset (mm)
1999-09-21	51442.5	antenna change	-11.04±2.05
2009-05-13	54964.5	antenna/receiver change	-4.15±1.99
2010-12-21	55551.5	antenna/receiver change	6.45±1.97
	HOLM - all equipment changes		
1997-01-07	50455.5	antenna/receiver change	-9.07±2.02
1998-09-23	51079.5	receiver change	6.33±2.52
1999-05-26	51324.5	firmware update	-5.30±2.04
1999-09-21	51442.5	antenna change	-11.34±2.01
2004-11-23	53332.5	unknown	-6.64±1.97
2009-05-13	54964.5	antenna/receiver change	-4.55±1.95
2010-12-21	55551.5	antenna/receiver change	5.63±1.94
	HOLM - two sigma		
2002-08-09	52495.5	antenna change	-4.48±1.61
2010-12-07	55537.5	receiver change	3.41±1.66
	INVK - all equipment changes		
2002-07-31	52486.5	receiver change	-2.40±2.20
2003-08-21	52872.5	antenna change	-20.95±2.21
2004-03-25	53089.5	firmware change	3.57±2.09
2005-05-13	53503.5	receiver change	2.15±2.07
	INVK - two sigma		
2003-08-21	52872.5	antenna change	-20.75±2.03
	NLIB - all equipment changes		
1994-10-24	49649.5	firmware upgrade	-2.29±1.81
1999-07-09	51368.5	firmware upgrade	0.82±1.97
1999-08-31	51421.5	firmware upgrade	2.23±1.97
2002-09-07	52524.5	unknown	9.79±1.80
2005-04-15	53475.5	receiver change	1.17±2.02
	NLIB - two sigma		
2002-09-07	52524.5	unknown	9.89±1.81
	PICL - all equipment changes		
2003-12-13	52986.5	antenna change	-1.16±2.56
2004-06-05	53161.5	receiver change	-2.85±2.46
2004-12-17	53356.5	antenna change	-5.31±2.62
2006-08-02	53949.5	antenna change	-2.75±2.30
	PICL - two sigma		
2004-12-17	53356.5	antenna change	-6.30±2.51
	PRDS - all equipment changes		
1999-06-24	51353.5	antenna/receiver change	0.10±1.81
2002-11-01	52579.5	antenna change	9.05±2.38
2003-05-21	52780.5	antenna change	-8.95±2.04

... Table 4.2 continued

Date (yyyy-mm-dd)	Julian day	description	Offset (mm)
2006-07-18	53934.5	antenna/receiver change	3.92±1.78
2012-07-27	56135.5	antenna/receiver change	1.79±1.75
		PRDS - two sigma	
2002-11-01	52579.5	antenna change	8.84±2.37
2003-05-21	52780.5	antenna change	-9.09±2.03
2006-07-18	53934.5	antenna/receiver change	3.77±1.77
		SASK - all equipment changes	
2008-09-13	54722.5	receiver change	-0.99±1.52
2008-12-10	54810.5	receiver change	0.89±1.50
2013-08-31	56535.5	antenna/receiver change	0.40±2.94
		YELL - all equipment changes	
1994-03-16	49427.5	antenna/receiver change	16.90±2.06
1994-05-11	49483.5	receiver change	0.23±1.98
1994-10-14	49639.5	antenna change	-0.83±1.95
1995-10-24	50014.5	firmware upgrade	-1.38±1.81
1996-08-22	50317.5	antenna change	-12.00±1.86
1996-12-19	50436.5	receiver change	-4.29±1.94
1999-08-10	51400.5	receiver change	0.73±1.77
2007-07-25	54306.5	receiver change	0.36±1.79
2013-07-17	56490.5	antenna/receiver change	1.12±1.86
		YELL - two sigma	
1994-03-16	49427.5	antenna/receiver change	16.74±1.99
1996-08-22	50317.5	antenna change	-12.30±1.84
1996-12-19	50436.5	receiver change	-4.48±1.93

4.2.2 Baker Lake, Nunavut (BAKE)

Baker Lake has the largest uplift rate of all the stations examined in this study (Fig. 4.4). The station has a recording gap of over two years between 2007 and 2010, but there was no significant calculated offset when recording resumed. The residuals show that a simple annual signal does not characterise the noise well, and only one equipment change appears to introduce a significant offset. In the first recording period (2003-2007), the residuals reach a maximum in the middle of the year, and a minimum in the winter period. In the second recording period

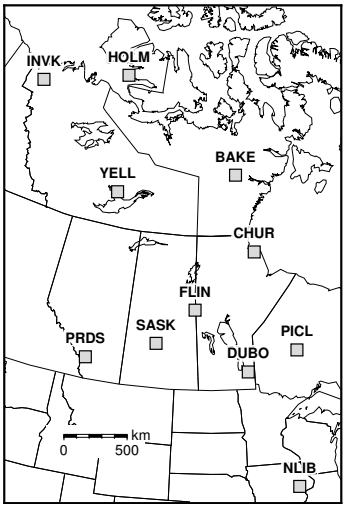

Figure 4.1: Location and uplift rates of GPS stations in the study area. See Table 4.1 for the location names.

(2009-2013), the situation is reversed. The cause of the reversal in timing of the peak annual amplitude is unknown. The velocity with the single offset in 2011 is 12.56±0.42 mm.yr^{-1}.

4.2.3 Churchill, Manitoba (CHUR)

The station at Churchill has data from 1994 to 2013 (Fig 4.5). This station has nearly 20 years of continuous data, from 1994 to 2013. There is an offset in the time series on February 2, 2011, though the cause is unknown (Julian day 55594). This offset appears in the residuals if not corrected for, so it is included. There were 15 equipment and firmware changes during the recording period. The largest calculated offset remains on February 2, 2011, twice as large in magnitude times as the largest calculated offset equipment changes. The largest calculated offset coinciding with an equipment change was on July 19, 2000. The residuals remain relatively uniform throughout the recording period, with the exception of 1998 to 2001, where they are higher than average. The calculated rate of 10.33±0.26 mm.yr^{-1} is the second largest of all the stations investigated in this study.

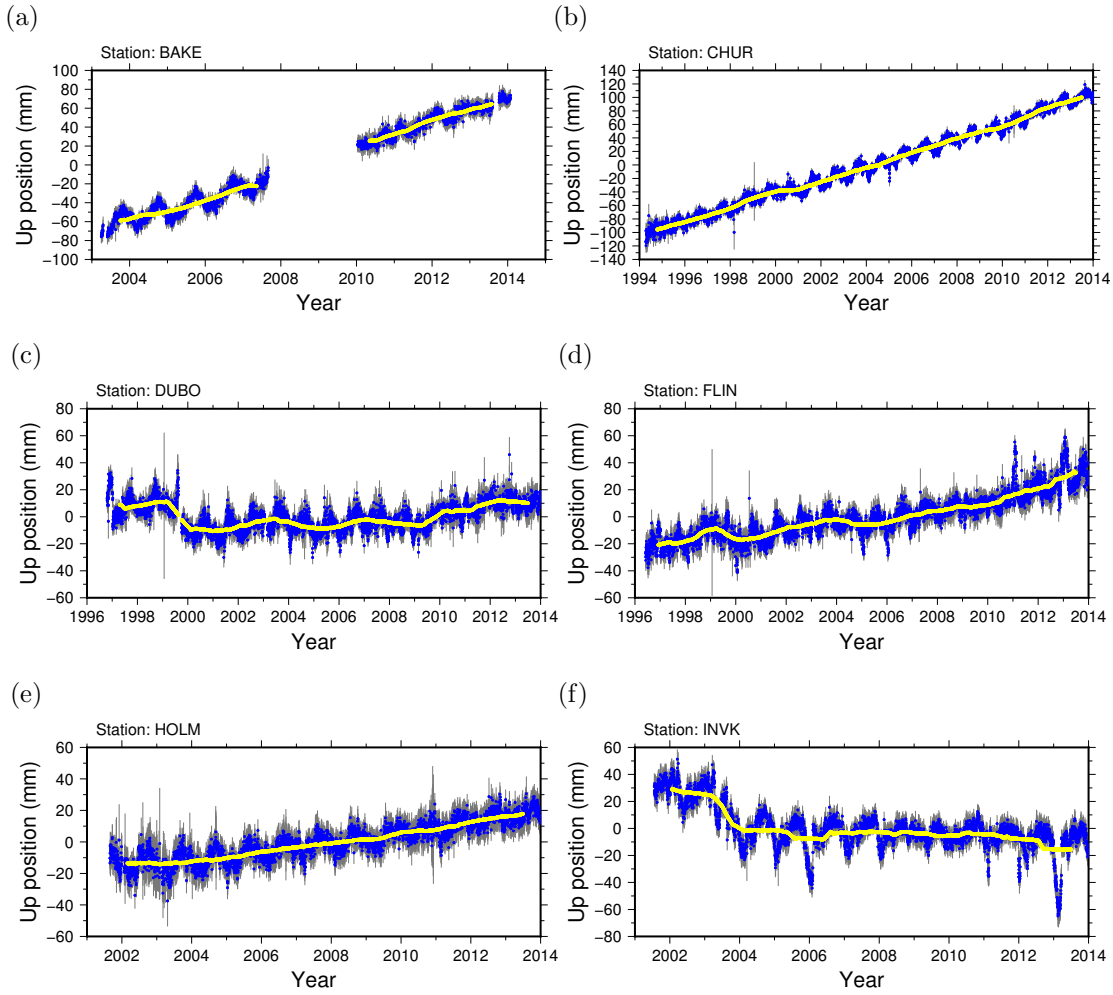

Figure 4.2: Raw vertical GPS time series. Blue dots are the daily solutions, grey lines are the one-sigma uncertainties, and the yellow line is the 365 day moving average. (a) Baker Lake, Nunavut (BAKE), (b) Churchill, Manitoba (CHUR), (c) Lac Du Bonnet, Manitoba (DUBO), (d) Flin Flon, Manitoba (FLIN), (e) Holman, Northwest Territories (HOLM), (f) Inuvik, Northwest Territories (INVK)

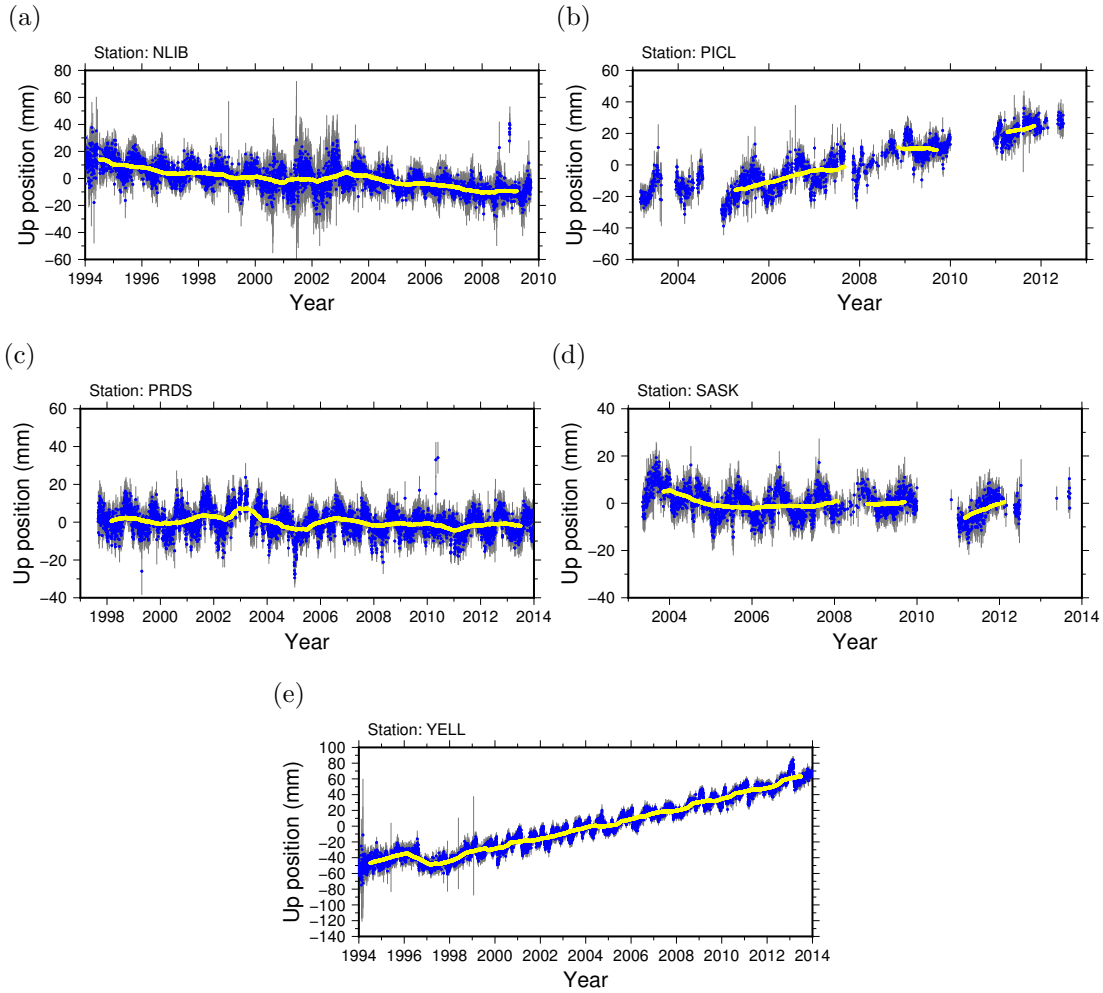

Figure 4.3: Raw vertical GPS time series. Blue dots are the daily solutions, grey lines are the one-sigma uncertainties, and the yellow line is the 365 day moving average. (a) North Liberty, Iowa (NLIB), (b) Pickle Lake, Ontario (PICL), (c) Calgary, Alberta (PRDS), (d) Saskatoon, Saskatchewan (SASK), (e) Yellowknife, Northwest Territories (YELL)

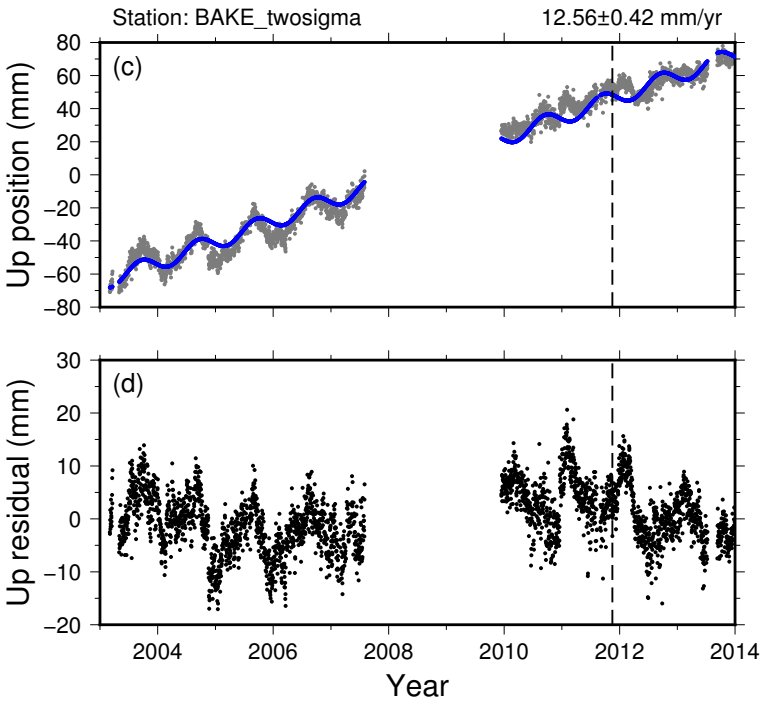

Figure 4.4: GPS Station at Baker Lake, Nunavut (BAKE). (a) Observed versus modelled data including calculated offsets at selected equipment changes (marked by the dashed vertical lines). Grey dots are the daily elevation estimates, the blue line is the modelled linear uplift plus annual rate calculated using Hector. (b) residuals (observations minus model)

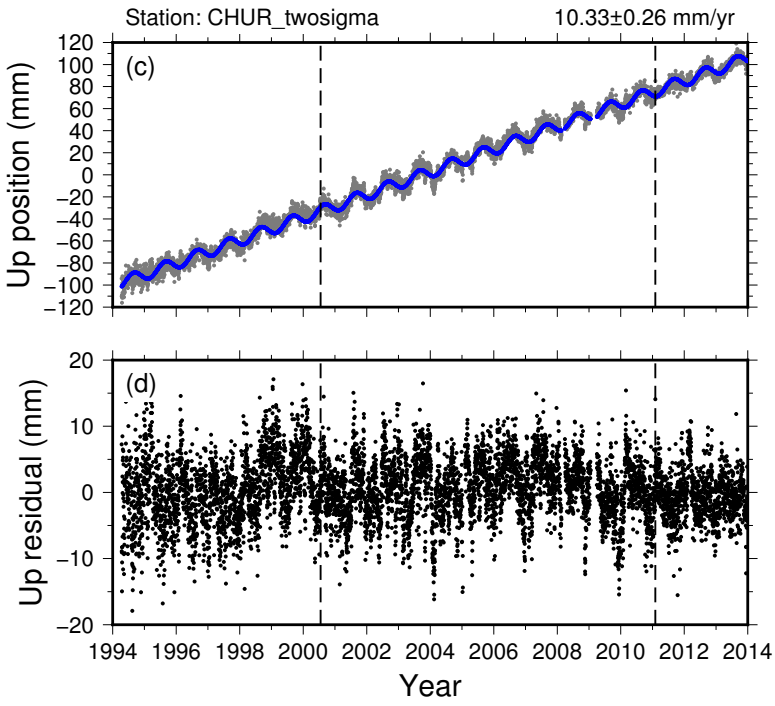

Figure 4.5: GPS Station at Churchill, Manitoba (CHUR). (a) Observed versus modelled data including calculated offsets at selected equipment changes (marked by the dashed vertical lines). Grey dots are the daily elevation estimates, the blue line is the modelled linear uplift plus annual rate calculated using Hector. (b) residuals (observations minus model)

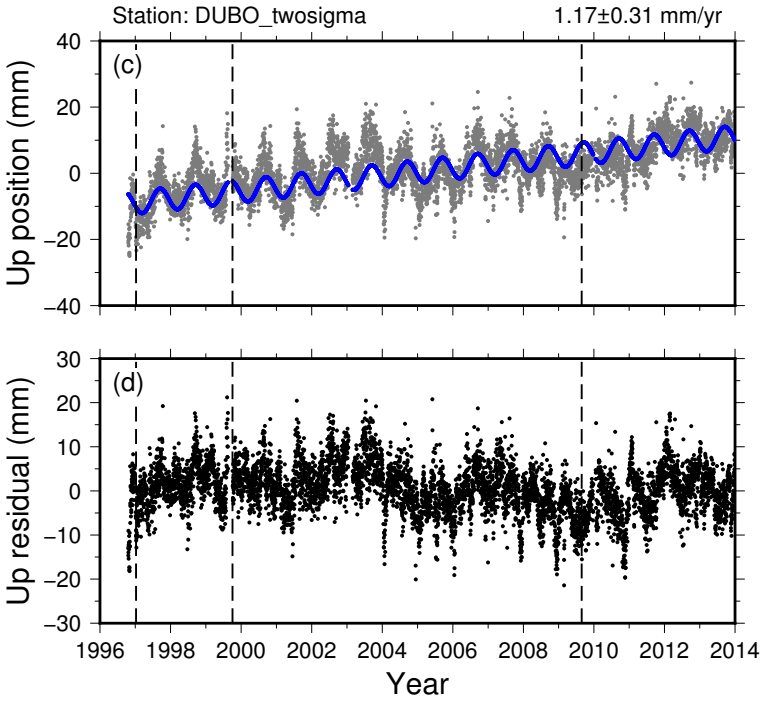

Figure 4.6: GPS Station at Lac Du Bonnet, Manitoba (DUBO). a) Observed versus modelled data including calculated offsets at selected equipment changes (marked by the dashed vertical lines). Grey dots are the daily elevation estimates, the blue line is the modelled linear uplift plus annual rate calculated using Hector. (b) residuals (observations minus model)

4.2.4 Lac Du Bonnet, Manitoba (DUBO)

The station at Lac Du Bonnet has data from 1996 to 2013 (Fig. 4.6). Offsets are readily apparent when antenna changes happened on January 8, 1997 and October 4, 1999. An offset introduced during a equipment change on August 27, 2009 is also significant. The resulting vertical velocity is 1.17±0.31 mm.yr^{-1}. The residuals show that there is significant correlated noise at periods greater than one year.

4.2.5 Flin Flon, Manitoba (FLIN)

The station at Flin Flon has data between 1996 and 2013 (Fig. 4.7). During the recording period, there were four antenna changes and eight receiver/firmware changes. Five of these changes were significant at the two-sigma level. The offsets

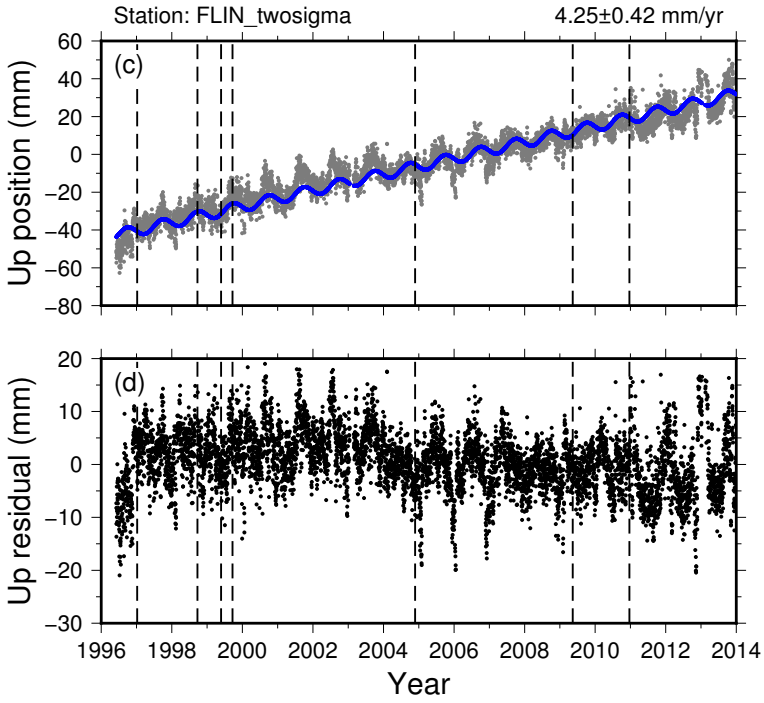

Figure 4.7: GPS Station at Flin Flon, Manitoba (FLIN). (a) Observed versus modelled data including calculated offsets at selected equipment changes (marked by the dashed vertical lines). Grey dots are the daily elevation estimates, the blue line is the modelled linear uplift plus annual rate calculated using Hector. (b) residuals (observations minus model)

calculated for the equipment changes in 2009 and 2010 have similar magnitude but opposite sign. There appears to be an offset in late 2004, although the cause is unknown. The calculated offset at this time is significant at the two-sigma level. The resulting rate is 4.25±0.42 mm.yr^{-1}.

4.2.6 Ulukhaktok (Holman), Northwest Territories (HOLM)

The station at Ulukhaktok has data from 2001 to 2013 (Fig. 4.8). An equipment change on August 9, 2002 and a receiver change on December 7, 2010 introduced offsets that were significant at the two-sigma level. The uncorrected rate is 2.70±0.33 mm.yr^{-1}.

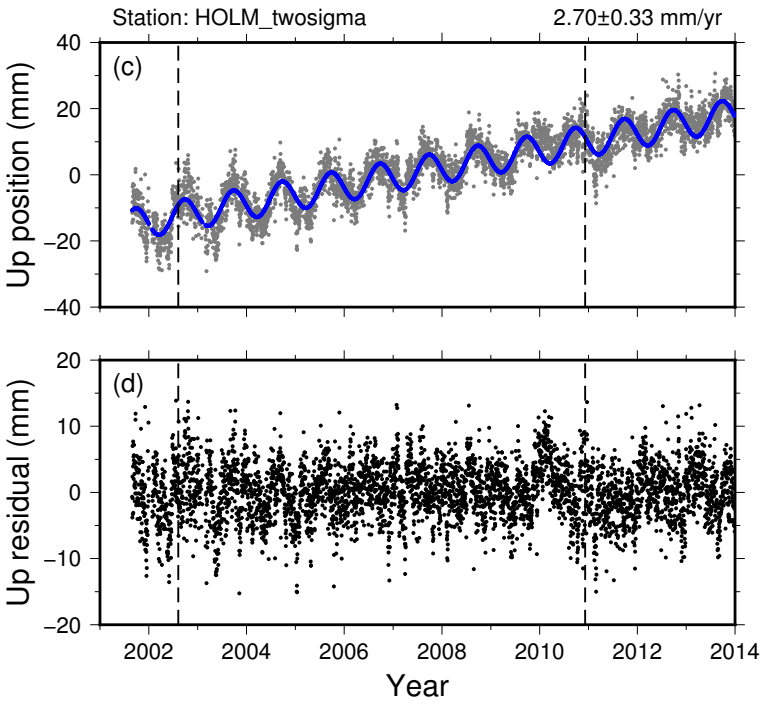

Figure 4.8: GPS Station at Ulukhaktok, Northwest Territories (HOLM). Observed versus modelled data including calculated offsets at selected equipment changes (marked by the dashed vertical lines). Grey dots are the daily elevation estimates, the blue line is the modelled linear uplift plus annual rate calculated using Hector. (b) residuals (observations minus model)

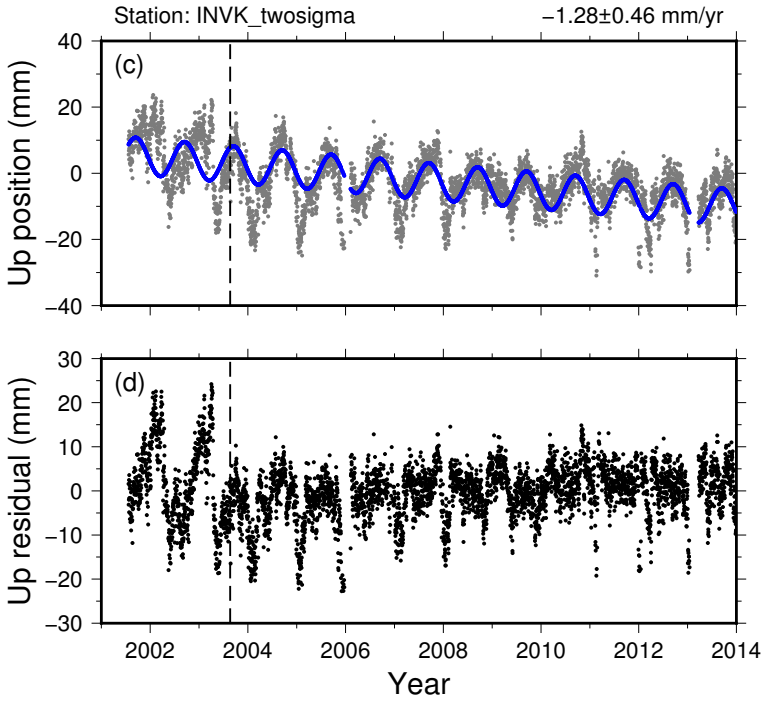

Figure 4.9: GPS Station at Inuvik, Northwest Territories (INVK). (a) Observed versus modelled data including calculated offsets at selected equipment changes (marked by the dashed vertical lines). Grey dots are the daily elevation estimates, the blue line is the modelled linear uplift plus annual rate calculated using Hector. (b) residuals (observations minus model)

4.2.7 Inuvik, Northwest Territories (INVK)

The station and Inuvik has data from 2001 to 2013 (Fig. 4.9). There are only four equipment changes to note during this period, with the antenna change on August 21, 2003 producing a large offset. The rate calculated with this offset is used in this study (-1.28±0.46 mm.yr^{-1}). The site notes for this station indicate that snow accumulation commonly happened on antenna, which may be the cause of the large residuals during the winter. No attempt has been made to remove these data beyond the three sigma criteria employed by Hector.

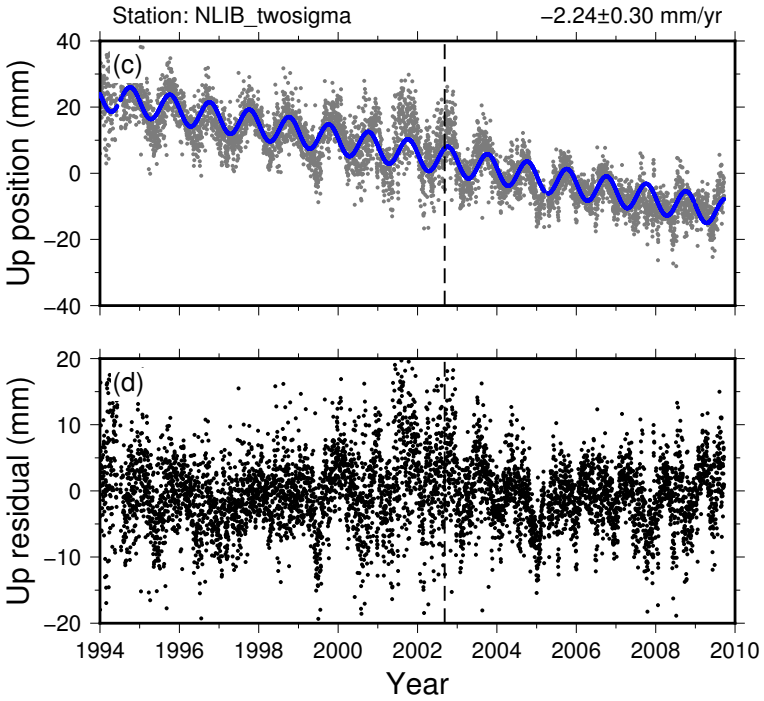

Figure 4.10: GPS Station at North Liberty, Iowa (NLIB). Observed versus modelled data including calculated offsets at selected equipment changes (marked by the dashed vertical lines). Grey dots are the daily elevation estimates, the blue line is the modelled linear uplift plus annual rate calculated using Hector. (b) residuals (observations minus model)

4.2.8 North Liberty, Iowa (NLIB)

This station is the furthest south of the GPS stations selected for investigation. It has data between 1994 and 2008, when it was taken offline due to equipment damage that happened in 2009 (`http://facility.unavco.org/highlights/2009/ggn_nlib.html`, Fig. 4.10). This site used the same antenna throughout the recording period, and there are no obvious offsets introduced by the receiver upgrades. An significant offset appears to have been introduced on September 7, 2002, although nothing in the site logs indicate that any maintenance at this time. The velocity estimated when including a correction for this offset is -2.24±0.30 mm.yr^{-1}.

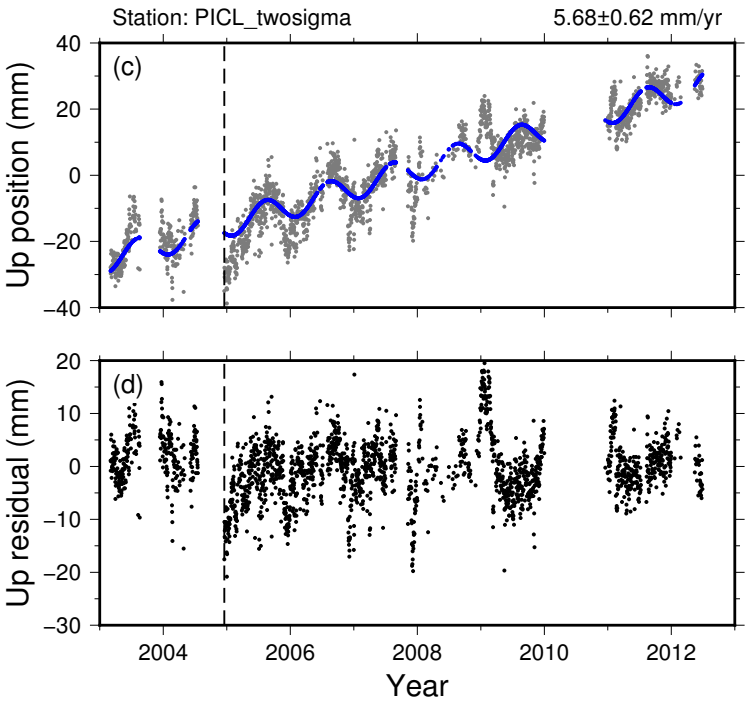

Figure 4.11: GPS Station at Pickle Lake, Ontario (PICL). (a) Observed versus modelled data including calculated offsets at selected equipment changes (marked by the dashed vertical lines). Grey dots are the daily elevation estimates, the blue line is the modelled linear uplift plus annual rate calculated using Hector. (b) residuals (observations minus model)

4.2.9 Pickle Lake, Ontario (PICL)

The station at Pickle Lake has data from 2003 to 2013 (Fig. 4.11). This station has several gaps in recording that are several months in duration. Due to this, and the irregularity of the residuals, it is difficult to assess the continuity in estimated height for the entire time series. It does appears that an offset was introduced when recording resumed in December 2004, which is included in the final rate calculation (5.68 ± 0.62 mm.yr^{-1}).

4.2.10 Calgary, Alberta (PRDS)

The station in Calgary, Alberta has data between 1997 and 2013 (Fig. 4.12). Three of the five equipment changes produced significant offsets. The rate with these

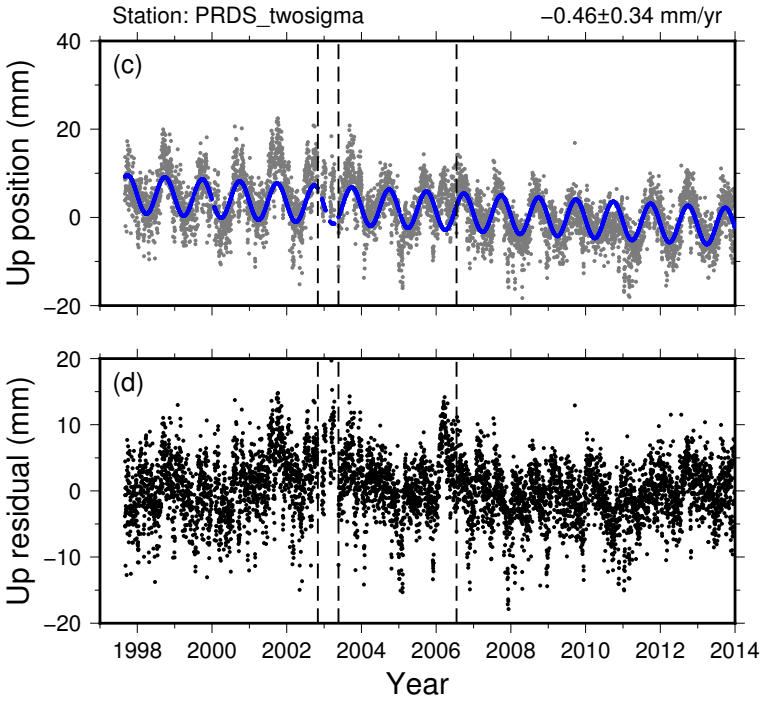

Figure 4.12: GPS Station at Calgary, Alberta (PRDS). Observed versus modelled data including calculated offsets at selected equipment changes (marked by the dashed vertical lines). Grey dots are the daily elevation estimates, the blue line is the modelled linear uplift plus annual rate calculated using Hector. (b) residuals (observations minus model)

offsets is a-0.46±0.34 mm.yr^{-1}.

4.2.11 Saskatoon, Saskatchewan (SASK)

The station at Saskatoon, Saskatchewan has data between 2003 and 2013, though after 2009 there were only intermittent measurements (Fig. 4.13) There are three equipment changes, though no appreciable offset was calculated at those points. The uncorrected rate of -0.32±0.31 mm.yr^{-1} is used for this study.

4.2.12 Yellowknife, Northwest Territories (YELL)

The station at Yellowknife, Northwest Territories has continuous data between 1994 and 2013. The residuals for this station are highly irregular. To account for this, rates were calculated using both annual and semiannual signals. Three offsets prior

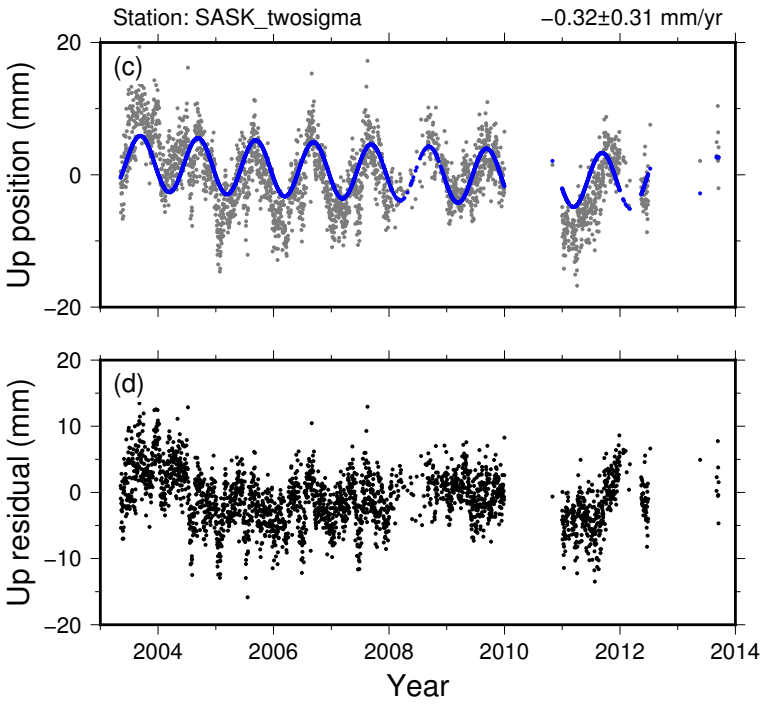

Figure 4.13: GPS Station at Saskatoon, Saskatchewan (SASK). Observed versus modelled data including calculated offsets at all equipment changes (marked by the dashed vertical lines). Grey dots are the daily elevation estimates, the blue line is the modelled linear uplift plus annual rate calculated using Hector. (b) residuals (observations minus model)

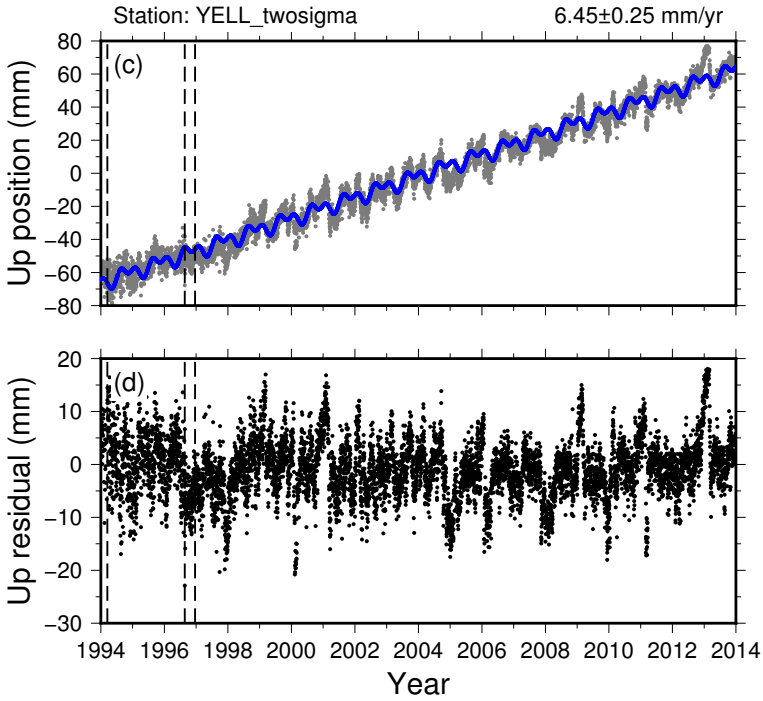

Figure 4.14: GPS Station at Yellowknife, Northwest Territories (YELL). (a) Observed versus modelled data including calculated offsets at all equipment changes (marked by the dashed vertical lines). Grey dots are the daily elevation estimates, the blue line is the modelled linear uplift plus annual and semiannual rate calculated using Hector. (b) residuals (observations minus model)

to 1997 were determined to be significant. The calculated uplift rate is 6.45±0.25 mm.yr^{-1}. There are many spikes in the residuals during the winter months, which may indicate that snow cover on the equipment may be partially responsible for the unusual residuals.

4.3 Noise models

4.3.1 Influence of annual noise

Most of the time series in this study have obvious annual signals, but how much does this affect the calculated rates? Blewitt and Lavallée (2002) determined that 4.5 years of measurement time should be sufficient to overcome the bias introduced by an annual signal, and all of the stations have time series that are longer than that. Table 4.3 shows the difference between the uplift rates with and without the annual signal included. Hector was unable to calculate the rate at Inuvik because of the large offset early in the time series, so the offset was added manually before calculation. Annual variability does not appear to have a strong influence on the linear uplift rates, and all of the rates are identical at the one-sigma level.

Table 4.3: Vertical velocity rates at GPS stations with and without modelled annual signals (in mm.yr^{-1}), and with white noise.

Station	With annual	Without annual	White Noise
BAKE	12.56±0.43	12.83±0.45	13.14±0.04
CHUR	10.33±0.26	10.31±0.30	10.46±0.02
DUBO	1.17±0.31	1.18±0.33	0.61±0.03
FLIN	4.25±0.42	4.33±0.43	4.03±0.06
HOLM	2.70±0.33	2.76±0.43	2.87±0.03
INVK	-1.28±0.46	-1.33±0.44	-0.72±0.03
NLIB	-2.24±0.30	-2.24±0.34	-2.10±0.03
PICL	5.68±0.62	5.86±0.64	6.17±0.06
PRDS	-0.46±0.34	-0.60±0.38	-0.17±0.03
SASK	-0.32±0.31	-0.21±0.34	-0.60±0.03
YELL	6.45±0.25	6.45±0.27	6.53±0.01

4.3.2 White noise model

The analysis with Hector used in the prior sections use a power law plus white noise model. What if only white noise is assumed? Table 4.3 shows the results of the

analysis without power law noise. The calculated uncertainty is much smaller than if power law noise is assumed to exist. The largest differences are with the sites at Baker Lake, Lac Du Bonnet, Inuvik and Pickle Lake, which have a discrepancy of 0.5 to 0.6 mm.yr^{-1}. This indicates that using a purely white noise model is not sufficient to accurately determine the uplift rates at these sites. More recording time will be necessary to overcome the correlated noise.

4.4 GRACE results

The GRACE satellites also may be used to measure GIA, provided the time series is sufficiently long to overcome transient hydrological effects. In areas where GIA is causing uplift, there is an associated gain in mass due to the redistribution of mass within the Earth, which in turn affects the gravitational field (Peltier, 1974). The atmospheric correction to the GRACE data were the same as the GPS analysis, and a non-tidal loading was included. (P. Tregoning, *pers comms.*, 2015) The uplift rates in this section derived from GRACE data were calculated under the assumption that all of the signal was due to viscoelastic deformation by glacio-isostatic adjustment (Purcell et al., 2011). Since viscoelastic GIA processes decay on time scales of thousands of years, over the observation period of the GRACE satellites, the signal can be considered to be linear. Since the GIA processes involves mantle material moving back towards areas with positive uplift rates, it will correspond to an increase of gravity. Changes in the distribution of water on the surface of the Earth also affect the gravitational field, and will contaminate the viscoelastic deformation calculation. If there is an increase in surface water storage, this will incorrectly be interpreted as uplift, and vice versa. In addition, hydrological loading will also cause a deformational effect, often assumed to be elastic (*i.e.* Wahr et al., 1995; Tregoning et al., 2009b). The separation of the two signals has been previously attempted by removing the hydrological component using a global water storage model (*e.g* Tre-

goning et al., 2009b), or by using removing the GIA component using GPS uplift rates (*e.g.* Wang et al., 2013).

The results of the GRACE data analysis are shown on Figs. 4.15–4.25 and summarised in Table 4.4. In most cases, a purely linear plus annual model does not characterise the data well. This implies that the non-GIA signals measured by GRACE are too large to separate out the uplift rate due to GIA (elastic deformation due to water loading is examined in the next section). Many of the calculated rates do not match the GPS uplift rates at the two-sigma level (Table 4.4). The stations with the largest differences are Saskatoon (Fig. 4.24) and Flin Flon (Fig. 4.18). The rates Churchill, Lac Du Bonnet, North Liberty and Yellowknife are the same at the two-sigma level.

Table 4.5 shows a comparison of the modelled annual signal from GRACE assuming viscoelastic deformation and GPS. If the modelled annual signal is purely due to the effects of local water loading, then it will be out of phase by 180°(or about 163 days), since the water mass gain will be converted to an apparent uplift. At North Liberty, Calgary, and Yellowknife, this is the case. At these stations, the modelled amplitude of the GRACE data is roughly double that of the GPS. Unsurprisingly, the phase annual signal does not match up well in sites like Lac Du Bonnet, Flin Flon and Saskatoon, where the residuals are highly non-linear.

Table 4.4: Comparison of uplift rates from GRACE (assuming viscoelastic deformation) and GPS (in mm.yr^{-1})

Station	GRACE rate	GRACE rate (no annual)	GPS Rate	Difference
BAKE	8.65±1.06	8.46±1.33	12.56±0.43	-3.91±1.14
CHUR	12.64±1.19	12.97±1.57	10.33±0.26	2.31±1.22
DUBO	3.13±1.34	3.18±1.41	1.17±0.31	1.96±1.38
FLIN	8.29±1.20	8.25±1.21	4.25±0.42	4.04±1.27
HOLM	5.72±0.85	5.58±1.01	2.70±0.33	3.02±0.91
INVK	-3.40±0.86	-3.58±1.06	-1.28±0.46	-2.12±0.98
NLIB	-1.23±1.28	-1.67±1.56	-2.24±0.30	1.01±1.31
PICL	9.61±1.24	9.58±1.24	5.68±0.62	3.93±1.39
PRDS	2.84±1.15	2.48±1.34	-0.46±0.34	3.30±1.20
SASK	6.25±1.31	5.84±1.59	-0.32±0.31	6.57±1.35
YELL	6.56±1.08	6.23±1.31	6.45±0.25	0.11±1.11

Table 4.5: Comparison of modelled annual amplitude (in mm) and phase (in days) of GRACE viscoelastic deformation, and GPS

Station	GRACE Amplitude (mm)	GRACE Phase (days)	GPS Amplitude (mm)	GPS Phase (days)	Amplitude Ratio	Days out of phase
BAKE	7.43	128.78	4.90	−107.14	0.66	235.92
CHUR	9.10	−59.06	5.13	−126.39	0.56	67.33
DUBO	1.67	144.58	3.42	−108.43	2.05	253.01
FLIN	1.67	144.58	2.82	−94.72	1.69	239.30
HOLM	4.81	125.35	4.69	−99.65	0.98	225.00
INVK	7.05	113.21	5.51	−106.48	0.78	219.69
NLIB	10.77	108.51	4.24	−82.82	0.39	191.33
PICL	1.10	140.40	3.89	−141.66	3.54	282.06
PRDS	9.39	108.64	4.26	−93.94	0.45	202.58
SASK	11.37	118.23	4.17	−111.62	0.37	229.85
YELL	7.90	104.14	3.14	−71.06	0.40	175.20

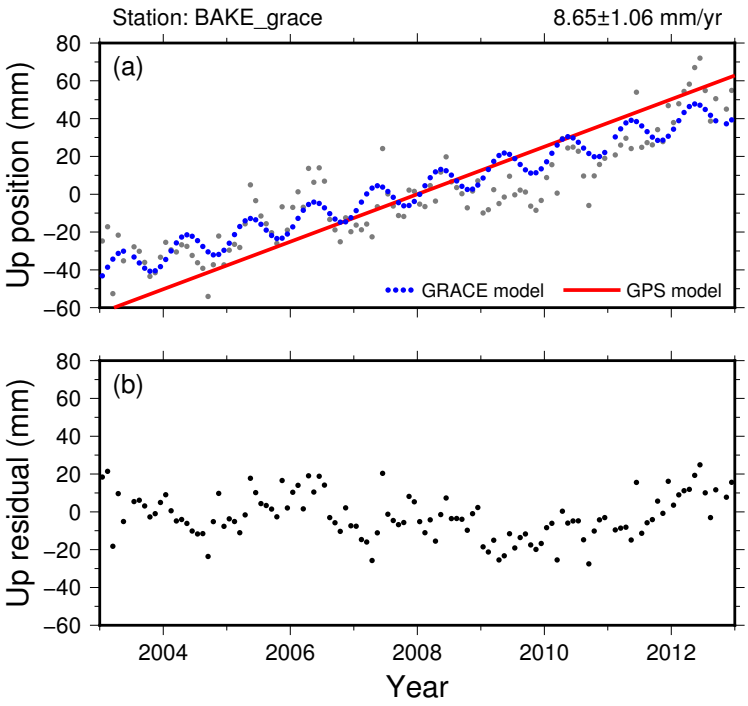

Figure 4.15: GRACE viscoelastic response at Baker lake, Nunavut (BAKE). (a) Raw data (grey dots) with linear plus annual modelled signal (blue dots). (b) residuals.

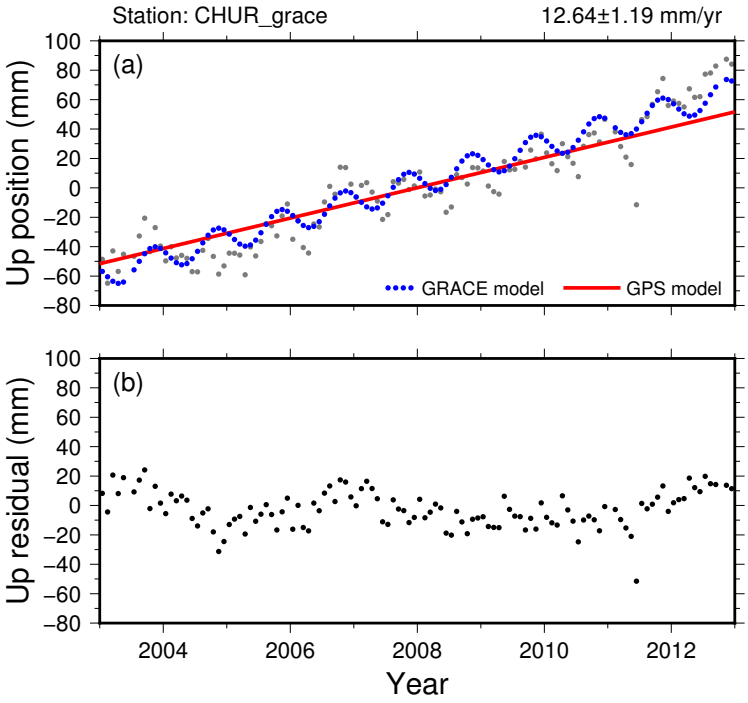

Figure 4.16: GRACE viscoelastic response at Churchill, Manitoba (CHUR). (a) Raw data (grey dots) with linear plus annual modelled signal (blue dots). (b) residuals.

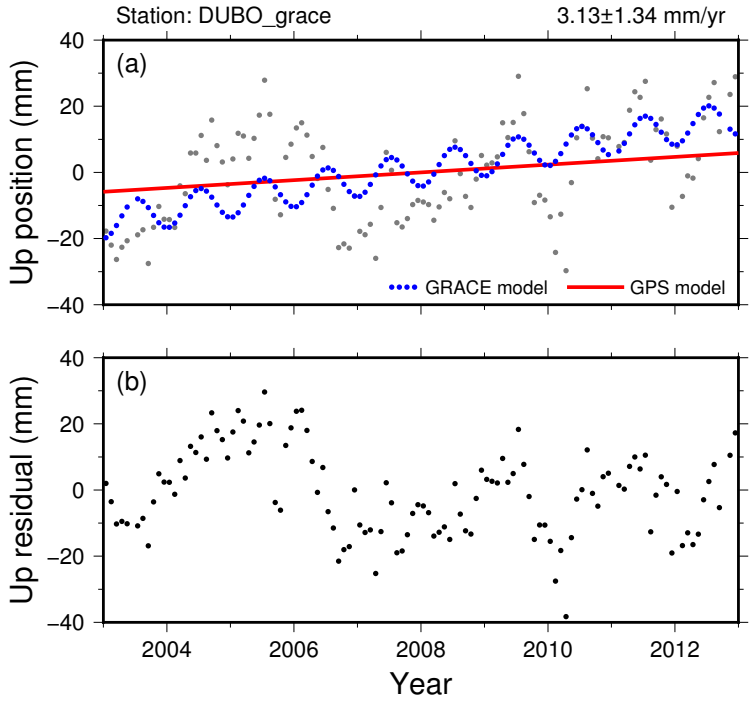

Figure 4.17: GRACE viscoelastic response at Lac Du Bonnet, Manitoba (DUBO). (a) Raw data (grey dots) with linear plus annual modelled signal (blue dots). (b) residuals.

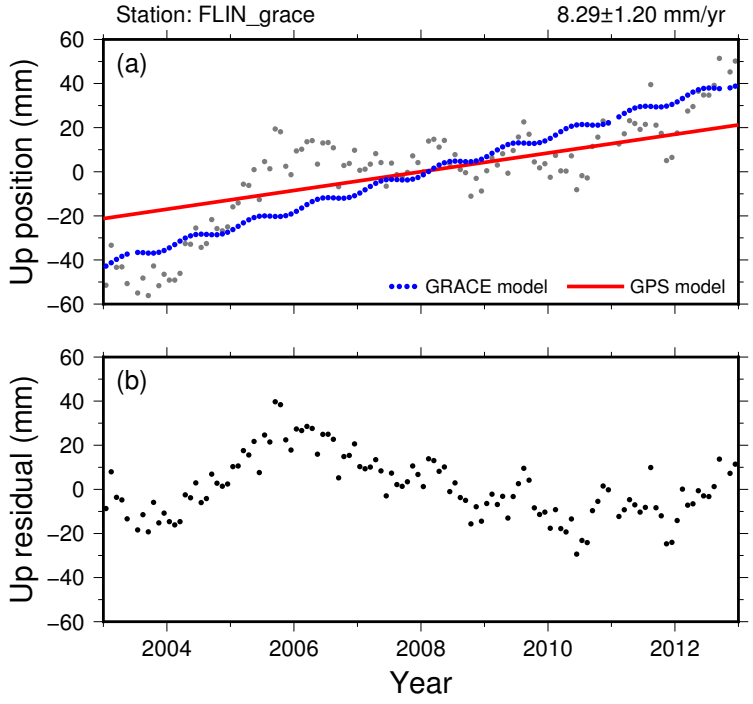

Figure 4.18: GRACE viscoelastic response at Flin Flon, Manitoba (FLIN). (a) Raw data (grey dots) with linear plus annual modelled signal (blue dots). (b) residuals.

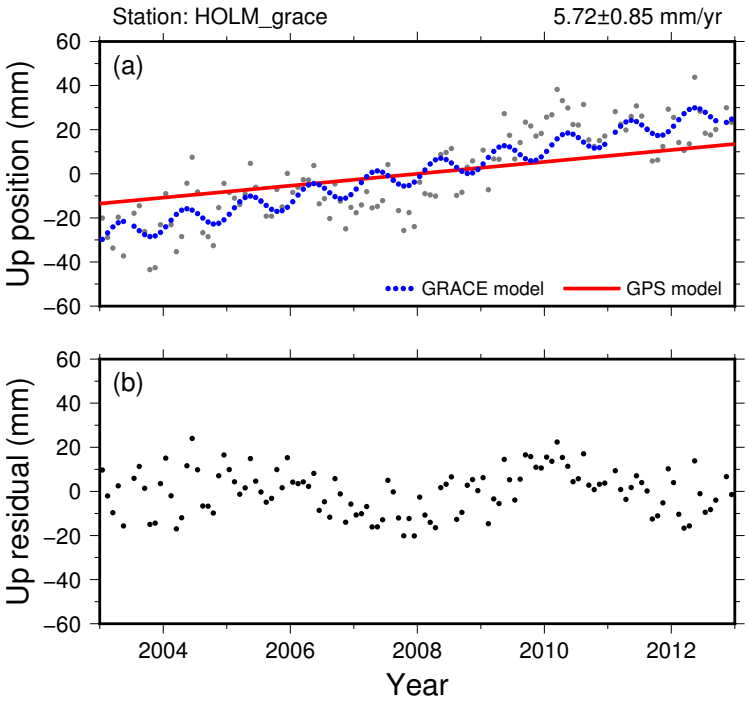

Figure 4.19: GRACE viscoelastic response at Ulukhaktok, Northwest Territories (HOLM). (a) Raw data (grey dots) with linear plus annual modelled signal (blue dots). (b) residuals.

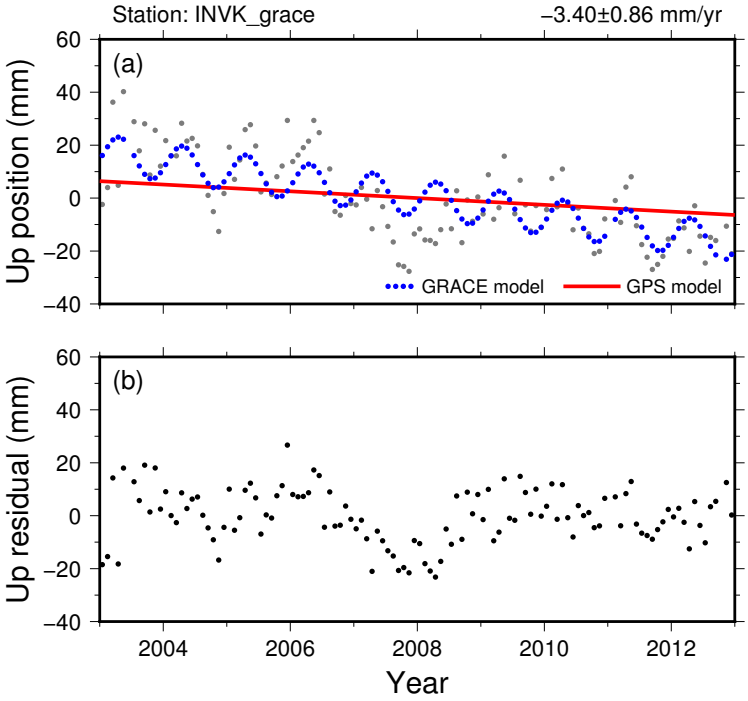

Figure 4.20: GRACE viscoelastic response at Inuvik, Northwest Territories (INVK). (a) Raw data (grey dots) with linear plus annual modelled signal (blue dots). (b) residuals.

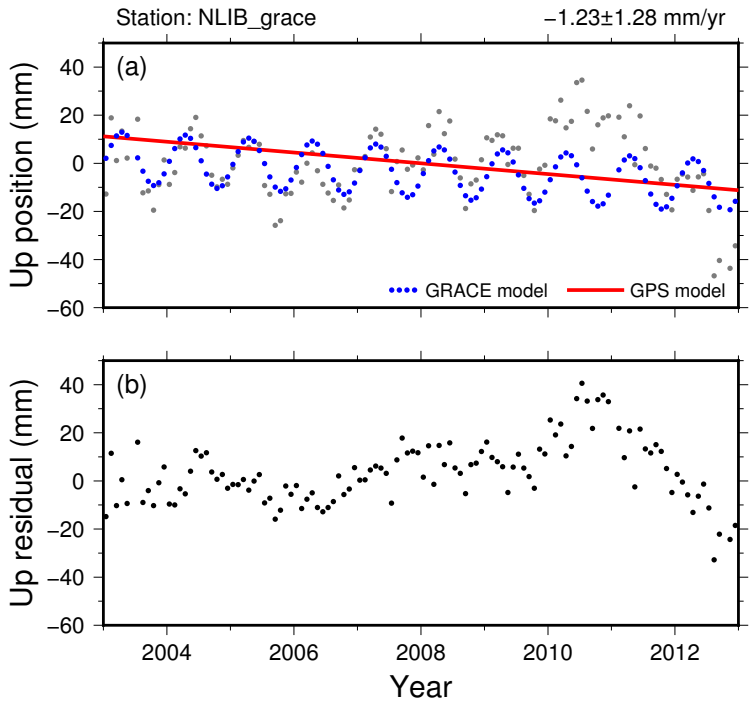

Figure 4.21: GRACE viscoelastic response at North Liberty, Iowa (NLIB) Raw data (grey dots) with linear plus annual modelled signal (blue dots). (b) residuals.

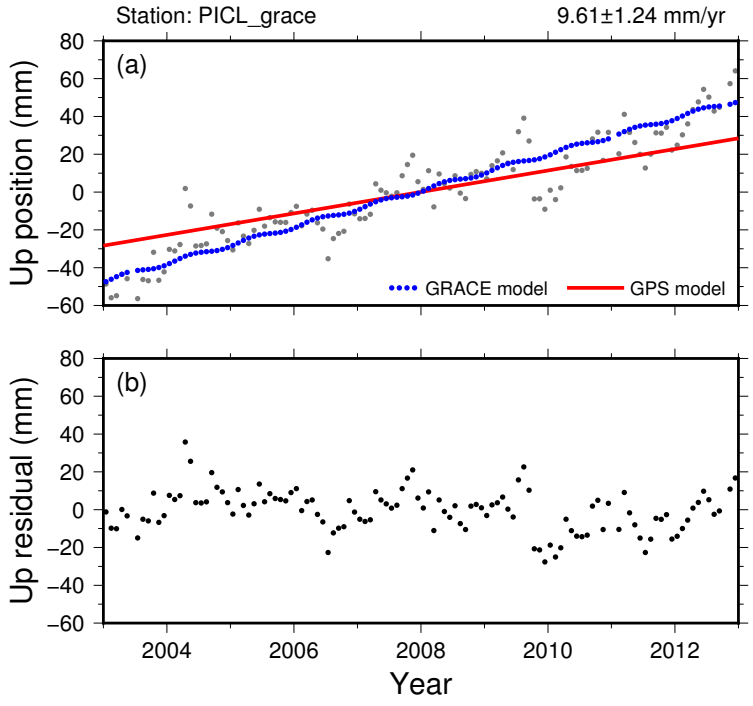

Figure 4.22: GRACE viscoelastic response at Pickle Lake, Ontario (PICL) Raw data (grey dots) with linear plus annual modelled signal (blue dots). (b) residuals.

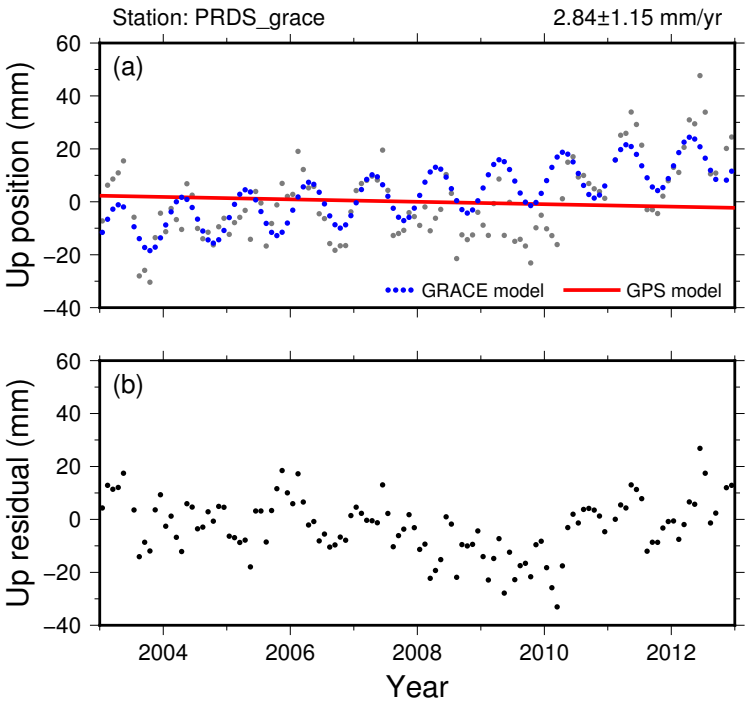

Figure 4.23: GRACE viscoelastic response at Calgary, Alberta (PRDS) Raw data (grey dots) with linear plus annual modelled signal (blue dots). (b) residuals.

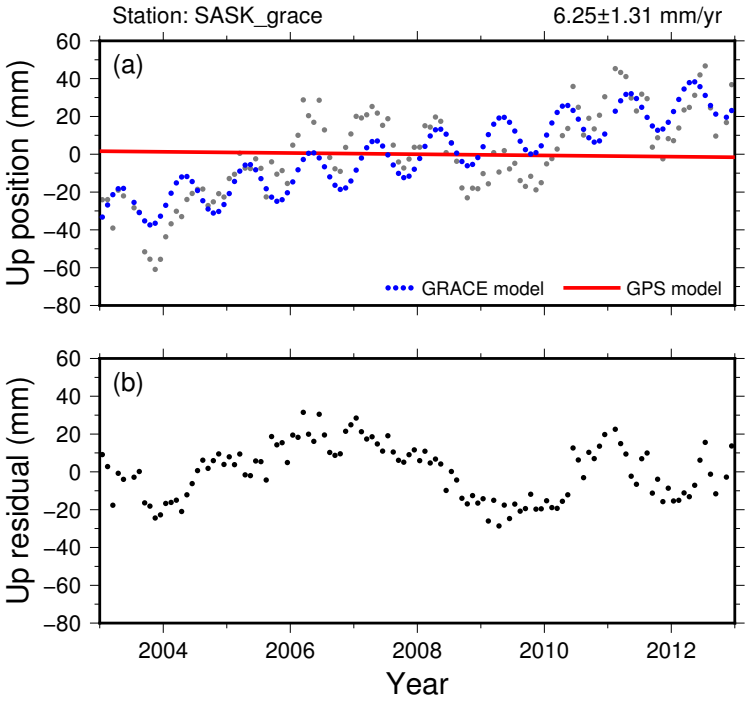

Figure 4.24: GRACE viscoelastic response at Saskatoon, Saskatchewan (SASK) Raw data (grey dots) with linear plus annual modelled signal (blue dots). (b) residuals.

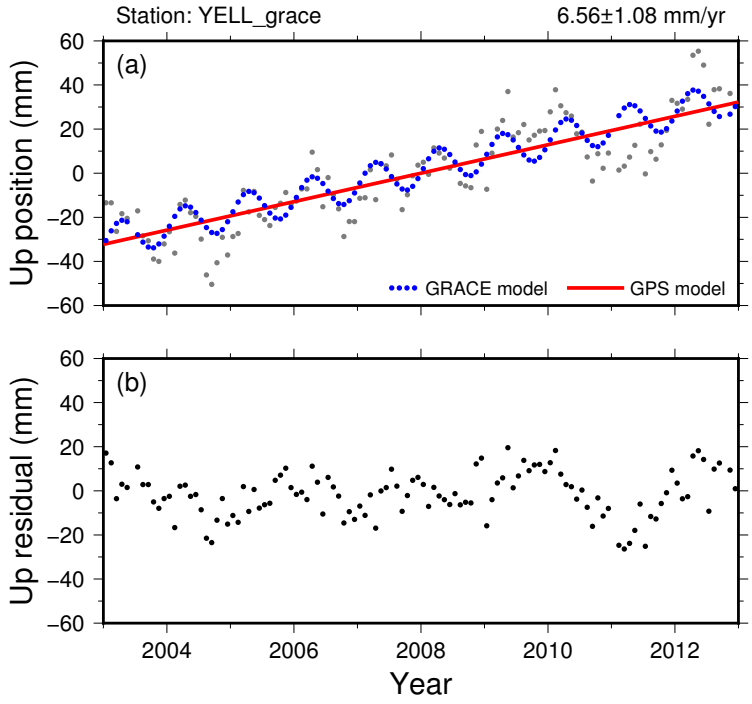

Figure 4.25: GRACE viscoelastic response at Yellowknife, Northwest Territories (YELL) Raw data (grey dots) with linear plus annual modelled signal (blue dots). (b) residuals.

4.5 Effects of hydrology on the data

Although the effects of GIA are expected to be the dominant signal in GPS measurements in areas of western Canada, changes in hydrology cause elastic deformation that may also produce a measurable signal (Tregoning et al., 2009b). van Dam et al. (2001) found that changes in hydrology can be responsible for deformation of upwards of 30 mm per year, and that long term variability in hydrology could be misinterpreted as GIA. Tregoning et al. (2009a) attempted to remove the hydrological component of the vertical uplift of GPS sites in Canada using the GLDAS global hydrology model. They found that the hydrology model was unable to account for all of the observed deformation, and required a scaling parameter to fit the data. Correcting for hydrology produced a GIA pattern that better matched the GIA models. Zou et al. (2014) found that seasonal signals are a significant component of GPS height measurements. The source of seasonal signals was proposed to be from inadequate tidal models, thermal expansion and contraction, changes in aquifer level, instability in the GPS monument, snow loading and lake level fluctuations. They found that a GRACE-based loading model fit most seasonal GPS observations, but there were inconsistencies where the source load was small in extent.

It is suspected that hydrology affects the data at time scales longer than one year, and possibly introduces a bias in the calculated uplift rates. Several stations exhibit long term changes in height that cannot be attributed to a linear uplift rate due to postglacial rebound or a steady annual signal. This is most apparent in the stations at Saskatoon (Fig. 4.13), Flin Flon (Fig. 4.7) and Lac Du Bonnet (Fig. 4.6), which record subsidence between 2003 and 2005 but records uplift outside this period. Previous reported uplift rates for these sites, using shorter duration time series were significantly lower than what is calculated in this study. For instance, Mazzotti et al. (2011) reported uplift rates of -1.01±0.14 mm.yr^{-1}, 2.05±0.08 mm.yr^{-1} and -0.17±0.08 mm.yr^{-1} for these three sites, respectively. These sites are clearly mea-

suring a non-stationary processes that biased the rates when the time series were shorter. Loss of subsurface water due to long term droughts is known to cause measurable uplift, for instance in the recent drought in California (Borsa et al., 2014). The coincidence of having three stations located on the Canadian Prairies having similar subsidence in 2003–2006 suggests that there may be a shared cause.

GRACE-derived uplift rates are used to assess the magnitude of hydrology effects on selected GPS sites. Elastic deformation due to hydrology is a dominant signal in height changes determined by GRACE (Tregoning et al., 2009b). If all deformation determined from GRACE is assumed to be elastic, areas that are undergoing uplift due to GIA that would be misinterpreted to cause subsidence. GIA processes increase gravity in rebounding areas due to shifting mass in the Earth, which would be incorrectly calculated as an increase in water mass. In order to directly compare hydrological signals between GRACE and GPS, it is necessary to remove the trend due to GIA. GRACE data were downloaded from the ANU GRACE data visualisation tool (`http://grace.anu.edu.au/overlay.php`, Darbeheshti et al., 2013). The GRACE data computed as elastic surface deformation were processed using Hector, using the same parameters as the GPS time series.

Since the footprint of the GRACE signal is large, the signal may be aliased, depending on the spatial distribution of the hydrological change. Figs. 4.26 to 4.28 show annual precipitation anomaly against the 1992–2011 average across western Canada. This period was chosen as the average, as it encompasses most of the years when GPS data was collected. The precipitation values were corrected for effects such as wind, and are only used if data exist for all twelve months of the year (Mekis and Vincent, 2011). Though precipitation is only one parameter in the variability of hydrology through time, long term changes in precipitation have been implicated in causing changes in gravity in the study area (Lambert et al., 2013). The distribution of anomalous precipitation is non-uniform between the locations of

GPS stations. For example, 2006 had above normal precipitation in the vicinity of Saskatoon and Flin Flon, while the Lac Du Bonnet region had lower than normal precipitation. If these precipitation anomalies are correlated with hydrological storage that is measured with GRACE, the gravity contrast between the areas may be reduced.

In contrast to the viscoelastic calculation, the phase of the annual signal from GRACE assuming elastic deformation and GPS is very similar (Table 4.6). The largest difference is at Pickle Lake, which has a relatively discontinuous GPS time series that may affect the modelled annual signal. In every case, the modelled amplitude of annual signal in the GPS data is larger than that determined from GRACE. The difference in amplitude is similar to the scaling factors from the GLDAS hydrology model used by Tregoning et al. (2009a) to correct the hydrological component of GPS deformation for the stations at Baker Lake, Flin Flon and Yellowknife.

Table 4.6: Comparison of modelled annual amplitude (in mm) and phase (in days) of GRACE elastic deformation, and GPS, as well as the GLDAS ratio from Tregoning et al. (2009a)

Station	GRACE (elastic)		GPS		Ratio	Days out of phase	GLDAS Ratio
	amplitude	phase	amplitude	phase			
BAKE	1.68	−92	4.90	−106	2.91	13	2.8
CHUR	1.03	−142	5.13	−125	4.98	−17	2.0
DUBO	1.48	−88	3.42	−107	2.31	19	1.2
FLIN	1.80	−96	2.82	−95	1.56	−1	1.2
HOLM	1.35	−89	4.69	−98	3.46	10	–
INVK	1.76	−96	5.51	−105	3.14	9	–
NLIB	2.13	−90	4.24	−82	1.99	−9	0.8
PICL	1.22	−112	3.89	−140	3.18	28	–
PRDS	3.33	−93	4.26	−93	1.28	−1	–
SASK	2.63	−88	4.17	−110	1.59	22	–
YELL	2.50	−96	3.14	−70	1.25	−26	1.2

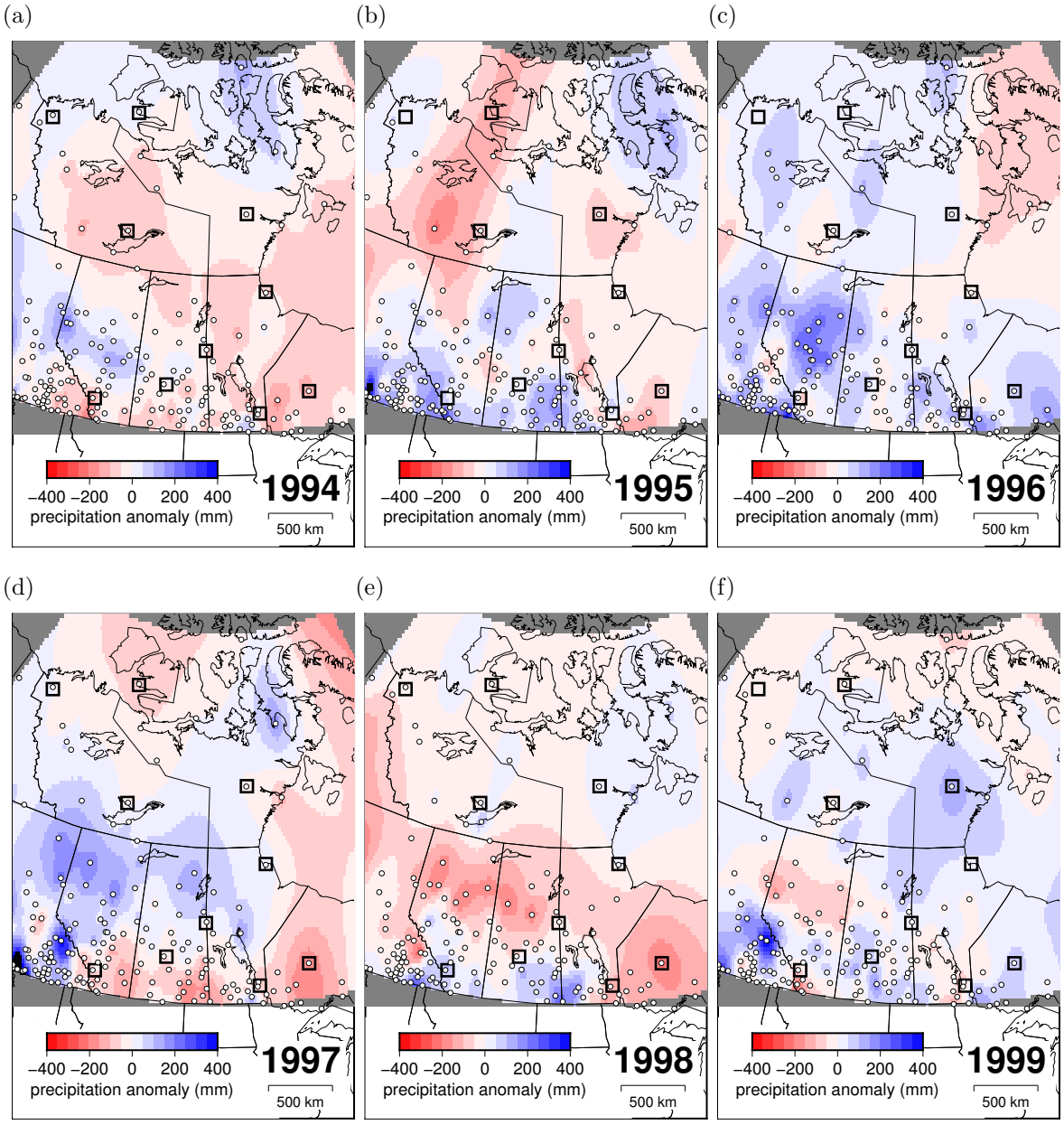

Figure 4.26: Annual precipitation anomaly from the 1992-2011 average for western Canada (Mekis and Vincent, 2011). White circles are stations where there are rain gauge data for all 12 months of the year. Black squares are the location of GPS receivers. (a) 1994, (b) 1995, (c) 1996, (d) 1997, (e) 1998, (e) 1998

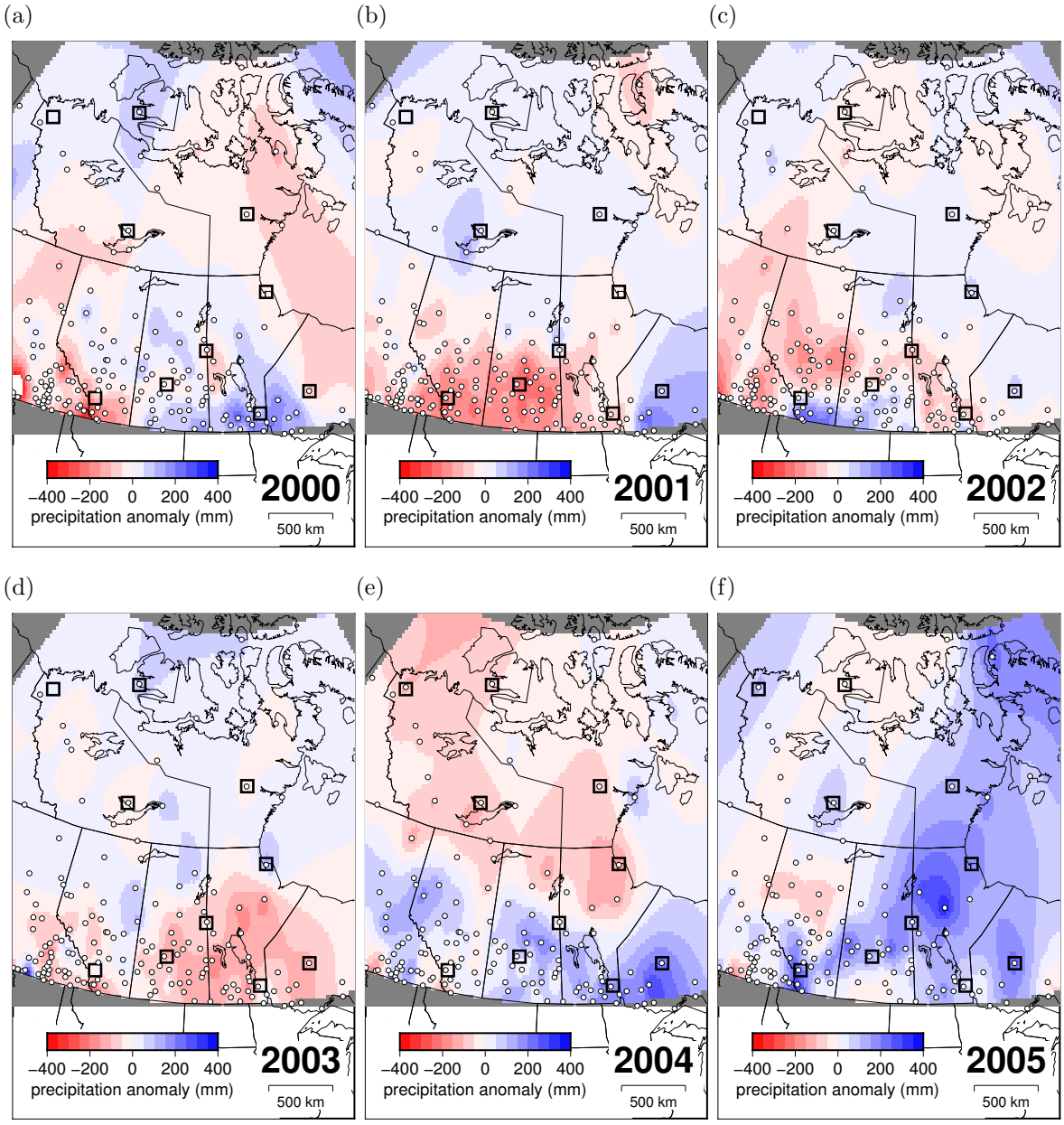

Figure 4.27: Annual precipitation anomaly from the 1992-2011 average for western Canada (Mekis and Vincent, 2011). White circles are stations where there are rain gauge data for all 12 months of the year. Black squares are the location of GPS receivers. (a) 2000, (b) 2001, (c) 2002, (d) 2003, (e) 2004, (f) 2005

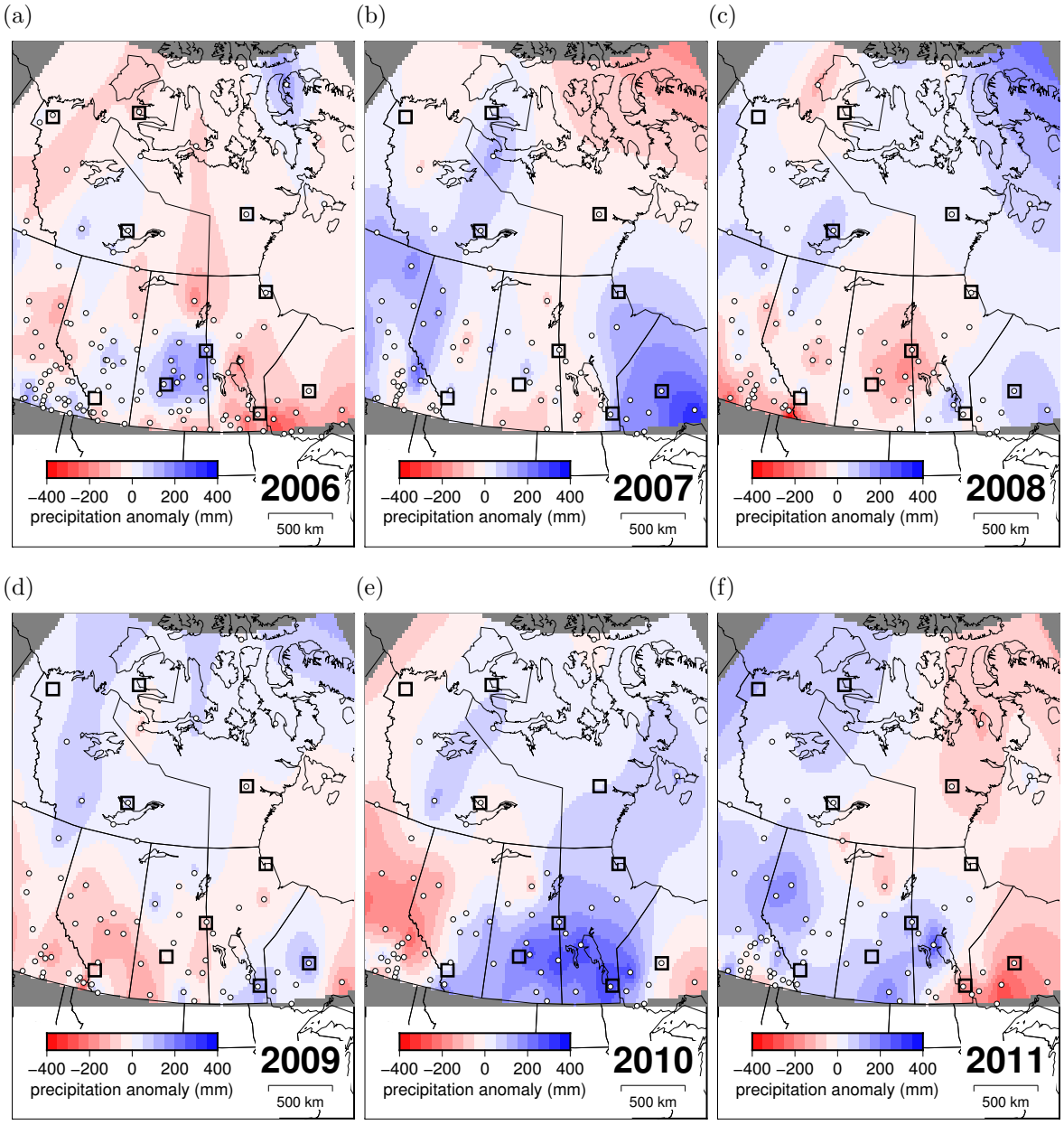

Figure 4.28: Annual precipitation anomaly from the 1992-2011 average for western Canada (Mekis and Vincent, 2011). White circles are stations where there are rain gauge data for all 12 months of the year. Black squares are the location of GPS receivers. (a) 2006, (b) 2007, (c) 2008, (d) 2009, (e) 2010, (f) 2011

4.6 Effects of hydrology in west-central Canada

The GPS stations at Flin Flon, Lac Du Bonnet and Saskatoon all show similar patterns of height change that do not appear to be related to long term GIA, as seen in the residuals (Fig. 4.29). In particular, the period between the middle of 2003 and the start of 2006 shows a decrease in elevation at all sites. In addition, there are similar magnitude seasonal changes from 2006–2010. The height generally reaches a minimum point during the winter, and maximum during the middle of the summer. At all sites, the maximum elevation after trend removal is in the summer of 2003, and the minimum is in the winter of 2006. The raw data shows that the strong minimum is influenced by a sharp subsidence in January 2006. Even if these data were excluded, the winter of 2006 was a time when the GPS sites had relatively low height.

Tregoning et al. (2009b) showed that motions of GPS stations, in particular the vertical component, can be strongly affected by elastic deformation due to hydrological loading. Could this explain why the GPS positions show multi-year changes? From 1999–2005, there was a significant drought in most of western Canada, reaching a peak in 2001 and 2002 (Hanesiak et al., 2011). By mid-2005, most of the region experienced above normal precipitation, signifying the end of the drought. Precipitation values in southern Saskatchewan and Manitoba actually began increasing in 2004 (Fig. 4.27), before falling off in 2006 and 2007 (Fig. 4.28). The GPS relative vertical position decreased between 2003 and 2005 at the stations DUBO, SASK and FLIN, which are all in the vicinity of these climatic conditions (Figs. 4.6, 4.13, and 4.7). When the long term GIA rate and seasonal signal are removed, the decrease is even more pronounced (Fig. 4.29), with DUBO subsiding by about 10 mm, SASK by 6 mm and FLIN by 5 mm (note that the recordings for SASK started partway through 2003). These results correspond closely to the increase of precipitation after 2003, which peaked in 2005.

This signal is also measured in the GRACE data (Figs. 4.17, 4.18, and 4.24), marked by an apparent increase in calculated height. The apparent height increases steadily between 2003 and 2006 at the locations of FLIN and DUBO, while at SASK, this increase started in 2004 and continued through to 2006. The detrended GRACE elastic deformation time series was applied to the GPS data to see if the vertical uplift rate would change if the hydrological component of the deformation was removed (assuming the correlated noise in the GPS is from hydrological deformation). The detrended elastic data were scaled using the values in Table 4.6. Since the sampling period of GRACE is monthly, the GRACE deformational values were linearly interpolated to daily values to match the GPS sampling rate. The results in Table 4.7 show a comparison of the uplift rates calculated with and without without correction. The uncorrected rates may be different from the results in the previous section, as they only cover the period between 2003 and 2012. Using GRACE to correct the data does not have a large effect on the resulting modelled uplift rate, and are identical at the two-sigma level. When the GPS data are corrected using the GRACE data, the difference between 2003 and 2005 height decreases by a factor of two (Fig. 4.29). The residuals are generally smoother after correction. This increases confidence that the non-linear signals are geophysical in nature, and not a systematic error with the GPS data at a site level. However, considering that the need of a scaling factor, and the lack of clear difference in the GPS rate, using GRACE to correct the GPS data does not likely to an lead appreciable improvement in determining the linear rate due to GIA.

Table 4.7: Vertical velocity of the GPS from the period between 2003 and 2012 with and without correction from GRACE

Station	Uncorrected	Corrected
BAKE	12.97±0.46	12.68±0.48
CHUR	9.78±0.48	9.94±0.50
DUBO	1.08±0.50	0.96±0.50
FLIN	3.76±0.64	3.41±0.64
HOLM	2.70±0.43	2.67±0.53
INVK	-1.56±0.55	-1.15±0.54
NLIB	-2.10±0.54	-2.23±0.56
PICL	6.39±0.65	5.53±0.62
PRDS	0.03±0.45	-0.60±0.46
SASK	-0.44±0.32	-0.42±0.32
YELL	6.68±0.43	6.68±0.43

4.7 Implications of hydrology on the measurement of GIA

The effects of the change from drought conditions in 2003 to wet conditions in 2005 in southern Saskatchewan and Manitoba are apparent in the GPS data. There is a decrease in the GPS vertical position between those years, amounting to 5-10 mm of subsidence. This also corresponds to an increase in mass for these locations, as measured by GRACE. Scaled GRACE data assuming that the deformation was elastic could account for roughly half of this subsidence. The long duration of this increase in water loading may bias the calculated linear rate, and has probably caused incorrectly high rates GIA subsidence to be reported at these sites. As the duration of GPS recording increases, the impact of multi-year changes in hydrology will have less impact as they are transient in nature. It is possible that the elastic response calculation could be improved in the future using a variable Earth model (*i.e.* Chanard et al., 2014).

The fact that the measured elastic deformation determined by GRACE and

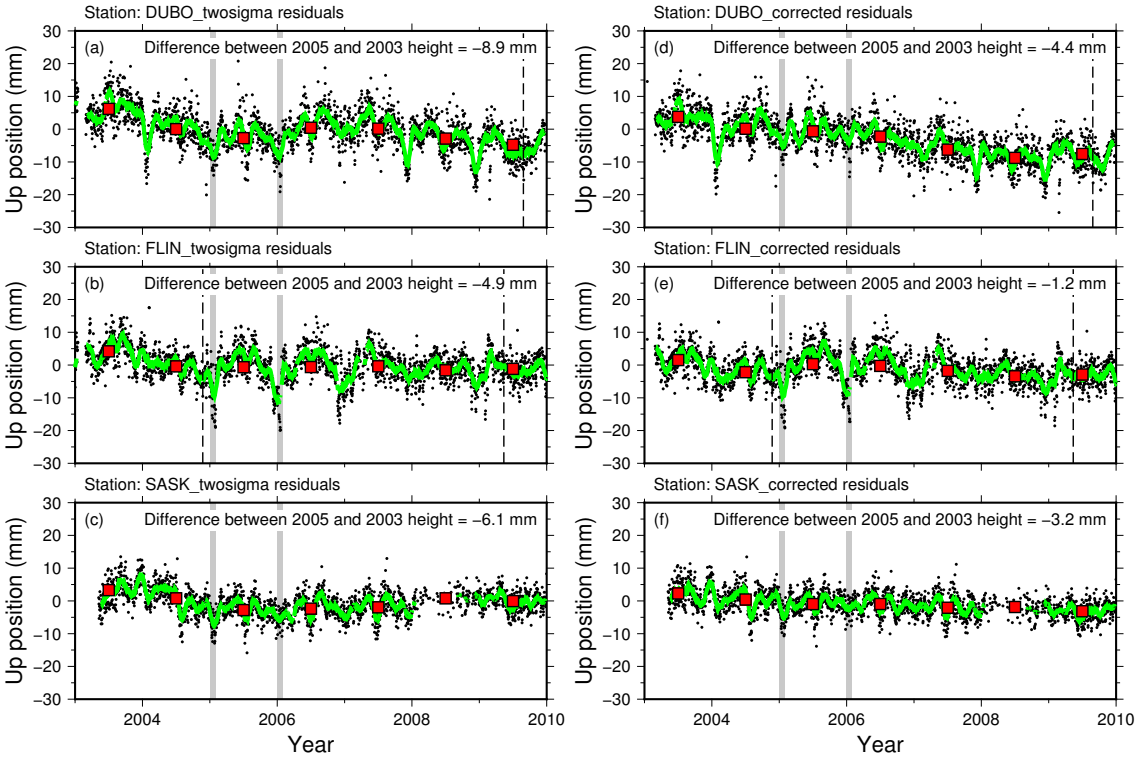

Figure 4.29: Time series of the residuals for stations DUBO, FLIN and SASK, after removing the calculated GIA rate and annual signal. The green line is a 30 day running average of the data. Red squares represent the average residual for the year. The grey bars represent January 2005 and 2006, when the vertical position is near a minimum position. The difference between the average height of the station in 2005 and 2003 is also calculated. (a) (b) and (c) represent the residuals of the raw time series, while (d) (e) and (f) represent the residuals after correction with scaled GRACE data.

GPS exhibit similar annual and multi-year patterns increases the confidence that there is a significant component of hydrological deformation in this region. The nature of hydrological loading is likely to be a complex interplay between snowfall, groundwater storage, drainage and basin capacity. The multi-year fluctuations in station height are larger than the rate of uplift due to GIA at many of these sites. This may be especially true for a site like Saskatoon, where negative GIA rates have been reported (*e.g.* Sella et al., 2007; Mazzotti et al., 2011; Lambert et al., 2013). The negative value determined at this site in previous studies is likely due to the subsidence that happened between 2003 and 2006 (Fig. 4.13).

The question then is, what is the duration of continuous recording required to produce an estimate of GIA that is reliable? Since some of the time series investigated in this study are approaching 20 years of measurements, it should be possible to assess this. Fig. 4.30 shows the evolution of modelled uplift rate through time. The most stable stations appear to be Churchill and Yellowknife, which gives roughly the same velocity after six to seven years of measurement. Another station with a long time series is Lac Du Bonnet, which has only reached stability after about 14 years of recording. A recording period of less than five years is insufficient to give high confidence in the modelled uplift rate, and most sites require at least eight to ten years of measurement before the modelled value stabilise. This is most noticeable for the station FLIN, where the modelled velocity declines steadily until after ten years of measurement. For all of the sites that began recording in 2002-2003 (Baker Lake, Ulukhaktok, Inuvik, Pickle Lake, Saskatoon), the modelled rate may only now be sufficiently stable to be considered reliable. Rates determined from shorter (<5 years) and campaign stations (*e.g.* Sella et al., 2007) should be treated with caution.

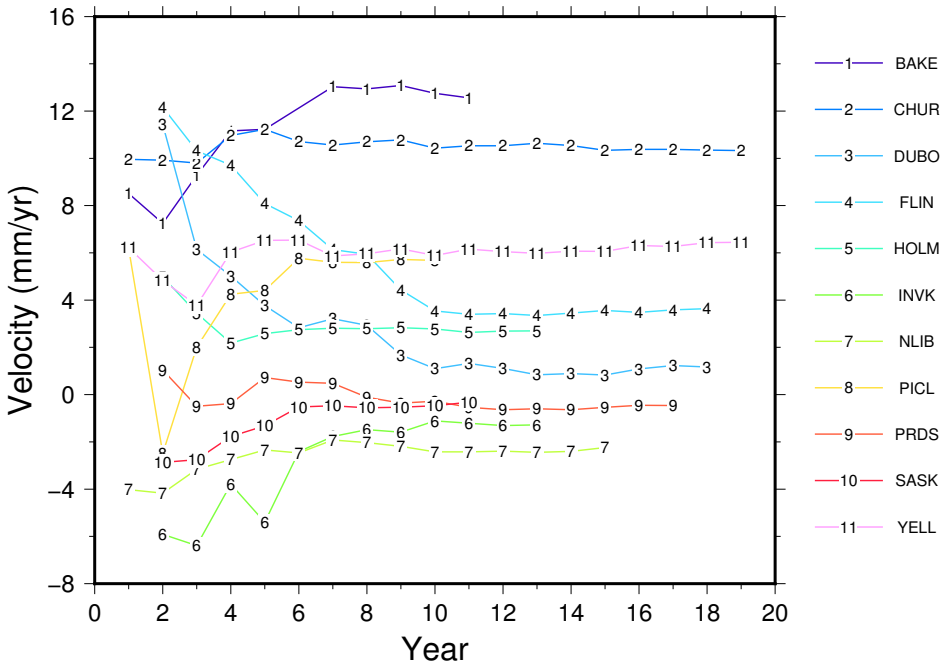

Figure 4.30: Modelled velocity after multiple years of measurements. The modelled velocity after only one year can be extremely high and is not shown.

4.8 Tide gauges

Tide gauges provide another independent measure of GIA in the study area. There are tide gauges located at Churchill, Inuvik and Ulukhaktok. Sea level data were downloaded from the Permanent Service for Mean Sea Level website (Holgate et al., 2012; Permanent Service for Mean Sea Level, 2014). An arbitrary value of about 7000 mm is added to all gauge data (IOC-UNESCO, 2006), which has been subtracted prior to analysis. The tide gauge in Churchill has been in operation since 1940 (Fig. 4.31), while the gauge at Ulukhaktok has been in operation since 2002 (Fig. 4.32). The gauge at Inuvik was operated between 1962 and 1982. After a gap of over 20 years, resumed operation in 2003 (Fig. 4.33). The residuals in the tide gauge data, even after removal of an annual signal, are about an order of magnitude larger than the residuals in the GPS data. The resulting linear rates of sea level change thus have a much larger uncertainty. Sea level change at these sites will be a combination of GIA, global sea level change and local effects. It is difficult to quantify the magnitude of local effects due to insufficient observations. The rate of sea level change was calculated from the tide gauge data using Hector, using the same procedure as the GPS analysis.

The GIA rates at these locations are determined by combining the global sea level change rate with the observed rate. Church and White (2011) determined a GIA-corrected estimate of global sea level rise through the 20th and early 21st centuries using the global network of tide gauges. They determined that the sea level rise from 1936 to 2009 was 1.8±0.3 mm.yr^{-1}. If this value is combined with the calculated rate from Churchill (-8.86±0.81 mm.yr^{-1}) and assuming that local effects are negligible, the uplift rate due to GIA is 10.66±0.91 mm.yr^{-1}. This is consistent with the rate calculated by GPS at the one-sigma level. Sea level change in Churchill is not linear throughout the recording period. Sea level fell more rapidly between 1970 and 1990 than the bracketing time periods. Gough and Robinson (2000) attribute the reduced

sea level fall since 1985 in Hudson Bay to thermal expansion of water. While the assumption that local effects are negligible is not necessarily valid over short periods of time, estimating the rate over the seventy year recording period appears to have overcome this. The station at Inuvik has a recordings since the 1960s. Church and White (2011) calculated a global sea level rise of 1.9±0.4 mm.yr^{-1} for the period between 1961 and 2009. If this value is added to the calculated sea level change (2.72±1.14 mm.yr^{-1}), the GIA rate becomes 0.82±1.21 mm.yr^{-1}. This value is not statistically different from the rate calculated by GPS (-1.56±0.55 mm.yr^{-1}) at the two sigma level. The globally averaged rate of sea level rise between 1993 and 2009, as measured from satellite altimetry was 3.2±0.4 mm.yr^{-1} (Church and White, 2011). If this value is combined with the sea level change recorded at Ulukhaktok (-8.83±3.89 mm.yr^{-1}), the GIA rate becomes 12.03±3.91 mm.yr^{-1}. This value is more than four times the rate calculated from the GPS data (2.77±0.30 mm.yr^{-1}). This indicates that a sea level record less than 10 years is not sufficient to assess GIA, assuming that the GPS data are correct. Whether the use of a global sea level rate is appropriate to use in northern Canada is debatable (since global sea level is not uniform).

4.9 Conclusions

Though all of the GPS sites within the study area have been used for studying GIA, careful assessment of the signals shows that many of the sites have non-linear, multi-year fluctuations in height that are not related to GIA, on the order of 5 mm.yr^{-1}. These fluctuations may be related to hydrological loading. Stations that appear to be affected by hydrological effects include Lac Du Bonnet, Flin Flon and Saskatoon. This correlated noise affects the calculation of linear uplift rate due to GIA, and GPS time series that are less than eight to ten years may be of insufficient length to accurately characterise the true rate where these signals are present.

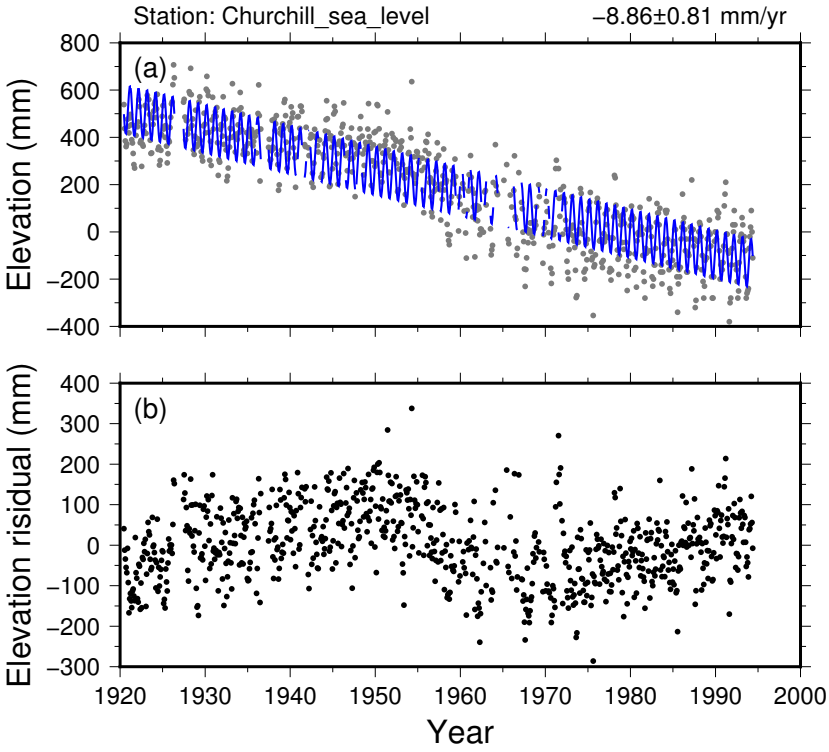

Figure 4.31: Sea level at Churchill, Manitoba (grey dots) with linear plus annual modelled signal (blue line). (b) residuals.

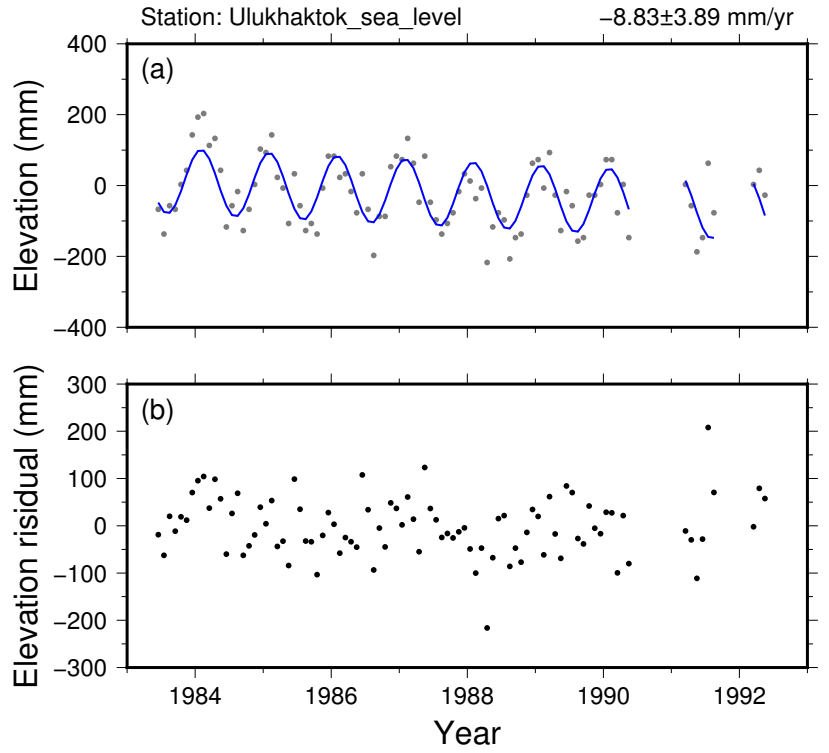

Figure 4.32: Sea level at Ulukhaktok, Northwest Territories (grey dots) with linear plus annual modelled signal (blue line). (b) residuals.

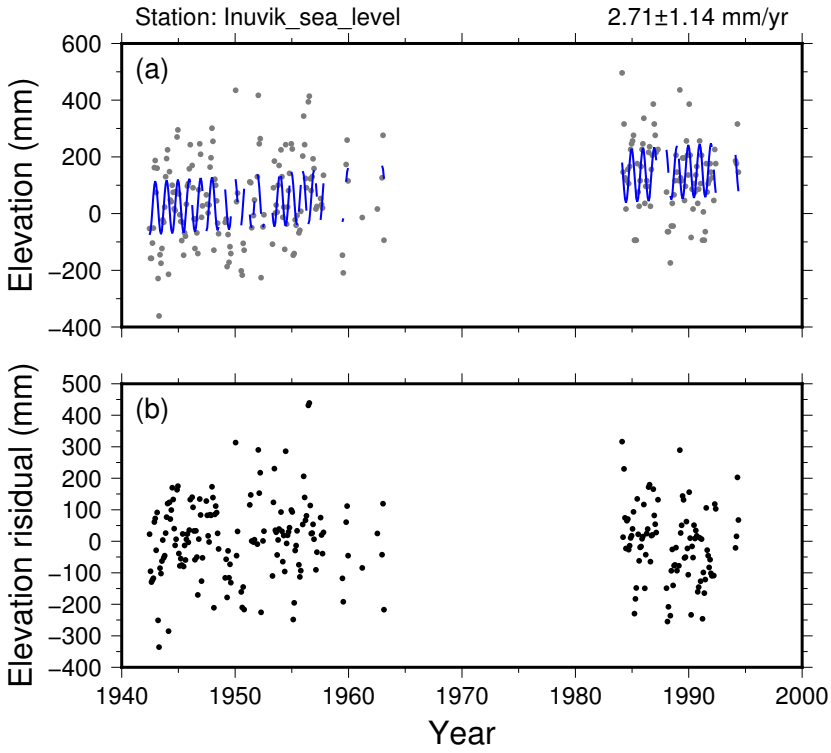

Figure 4.33: Sea level at Inuvik, Northwest Territories (grey dots) with linear plus annual modelled signal (blue line). (b) residuals.

The GRACE data are strongly affected by hydrological changes. A comparison of the uplift rates from GRACE data calculated as viscoelastic deformation with GPS uplift rates shows that the duration of measurement recording time is currently insufficient to calculate a reliable GIA rate. This is caused by a significant non-GIA signals (*i.e.* changes in hydrology that are incorrectly interpreted as viscoelastic uplift) that bias the calculated viscoelastic signals. At present, GIA uplift rates derived from raw GRACE data are tenuous at best.

Despite these caveats, the modelled rates from GPS time series spanning eight to ten years, as is applicable to all the stations used in this study, are likely close enough to the true rate to be used to constrain ice sheet models. Even in the worst cases, the fluctuation of the calculated uplift rate after ten years of measurement time generally do not exceed 0.5 mm.yr^{-1}. Such large fluctuations may make a difference in areas where the residual uplift is small, but in areas where the rate

is high (such as Baker Lake, Churchill, Yellowknife and Pickle Lake) and in areas where there are few if any other constraints on the GIA models, this magnitude of error may be acceptable.

Chapter 5

Glacio-isostatic adjustment detected by differential water levels of lakes in western Canada

5.1 Introduction

Observations of lake tilt provide a way to assess the magnitude of contemporary GIA in inland North America. By finding the long term change in lake level between water gauges relative to a fixed datum, it is possible to determine the gradient of GIA within the lake basin. There are several lakes in western Canada that are sufficiently large that a gradient measurement across the lake should be possible. Long duration time series from lake level gauges can be used to measure the amount of tilt if the duration is sufficient to overcome various sources of noise, such as seiching (standing waves), wind run up (persistent directional winds) and currents due to water inflow.

5.2 Previous Work

Tilt of lakes within Canada and the northern United States due to GIA has been investigated in several prior studies, made possible by the long duration of the some of the gauge measurements. Much of the focus has been on the Great Lakes, where

some gauges have been in operation since the 1800s (*i.e.* Walcott, 1972; Carrera et al., 1991; Mainville and Craymer, 2005). In western Canada, tilt values have been determined by Carrera et al. (1991) and Tackman et al. (1999). It has been over 15 years since the last study of the tilt of these lakes, offering the possibility that the additional duration of measurements will lead to an improved estimate of lake tilt. The tilting of the Great Lakes has been examined in detail in past studies (*e.g.* Mainville and Craymer, 2005), though these were not used to constrain the ice model due to their location outside of the study area.

The contemporary tilt of several lakes in the study have been examined in two past studies. Carrera et al. (1991) determined the tilt of Lake Winnipeg, Lake Manitoba, Lake of the Woods, Lake Winnipegosis, Great Slave Lake and Lake Athabasca. They used only data from July to September in each year in order to minimise the effects of river discharge on the gauges, many which are located near the mouths of rivers. They used a spatial coherence test to assess the gauges and to exclude anomalous sites. Tackman et al. (1999) calculated the tilt of Lake Winnipegosis, Lake Winnipeg, Lake Manitoba and Lake of the Woods. Since there were high levels of noise during the summer months due to weather events and seiches, they decided to use the four month averages between December and March, when these lakes are usually frozen over. Though there are fewer noise sources during the winter months at most site pairs analysed in these lakes, this approach discards many observations that may still be useful to constrain lake tilt.

5.3 Methods

Daily water gauge data were downloaded from the Water Survey of Canada website (`http://www.wsc.ec.gc.ca/applications/H2O/index-eng.cfm`). To reduce the influence of large daily variability of lake levels between different parts of the lakes (due to wind run up and seiching), the data were averaged into ten day bins. This

also made computation more feasible, considering that some sites have over 80 years of continuous data. If a bin had fewer than eight days of measurements, it was excluded from analysis.

Three methods were used to assess the tilt of lakes measured by gauges. The first method was to take the difference of the lake levels between individual gauges, and to use Hector to compute the tilt rate (Bos et al., 2013). As with the GPS analysis (see Chapter 4), the tilt rate was computed along with an annual signal and a white plus power law noise model. Any data point with a residual greater than three times the interquartile range was rejected. Since some of the gauges within the lake are not at the same datum, the average relative level over the entire time series was subtracted from each point.

A second method, using a Markov Chain Monte Carlo (MCMC) approach, was provided by Jean-Philippe Montillet. The mathematical details of this method can be found in Olivares and Teferle (2013). The current implementation has been applied to GPS time series by Montillet and Yu (2014). This technique models the noise as white from Gaussian distribution without coloured noise, as well as modelling an annual signal and linear rate. This technique gives a better estimation of the uncertainties of time series with only a few hundred points than is found using Hector or weighted least squares, as is the case with the gauge pairs in this study (J.-P. Montillet, *pers comm.*, 2015).

The third method takes advantage of the fact that all gauges are measuring relatively uniform changes in lake level across the entire lake. This method, originally developed by Mainville and Craymer (2005), calculates the tilt rate taking into account monthly lake level and site-dependent biases (referred to as the MC method in the rest of this study). The site dependent bias will be a constant value between the elevation of the lake as measured by the gauge relative to the expected elevation relative to a common datum. Essentially, it can be viewed as the error in surveyed

elevation of the gauge. The method has been expanded in this study to include offsets and periodic signals. This method is summarised by the formula:

$$w_{ij}^{obs} = \alpha_i + b_j + v_i(t_j - t_o) - offset_j + A_i \cos(\omega t_j + \phi_i) \tag{5.1}$$

The measured water level and residual at each gauge, i, at each time epoch, j, is denoted as w^{obs}. The parameter α is a site dependent bias, which is the average measured difference in water level of a particular gauge relative to a reference gauge. The average lake level at each time epoch is denoted b. The vertical velocity of the gauge relative to a reference gauge is v. The water level is referenced a set year $t_o = 1985$, to be consistent with the study in Mainville and Craymer (2005). If there is an undocumented adjustment in the gauge elevation, this is calculated by least squares using $offset$. The calculated spectra at many of the site pairs in this study indicate that there can be substantial annual variability between them. This is modelled using a sinusoidal function with frequency $\omega = 2\pi/365.25$, amplitude A and phase ϕ.

The method to determine the offsets follows Williams (2003), which estimates offsets by least squares, assuming white noise. This method is better than trying to estimate the offsets a-priori by taking the slope on either side of the offset. If there is large amplitude coloured noise, this method may give biased results when there are fewer than 100 samples (*i.e.* about three years using ten day sampling) (Montillet et al., 2015). It is necessary to investigate the stochastic properties of the data in this case. Fortunately, the time series that are suspected to have are offsets are generally longer than twenty years, which means that the use of least squares to estimate offsets should be relatively unbiased.

This equation is solved using a weighted linear least squares inversion. It results in $4(i-1) + j - 2 + offset_j$ unknowns to solve for, with one gauge is serving as a reference with velocity, site bias and sinusoidal components set to zero. The data

are weighted by the inverse of the variance of the ten day averages. The inversion is iterated to remove any data that is outside three times the interquartile range. As mentioned above, weighted least squares may underestimate the uncertainty if there is a large component of correlated noise. Stations identified to have large correlated noise sources are excluded from the MC analysis. Since this is a joint analysis, even if there is some correlated noise in the gauge data, the rates from this method are considered to be the most robust, and are used for constraining the ice sheet model. The time series in this chapter show the data after the modelled lake bias, site bias and offsets have been removed from the measured water level. All reported uncertainties are at one-sigma.

5.4 GRACE data

GRACE data were downloaded from the ANU GRACE data visualisation tool (`http://grace.anu.edu.au/overlay.php`, Darbeheshti et al., 2013). The GRACE data were converted to uplift rates by assuming that the complete signal was due to viscoelastic deformation (Purcell et al., 2011). This is not a valid assumption in areas with significant changes in water storage through time. Though the hydrological signals are regional in nature, it is possible that they are similar in magnitude within the distances of a lake basin. If this is the case, then referencing the viscoelastic deformation between the locations of a lake gauge may give a reasonable estimate of the GIA gradient. One of the goals of this study is to compare the gradient of GRACE with the change in lake level over time and see if this is a valid assumption. The reported GRACE rate in this study will have the opposite sign to that of the lake gauge rates, since the gauges are measuring a change in lake level, which will be going down in areas with higher uplift rates.

5.5 Lake Gauge Data

A total of ten lakes that had at least two gauges were considered for this study (Fig. 5.1). It is assumed that there are no errors in relating lake gauges to a reference height datum. Gauges with suspected undocumented adjustments are discussed in this section. The location and recording duration of the gauges are on Table 5.1.

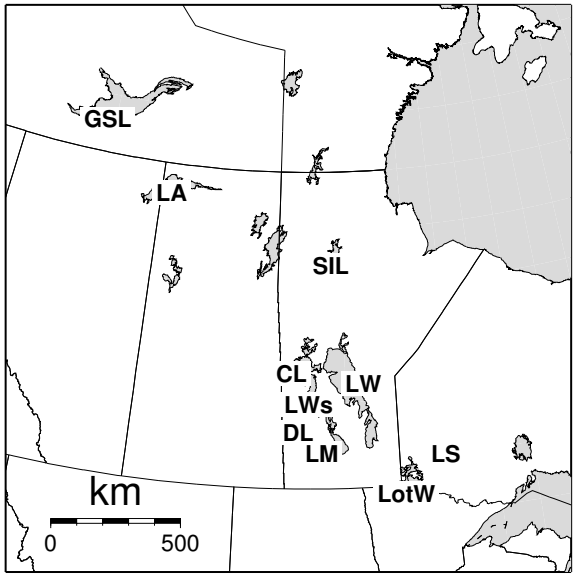

Figure 5.1: Location of the lakes considered in this study. CL – Cedar Lake; DL – Dauphin Lake; GSL – Great Slave Lake; LA – Lake Athabasca; LM – Lake Manitoba; LotW – Lake of the Woods; LS – Lac Seul; LW – Lake Winnipeg; LWs – Lake Winnipegosis; SIL – Southern Indian Lake

Table 5.1: Location and recording time of gauges used in this study

Gauge Name	Latitude	Longitude	Start time	End time
Cedar Lake				
Easterville	53.108	−99.823	1966	1982
Oleson Point	53.320	−100.279	1966	1982
Dauphin Lake				
Outlet	51.440	−99.950	1951	2009
Ochre Beach	51.127	−99.789	1951	2009
Great Slave Lake				
Yellowknife Bay	62.442	−114.350	1938	2013
Hay River	60.860	−115.734	1988	2013
Fort Resolution	61.164	−113.679	1940	1981
Snowdrift	62.404	−110.742	1959	1975
Reliance	62.713	−109.165	1983	1994

Table 5.1 continued...

Gauge Name	Latitude	Longitude	Start time	End time
Lac Seul				
Lac Seul	50.323	−92.265	1985	2012
Hudson	50.092	−92.170	1952	2012
Goldpines	50.637	−93.178	1952	1952
Lake Athabasca				
Crackingstone Point	59.384	−108.894	1961	2011
Fort Chipewyan	58.711	−111.147	1961	2011
Bustard Island	58.782	−110.778	1975	1995
Lake Manitoba				
Steep Rock	51.444	−98.803	1923	2013
Meadow Portage	51.621	−99.575	1952	1968
The Narrows	51.081	−98.781	1967	1996
Toutes Aides	51.522	−99.540	1969	1994
Delta	50.188	−98.317	1923	1969
Westbourne	50.251	−98.588	1964	2013
Lake of the Woods				
Warroad	48.904	−95.316	1916	2010
Hanson Bay	49.133	−94.283	1962	2013
Clearwater Bay	49.711	−94.809	1963	2013
Cyclone Island	49.328	−94.853	1983	2013
Keewatin	49.764	−94.554	1913	2013
Kenora	49.771	−94.490	1915	1959
Lake Winnipeg				
Victoria Beach	50.695	−96.562	1959	2013
Berens River	52.353	−97.022	1953	2013
George Island	52.818	−97.620	1983	2013
Montreal Point	53.625	−97.844	1969	2011
Pine Dock	51.640	−96.803	1958	2013
Matheson Island Landing	51.724	−96.915	1957	2013
Mission Point	53.191	−99.212	1953	2013
Gimli	50.631	−96.982	1966	2013
Anama Bay	51.997	−98.057	1960	1972
Lake Winnipegosis				
Dawson Bay	52.975	−100.979	1963	1994
Winnipegosis	51.647	−99.923	1963	1994
Southern Indian Lake				
Opachuanau Lake	56.783	−99.525	1985	2013
South Indian Lake	56.779	−98.941	1977	2013
South Bay	56.687	−99.023	1977	2013
Missi Falls	57.313	−98.161	1985	2013

5.5.1 Cedar Lake, Manitoba

Cedar Lake, Manitoba has two gauges with a time series spanning 16 years from the late 1960s to early 1980s (Fig. 5.2). The lake level is regulated by a dam located at its outlet, which was completed in 1968 (Manitoba Hydro, 2014).

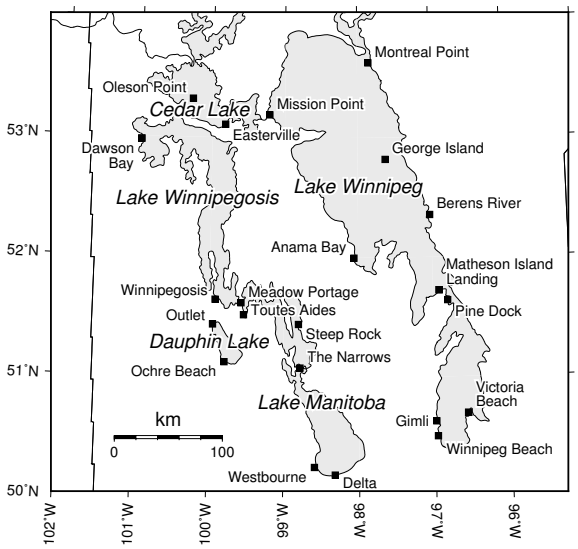

Figure 5.2: Lake gauges investigated in Manitoba, including Cedar Lake, Dauphin Lake, Lake Manitoba, Lake Winnipeg and Lake Winnipegosis.

5.5.2 Dauphin Lake, Manitoba

There are two gauges in Dauphin Lake with an overlapping record of 58 years. The tilt rate is measured relative to Ochre Beach at the south end of the lake. After 1983, the gauge at Ochre Beach did not record continuously throughout the year. The observations are often missing between the months of December and April. Dauphin Lake is regulated at the outlet to prevent low water levels (Government of Manitoba, 2013).

5.5.3 Great Slave Lake, Northwest Territories

There are five gauges in Great Slave Lake (Fig. 5.3), though only three of the gauges have measurements that exceed 20 years. The gauge at Yellowknife Bay is the only continuous time series that overlaps with all of the other gauges, so it is used as the reference. The gauge at Hay River appears to have operated at two different datums prior to 1988, so offsets were calculated at June 23, 1983 and April 7, 1988. The gauges at Reliance and Fort Resolution are not referenced to the same datum as the other three gauges, but appear to remain at a consistent level throughout the duration of recording.

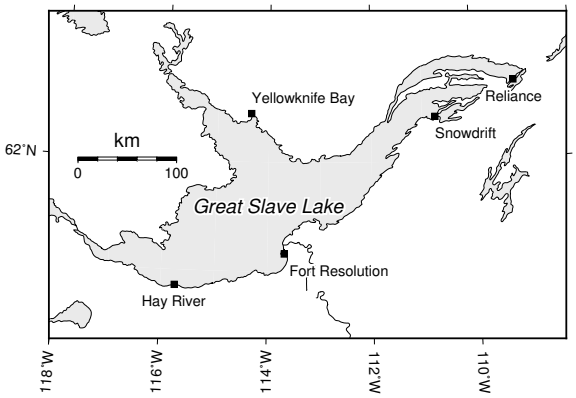

Figure 5.3: Lake gauges investigated at Great Slave Lake.

5.5.4 Lac Seul

There are three gauges at Lac Seul (Fig. 5.4). Measurements at all three gauges go back to the 1910s and 1920s, though the level at the three gauges was unlikely to be the same prior to the completion of the hydroelectric dam at the outlet in the 1930s. Only data after 1952 are used, as prior to this time the gauges appear to have operated at different datums. The gauge at Hudson is located in Lost Lake, which is usually part of the Lac Seul basin (Lake of the Woods Control Board, `http://www.lwcb.ca/reg-guide/rgp-PT2-LACSEUL.html`, accessed December 29th, 2014).

During times of high flow of the English River, Lost Lake is isolated from the main part of Lac Seul, but usually by no more than 10 cm. Due to this, the measurements of Hudson may not be representative of the Lac Seul lake level. Tilt measurements are relative to the gauge at Lac Seul.

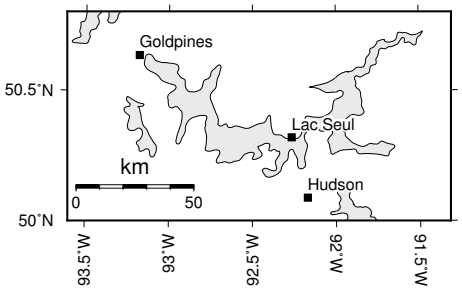

Figure 5.4: Lake gauges investigated at Lac Seul.

5.5.5 Lake Athabasca, Alberta/Saskatchewan

Lake Athabasca has three gauges (Fig. 5.5), which are referenced to Crackingstone Point. Regulation of the Peace River in 1968 and the construction of weirs at the outlet of the lake in 1975 and 1976 have contributed to reduced fluctuations of lake level between winter and summer (Peters, 2014).

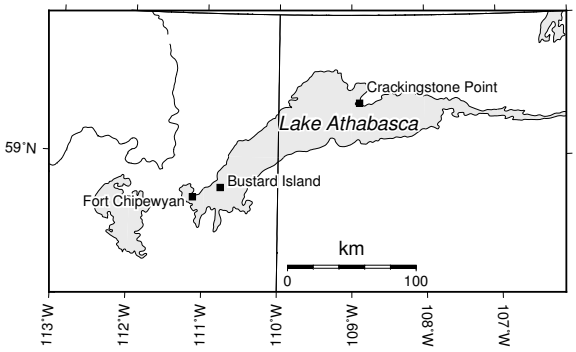

Figure 5.5: Lake gauges investigated at Lake Athabasca.

5.5.6 Lake Manitoba, Manitoba

There are six gauges in Lake Manitoba that are considered for analysis (Fig. 5.2). The gauge at Steep Rock is used as the reference as it is the only one with measurements that overlap with all the other gauges. Since 1961, the lake level has been regulated to remain between 247.04 and 247.65 m by a control structure located at the outlet (Government of Manitoba, 2013). The gauge at The Narrows has at least two apparent offsets in the time series. The most obvious of these are on January 29, 1962 and April 28, 1966. Offsets are calculated for both of these times. These offsets were likely introduced during the construction of a causeway in the vicinity of The Narrows between 1960 and 1966 (Tackman et al., 1999).

5.5.7 Lake of the Woods, Ontario

Lake of the Woods has one of the longest and best lake level records in the study area, due to the large number of gauges (Fig. 5.6). The lake is regulated to remain between 321.87 and 323.39 m (Lake of the Woods Control Board, 2013). Lake of the Woods has six gauges that are of sufficient duration to be suitable for analysis. The data for Clearwater Bay had an offset in 2005 relative to the other gauges. This was caused by a 57 mm adjustment that had been applied to the gauge on May 12, 2005, which had not been accounted for in the Water Survey of Canada data. The gauge at Warroad was operated by the Canada Water Survey until 1978, when operations were taken over by the United States Geological Survey (USGS). Direct comparison of the Water Survey of Canada and USGS datasets for this gauge reveals a 16 mm discrepancy starting in January 1980. The cause of this discrepancy is unknown, but probably due to an undocumented adjustment to the gauge that was not applied by the Canada Water Survey. For consistency, the Water Survey of Canada data are still used, adjusted for the 16 mm offset after 1980. All tilt measurements are

calculated relative to Warroad, the southernmost gauge.

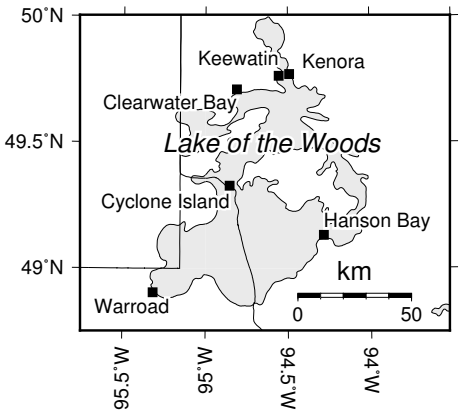

Figure 5.6: Lake gauges investigated at Lake of the Woods.

5.5.8 Lake Winnipeg, Manitoba

Lake Winnipeg has nine gauges that are considered (Fig. 5.2). Since 1976, the level of Lake Winnipeg has been regulated by a dam at the northern outlet, to keep the lake level between 711 and 714 feet (216.71 and 217.93 m) (Baird & Associates, 2000). The gauges at Pine Dock and Matheson Island Landing have apparent offsets in late 2000-early 2001 relative to other gauges. These two gauges were adjusted in late 2001 and early 2002 to account for instrument drift (23 mm and 60 mm, respectively), but the observed offsets at these gauges are too early and not the same magnitude as these adjustments. Offsets were calculated on April 15, 2001 for the gauge at Pine Dock, and on January 1, 2001 for Matheson Island Landing. The gauge at Anama Bay is not referenced to the same datum as the other gauges, and has a short recording period. Tilt measurements are relative to the southernmost gauge at Victoria Beach. Tackman et al. (1999) suggested that there might be an offset in the Victoria Beach data after an adjustment to the gauge benchmark in 1970. The gauge was apparently damaged in 1961 and, from direct comparison of Victoria Beach and the other gauges with overlapping measurements, it is noisier prior to 1970. However, there is no visually obvious offset in 1970, so it is not

included in the analysis. There is a gauge at Winnipeg Beach which appears to have been recorded at a different datum from the only other gauge with an overlapping time series (Berens River). It is not included in the analysis because it does not overlap significantly with the reference gauge at Victoria Beach.

5.5.9 Lake Winnipegosis, Manitoba

There are two gauges in Lake Winnipegosis with an overlapping record that is sufficiently long to be considered (Fig. 5.2). The calculated rate is relative to the gauge at Winnipegosis. Measurements resumed at the Dawson Bay gauge in 2012 after a hiatus of 18 years. The level of Lake Winnipegosis is not artificially regulated (Government of Manitoba, 2013).

5.5.10 Southern Indian Lake, Manitoba

Southern Indian Lake has four gauges, and are referenced to the gauge at Opachuanau Lake (Fig. 5.7). Since 1986, the lake level has been regulated to remain between 256.95 and 258.32 m (Manitoba Hydro, 2010).

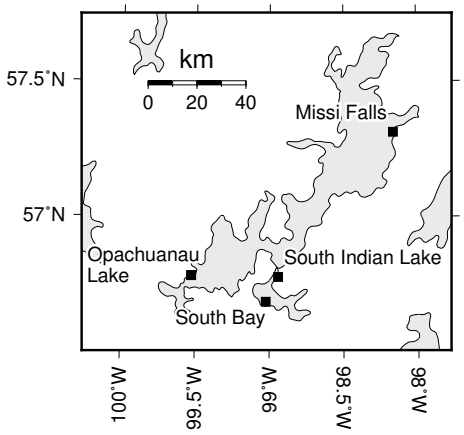

Figure 5.7: Lake gauges investigated at Southern Indian Lake.

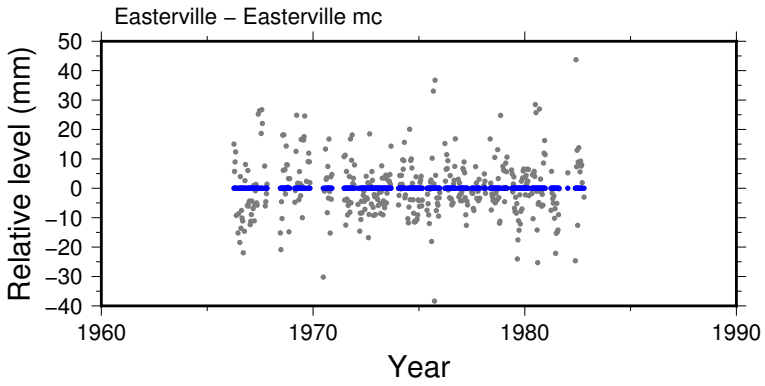

Figure 5.8: Residuals of Easterville gauge in Cedar Lake from the MC method. By definition, the rate is zero.

5.6 Results

5.6.1 Cedar Lake, Manitoba

This gauge pair has a calculated rate that indicates that the gauge at Oleson Point is uplifting relative to Easterville (Table 5.2). The data are shown on Figs .5.8 and 5.9). The modelled tilt rate between the three methods (Hector, MCMC and MC Method) are the same at the one-sigma level. If this is the result of GIA, then it indicates that the uplift rate increases towards the northwest. The result from GRACE is smaller in magnitude than the gauge results, and is not significant at the two-sigma level.

Table 5.2: Lake tilt results of Cedar Lake relative to the gauge at Easterville ($mm.yr^{-1}$)

	Hector	MCMC	MC Method	GRACE
Oleson Point	1.35±0.66	1.50±0.38	1.45±0.19	0.22±0.16

5.6.2 Dauphin Lake, Manitoba

Dauphin Lake has a single gauge pair, which are 37 km apart. The results of the MC method are shown in Figs. 5.10 and 5.11. The results show that after six decades of

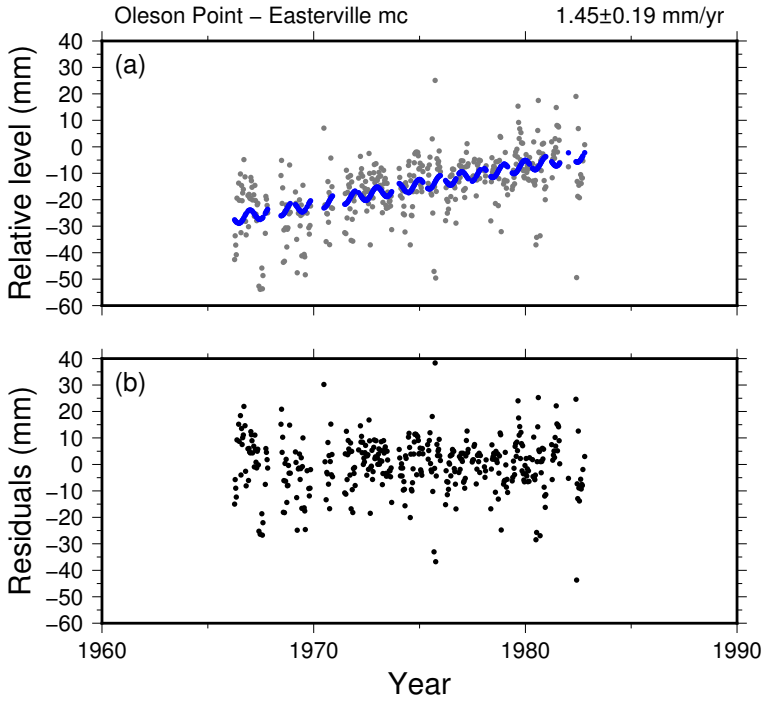

Figure 5.9: Difference between Oleson Point and Easterville gauges in Cedar Lake from the MC method, along with the linear plus annual model (blue). (b) residuals.

measurements, the relative uplift between the gauges is negligible at the one-sigma level from the Hector and MCMC results, while the MC method shows a small tilt is significant at the two-sigma level (Table 5.3). This may indicate there is a small amount of relative uplift at the outlet relative to Ochre Beach. The result from GRACE indicates an uplift rate of the outlet relative to Ochre Beach that is significant at the two-sigma level. The non-linear residuals indicate that this rate may be affected by correlated noise (Fig. 5.12).

Table 5.3: Lake tilt results of Dauphin Lake relative to the gauge at Ochre Beach ($mm.yr^{-1}$)

	Hector	MCMC	MC Method	GRACE
Outlet	-0.18±0.20	-0.15±0.22	-0.14±0.06	0.58±0.17

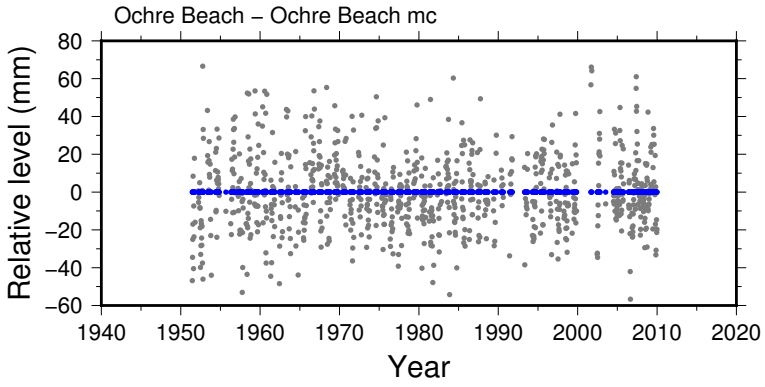

Figure 5.10: Residuals of Ochre Beach gauge in Dauphin Lake from the MC method. By definition, the rate is zero.

5.6.3 Great Slave Lake, Northwest Territories

The results of Great Slave lake from the MC method are shown in Table 5.4 and from the individual comparisons using Hector and MCMC are shown in Table 5.5 and 5.6. Plots using the MC method relative to Yellowknife Bay are in Figs. 5.13 to 5.17. The offsets calculated for Hay River are 60±9 mm in 1983 and 191±5 mm for 1988 using the MC method. The calculated errors of the relative lake level with Yellowknife Bay are very high, with the exception of Hay River. The rate between of Hay River and Yellowknife can be considered to be negligible at the two-sigma level. The rates with respect to Reliance are not significant at the one-sigma level, regardless of modelling method. This can be attributed to the short recording period (12 years) and the lack of continuity of measurements. Both Fort Resolution and Snowdrift have rates that are significant at the two-sigma level with respect to Yellowknife Bay. In both cases, there is falling lake level relative to Yellowknife Bay, which indicates there is relative uplift at these gauges. The GRACE rates are inconsistent with the gauges. The rates with respect to Fort Resolution and Hay River are not distinguishable from zero at the two sigma level.

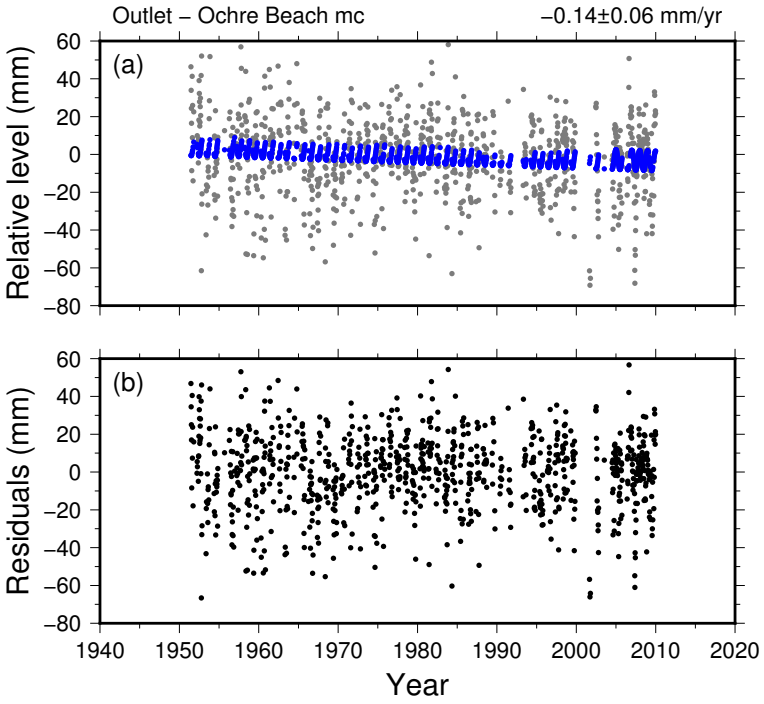

Figure 5.11: Difference between Outlet and Ochre Beach gauges in Dauphin Lake from the MC method, along with the linear plus annual model (blue). (b) residuals.

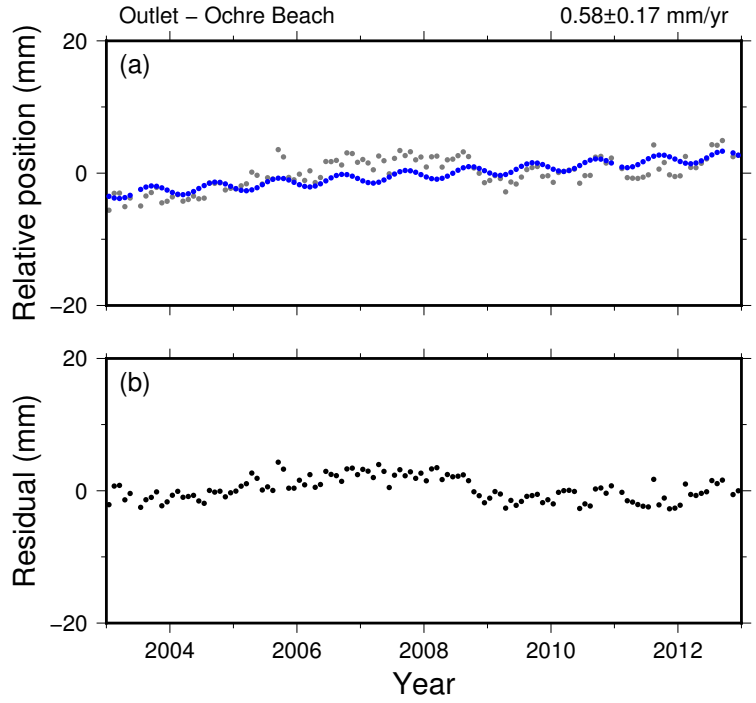

Figure 5.12: Difference between GRACE data between the Outlet and Ochre Beach gauges in Dauphin Lake using a linear plus annual model (blue). (b) residuals.

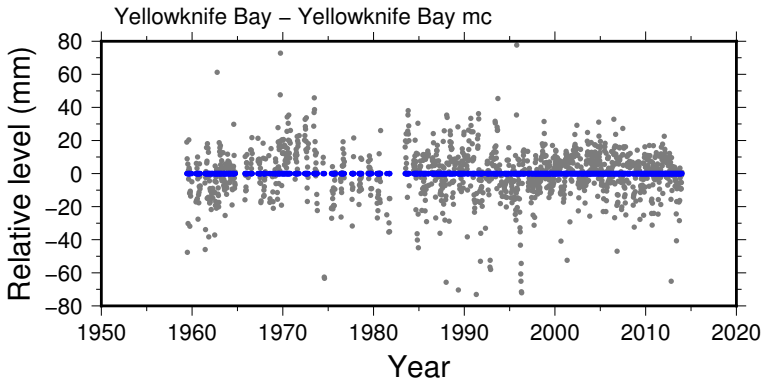

Figure 5.13: Residuals of Yellowknife Bay gauge in Great Slave Lake from the MC method. By definition, the rate is zero.

Table 5.4: Lake tilt results of Great Slave Lake relative to the gauge at Yellowknife Bay (mm.yr^{-1})

	Hector	MCMC	MC Method	GRACE
Fort Resolution	-0.13±1.17	-0.18±0.81	-0.77±0.30	-0.54±0.43
Hay River	0.23±0.84	0.17±0.20	0.16±0.09	-0.8±0.63
Reliance	-0.31±2.08	0.15±2.19	-0.20±1.07	2.19±0.53
Snowdrift	-3.2±0.87	-2.68±0.59	-2.67±0.42	1.00±0.35

Table 5.5: Lake tilt results of Great Slave Lake from the comparison of all gauges calculated with Hector (mm.yr^{-1})

	Yellowknife Bay	Fort Resolution	Hay River	Reliance	Snowdrift
Yellowknife Bay	-	0.13±1.17	-0.23±0.84	0.31±2.08	3.20±0.87
Fort Resolution	-0.13±1.17	-	1.28±2.05	-	0.52±0.88
Hay River	0.23±0.84	-1.28±2.05	-	7.67±7.07	2.37±1.14
Reliance	-0.31±2.08	-	-7.67±7.07	-	-
Snowdrift	-3.20±0.87	-0.52±0.88	-2.37±1.14	-	-

Table 5.6: Lake tilt results of Great Slave Lake from the comparison of all gauges calculated with MCMC (mm.yr^{-1})

	Yellowknife Bay	Fort Resolution	Hay River	Reliance	Snowdrift
Yellowknife Bay	-	0.18±0.81	-0.17±0.20	0.15±2.19	2.68±0.59
Fort Resolution	-0.18±0.81	-	-	-	98.17±46.10
Hay River	0.17±0.20	-	-	3.78±18.22	0.38±0.18
Reliance	-0.15±2.19	-	-3.78±18.22	-	-
Snowdrift	-2.68±0.59	-98.17±46.10	-0.38±0.18	-	-

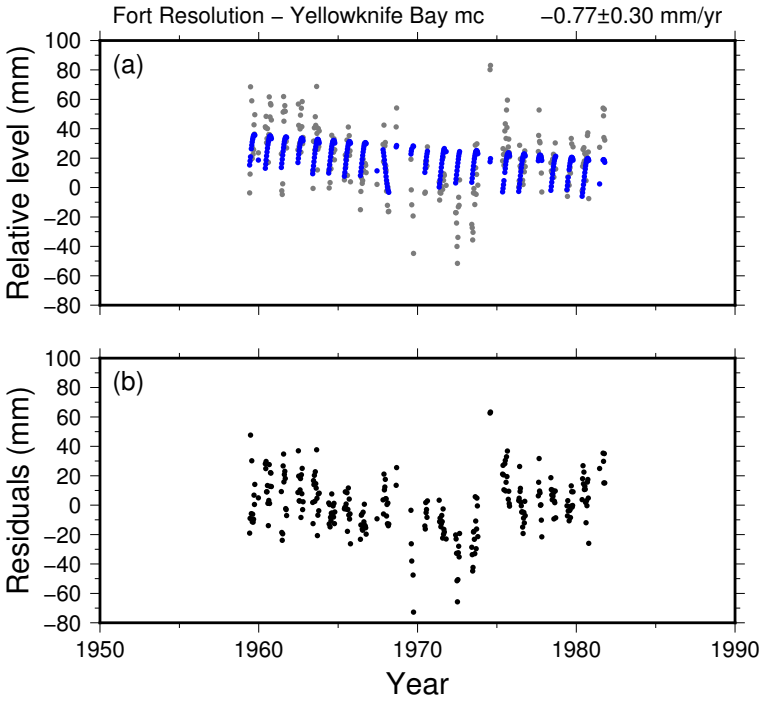

Figure 5.14: Difference between the Fort Resolution and Yellowknife Bay gauges in Great Slave Lake from the MC method, along with the linear plus annual model (blue). (b) residuals.

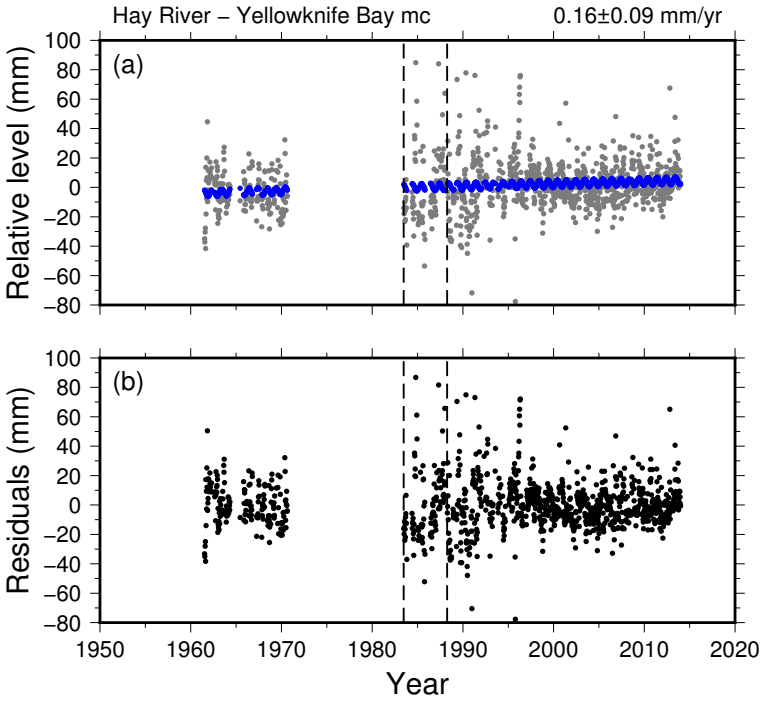

Figure 5.15: Difference between the Hay River and Yellowknife Bay gauges in Great Slave Lake from the MC method, along with the linear plus annual model (blue). The dashed vertical line represents when an offset was calculated. (b) residuals.

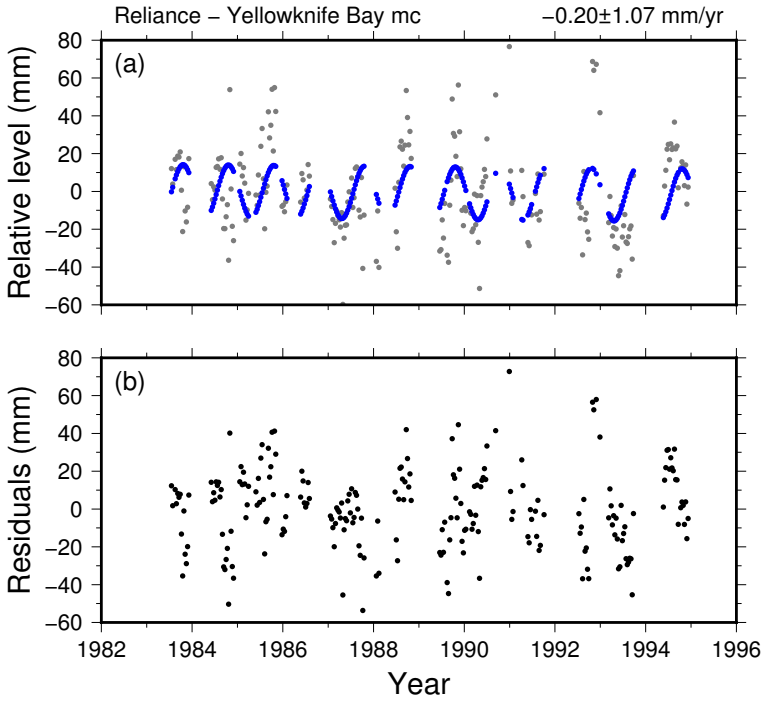

Figure 5.16: Difference between the Reliance and Yellowknife Bay gauges in Great Slave Lake from the MC method, along with the linear plus annual model (blue). (b) residuals.

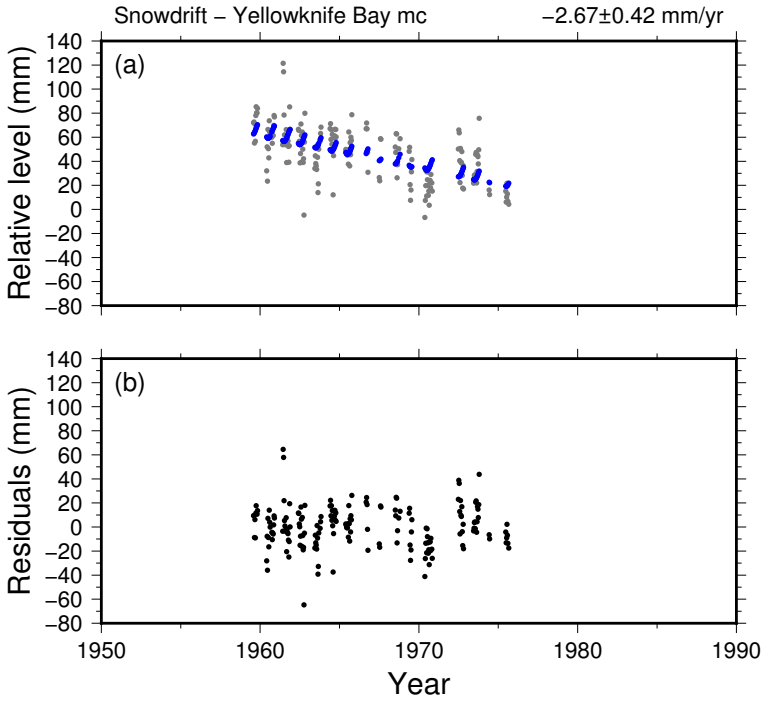

Figure 5.17: Difference between the Snowdrift and Yellowknife Bay gauges in Great Slave Lake from the MC method, along with the linear plus annual model (blue). (b) residuals.

5.6.4 Lac Seul, Ontario

The rates calculated with the gauges at Lac Seul are complicated if Hudson is included, as it is a separate basin that is occasionally isolated from Lac Seul. The isolation of the lake contributes to a large modelled annual signal when lake levels are compared with this gauge (Fig. 5.18). In addition, the residuals of Hudson and Goldpines, which were the only two gauges in operation prior to 1985, do not have a clear linear relationship prior to the start of recording at Lac Seul. The rate of the direct comparison of Hudson and Lac Seul using Hector and MCMC are also significantly different from that calculated with the MC method. These factors lead to the rejection of rates calculated with respect to Hudson. The calculated tilt between Goldpines and Lac Seul since 1985 is negligible at the two-sigma level if Hudson is excluded (Figs. 5.19 and 5.20).

Table 5.7: Lake tilt results of Lac Seul relative to the gauge at Lac Seul, with and without Hudson ($mm.yr^{-1}$)

	Hector	MCMC	MC Method	MC Method (no Hudson)	GRACE
Goldpines	-0.04±0.55	-0.14±0.08	0.40±0.13	-0.10±0.12	0.55±0.17
Hudson	1.28±1.40	1.74±0.36	0.22±0.03	–	-0.82±0.11

5.6.5 Lake Athabasca, Alberta/Saskatchewan

The results of the analysis of the gauges in Lake Athabasca are given in Table 5.8 and Figs. 5.21-5.23. There is a substantial rate of lake level fall recorded at the gauge at Crackingstone Point relative to Fort Chipewyan. It is also significant relative to Bustard Island at the two sigma level. This would indicate that the rate of GIA uplift increases towards the west. There is a strong modelled annual signal at Fort Chipewyan (Amplitude= 49 mm), which likely indicates this gauge is affected by the influence of the Athabasca and Slave Rivers. This may also explain the discrepancy between the rates calculated with the MCMC method and the other two methods.

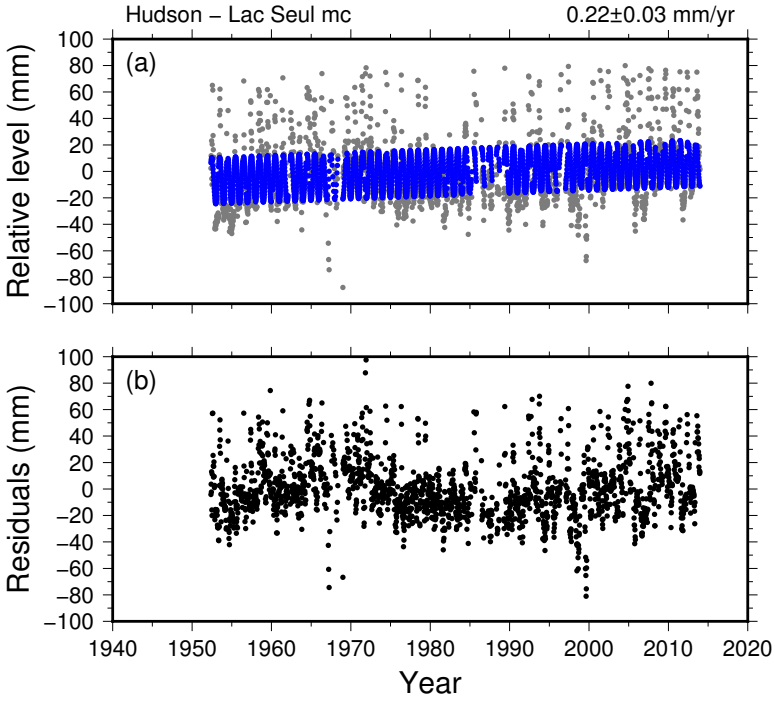

Figure 5.18: Difference between the Hudson and Lac Seul gauges in Lac Seul from the MC method, along with the linear plus annual model (blue). (b) residuals.

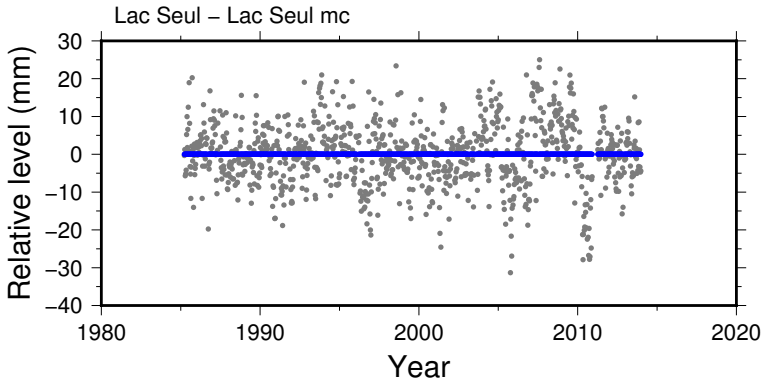

Figure 5.19: Residuals of the Lac Seul gauge in Lac Seul from the MC method (without the gauge at Hudson). By definition, the rate is zero.

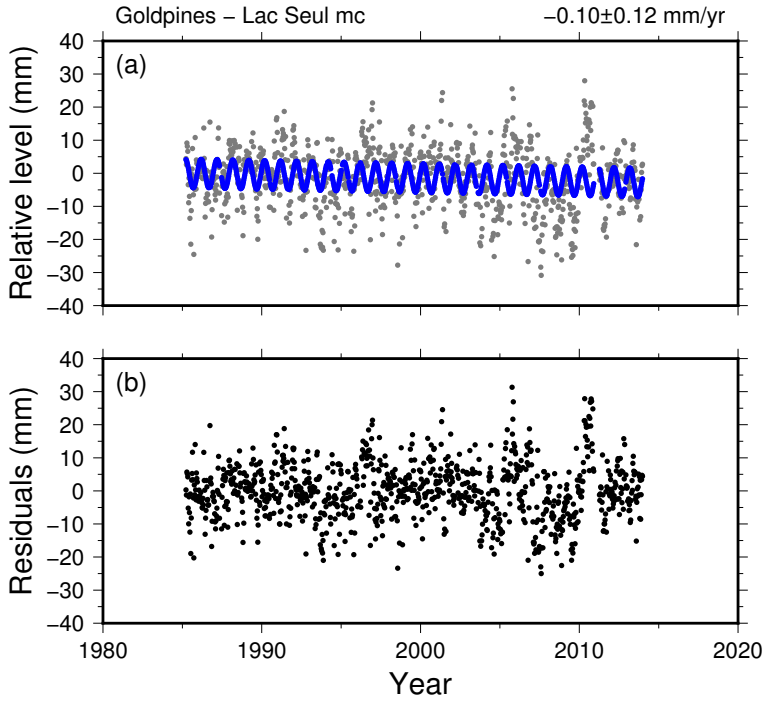

Figure 5.20: Difference between the Goldpines and Lac Seul gauges in Lac Seul from the MC method (without the gauge at Hudson), along with the linear plus annual model (blue). (b) residuals.

The rate calculated from the GRACE data is similar in magnitude, and also has a strong seasonal signal (*e.g.* Fig 5.24). However, GRACE measures relative uplift at Crackingstone Point, opposite of what is indicated by the lake gauge data.

Table 5.8: Lake tilt results of Lake Athabasca relative to the gauge at Crackingstone Point ($mm.yr^{-1}$)

	Hector	MCMC	MC Method	GRACE
Fort Chipewyan	2.49±1.41	3.06±1.07	1.69±0.07	1.30±0.30
Bustard Island	1.06±1.29	-1.36±0.78	0.77±0.30	1.12±0.25

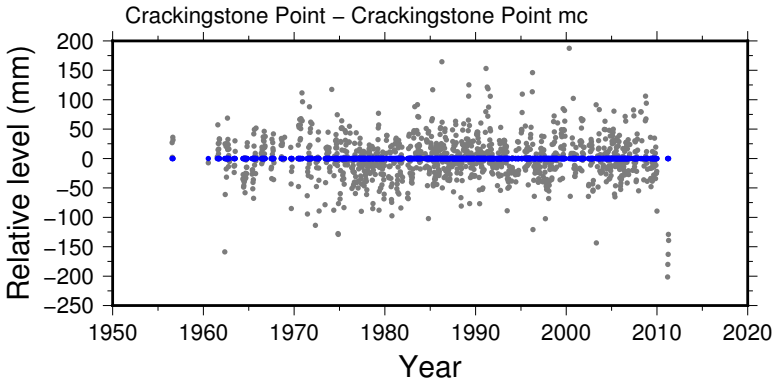

Figure 5.21: Residuals of the Crackingstone Point gauge in Lake Athabasca from the MC method. By definition, the rate is zero.

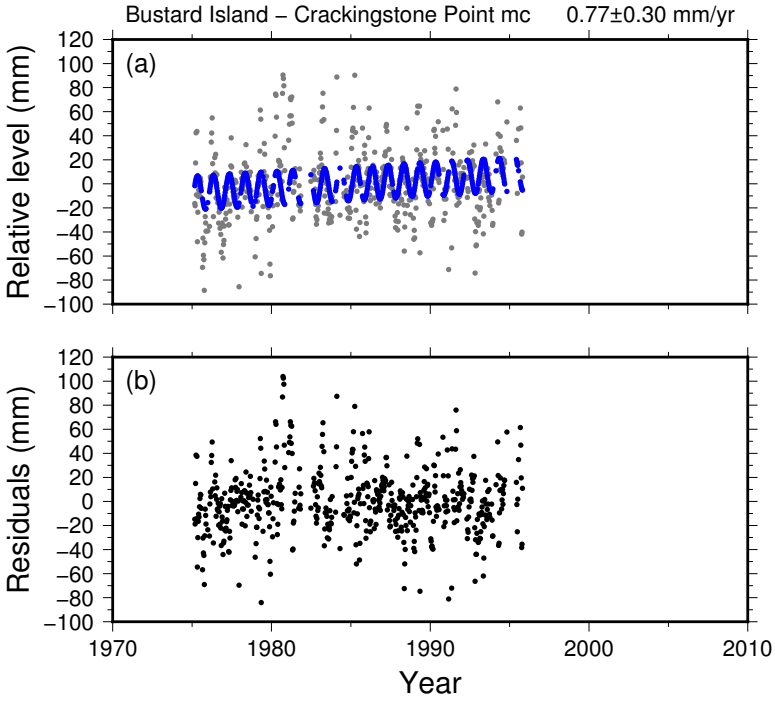

Figure 5.22: Difference between the Bustard Island and Crackingstone Point gauges in Lake Athabasca from the MC method, along with the linear plus annual model (blue). (b) residuals.

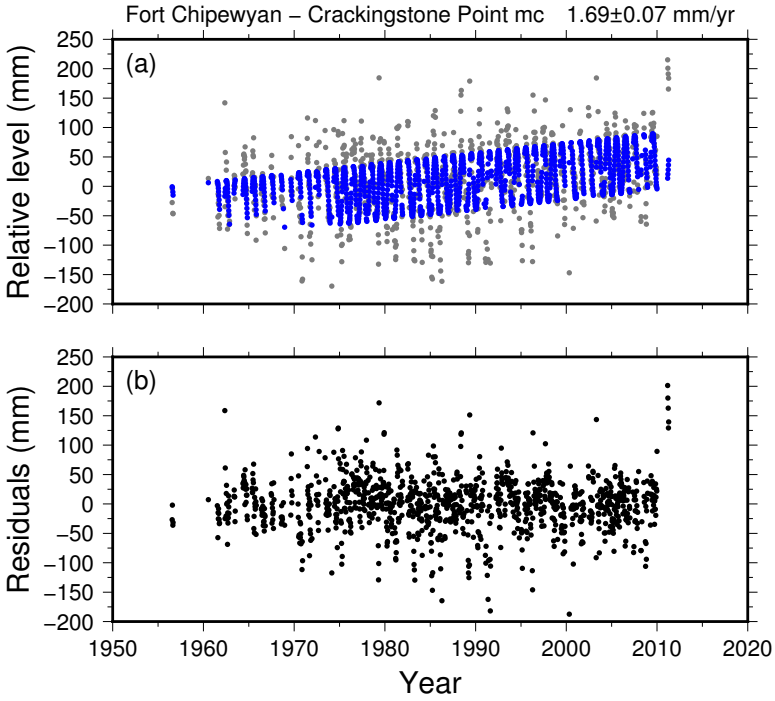

Figure 5.23: Difference between the Fort Chipewyan and Crackingstone Point gauges in Lake Athabasca from the MC method, along with the linear plus annual mode (blue). (b) residuals.

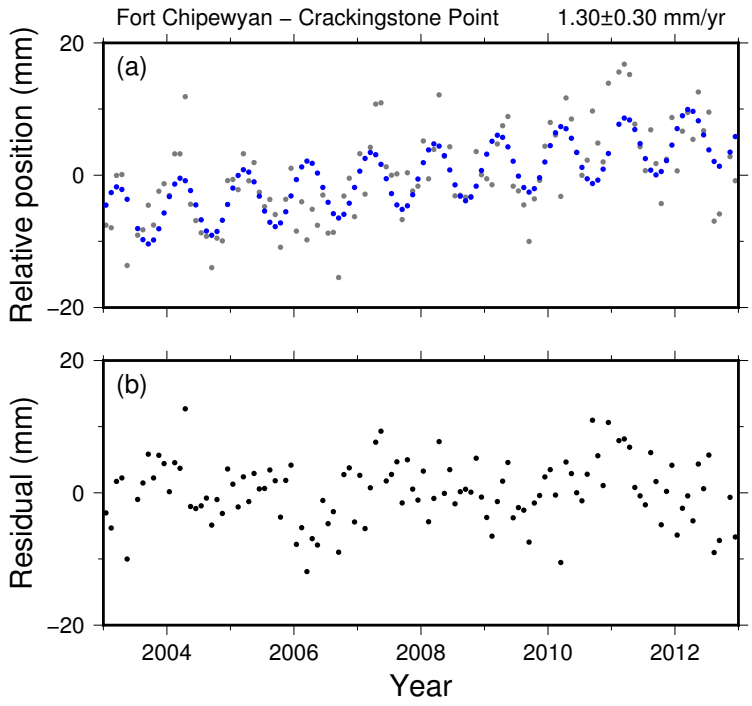

Figure 5.24: Difference between GRACE data between the Fort Chipewyan and Crackingstone Point gauges in Lake Athabasca using a linear plus annual model (blue). (b) residuals.

5.6.6 Lake Manitoba, Manitoba

The results of Lake Manitoba are shown on Tables 5.9–5.11. The results of the MC analysis relative to Steep Rock are on Figs. 5.25 to 5.30. The gauges at Delta and Westbourne should have a similar rate, as they are located only 21 km apart at the southern end of the lake, but they differ by over 0.6 mm.yr^{-1}, regardless of the method of calculation. The Delta gauge is considered to be less reliable, because the residuals show there is correlated noise affecting one of the gauges (Fig. 5.28). The Delta dataset does not influence the MC method calculation at the other gauges, as it does not have significant overlap with the gauges at Toutes Aides, Westbourne and The Narrows. The rates relative to Meadow Portage and The Narrows are not significant at the two-sigma level, regardless of technique. The calculated offsets for The Narrows are -12±4 mm for January 29, 1962 and -29±2 mm for April 28, 1966 using the MC method. The calculated rates relative to Westbourne and Toutes Aides indicate that there is differential uplift at Steep Rock compared to the western and southern parts of the lake. The GRACE rates are considered to be unreliable, because the time series is strongly non-linear, especially between gauges at opposite ends of the lake (*e.g.* Fig. 5.31). In particular, there is a strong change in the calculated relative elevation in 2008 and 2009.

Table 5.9: Lake tilt results of Lake Manitoba relative to the gauge at Steep Rock (mm.yr^{-1})

	Hector	MCMC	MC Method	GRACE
The Narrows	-0.53±0.48	-0.01±0.01	-0.01±0.16	-0.74±0.18
Toutes Aides	0.59±0.43	0.48±0.15	0.67±0.17	0.02±0.19
Delta	1.80±0.75	1.24±0.15	1.21±0.06	-2.56±0.65
Westbourne	0.29±0.30	0.43±0.11	0.45±0.08	-2.43±0.61
Meadow Portage	2.17±1.68	2.47±0.67	0.83+0.94	0.20±0.23

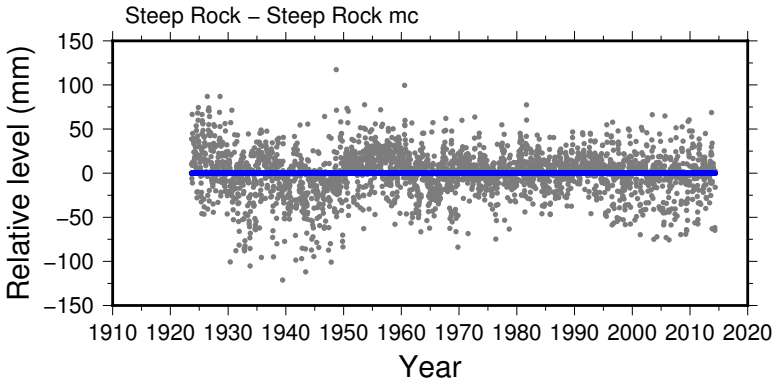

Figure 5.25: Residuals of the Steep Rock gauge in Lake Manitoba from the MC method. By definition, the rate is zero.

Table 5.10: Lake tilt results of Lake Manitoba from the comparison of all gauges calculated with Hector ($mm.yr^{-1}$)

	Steep Rock	The Narrows	Toutes Aides	Delta	West-bourne	Meadow Portage
Steep Rock	-	0.53±0.48	-0.59±0.42	-1.80±0.75	-0.29±0.30	-2.17±1.68
The Narrows	-0.53±0.48	-	-0.49±0.26	-	-0.44±0.54	-
Toutes Aides	0.59±0.42	0.49±0.26	-	-	0.72±0.51	-
Delta	1.80±0.75	-	-	-	0.51±4.97	-0.84±4.83
Westbourne	0.29±0.30	0.44±0.54	-0.72±0.51	-0.51±4.97	-	-
Meadow Portage	2.17±1.68	-	-	-0.84±4.83	-	-

Table 5.11: Lake tilt results of Lake Manitoba from the comparison of all gauges calculated with MCMC ($mm.yr^{-1}$)

	Steep Rock	The Narrows	Toutes Aides	Delta	West-bourne	Meadow Portage
Steep Rock	-	0.01±0.01	-0.48±0.15	-1.24±0.15	-0.43±0.11	-2.47±0.67
The Narrows	-0.01±0.01	-	-0.04±0.02	-0.46±0.12	-0.02±0.02	-0.58±0.09
Toutes Aides	0.48±0.15	0.04±0.02	-	-	0.73±0.33	-
Delta	1.24±0.15	0.46±0.12	-	-	-	-4.01±3.53
Westbourne	0.43±0.11	0.02±0.02	-0.73±0.33		-	-
Meadow Portage	2.47±0.67	0.58±0.09	-	4.01±3.53	-	-

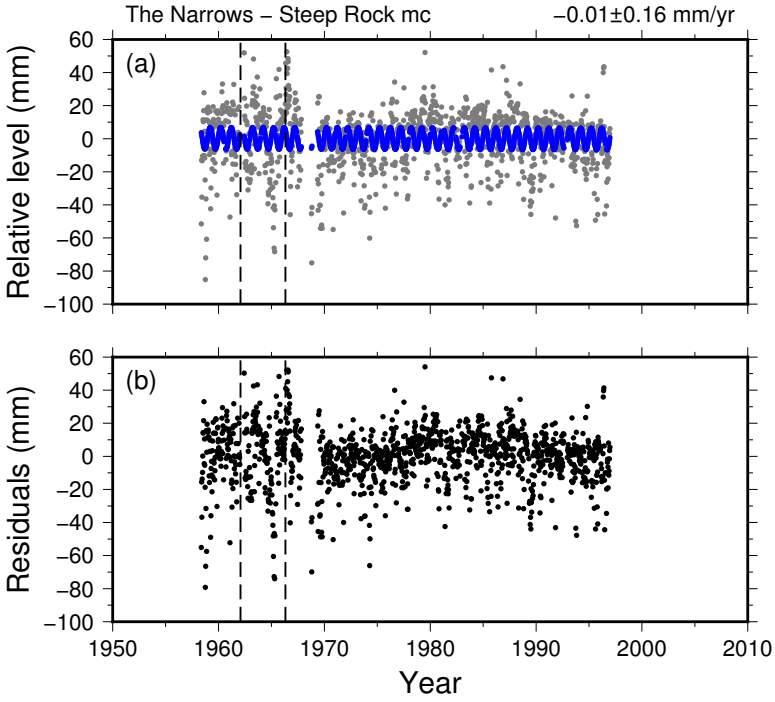

Figure 5.26: Difference between the The Narrows and Steep Rock gauges in Lake Manitoba from the MC method, along with the linear plus annual model (blue). The dashed vertical line represents when an offset was calculated. (b) residuals.

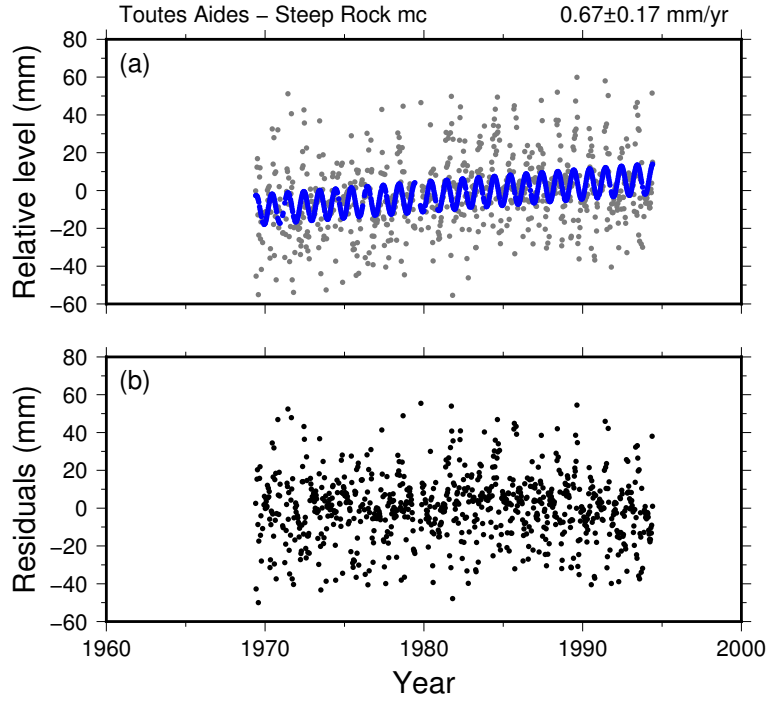

Figure 5.27: Difference between the Toutes Aides and Steep Rock gauges in Lake Manitoba from the MC method, along with the linear plus annual model (blue). (b) residuals.

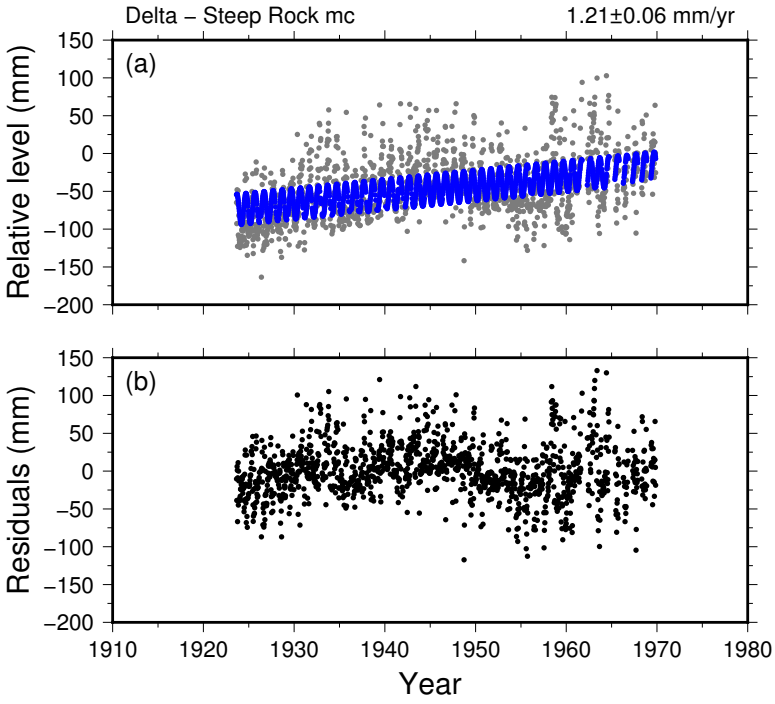

Figure 5.28: Difference between the Delta and Steep Rock gauges in Lake Manitoba from the MC method, along with the linear plus annual model (blue). (b) residuals.

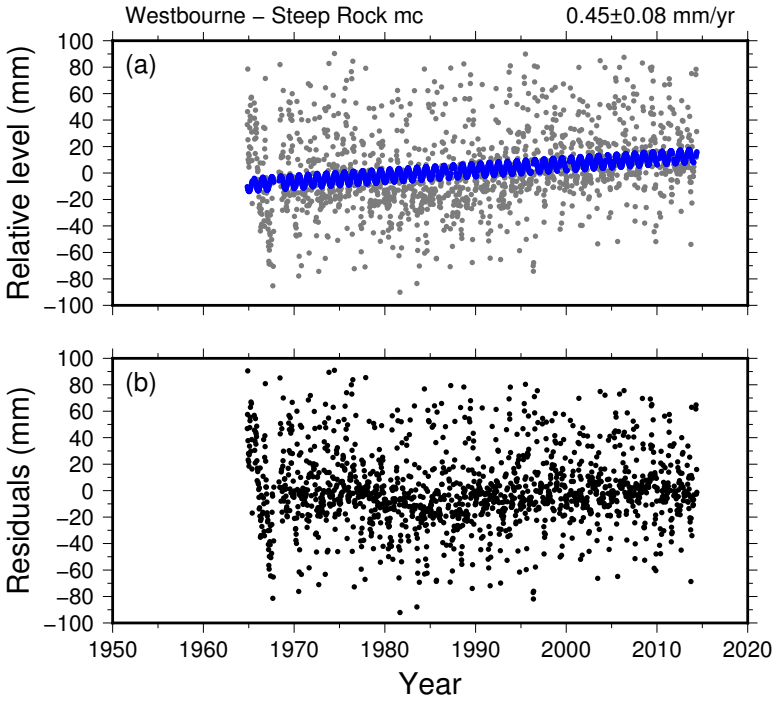

Figure 5.29: Difference between the Westbourne and Steep Rock gauges in Lake Manitoba from the MC method, along with the linear plus annual model (blue). (b) residuals.

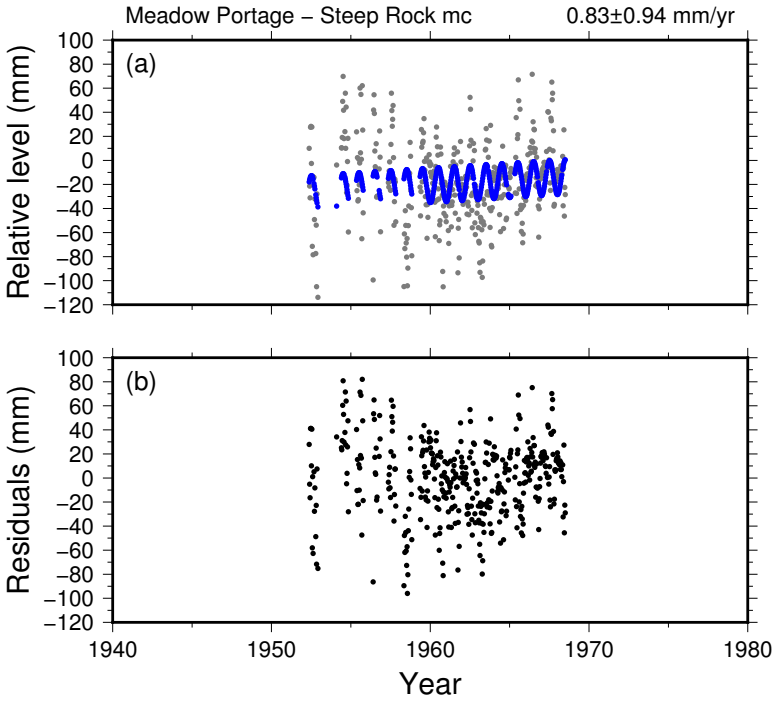

Figure 5.30: Difference between the Meadow Portage and Steep Rock gauges in Lake Manitoba from the MC method, along with the linear plus annual model (blue). (b) residuals.

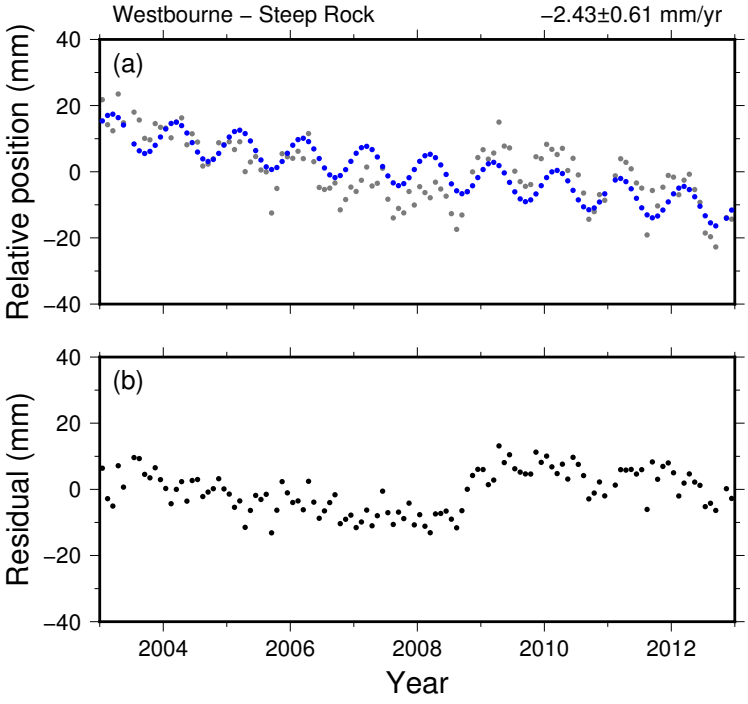

Figure 5.31: Difference between GRACE data between the Westbourne and Steep Rock gauges in Lake Manitoba using a linear plus annual model (blue). (b) residuals.

5.6.7 Lake of the Woods

The results of the analysis of the gauges in Lake of the Woods are shown on Tables 5.12– 5.14. The plots of the results of the MC method are on Figs. 5.32-5.37. Lake of the Woods has some of the highest quality data of all the lakes in this study. Five of the six stations have at least 50 years of continuous data, which leads to high confidence in the calculated rates. The only questionable station is Kenora, which has a rate of roughly half that of the nearby Keewatin station. The rate from the Keewatin station is considered more reliable, as there is nearly 100 years of overlap with the station at Warroad and is more consistent with larger uplift rates towards the northeast as measured with the other gauges. A direct comparison of the Kenora and Keewatin gauges (Table 5.13) reveals a significant non-zero tilt rate, which is likely unrealistic considering they are only five km apart. The rates derived from GRACE do not match those derived from the gauges at the two-sigma level, except Hanson Bay (Table 5.12). This may in part be caused by correlated noise in the GRACE data, and the duration of the time series is not enough to account for this, or it is being affected by a long period non-GIA signal (*e.g.* Fig. 5.38).

Table 5.12: Lake tilt results of Lake of the Woods relative to the gauge at Warroad ($mm.yr^{-1}$)

	Hector	MCMC	MC Method	GRACE
Clearwater Bay	-0.84±0.13	-0.73±0.04	-0.98±0.01	2.48±0.45
Cyclone Island	-0.39±0.15	-0.36±0.10	-0.60±0.03	1.25±0.27
Hanson Bay	-0.83±0.11	-0.69±0.05	-0.75±0.02	0.82±0.30
Keewatin	-1.03±0.32	-0.80±0.03	-0.928±0.004	2.79±0.51
Kenora	-0.45±0.51	-0.57±0.07	-0.61±0.03	2.85±0.52

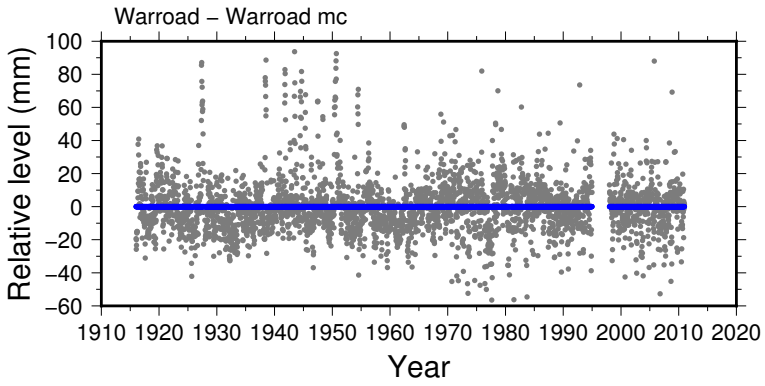

Figure 5.32: Residuals of the Warroad gauge in Lake of the Woods from the MC method. By definition, the rate is zero.

Table 5.13: Lake tilt results of Lake of the Woods from the comparison of all gauges calculated with Hector (mm.yr^{-1})

	Warroad	Clearwater Bay	Cyclone Island	Hanson Bay	Keewatin	Kenora
Warroad	-	0.84±0.13	0.39±0.15	0.83±0.11	1.03±0.32	0.45±0.51
Clearwater Bay	-0.84±0.13	-	-0.54±0.38	-0.26±0.19	-0.01±0.35	-
Cyclone Island	-0.39±0.15	0.54±0.38	-	-0.28±0.36	0.60±0.76	-
Hanson Bay	-0.83±0.11	0.26±0.19	0.28±0.36	-	0.42±0.65	-
Keewatin	-1.03±0.32	0.01±0.35	-0.60±0.76	-0.42±0.65	-	-0.34±0.18
Kenora	-0.45±0.51	-	-	-	0.34±0.18	-

Table 5.14: Lake tilt results of Lake of the Woods from the comparison of all gauges calculated with MCMC (mm.yr^{-1})

	Warroad	Clearwater Bay	Cyclone Island	Hanson Bay	Keewatin	Kenora
Warroad	-	0.73±0.04	0.36±0.10	0.69±0.05	0.80±0.03	0.57±0.07
Clearwater Bay	-0.73±0.04	-	-0.45±0.05	-0.18±0.04	-0.04±0.05	-
Cyclone Island	-0.36±0.10	0.45±0.05	-	-0.05±0.06	0.58±0.15	-
Hanson Bay	-0.69±0.05	0.18±0.04	0.05±0.06	-	0.17±0.06	-
Keewatin	-0.80±0.03	0.04±0.05	-0.58±0.15	-0.17±0.06	-	-0.25±0.02
Kenora	-0.57±0.07	-	-	-	0.25±0.02	-

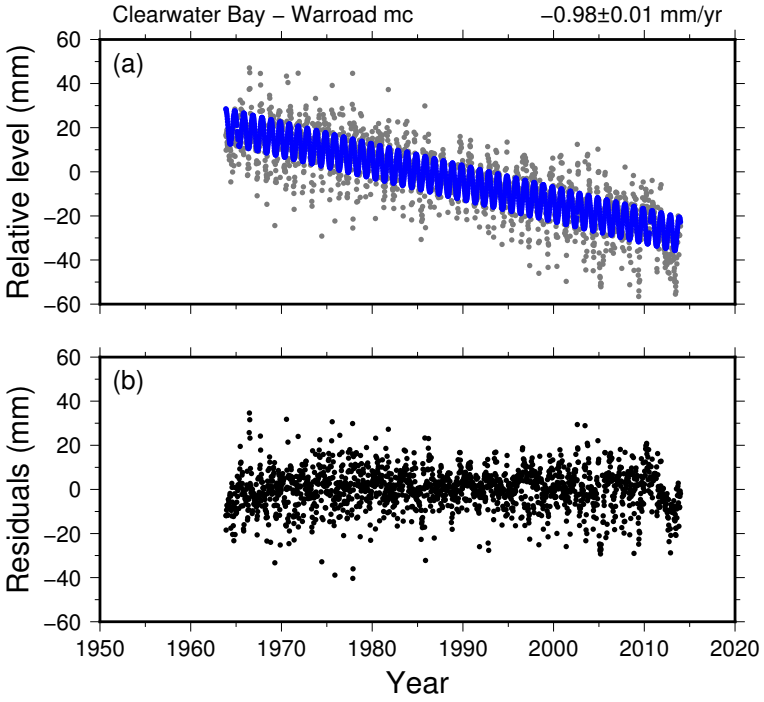

Figure 5.33: Difference between the Clearwater Bay and Warroad gauges in Lake of the Woods from the MC method, along with the linear plus annual model (blue). (b) residuals.

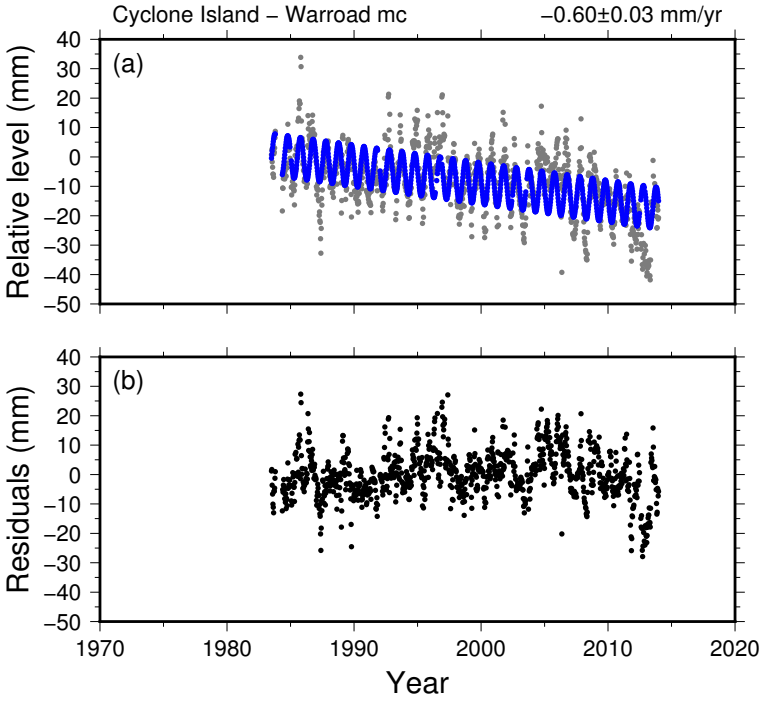

Figure 5.34: Difference between the Cyclone Island and Warroad gauges in Lake of the Woods from the MC method, along with the linear plus annual model (blue). (b) residuals.

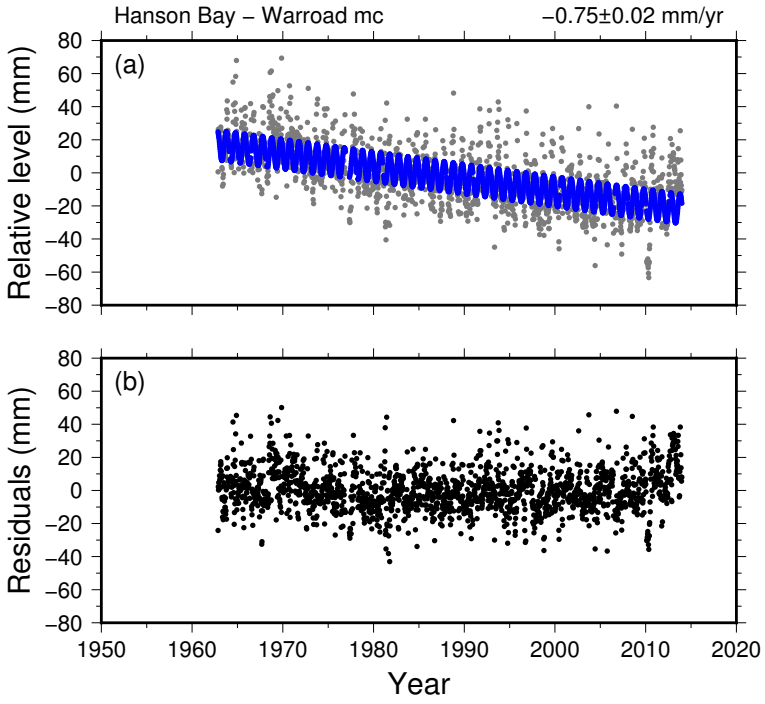

Figure 5.35: Difference between the Hanson Bay and Warroad gauges in Lake of the Woods from the MC method, along with the linear plus annual model (blue). (b) residuals.

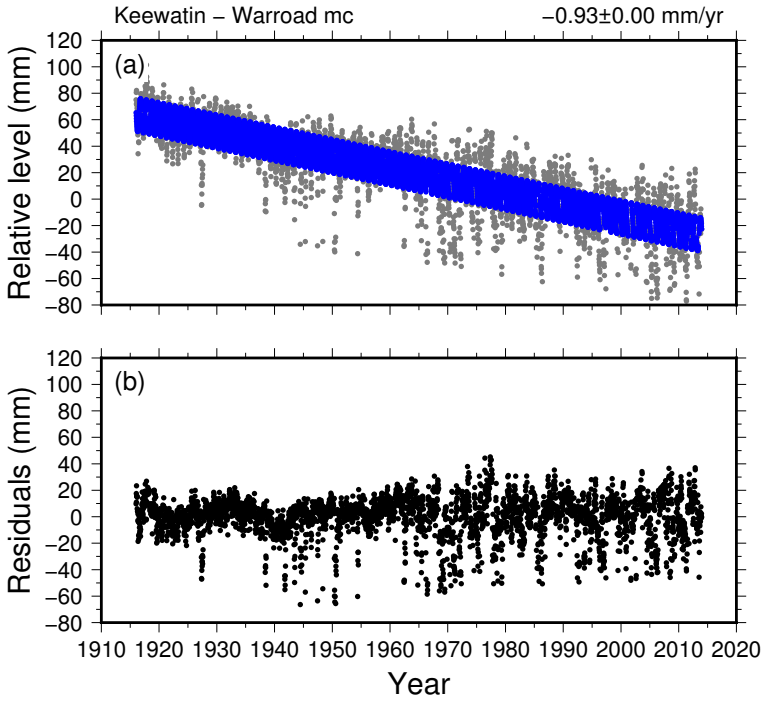

Figure 5.36: Difference between the Keewatin and Warroad gauges in Lake of the Woods from the MC method, along with the linear plus annual model (blue). (b) residuals.

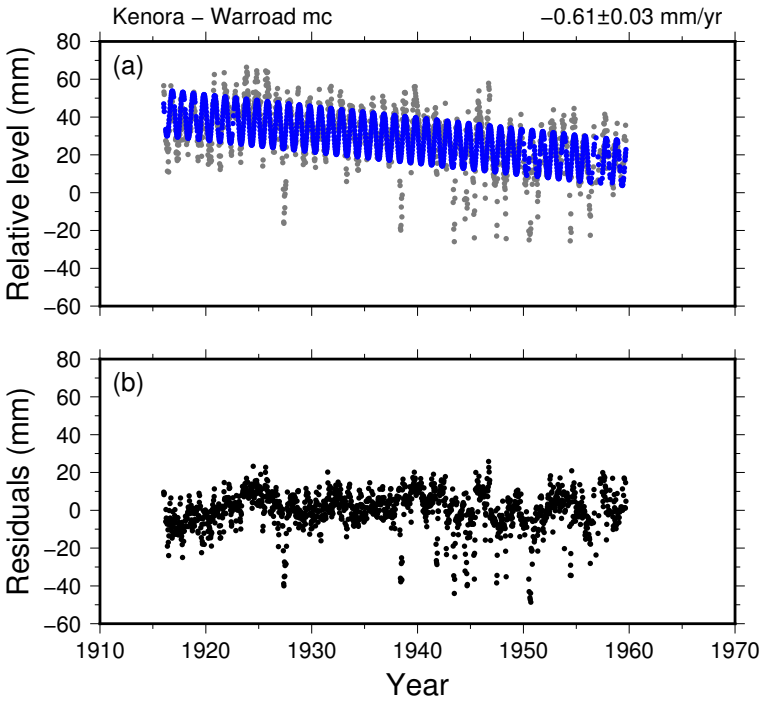

Figure 5.37: Difference between the Kenora and Warroad gauges in Lake of the Woods from the MC method, along with the linear plus annual model (blue). (b) residuals.

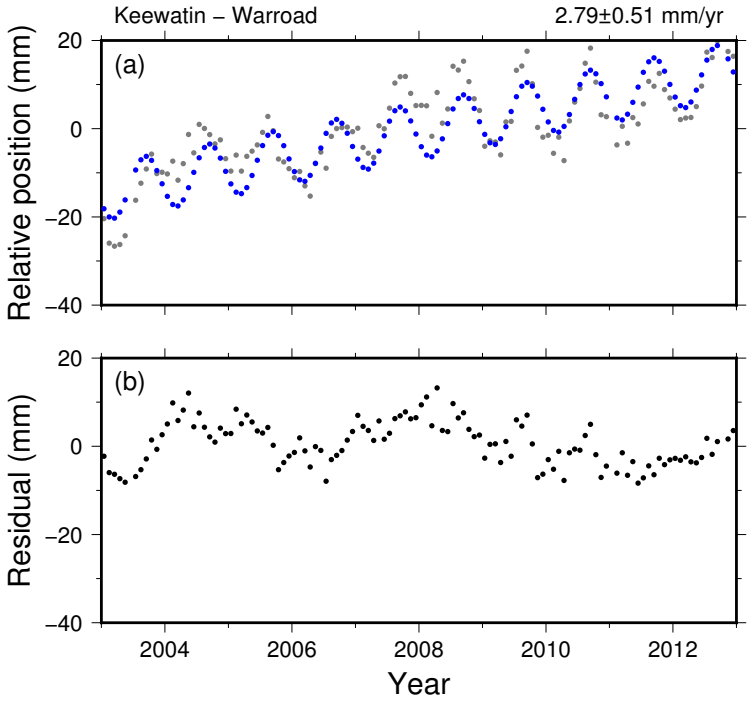

Figure 5.38: Difference between GRACE data between the Keewatin and Warroad gauges in Lake of the Woods using a linear plus annual model (blue). (b) residuals.

5.6.8 Lake Winnipeg

The results of the analysis of the gauges in Lake Winnipeg are shown on Tables 5.16–5.17. The gauge at Anama Bay has very large uncertainty and opposite trend to nearby gauges, likely due to its short recording period and possibly because it was not referenced to the same datum as the other gauges. The gauge at Gimli is also problematic. When compared to the other gauges, it appears that this gauge was not measured with respect to the same reference level throughout the recording time. This is most evident when comparing with the nearby gauge at Victoria Beach (Fig. 5.39). The cause of this discrepancy is unknown, as there are no documented problems or adjustments at this gauge prior to 1990 (A. Fojt, *pers. comms.* 2014). Excluding these gauges from the MC method analysis has little impact on the modelled rates at other gauges, though (Table 5.16). The results of the MC analysis relative to Victoria Beach, excluding Gimli and Anama Bay, are shown on Figs. 5.40 to 5.46. The results are consistent with a increasing uplift towards the north. The calculated offsets using the MC method are 51±6 mm for Pine Dock at April 15, 2001 and 24±3 mm for Matheson Island Landing on January 1, 2001. The GRACE rates are larger in magnitude than what is calculated using the lake gauges. The differenced viscoelastic deformation appears to be affected by signals unrelated to GIA (*e.g.* Fig. 5.47).

Table 5.15: Lake tilt results of Lake Winnipeg relative to the gauge at Victoria Beach ($mm.yr^{-1}$)

	Hector	MCMC	MC Method	MC Method	GRACE
Anama Bay	4.04±6.28	6.46±2.30	1.00±2.94	–	2.08±0.75
Berens River	-1.57±0.20	-1.33±0.09	-1.48±0.23	-1.47±0.23	3.20±0.75
George Island	-0.76±0.26	-0.65±0.25	-1.08±0.68	-1.02±0.69	3.37±0.97
Gimli	-0.08±0.34	-0.20±0.05	-0.15±0.40	–	-0.40±0.11
Matheson Island Landing	-1.78±0.37	-0.12±0.01	-1.62±0.37	-1.64±0.49	2.25±0.49
Mission Point	-1.70±0.25	-1.39±0.19	-1.68±0.42	-1.66±0.30	3.24±1.21
Montreal Point	-2.79±0.27	-3.42±0.33	-2.52±0.41	-2.50±0.53	3.63±1.25
Pine Dock	-1.17±0.29	-0.11±0.01	-1.30±0.61	-1.36±0.38	2.15±0.45

Table 5.16: Lake tilt results of Lake Winnipeg relative to the gauge at Victoria Beach calculated with Hector ($mm.yr^{-1}$)

	Victoria Beach	Berens River	Gimli	George Island	Matheson Island Landing	Mission Point	Montreal Point	Pine Dock	Anama Bay
Victoria Beach	-	1.57±0.20	0.76±0.26	0.08±0.34	1.78±0.37	1.70±0.25	2.79±0.27	1.17±0.29	-4.04±6.28
Berens River	-1.57±0.20	-	-0.45±0.49	-1.36±0.27	0.34±0.64	0.00±0.28	0.96±0.48	-0.32±0.34	-1.69±5.04
Gimli	-0.76±0.26	0.45±0.49	-	-1.74±0.35	2.24±0.74	0.18±0.72	1.34±1.24	-0.42±0.61	-
George Island	-0.08±0.34	1.36±0.27	1.74±0.35	-	2.21±0.49	1.49±0.36	2.32±0.41	1.18±0.23	3.83±6.00
Matheson Island Landing	-1.78±0.37	-0.34±0.64	-2.24±0.74	-2.21±0.49	-	-0.76±0.97	0.55±0.55	-0.96±0.43	-2.61±4.95
Mission Point	-1.70±0.25	0.00±0.28	-0.18±0.72	-1.49±0.36	0.76±0.97	-	1.36±1.04	-0.33±0.34	0.61±4.24
Montreal Point	-2.79±0.27	-0.96±0.48	-1.34±1.24	-2.32±0.41	-0.55±0.55	-1.36±1.04	-	-1.11±0.45	-2.97±8.41
Pine Dock	-1.17±0.29	0.32±0.34	0.42±0.61	-1.18±0.23	0.96±0.43	0.33±0.34	1.11±0.45	-	-0.84±4.40
Anama Bay	4.04±6.28	1.69±5.04	-	-3.83±6.00	2.61±4.95	-0.61±4.24	2.97±8.41	0.84±4.40	-

Table 5.17: Lake tilt results of Lake Winnipeg relative to the gauge at Victoria Beach calculated with MCMC ($mm.yr^{-1}$)

	Victoria Beach	Berens River	Gimli	George Island	Matheson Island Landing	Mission Point	Montreal Point	Pine Dock	Anama Bay
Victoria Beach	-	1.33±0.09	0.20±0.05	0.65±0.25	0.12±0.01	1.39±0.19	3.42±0.33	0.11±0.01	-6.46±2.30
Berens River	-1.33±0.09	-	-1.20±0.10	-0.43±0.10	0.00±0.01	-0.20±0.12	1.23±0.22	-0.01±0.01	-4.27±2.56
Gimli	-0.20±0.05	1.20±0.10	-	1.35±0.23	0.13±0.02	1.32±0.16	2.96±0.35	0.09±0.01	-
George Island	-0.65±0.25	0.43±0.10	-1.35±0.23	-	0.19±0.03	0.30±0.19	1.51±0.32	-0.05±0.03	-
Matheson Island Landing	-0.12±0.01	0.00±0.01	-0.13±0.02	-0.19±0.03	-	-0.05±0.02	0.03±0.04	-0.02±0.01	-0.31±0.18
Mission Point	-1.39±0.19	0.20±0.12	-1.32±0.16	-0.30±0.19	0.05±0.02	-	1.57±0.22	0.02±0.02	-
Montreal Point	-3.42±0.33	-1.23±0.22	-2.96±0.35	-1.51±0.32	-0.03±0.04	-1.57±0.22	-	-0.12±0.03	-
Pine Dock	-0.11±0.01	0.01±0.01	-0.09±0.01	0.05±0.03	0.02±0.01	-0.02±0.02	0.12±0.03	-	-
Anama Bay	6.46±2.30	4.27±2.56	-	-	0.31±0.18	-	-		-

5.6.9 Lake Winnipegosis

The results of the analysis of the two gauges in Lake Winnipegosis are shown in Table 5.18. The time series from the MC analysis are in Figs. 5.48 and 5.49. The calculated rate is the largest of any of the lakes investigated in this study. There is a large difference between the rates calculated using direct differencing with Hector and the MC method. This is in part due to Hector pre-processing removing the data collected when measurements resumed in Dawson Bay in 2011. The MCMC rate is the same at the two-sigma level. There is a possibility that the Dawson Bay gauge is not at the same level as the pre-1994 data, but a longer recording time is likely necessary to confirm this.

Table 5.18: Lake tilt results of Lake Winnipegosis relative to the gauge at Winnipegosis ($mm.yr^{-1}$)

	Hector	MCMC	MC Method	GRACE
Dawson Bay	-5.03±0.44	-4.11±0.29	-3.77±0.67	2.14±0.70

5.6.10 Southern Indian Lake

The results of the analysis of the gauges in Southern Indian Lake are in Table 5.19 and plotted in Figs. 5.50-5.53. The gauges at South Bay and South Indian Lake are suspected to be periodically affected by conditions that are different from the rest of the lake. The part of this lake in which these two gauges are located is connected to the rest of the lake by a narrow (about 200 m) strait. The relatively large calculated annual signal (*e.g.* Fig. 5.51) supports this hypothesis. However, the calculated rate with the MC method at Missi Falls is the same at the one-sigma level regardless of whether they other two gauges are included or not. The GRACE rates between Opachuanau Lake and the other gauges is close to zero, with no evidence of strong correlated noise (*e.g.* Fig. 5.54).

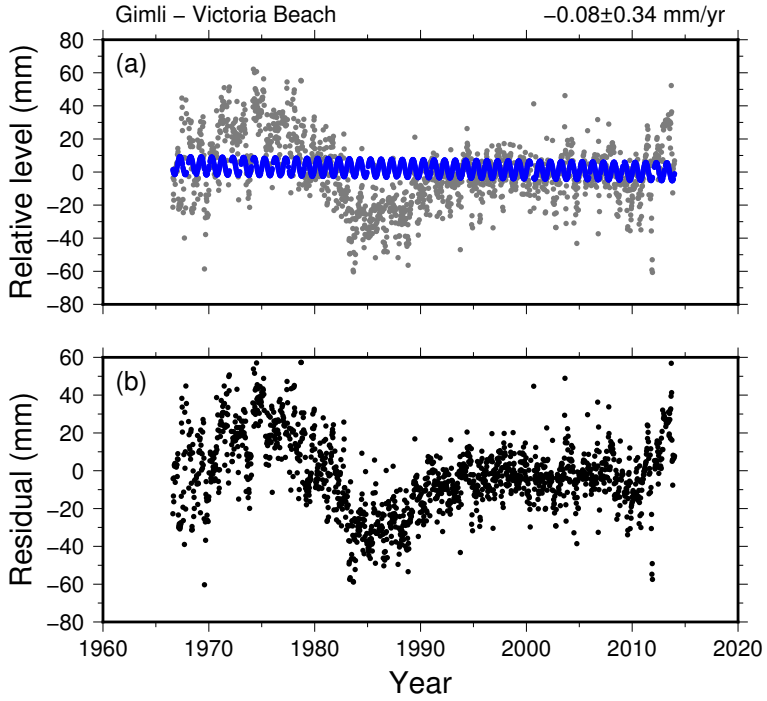

Figure 5.39: Difference between the Gimli and Victoria Beach gauges in Lake Winnipeg, along with the linear plus annual model using Hector (blue). (b) residuals.

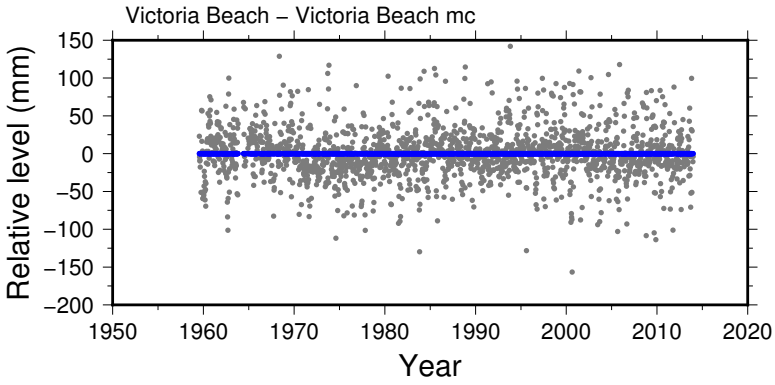

Figure 5.40: Residuals of the Victoria Beach gauge in Lake Winnipeg from the MC method. By definition, the rate is zero.

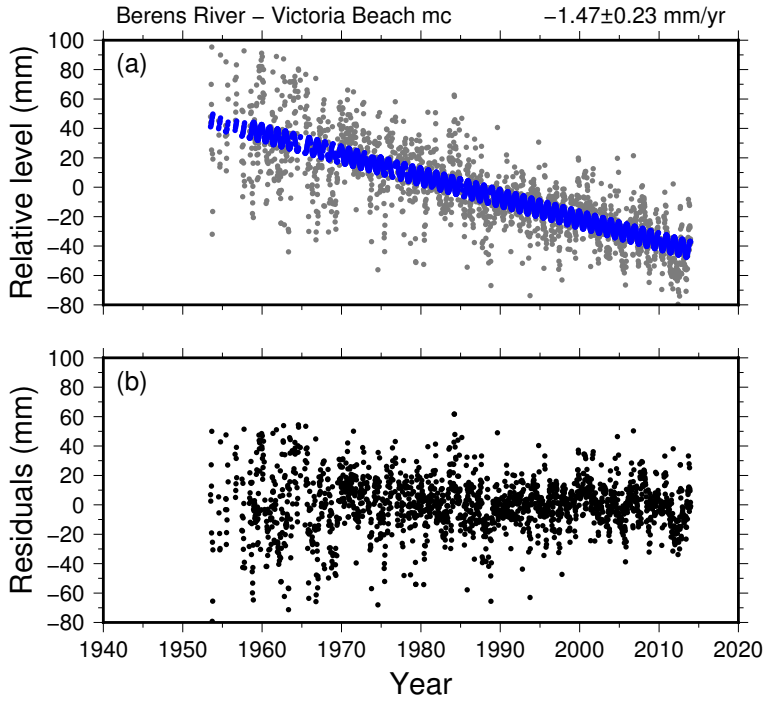

Figure 5.41: Difference between the Berens River and Victoria Beach gauges in Lake Winnipeg from the MC method, along with the linear plus annual model (blue). (b) residuals.

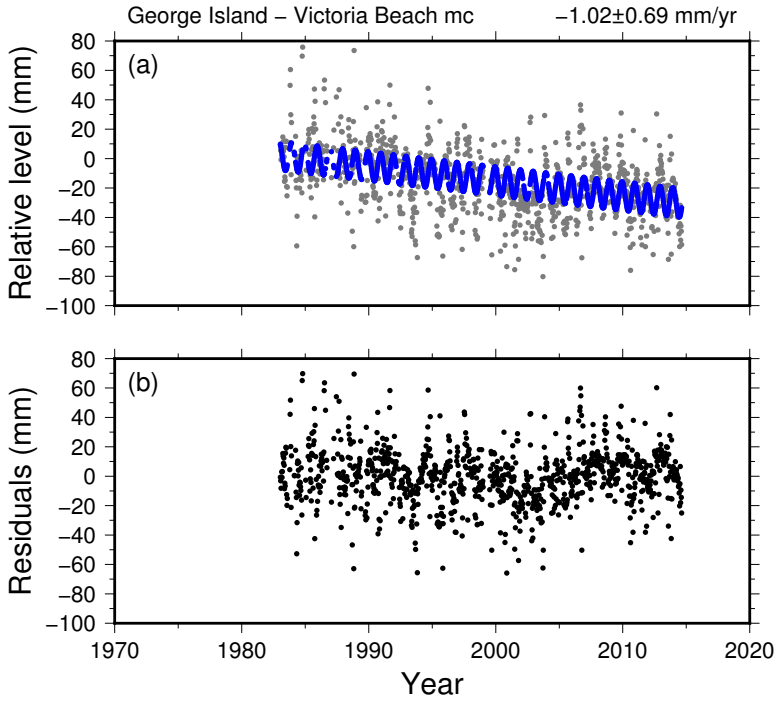

Figure 5.42: Difference between the George Island and Victoria Beach gauges in Lake Winnipeg from the MC method, along with the linear plus annual model (blue). (b) residuals.

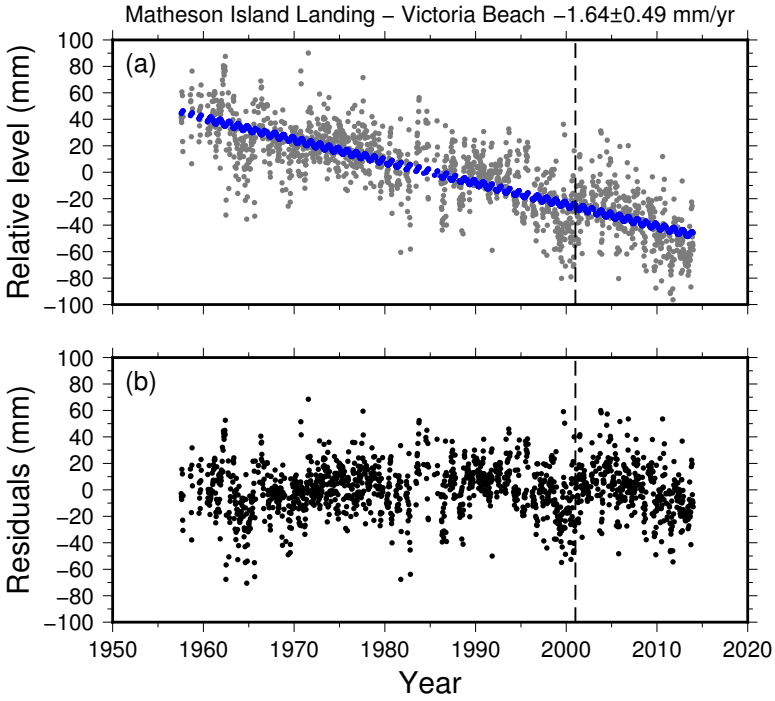

Figure 5.43: Difference between the Matheson Island Landing and Victoria Beach gauges in Lake Winnipeg from the MC method, along with the linear plus annual model (blue). The dashed vertical line represents when an offset was calculated. (b) residuals.

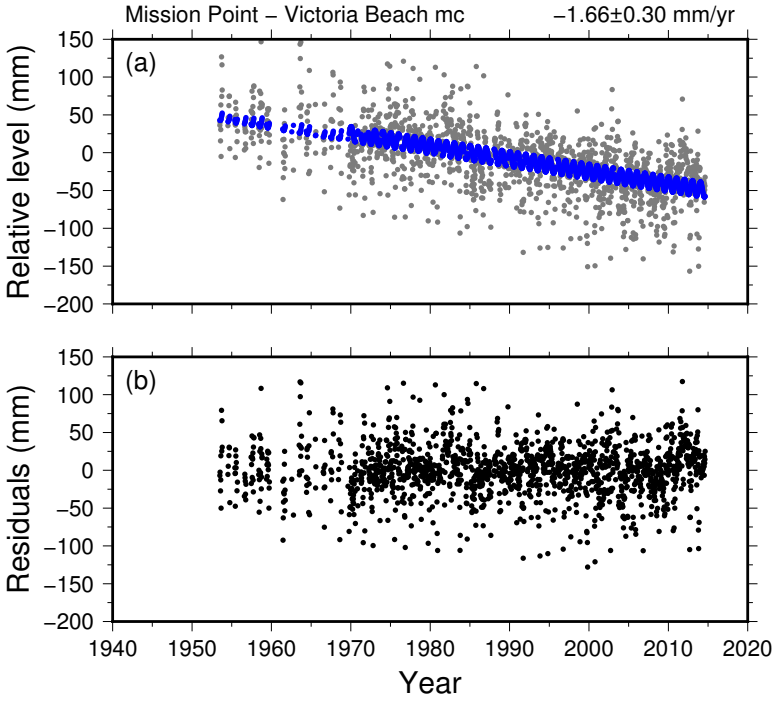

Figure 5.44: Difference between the Mission Point and Victoria Beach gauges in Lake Winnipeg from the MC method, along with the linear plus annual model (blue). (b) residuals.

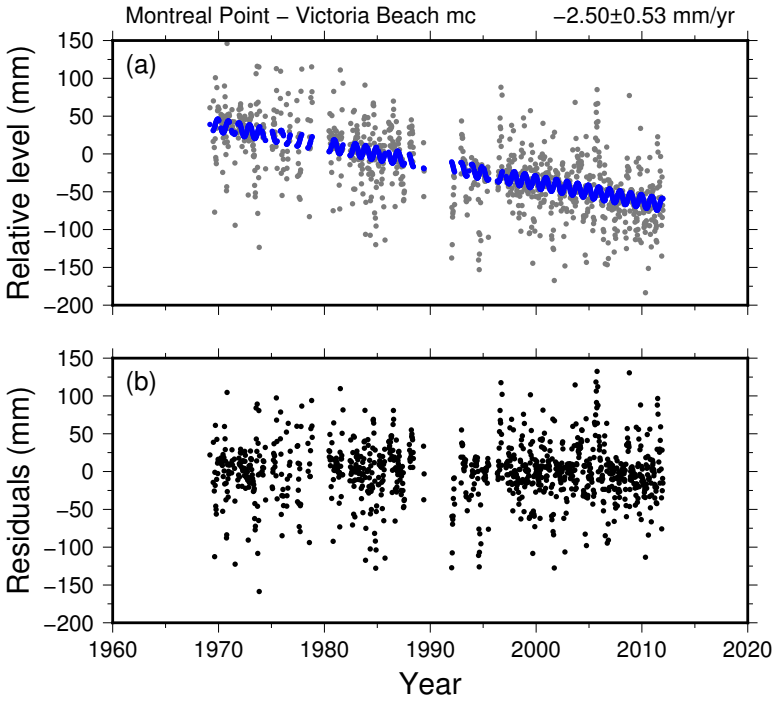

Figure 5.45: Difference between the Montreal Point and Victoria Beach gauges in Lake Winnipeg from the MC method, along with the linear plus annual model (blue). (b) residuals.

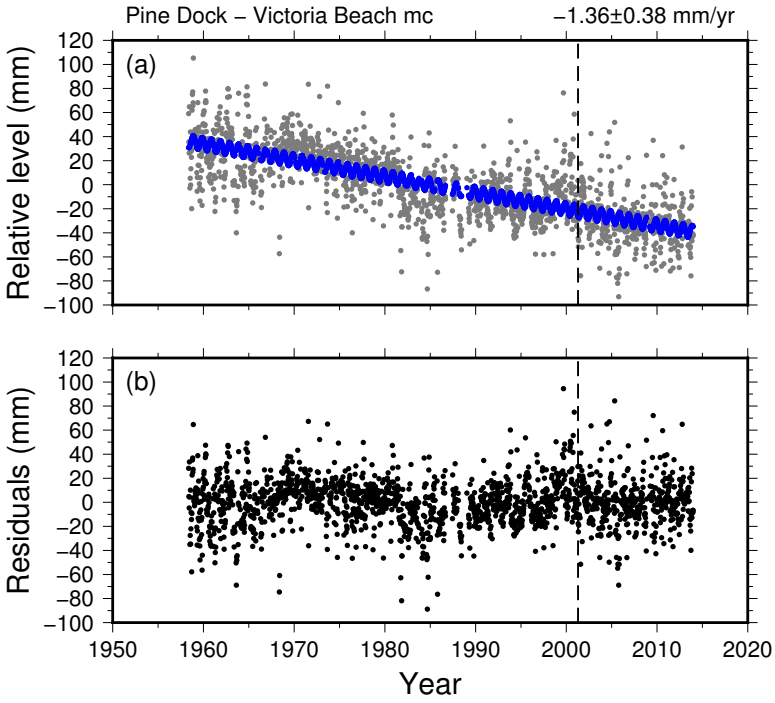

Figure 5.46: Difference between the Pine Dock and Victoria Beach gauges in Lake Winnipeg from the MC method, along with the linear plus annual model (blue). The dashed vertical line represents when an offset was calculated. (b) residuals.

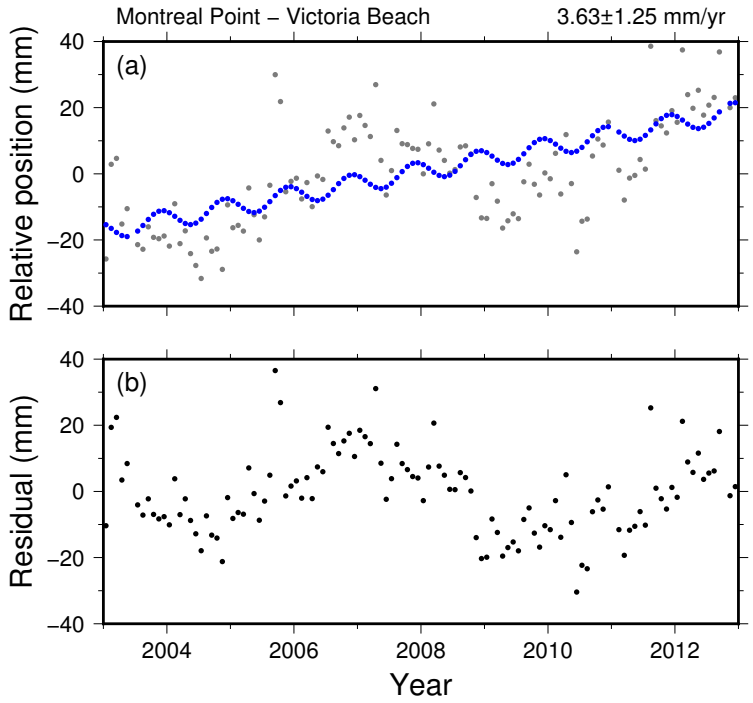

Figure 5.47: Difference between GRACE data between the Montreal Point and Victoria Beach gauges in Lake Winnipeg using a linear plus annual model (blue). (b) residuals.

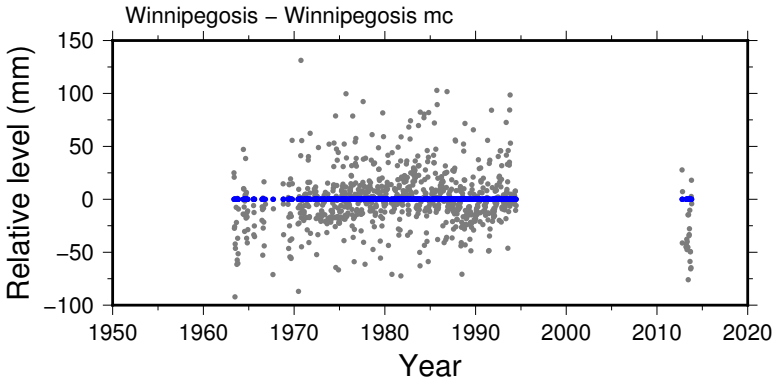

Figure 5.48: Residuals of the Winnipegosis gauge in Lake Winnipegosis from the MC method. By definition, the rate is zero.

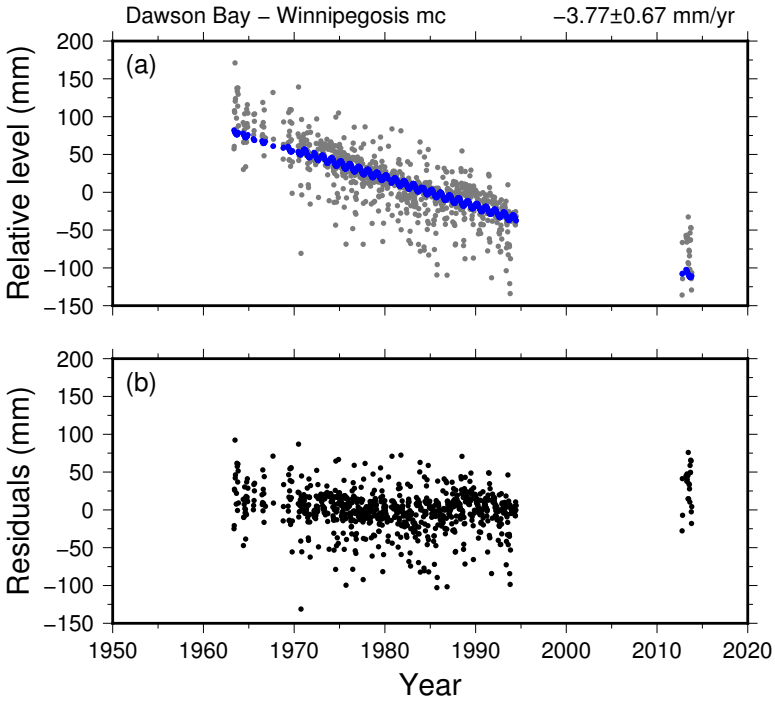

Figure 5.49: Difference between the Dawson Bay and Winnipegosis gauges in Lake Winnipegosis from the MC method, along with the linear plus annual model (blue). (b) residuals.

Table 5.19: Lake tilt results of Southern Indian Lake relative to the gauge at Opachuanau Lake (mm.yr^{-1})

	Hector	MCMC	MC Method	MC Method	GRACE
Missi Falls	-1.43±0.61	-1.35±0.10	-1.44±0.16	-1.53±0.25	0.77±0.37
South Bay	-0.81±0.67	-0.76±0.12	-0.84±0.08	–	0.09±0.10
South Indian Lake	-0.64±0.66	-0.66±0.12	-0.73±0.13	–	0.12±0.12

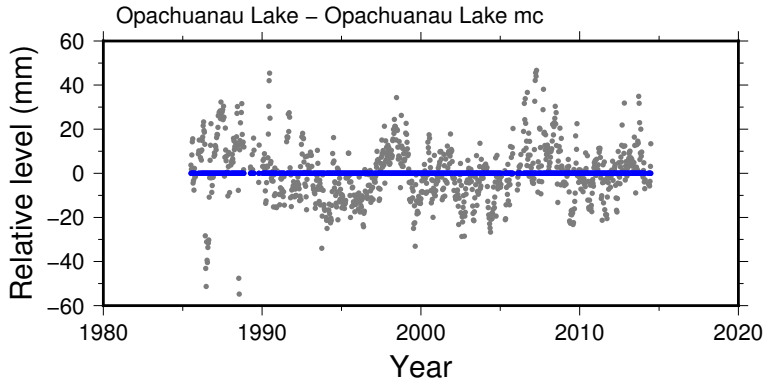

Figure 5.50: Residuals of the Opachuanau Lake gauge in Southern Indian Lake from the MC method. By definition, the rate is zero.

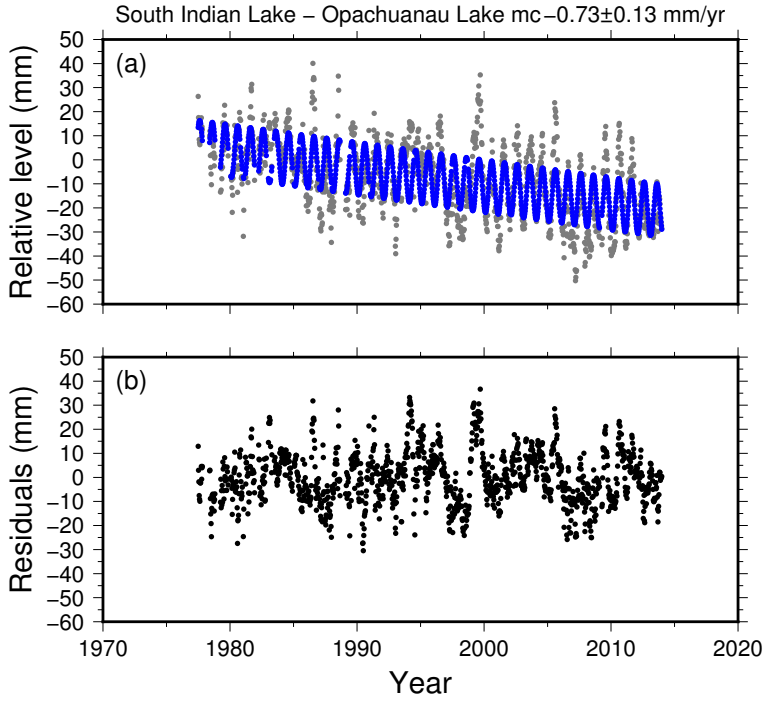

Figure 5.51: Direct difference between the South Indian Lake and Opachuanau Lake gauges in Southern Indian Lake, along with the linear plus annual model (blue). (b) residuals.

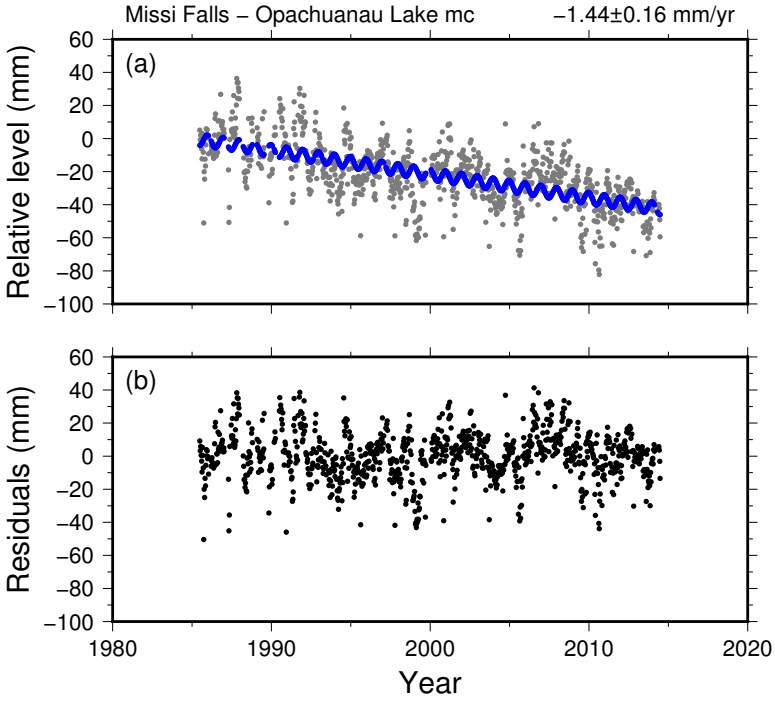

Figure 5.52: Difference between the Missi Falls and Opachuanau Lake gauges in Southern Indian Lake from the MC method, along with the linear plus annual model (blue). (b) residuals.

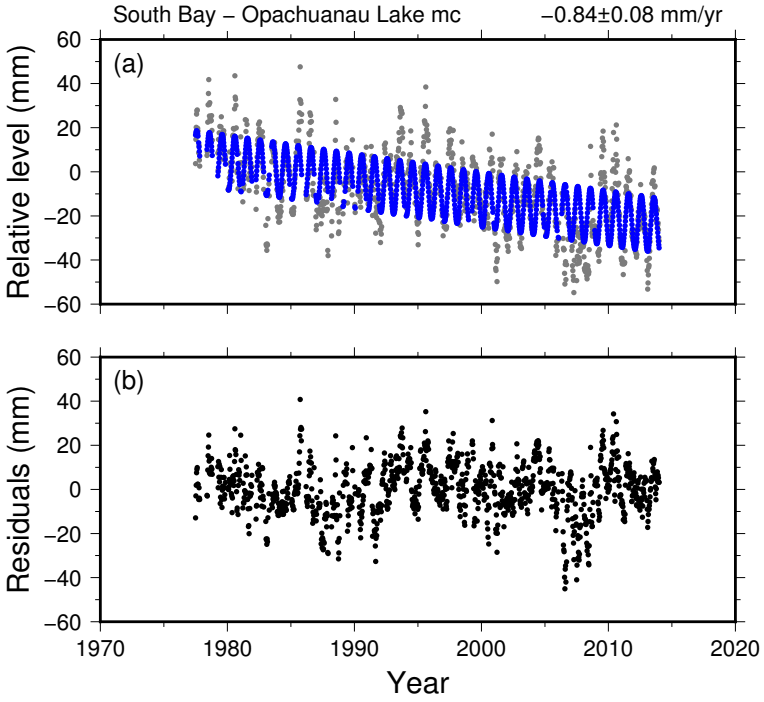

Figure 5.53: Difference between the South Bay and Opachuanau Lake gauges in Southern Indian Lake from the MC method, along with the linear plus annual model (blue). (b) residuals.

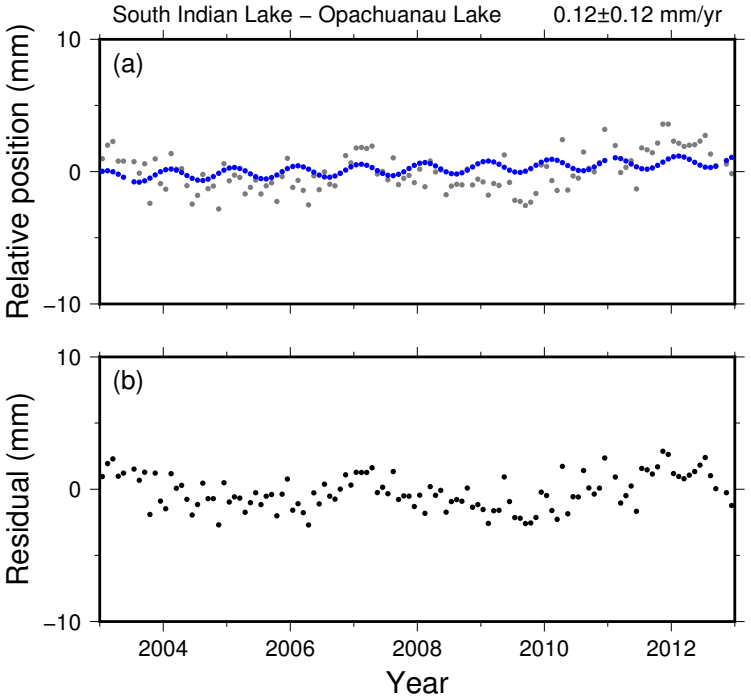

Figure 5.54: Difference between GRACE data between the South Indian Lake and Opachuanau Lake gauges in Southern Indian Lake using a linear plus annual model (blue). (b) residuals.

5.7 Discussion

5.7.1 GIA determined from lake gauges

The preceding analysis shows that the MC method was able to detect significant relative uplift rates between gauges in lakes located in western Canada. This method also was relatively insensitive to problematic gauges that had correlated noise that was unrelated to GIA. The uncertainty estimates for the tilt rates were lower than with the directly differenced methods (Hector and MCMC), which is at least partially due to the inability of weighted least squares to take into account coloured noise. Coloured noise is unlikely to introduce a large bias in the calculated rates for some of the datasets, which can exceed 50 years in duration. It may be more of a problem when the datasets are shorter, which is almost certainly the case for Great Slave Lake (which has three gauges with time series that are less than 25 years, and are not continuously recording throughout the year). Some of the reduced uncertainty is likely due to the joint analysis of all of the gauges, as it would reduce the effects of noise at the reference gauge. Of the two direct differenced methods, Hector had higher uncertainties, but the tilt rates often matched the rates calculated from the MC method at the two-sigma level.

The rates from the MC analysis are compared with the rates reported by Tackman et al. (1999) in Table 5.20 for Lake Winnipeg, Lake Manitoba and Lake of the Woods. The Tackman *et al.* study used the difference of lake level in the winter. The addition of more than 15 years of additional data, plus the use of the MC method should give higher confidence in the rates from this study. Several of the gauges have calculated rates that are different at the two-sigma level. The difference in the results in Lake of the Woods can be attributed in part to the different offset that Tackman et al. (1999) used for the Warroad gauge in the late 1970s (28 mm versus 16 mm used in this study). Tackman et al. (1999) avoided using data from the

summer due to increased noise levels, but including modelled annual signal reduces much of this noise and allows the summer data to contribute effectively to the rate estimate.

The MC method provides a robust way to measure relative uplift rates in a network of gauges within a single lake. Previous studies (*i.e.* Tackman et al., 1999) suggested that time series of at least 25 years, and preferably 40 years are needed to have confidence in the rates from gauge pair analysis. This does not seem to be a strict requirement, as a significant rate was detected at the gauge at Cedar Lake with just 17 years of data. Provided there are measurements throughout the year to estimate a seasonal signal, and the residuals are relatively small, it should be possible to accurately determine a tilt rate using the MC method with less than 25 years of data.

Table 5.20: Comparison of rates determined by the MC method and Tackman et al. (1999) (mm.yr^{-1})

Gauge	MC Method	Tackman *et al.*
Lake Winnipeg relative to Victoria Beach		
Berens River	-1.47±0.23	-2.232±0.250
Mission Point	-1.66±0.30	-1.753±0.319
Montreal Point	-2.50±0.53	-1.873±0.769
Lake Manitoba relative to Steep Rock		
The Narrows	-0.01±0.16	0.094±0.197
Toutes Aides	0.67±0.17	0.510±0.150
Westbourne	0.45±0.08	1.003±0.135
Lake of the Woods relative to Warroad		
Hanson Bay	-0.75±0.02	-0.440±0.133
Clearwater Bay	-0.98±0.01	-0.296±0.103
Keewatin	-0.928±0.004	-1.077±0.083

5.7.2 Suitability of using GRACE for GIA measurements

It was hypothesised that GRACE may be suitable for measuring the spatial gradient of GIA, assuming that the hydrological component of the signal was similar over small spatial area covered by these lakes. However, comparison of the relative uplift

rates measured by GRACE and the rates derived from the lakes with high quality data (*i.e.* Lake Winnipeg and Lake of the Woods) indicates that this is not a sound assumption. The rates determined using GRACE are up to twice as large as those calculated from lake gauges. The gradient values may be biased because the GRACE satellites measures over a large area (3.6°, roughly 400 km). If the gradient of GIA changes over the footprint of GRACE in the vicinity of the lakes, the calculated tilt will be incorrect. If there is a large hydrological signal near a gauge, the spherical harmonic decomposition of the GRACE data will include spectral leakage of this signal (Werth et al., 2009). Additional measurement time is required before GRACE can confidently be used to measure the gradient of GIA in areas with substantial differential hydrological signals, but little can be done if the gradient changes in the vicinity of the lake.

5.7.3 Sources of noise

In general, the noise due to short lived events (such as seiching and storm) does not affect the determination of the lake tilt rate. Many of these sites have time series that are in excess of several decades, and a relative uplift can clearly be seen in the time series after removal of lake-wide level and site offsets. Some gauges are affected by strong annual signals, likely the result of seasonality in noise sources, such as increased wind effects when the lake is not frozen, and increased runoff in the spring. Some of these gauges are located near or in the mouths or outlets of rivers, and changes in currents would undoubtedly also contribute to the seasonality of the noise. If the gauge is located at the mouth of a river, sediment deposition may cause localised subsidence, which would bias the overall rate. If the gauge itself was damaged, or if was located on an unstable surface, it may cause correlated noise that is on time scales longer than one year. This probably explains the non-linear effects in the gauge at Gimli (Fig. 5.39). Without notes on problems at specific

gauges, these effects are not possible to quantify.

5.8 Summary

In total, ten lakes in western Canada with at least two gauges are considered in this study. The data are of variable quality, but there is evidence of tilt due to GIA in most of them. Lake Winnipeg, Lake Manitoba and Lake of the Woods have the longest period of continuous lake level measurements and have a network of multiple gauges. These three lakes show that the GIA rate increases towards the northeast in southeastern Manitoba and northwestern Ontario. The rates from Cedar Lake and Lake Winnipegosis indicate that the GIA gradient changes direction further west in Manitoba, but this is based on shorter time series. The gauges in Southern Indian Lake indicate that the uplift rate increases towards the northeast in northwestern Manitoba. In Lake Athabasca, the rate of uplift increases towards the west. The gauges in Great Slave Lake have a patchy measurement record, but is consistent with increasing uplift rates towards the east. These values will be used to constrain the ice sheet model in Chapter 8.

Chapter 6

Determination of glacio-isostatic adjustment in the western Laurentide Ice Sheet from paleo-lake level and sea level change

6.1 Relative sea level indicators

6.1.1 Introduction

In areas that were covered by large continental ice sheets, relative sea level was tens to hundreds of metres higher than present after the ice retreated, due to delayed postglacial rebound (Farrell and Clark, 1976). High post-glacial relative sea level in the study area was first observed by Tyrrell (1894). Andrews (1970) presented the first attempt to characterise the pattern of post-glacial relative sea level change in Canada. The chronology of relative sea level change is primarily based on radiocarbon dates that give an indication of whether relative sea level was above or below the sample's elevation. Tushingham (1992) presented the most recently published

compilation of relative sea level data. Since this compilation, there have been many new data, primarily based on archaeological surveys by A.S. Dyke and J.M. Savelle.

Most relative sea level indicators used in this study come from an unpublished compilation from A.S. Dyke and T.S. James (*pers. comms.*, 2011). Before using these data, it is necessary to check for reliability of the dataset. One of the criteria for accepting radiocarbon dates are that the material dated is known. Shells from deposit feeding organisms such as Portlandia *sp.* are not used in this study, as they have been shown to have anomalously old ages, and there is no systematic way of determining an appropriate reservoir correction (England et al., 2013). Samples listed as being "marine shells" are not accepted because early conventional radiocarbon dates usually required a mixture of 10 to 100 individual shells, and there is the possibility that they could be contaminated with deposit feeding organisms (Morlan et al., 2000; McNeely and Brennan, 2005). Bulk freshwater sediment and plants are rejected, as they have been shown to have anomalously old ages due to hardwater effects (MacDonald, 1987; Grimm et al., 2009). Bulk peat samples are rejected, because they can have anomalously young ages due to the growth of young roots into older peat, and due to the circulation of acids within the peat (*i.e.* Nilsson et al., 2001; Brock et al., 2011). In addition, peat composed of freshwater species could be affected by hardwater effects, and may have anomalously old ages (MacDonald, 1987). In most peat samples in the compilation, the type of peat dated is not reported. Finally, the marine reservoir effect on marine mammals is uncertain for most species (Furze et al., in press). Only Balaena mysticetus (bowhead whale) has a well-determined reservoir age. Samples located in the study area and in peripheral regions within approximately 300 km are used to constrain ice sheet thickness.

There are 901 radiocarbon dates used to constrain the relative sea level history of the study area. Relative sea level indicators on areas peripheral to the study

area are included, as the regional ice volume can be inferred from these data. The location of relative sea level data is broken up into several regional groups, including southern Banks Island, Mackenzie Delta, Mackenzie District (mainland northern Nunavut, south of Victoria Island), southern Victoria Island, King William Island, Boothia Peninsula, Melville Peninsula, Southampton Island, northwestern Hudson Bay and southwestern Hudson Bay. The distribution of data is not even. For example, southern Victoria Island has 325 samples, while northern Hudson Bay has 31 samples over a much larger area.

6.1.2 Corrections and assessment of uncertainty

Marine organisms require a correction to account for the difference in radiocarbon concentration between the atmosphere and ocean (*e.g* McNeely et al., 2006; Coulthard et al., 2010). The magnitude of the correction depends on the local oceanographic conditions. Coulthard et al. (2010) divided the Arctic into areas that have similar oceanographic conditions, and determined the modern reservoir age from pre-bomb (*i.e.* pre-1950) shells of known age for all of those regions. This serves as the basis for correcting the majority of marine organisms in this study. Vickers et al. (2010) determined a late glacial reservoir age for the Hudson Strait, which was 100-300 years older than the modern age. This indicates that the reservoir age in the Arctic may change through time. Ross et al. (2012) found that the late glacial reservoir correction on Southampton Island, located in northern Hudson Bay, was not substantially different from the modern value. They attributed the difference between the reservoir age of Southampton Island and Hudson Strait to be due to local geological conditions. For late glacial samples on Southampton Island, their reservoir correction of 263±48 years is used to correct marine shells. Gowan (2013) found that the late glacial reservoir offset in southwestern Hudson Bay may have been older than the modern reservoir age. In that study, a minimum reservoir

offset was determined by using the coincidence of the 8.2 ka event and the initial inundation of marine water into this area (Lajeunesse and St-Onge, 2008). Complicating the calculated reservoir offset in Hudson Bay is the fact that it is based on only six samples for the entire basin. In the absence of further studies on the age of the reservoir in Hudson Bay, the modern value is used, except for samples older than 7000 ^{14}C yr BP, which have a reservoir correction of 470±100 years applied (Gowan, 2013).

Most elevation measurements do not have reported error ranges, and often do not even state the method used in determining the elevation. For most studies, a barometric altimeter was most likely to have been used to determine elevation. Leaman (1984) described the procedures necessary to acquire precise elevation readings using an altimeter. Errors in elevation determination are introduced by changes in air pressure, temperature, wind speed, and humidity. Local topography also can affect local air pressure in non-linear ways. Even using a base station, he found that errors were in excess of 10 m when there are topographic changes of more than 50 m, or if measurements were taken more than 1 km from the base. Errors in excess of 50 m are possible if no base station correction is applied and repeated calibration of the sensors were not made. Uncertainties are introduced on these measurements, described later in this section.

A number of radiocarbon dates used in this study come from archaeological sites (*e.g.* Dyke and Savelle, 2009; Dyke et al., 2011; Savelle and Dyke, 2009). There are several problems that could arise from samples derived from human settlements. The main problem is that radiocarbon dates on an archaeological site give the maximum age for human occupation at the site, rather than directly dating a relative sea level datum. For dates on wood, there could be problems if the people moved old wood from higher elevations (though Dyke and Savelle (2000a) note that driftwood in the Arctic quickly decays and fresh wood would have preferentially been used). This

could make a maximum limiting date on relative sea level at a particular elevation older than it should be. Similarly, humans could have moved whale bones to higher elevations, which cause an overestimation of where relative sea level may have been at the time (Dyke et al., 2011). Dates on animal bones are likely to be the most reliable, as they would have been killed contemporaneously with settlement (Friesen, 2004). It is generally assumed that the paleo-Eskimo and Thule people who lived in the Arctic built their settlements within a few metres of relative sea level, and most dates likely do correspond to when relative sea level was only slightly below the measured elevation. The majority of archaeological samples were collected using carefully calibrated elevation measurements and provide some of the most precise estimates of paleo-relative sea level change in the study area.

Radiocarbon dates require calibration to correct for the changes in the concentration of atmospheric radiocarbon over time. The data used here are calibrated using OxCal 4.2 (Bronk Ramsey, 2009), using the IntCal13 and Marine13 calibration curves (Reimer et al., 2013). Further details on the reporting of ages were described in Chapter 3.

The most recent studies on relative sea level change in the Arctic (*e.g.* Dyke and Savelle, 2009; Dyke et al., 2011) used altimeter measurements that were systematically checked against the high tide mark, and reported elevation errors less than 1 m. Ross et al. (2012) reported elevation errors between 2 and 13 m using a combination of in-field altimeter measurements and estimates from digital elevation models. Early samples collected by the Geological Survey of Canada were presumably measured in field using an altimeter (*e.g.* Craig, 1961), with no stated precision. Ross et al. (2012) noted a discrepancy between age and elevation of samples collected in the 1960s versus samples collected in their study on Southampton Island. They attributed this to problems with the radiocarbon age of the sample, but this could also be explained by errors in altimetric elevation readings. Dyke et al. (1991)

described the procedure of collecting elevation measurements in the surveys of the Arctic during the 1980s, which includes many samples used in this study. They used barometric altimeters, using a reference datum of the high tide mark. They regarded elevation readings to be accurate to within 2 m when less than 15 minutes elapsed between measurement between the sample site and reference site. For sites further inland, they regarded the accuracy to be within 10 m, and were compared to topographic maps with a contour interval of 30 m to check for quality. They repeated elevation measurements two to three times to ensure that they were reliable. They also determined some elevations using levelling surveys, which are precise to much less than a metre. If the procedures described by Dyke et al. (1991) were common practice for all Geological Survey of Canada samples, then the elevation measurements that are close to the coast are likely to be accurate to within 2 m, and samples further inland are likely accurate to within 10 m. For sites in the Mackenzie District, elevations were taken from a helicopter altimeter, and estimated to have an error of 6 m (Kerr, 1996). For many of the dates on the Melville Peninsula, Dredge (1995) calibrated the survey altimeter after each sample collection. The altimeter used in that survey had a precision of 2 m.

Walcott (1972) assigned error values of 1 m if the sample was within 1 km of sea level and measured by precise levelling, 2 m if it were further than this. For altimeter measurements, he used an error of 2-5 m if the measurement was close to the sea level benchmark, and 10 m if it was far from the benchmark or had poor survey control. Although the altimeters are potentially inaccurate, the elevations determined in Geological Survey of Canada studies were likely checked against topography maps, with contour intervals of 10-30 m (T.S. James, *pers. comms.*, 2014). Provided that there are minimal errors in these maps, the stated error is unlikely to be much higher than 5-10 m . For the purposes of this study, the criteria of Walcott (1972) is used to assign errors to elevation measurements with no

stated error. For sites that are within 1 km of the closest coastline, a error of 5 m is assigned if the survey method is uncalibrated altimetry or if there is no stated survey method. For sites that are further than this, an error of 10 m is assigned. The distance of the sample from the nearest coast is estimated using Google Earth. If the sample was collected at a coastal cliff or scarp, within 5 m of present sea level, an error of 1 m is assigned, as these elevations were likely measured directly. For surveys that use periodically calibrated altimetry (*e.g.* Dyke et al., 1991; Dredge, 1995), an error of 5 m is assigned. Surveys in the late 90s and early 2000s by Dyke and Savelle (*e.g.* Dyke and Savelle, 2001) used an altimeter with 0.5 m accuracy and were calibrated immediately after elevation measurement and they assume elevation errors will be less than 2 m. These samples are assigned an error of 1 m if they are within a few metres of sea level and 2 m if they are further away than this. Although precise levelling and altimetric measurements located close to the coast could have the potential of having sub-1 m uncertainties, it must be kept in mind that these regions have ongoing postglacial uplift. These samples have been collected over the course of over 60 years, in areas where the the postglacial uplift rate may exceed 1 cm per year. Since the contemporary relative sea level record is only known at three locations in the study area (Chapter 4), adding an uncertainty of 1 m is appropriate when it is uncertain what the relative sea level change rate is.

The majority of the samples from the database give only a minimum or maximum limit of relative sea level. In most samples where a bounded limit is stated, the minimum relative sea level is the elevation at which the sample is collected, and the maximum value is the local marine limit. Most of the maximum limit data come from archaeological sites, where relative sea level may have only been a few metres below the settlement. Minimum limit samples were mostly collected directly from marine sediments. The notes on some samples indicate that they come from redeposited sediments, but still serve as a minimum limit as long as they were not

redeposited by glacial action that could have pushed them to a higher elevation. Much of the Canadian Arctic is north of the treeline, so the dated wood arrived from elsewhere via currents (Dyke and Savelle, 2000a). There is an unknown time between tree growth and deposition. Dyke and Savelle (2000a) also caution that driftwood that is not embedded within sediments could possibly have been been moved by humans for use as firewood.

6.1.3 Southwestern Hudson Bay

There are 53 samples from the southwestern Hudson Bay region (Fig. 6.1). Most of these were summarised in the compilation of Manitoba radiocarbon dates by Morlan et al. (2000). The initial incursion of sea water in this region was after the collapse of the ice sheet in Hudson Bay, coinciding with the final drainage of Glacial Lake Agassiz (Dredge, 1983; Barber et al., 1999). The relative sea level history of this region was summarised by Dredge and Cowan (1989). After the initial incursion of marine water of the Tyrrell Sea, the coast was about 300 km from the modern shoreline, and reached elevations between 120 and 180 m higher than present. Their inferred curves for southwestern Hudson Bay showed gradual relative sea level fall from the highstand position, in contrast to areas further north that have a more rapid early drop in relative sea level. The current dataset is consistent with this interpretation, though there is a lack of data between 4000 and 6000 cal yr BP (Fig. 6.1).

6.1.4 Northwestern Hudson Bay

There are only 25 samples in northwestern Hudson Bay (Fig. 6.2). Due to the large spatial distribution of the samples, it is difficult to make interpretations on the general pattern of emergence in this region. There are also only two samples with ages between 5000 and 1000 cal yr BP. Dyke and Dredge (1989) characterised the

relative sea level change as being more gradual than areas to the north and south. Marine incursion went as far as 200 km inland from the modern coast in this region (Prest et al., 1968). Though there are few samples, relative sea level was likely over 80 m higher than present prior to 6000 cal yr BP, and was within 15 m of present level after 900 cal yr BP.

6.1.5 Southampton Island

There are 48 samples on Southampton Island (Fig. 6.3). The data show that between 7000 and 9000 cal yr BP, relative sea level was 120-190 m above present. Ross et al. (2012) give the most recent summary of relative sea level for this region. They argued that many of the archival dates (*i.e.* conventional samples dated in the 1960s and early 1970s) appeared to be 300-400 years older than their samples that were measured using accelerator mass spectrometry. If the archival dates are accepted, it would mean that relative sea level fell more rapidly during late glacial times than is suggested by their samples.

6.1.6 Melville Peninsula

There are 77 samples in the Melville Peninsula which, for the purposes of analysis, are separated into northern and southern regions (Fig. 6.4 and Fig. 6.5). The samples in the northern Melville Peninsula are located northeast of the defined study area, and are likely strongly affected by loading from the Foxe Ice Dome. These samples are used to characterise the approximate amount of ice in this region, though no attempt was made to revise the margin chronology by Dyke (2004). Dredge (1995) summarised the glacial and relative sea level history for the northern Melville Peninsula. She noted there was a much higher marine limit on the western side of the peninsula. In addition, the late-glacial relative sea level curves are irregular. This reflects a general eastward direction of retreat, and remnant ice on the Melville

Peninsula that persisted until after 6200 ^{14}C yr BP (about 7100 cal yr BP). Relative sea level in this area may also be affected by tectonic activity. The southern part of the Melville Peninsula was described by Dredge (2002). In this area, fossils that are appropriate for radiocarbon dating are rare. Most of the samples in this region come from deltaic deposits. Similar to Southampton Island, Dredge (2002) found that the archival dates were not consistent with more recently dated samples. The archival shells had an apparent age that was about 400 years older than more recently dated samples from the same sample locations. None of these archival dates are included in this study, as they did not meet the criteria of acceptance (unknown species dated). Relative sea level was 100-170 m higher than present at 7000-8000 cal yr BP in the southern Melville Peninsula (Fig. 6.4).

6.1.7 Boothia Peninsula

There are 151 samples in the Boothia Peninsula (Fig. 6.6 and Fig. 6.7). The samples from the southern part of the peninsula (south of 69.7°N) are within the study region, while the northern portion is just outside. Most of the samples were collected by A.S. Dyke and J.M Savelle, who were investigating the history of human occupation in the Arctic and relative sea level change (Dyke et al., 2011; Savelle and Dyke, 2009). As a result of these surveys, relative sea level in the Boothia Peninsula is tightly constrained from 6000 cal yr BP to present. The relative sea level history prior to that time was determined from studies by Craig (1961), Dyke (1984), Giangioppi et al. (2003) and Little (2006). Relative sea level highstand positions were higher (maximum 240 m) in the southeastern part of the southern Boothia Peninsula, than to the northwest (maximum 180 m) (Giangioppi et al., 2003). They interpreted this to be the result of southwestward retreat of the ice sheet. Little (2006) modelled the relative sea level fall in southwestern Committee Bay (located in the eastern part of Fig 6.6) with an exponential function. Relative sea level for the northern

parts of the Boothia Peninsula were determined in detail by Dyke et al. (2011). In general, relative sea level fall is exponential, with a larger magnitude drop towards the south.

6.1.8 King William Island

There are 51 samples from King William Island (Fig. 6.8), the majority reported by Dyke and Savelle (2009). After deglaciation, King William Island lay completely below the marine limit for this region (Dyke et al., 1991), so all samples were collected below 100 m. Dyke and Savelle (2009) noted that several of the samples appear to be too old if exponential relative sea level fall is assumed (samples UCIAMS-30443, UCIAMS-29587 and UCIAMS-29235). These samples are included in this study, though it is noted that they are anomalous.

6.1.9 Northwestern mainland Nunavut

Northern mainland Nunavut (in many studies denoted as "Mackenzie District"), is split into three regions for the purposes of this study: Bathurst Inlet and Kent Peninsula (Fig. 6.9), Coronation Gulf (Fig. 6.10) and Amundsen Gulf (Fig. 6.11). There are a total of 134 samples in this region. The relative sea level history of this region was documented in detail by Kerr (1996). The marine limits based on raised deltas range from 10-30 m in the western part of this area at Darnley Bay to over 220 m within Bathurst Inlet, reflecting greater glacial-isostatic depression towards the east as well as an eastward direction of retreat. Relative sea level at the western part of this region fell below present day sea level after 9400 ^{14}C yr BP (about 10 500-11 000 cal yr BP). Towards the east, relative sea level initially fell rapidly from their highstand position for the first 3000 years after deglaciation, then fell gradually to present level. Dyke and Savelle (2009) collected many of the samples on the Kent Peninsula (Fig. 6.9), giving a very tightly constrained relative

sea level fall from about 40 m above present between 6000 cal yr BP and present.

6.1.10 Mackenzie Delta

There are 32 samples from the Mackenzie Delta region (Fig. 6.12). The majority of these samples were discussed by Rampton (1988) and Hill et al. (1993). Relative sea level in this region likely remained below present sea level since deglaciation, and likely was below 45 m at the start of the Holocene (Hill et al., 1993). There has been between 3 and 10 m of relative sea level rise in the past 2500 years.

6.1.11 Victoria Island and Banks Island

Victoria Island and Banks Island lie north of the study area, but samples from the southern parts of these islands are used to constrain ice volume for the Arctic Archipelago adjacent to the northern mainland Laurentide Ice Sheet (Figs. 6.13-6.17). There are 45 samples from southeastern Victoria Island (Fig. 6.13), 113 samples from southwestern Victoria Island (Fig. 6.14), 112 samples from the Prince Albert Sound (Fig. 6.15), 46 samples from northwestern Victoria Island (Fig. 6.16), and nine samples on southern Banks Island (Fig. 6.17). Most of the samples from Victoria Island came from surveys by A.S. Dyke and J.M. Savelle (*i.e.* Dyke and Savelle, 2000a,b, 2001; Savelle and Dyke, 2002; Savelle et al., 2012). Similar to the adjacent mainland regions, the marine limit increases from west to east, reflecting increased glacial-isostatic depression. The relative sea level highstand position for western Banks Island is less certain, with Vincent (1989) interpreting the highstand position to be pre-late Wisconsin. Lakeman and England (2013) interpreted the highstand position to be late Wisconsin, though no age could be assigned. Eastern Banks Island did have a highstand in excess of 30 m above present day sea level (Fig. 6.17). Relative sea level likely remained below present level during the Holocene.

6.1.12 Summary of paleo-sea relative level indicators

The majority of the relative sea level indicators used in this study are from regions on the periphery of the study area. These provide constraints on relative sea level change during the retreat of the Laurentide Ice Sheet. Relative sea level was highest immediately after deglaciation, and generally fell in an exponential manner. The marine limit elevation increases towards the eastern mainland Nunavut, reflecting increased glacial-isostatic depression and later ice sheet retreat. The distribution of samples is uneven, with northwestern Hudson Bay having only limited chronological control on relative sea level change.

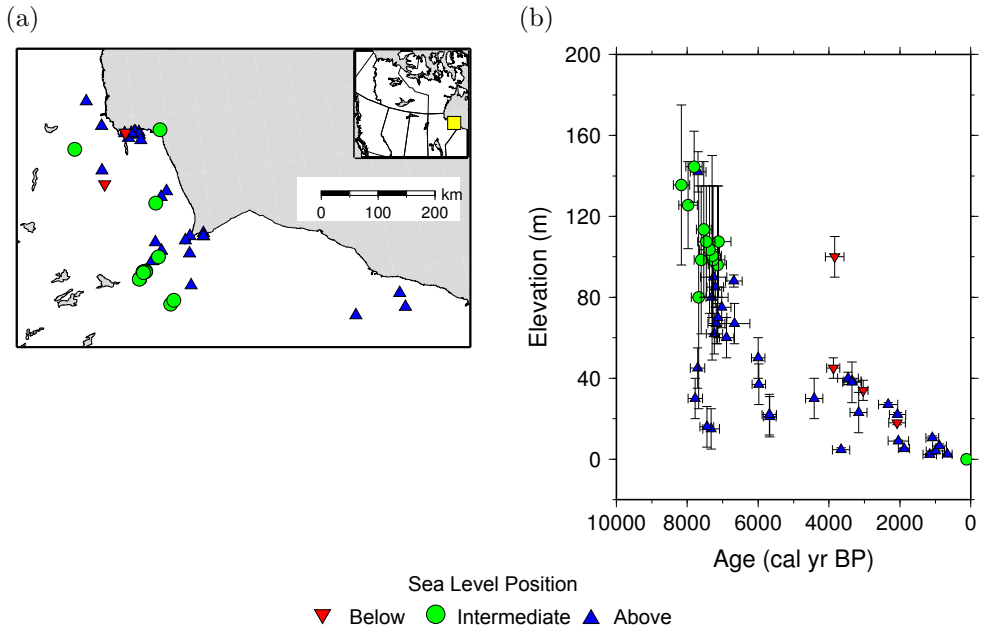

Figure 6.1: Relative sea level indicators from southwestern Hudson Bay. (a) Location of data. (b) Age and elevation of the indicators.

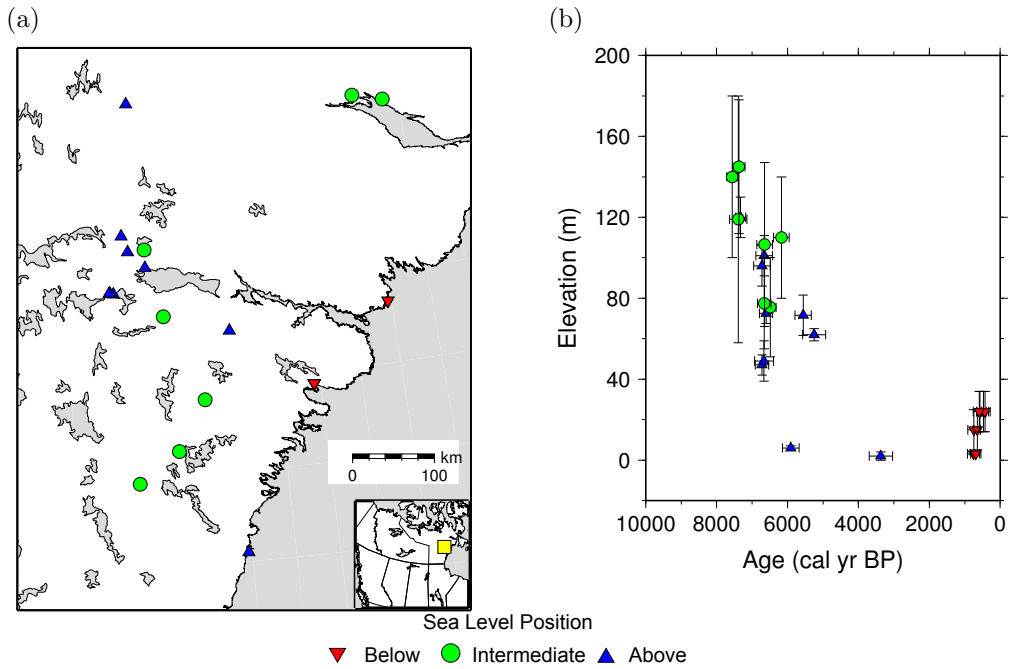

Figure 6.2: Relative sea level indicators from northwestern Hudson Bay. (a) Location of data. (b) Age and elevation of the indicators.

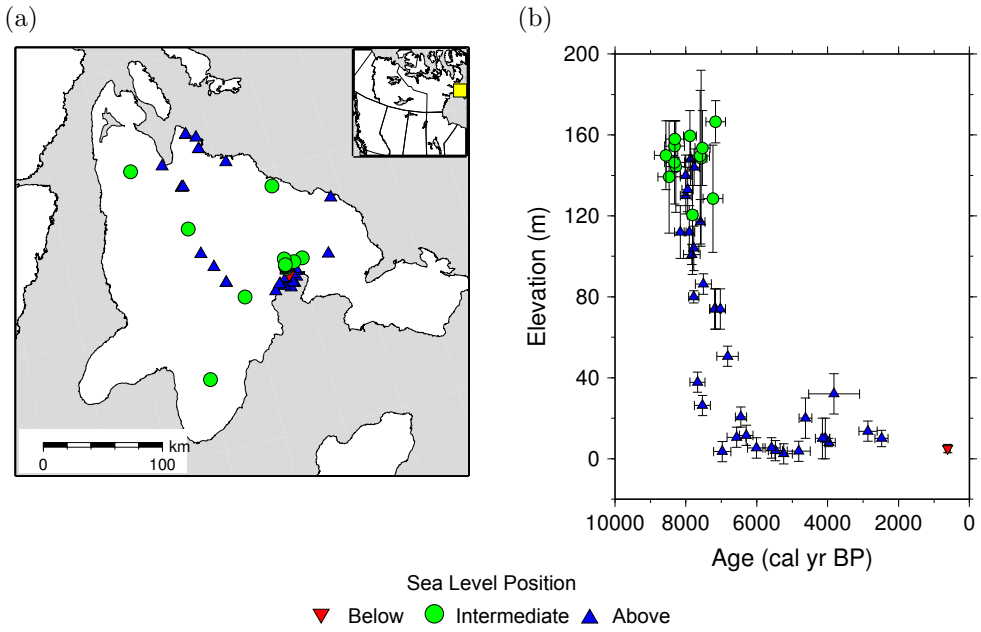

Figure 6.3: Relative sea level indicators from Southampton Island. (a) Location of data. (b) Age and elevation of the indicators.

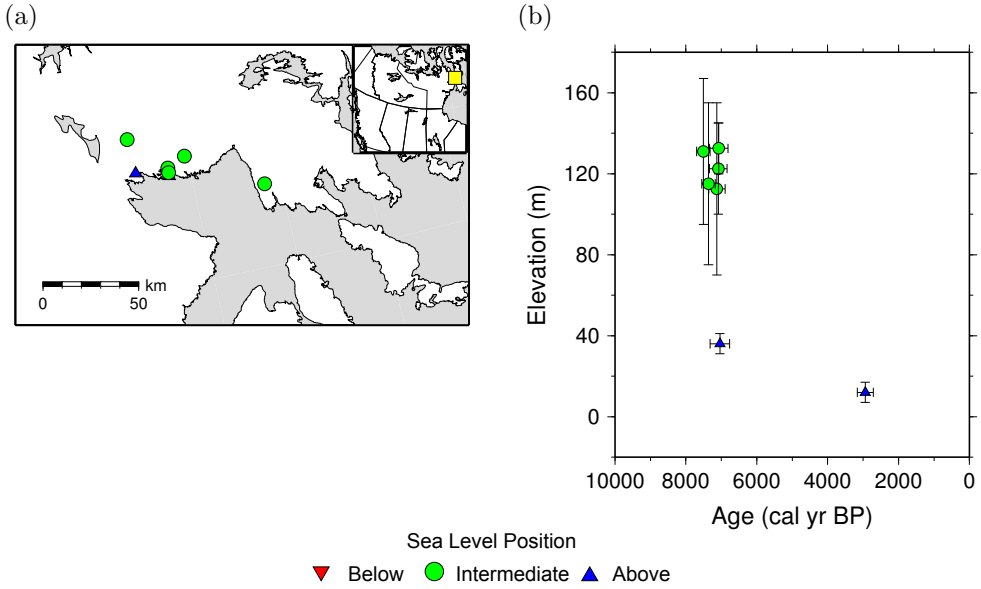

Figure 6.4: Relative sea level indicators from southern Melville Peninsula. (a) Location of data. (b) Age and elevation of the indicators.

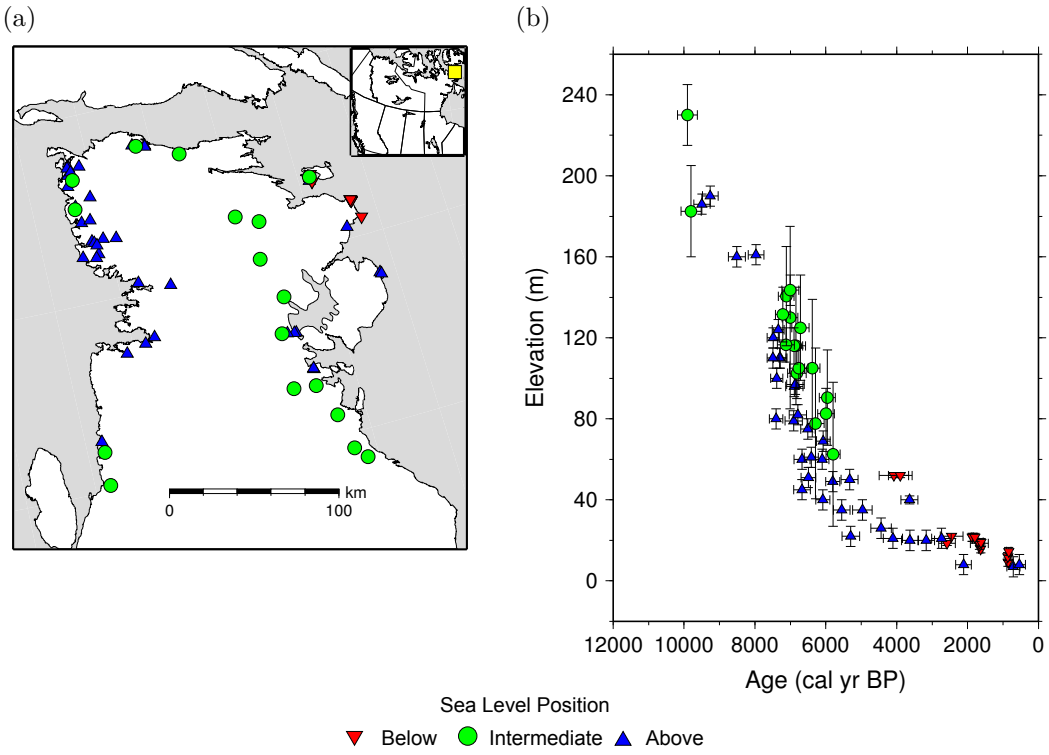

Figure 6.5: Relative sea level indicators from Melville Peninsula. (a) Location of data. (b) Age and elevation of the indicators.

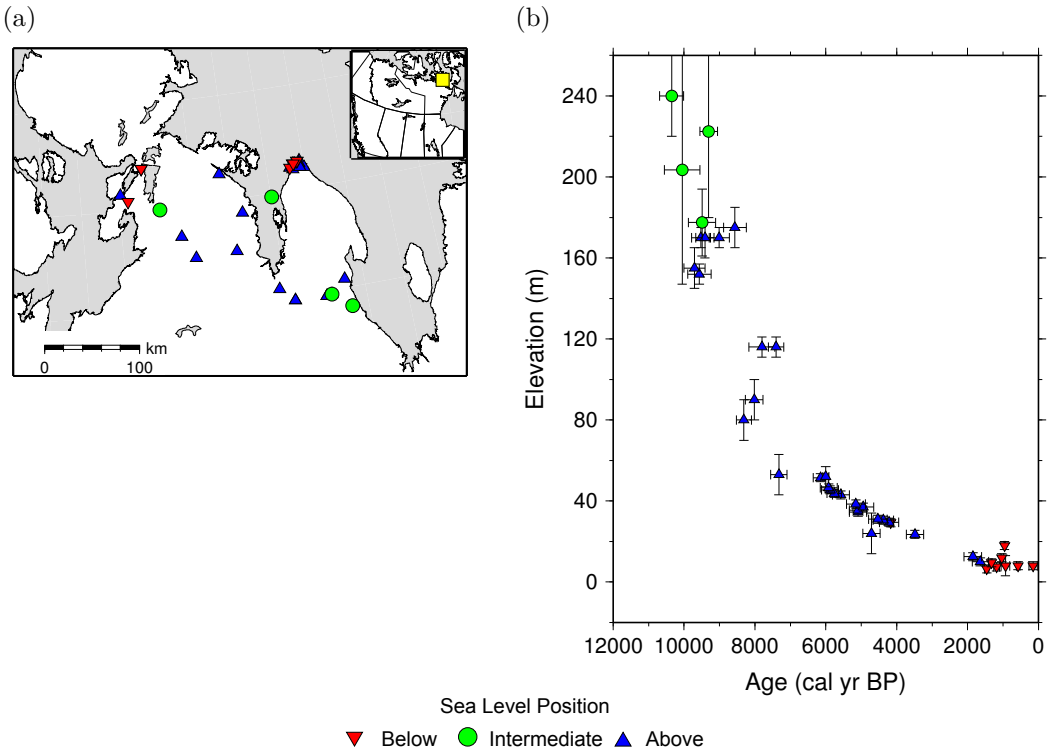

Figure 6.6: Relative sea level indicators from southern Boothia Peninsula. (a) Location of data. (b) Age and elevation of the indicators.

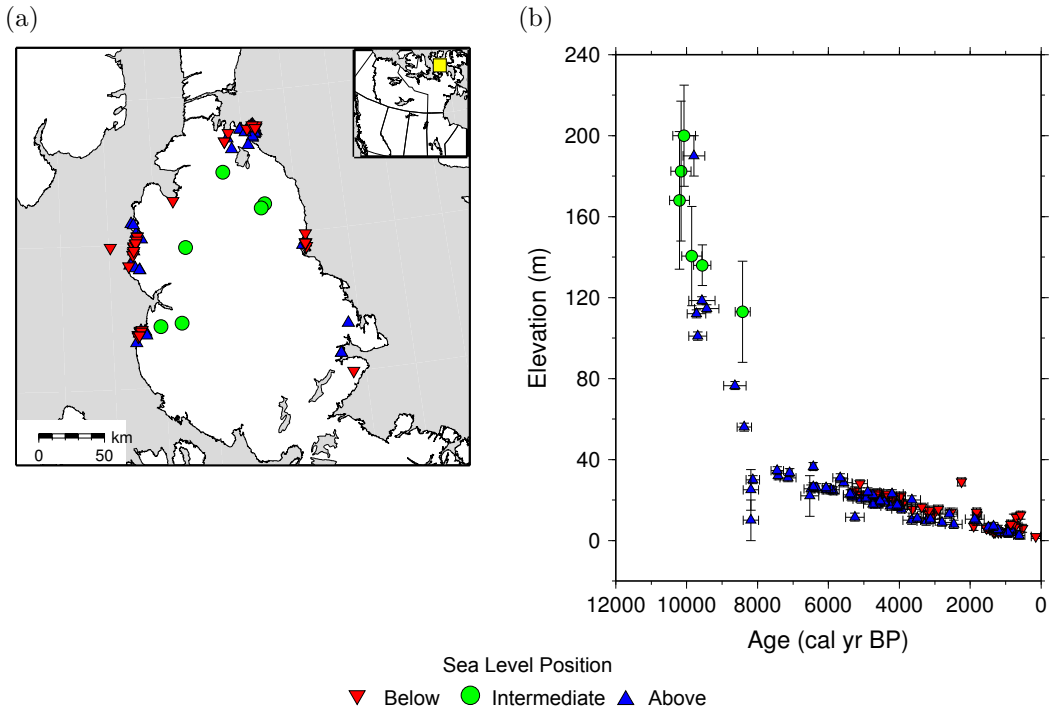

Figure 6.7: Relative sea level indicators from northern Boothia Peninsula. (a) Location of data. (b) Age and elevation of the indicators.

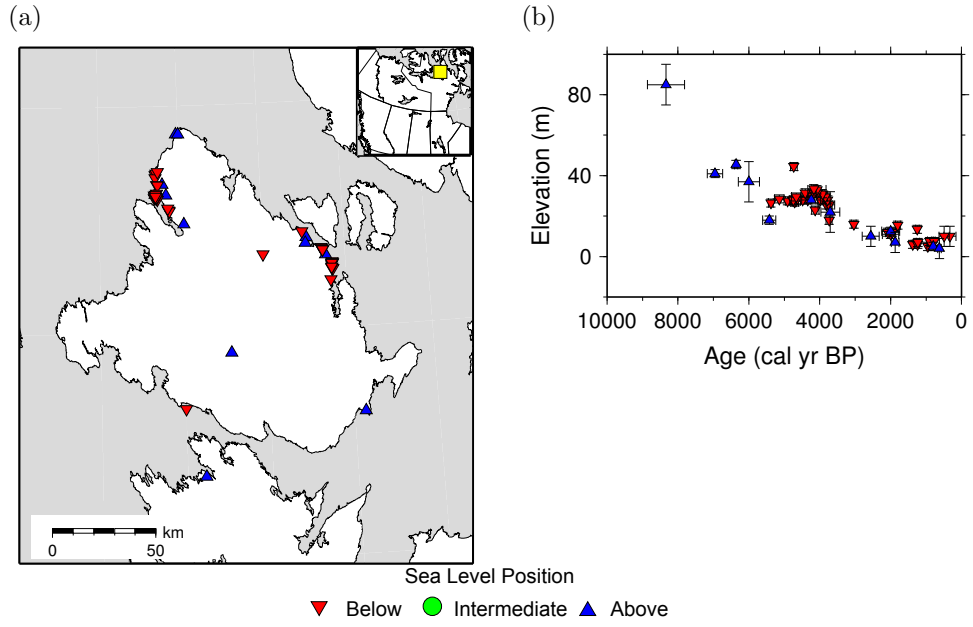

Figure 6.8: Relative sea level indicators from King William Island. (a) Location of data. (b) Age and elevation of the indicators.

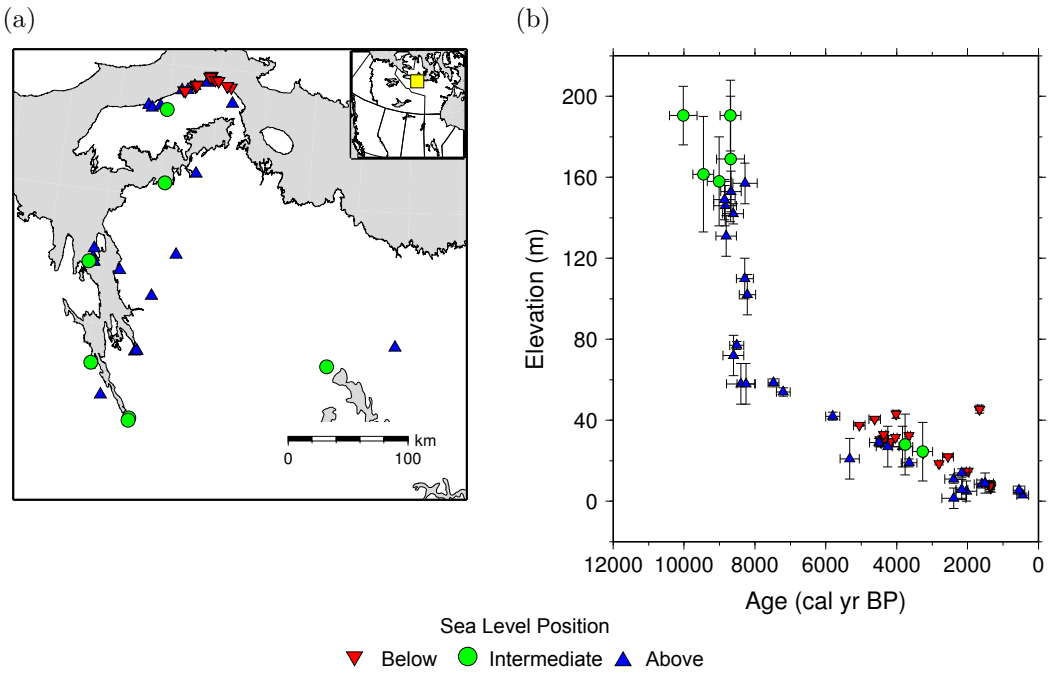

Figure 6.9: Relative sea level indicators from the Bathurst Inlet and Kent Peninsula region. (a) Location of data. (b) Age and elevation of the indicators.

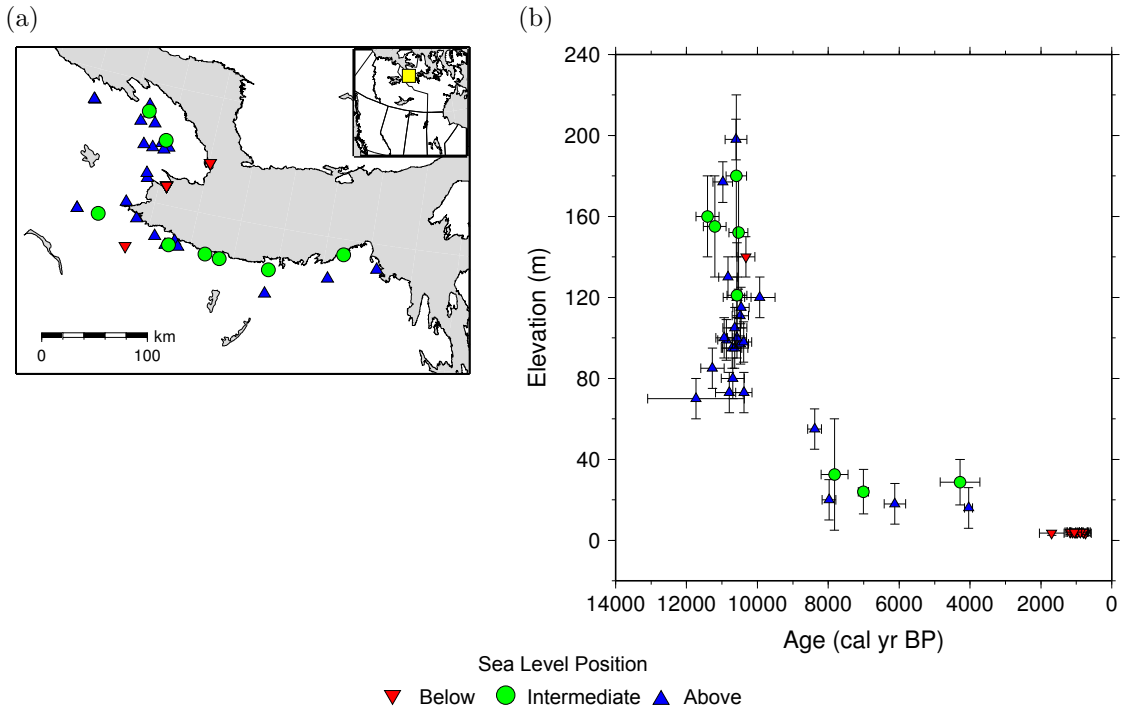

Figure 6.10: Relative sea level indicators from the mainland Coronation Gulf region. (a) Location of data. (b) Age and elevation of the indicators.

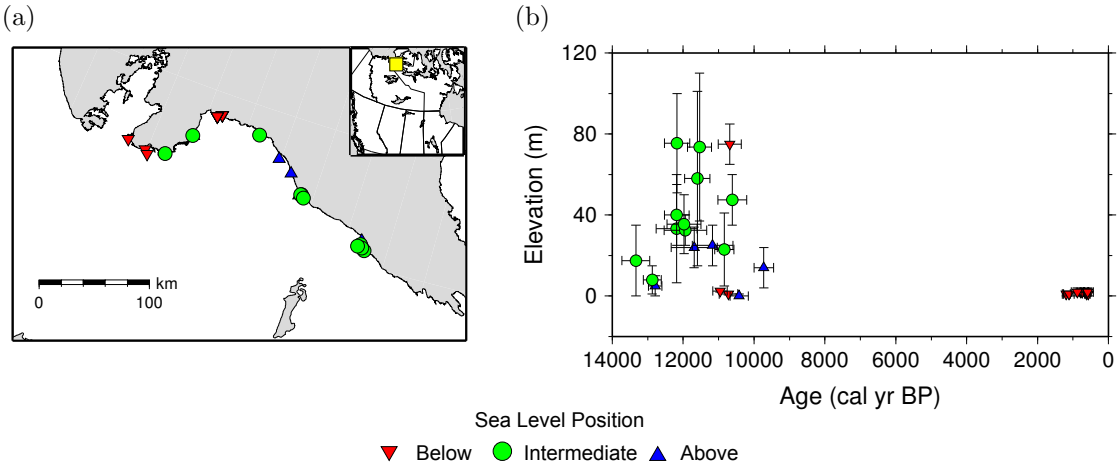

Figure 6.11: Relative sea level indicators from the mainland Amundsen Gulf region. (a) Location of data. (b) Age and elevation of the indicators.

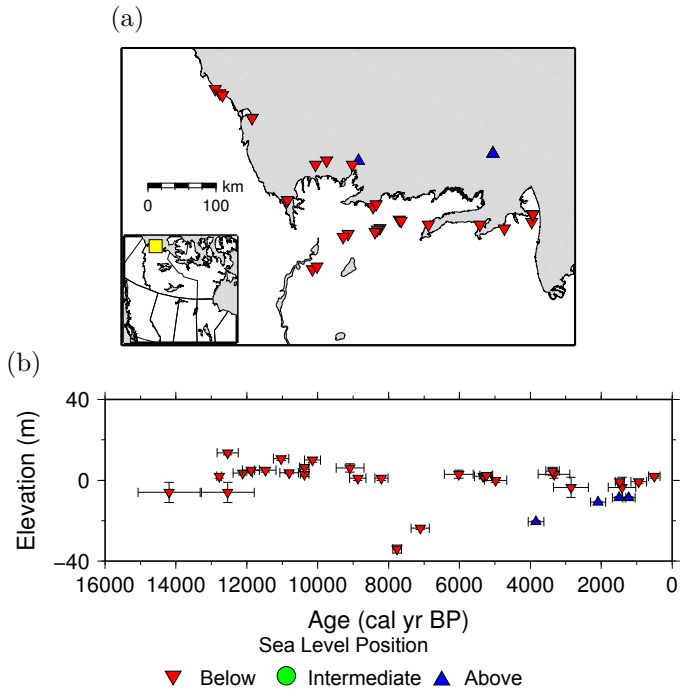

Figure 6.12: Relative sea level indicators from the Mackenzie Delta and adjacent regions. (a) Location of data. (b) Age and elevation of the indicators.

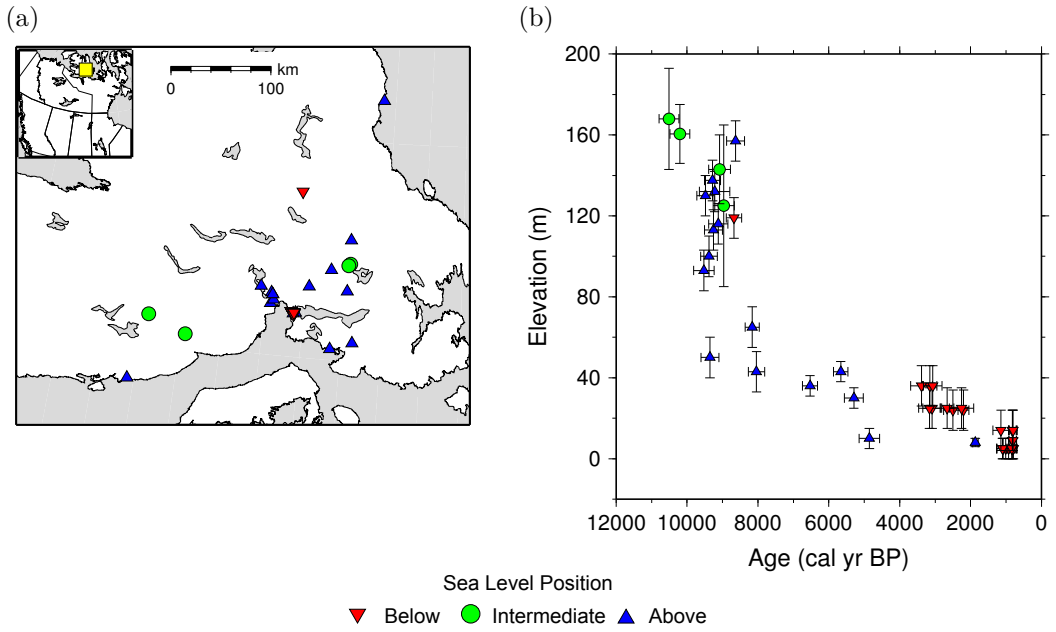

Figure 6.13: Relative sea level indicators from southeastern Victoria Island. (a) Location of data. (b) Age and elevation of the indicators.

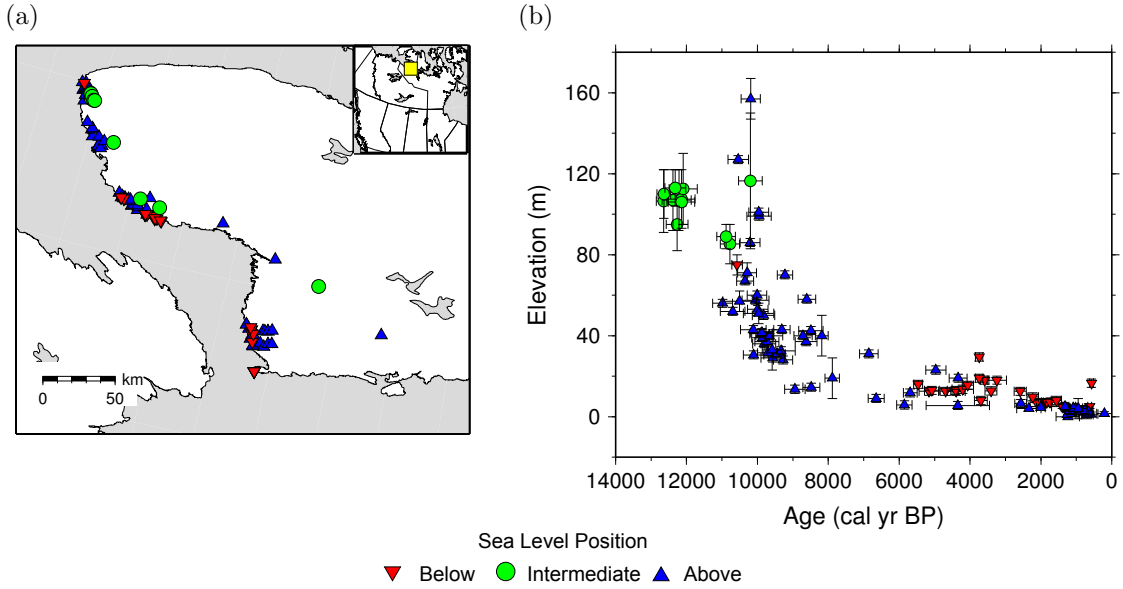

Figure 6.14: Relative sea level indicators from southwestern Victoria Island. (a) Location of data. (b) Age and elevation of the indicators.

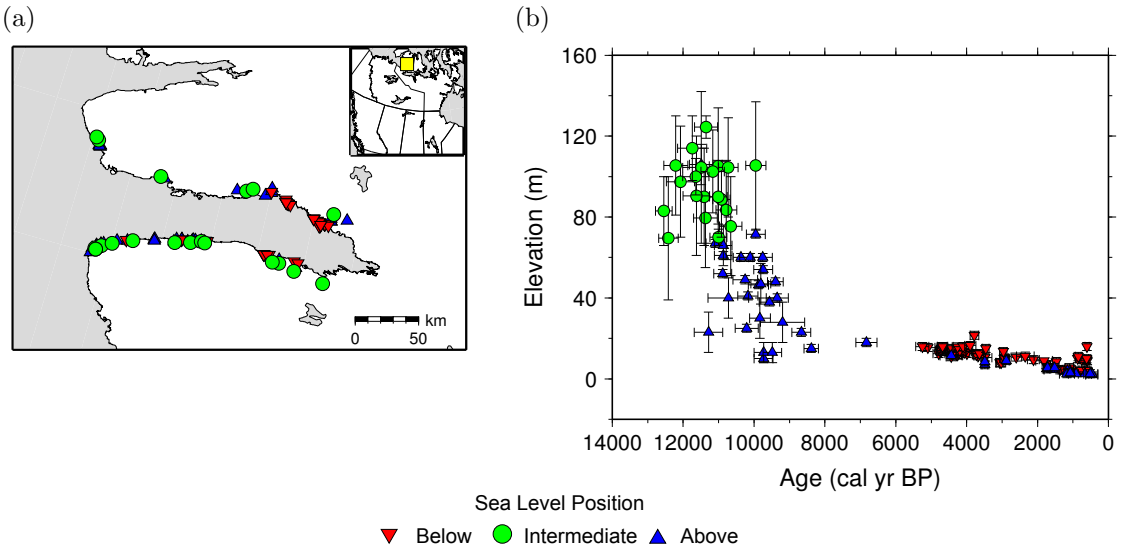

Figure 6.15: Relative sea level indicators from Prince Albert Sound in Victoria Island. (a) Location of data. (b) Age and elevation of the indicators.

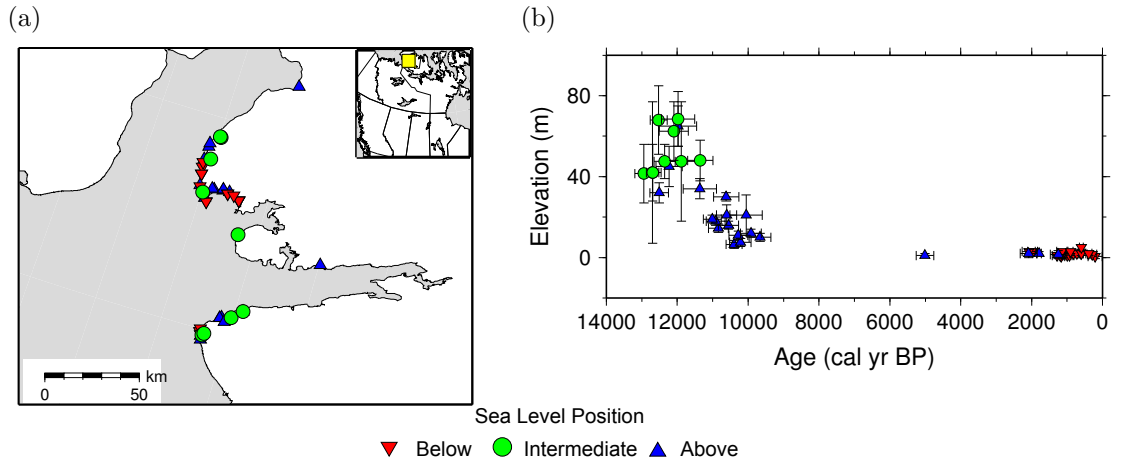

Figure 6.16: Relative sea level indicators from northwestern Victoria Island. (a) Location of data. (b) Age and elevation of the indicators.

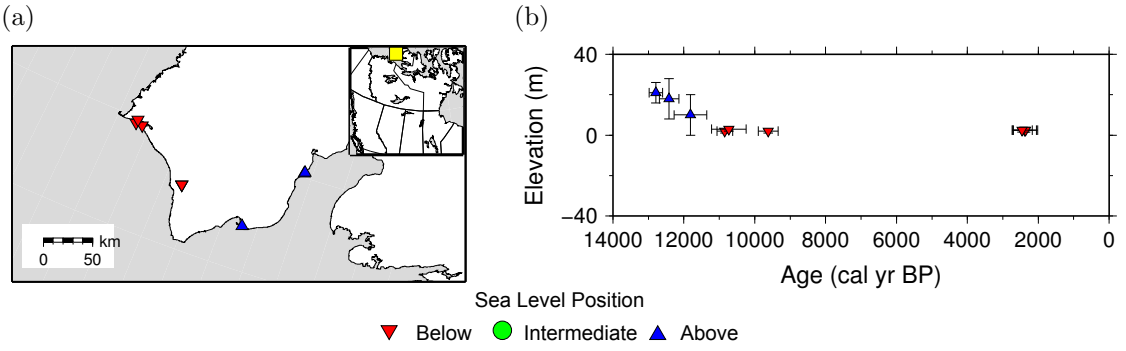

Figure 6.17: Relative sea level indicators from southern Banks Island. (a) Location of data. (b) Age and elevation of the indicators.

6.2 Glacial lake strandline tilt

6.2.1 Introduction

The tilt of proglacial lakes may be one of the sources of information to determine the amount of GIA during deglaciation in areas that are far from the ocean. Several proglacial lakes existed in the region occupied by the western Laurentide Ice Sheet. The largest of these lakes were glacial Lake Agassiz and Lake McConnell (Fig. 6.18). Though the extent of these lakes fluctuated depending on the configuration of the ice margin and elevation of the drainage outlet, correlation of lake levels over long distances are possible in some cases. The following section summarises the observed tilt in Lake Agassiz and McConnell. Much of the evidence for high water levels come from strandlines, which include beaches, scarps and spits that formed at the shore of the lakes. Since these strandlines formed thousands of years ago, there has been different amounts of post-glacial uplift in different parts of the basin. The differential uplift can be determined by finding the elevation at different locations along the strandline.

6.2.2 Potential sources of uncertainty

The level of a lake is determined by a surface of equipotential. All measurements of elevation in this section were done using an ellipsoidal approximation of the geoid, namely NAD83 and WGS84. The level of modern day lake would not correspond exactly to an even height using an ellipsoidal projection. Although the change in geoid height is not great over the distances of different parts of the paleo-lakes, the geoid height accounted for in the following section. The geoid height is calculated using the UNAVCO geoid height calculator (`http://www.unavco.org/software/geodetic-utilities/geoid-height-calculator/geoid-height-calculator.html`, Rapp, 1997). This calculator determines the difference in height of the

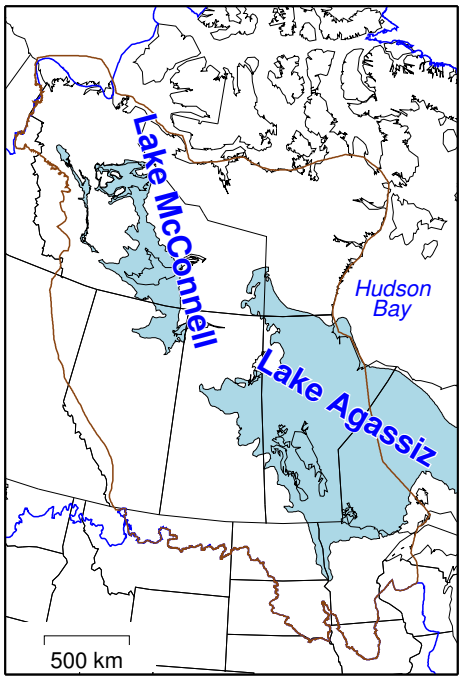

Figure 6.18: Location of Glacial Lake McConnell (Smith, 1994) and Lake Agassiz (Teller and Leverington, 2004). The brown line is the extent of the study area, and the blue line is the maximum extent of the North American ice sheet complex.

WGS84 projection relative to the EGM96 geoid model. The elevations reported in this section are orthometric heights, which are the WGS84 ellipsoidal height minus the geoid/ellipsoid separation. As an example, the maximum difference in geoid/ellipsoidal separation along the Upper Campbell strandline and the reference location near the southern end of the basin is about 4 m. The Lake McConnell elevations are also converted using the same method, though the projection used in the air photos was not stated in Smith (1994).

The lake surface height was unlikely to be be constant for any length of time, due to primarily to rapid postglacial uplift and changes to ice margin locations (Teller and Leverington, 2004). McMillan and Teller (2012) investigated other possible factors for the formation of strandlines within the Lake Agassiz basin. They concluded that factors like periodic opening and closing of secondary outlets, irregular erosion of the main outlet, and irregular postglacial uplift were not dominant factors in the formation of the beaches. Storm events that may have created deposits up to

four meters above the regular lake level may be responsible for some discontinuous beaches. The longer, continuous strandlines are likely the result of sustained wave action. Nevertheless, a beach deposit could be up to a few metres higher than the true paleo-lake level.

6.2.3 Northern Lake McConnell

During one of the early phases of Lake McConnell, the drainage outlet of the lake was through the modern Great Bear River (Smith, 1994, fig 6.19). The age of this phase of the lake is inferred to be about 11 500–11 000 ^{14}C yr BP (about 13 400–12 900 cal yr BP) based on a radiocarbon date of a piece of wood found in a delta where the lake drained into Glacial Lake Mackenzie (I-15020, 13 800–13 100 cal yr BP, Smith, 1992). Though not directly dated, Smith (1994) interpreted the highest strandlines on the northeastern side of the lake to closely correspond to when the Great Bear River outlet was the primary outlet, and that most of the observed tilt is due to subsequent rebound. He also suggested that drainage through this outlet stopped by 11 000 ^{14}C yr BP, with the opening of a southern outlet through the Mackenzie River. The highest strandlines likely corresponded to the earliest stages of this phase of the lake, as there would have been a substantial uplift rate immediately after deglaciation of the region. There was between 110 and 120 m of tilt between the Great Bear River outlet and strandlines on the northeastern part of the lake.

6.2.4 Southern Lake McConnell

After 11 000 ^{14}C yr BP, water from Glacial Lake McConnell was routed through the Mackenzie River (Fig. 6.20, Smith, 1994). The outlet of the lake is a large valley with a bottom elevation of 166 m. Two deltas from rivers that flowed into the outlet region occur at elevations of 180 and 181 m (195 m in orthographic projection), and

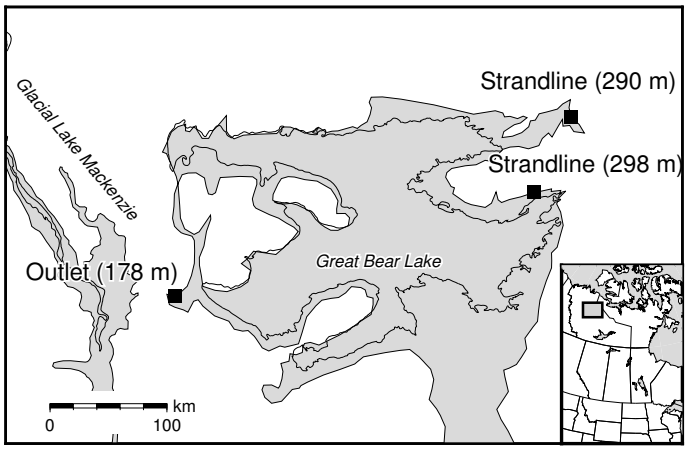

Figure 6.19: Northern Glacial Lake McConnell with the location of the Great Bear River outlet and two strandlines at the northeastern part of the lake. The grey area is the maximum extent of the lake. The black lines show the modern extent of Great Bear Lake.

likely represent a high water level before channel incision. A large amount of this incision happened when Glacial Lake Agassiz catastrophically drained into the lake, so the elevations of the deltas are used for determining tilt in this part of the lake. The high water mark on the southeastern part of the lake is associated with the formation of the Cree Lake Moraine, which was dated by Fisher et al. (2009) to be 11 200–10 800 cal yr BP. This is the age used to model the tilt of the southern part the lake, though it should be noted that none of these features has been directly dated.

6.2.5 Lake Agassiz Strandlines

The strandlines of Lake Agassiz were originally mapped using ground-based surveys and interpretations using air photos (*i.e.* Upham, 1895; Johnston, 1942; Elson, 1967; Teller and Clayton, 1983). The correlation and age of the strandlines over long distances were made based on assumptions of their relative vertical position. Recently, there have been efforts to map these strandlines to improve correlations of their lateral extent (Fisher, 2005; Lepper et al., 2007, 2011, 2013; Rayburn and

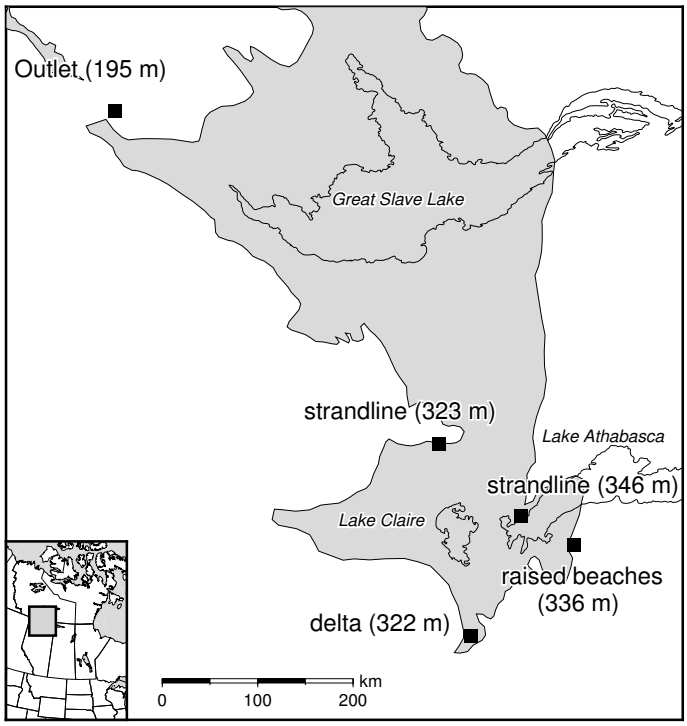

Figure 6.20: Southern Glacial Lake McConnell with the location of the Mackenzie River outlet and high water features. The grey area is the maximum extent of the lake.

Teller, 2007; Weller and Fisher, 2009; Yang and Teller, 2012). In addition, optical dating has allowed precise age determination of the strandlines, which was not possible with radiocarbon methods due to a lack of organic material (Fisher et al., 2008, 2011; Lepper et al., 2007, 2011, 2013). At present, the Herman, Norcross and Upper Campbell strandlines are sufficiently dated and mapped to be used to determine tilt due to GIA.

In areas where elevation measurements were not previously published, but the strandline location was identified, the elevation was determined using LIDAR and shuttle radar topography mission (SRTM) data. LIDAR data are available for all areas of the Lake Agassiz basin located within the United States. This data was downloaded as 1 m resolution tiles from the International Water Institute website (`http://www.iwinst.org/lidar/`). The elevation of LIDAR data has a stated vertical accuracy of less than 15 cm. The methodology for determining the elevation

of the beaches follows Yang and Teller (2012). The tiles were imported into ArcGIS, and elevation profiles were made perpendicular to the strandline. If the strandline was in the form of a beach ridge, the average height of the top of the ridge was taken to be representative of the water height. If the strandline was represented as a scarp, the level was taken to be the location of the break in slope of the scarp (Rayburn, 1997). For areas in Canada where there was no LIDAR data, the elevations were taken from SRTM data. In most of the area covered by Lake Agassiz, vertical accuracy of this data is 5 m or less (Farr et al., 2007). Elevations derived from SRTM data was compared with LIDAR data in the United States, and found to be consistently within 5 m.

The Herman Strandline is the oldest and highest continuous strandline of Lake Agassiz (Fig. 6.21), with an age of 14 100±300 yr BP (Lepper et al., 2013). Elevation measurements for the American locations were derived from LIDAR (Lepper et al., 2011, 2013; Yang and Teller, 2012). The location of the northeastern part of the strandline is derived from Weller and Fisher (2009), and elevations taken from LIDAR using the technique by Yang and Teller (2012) (the original study used topographic maps with contours of 5-10 feet, but the elevation/location pairs were not stated). The elevation of the strandline in Manitoba is taken from McMillan and Teller (2012). The lake level in the northern part of the Herman phase is complicated, and no distinct, continuous shorelines are observed due to the high rate of uplift when the lake was at that level (McMillan and Teller, 2012). They interpreted the beaches to be the result of storm action, with the lake level about 1.5 m below them. The Herman strandline occurs at an elevation of about 380 m in this area (Fig. 6.21). There is about 50–55 m of tilt between the northern and southern parts of Lake Agassiz during the Herman stage.

The Norcross strandline formed after the Herman strandline, at 13 600±200 yr BP (Lepper et al., 2013). Elevations were obtained from the same sources as the

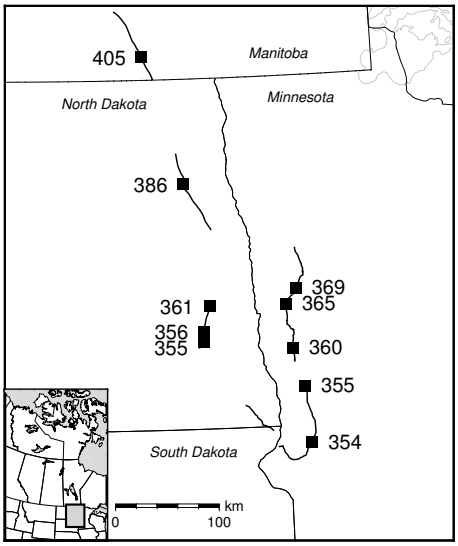

Figure 6.21: Elevation of selected parts of the Herman strandline. Extent of recently mapped parts of the strandline are shown in the heavy black line.

Herman Strandline. The strandline becomes discontinuous towards the northwestern part of the lake, and cannot easily be distinguished from Herman level beaches (Yang and Teller, 2012; McMillan and Teller, 2012). Beaches interpreted to be representative of the Norcross level occur at about 390 m in Manitoba (Fig. 6.22, McMillan and Teller, 2012). As with the Herman strandline, the elevation is less certain at the northern end of the lake, but indicate there is about 45–50 m of tilt between the northern and southern parts of the basin at this time.

The Upper Campbell Strandline is the longest continuous strandline in the Lake Agassiz basin (Fisher and Lowell, 2012). Optical dates from the southern part of the strandline have an age of 10 500±300 yr BP (Lepper et al., 2013), while the maximum age from several radiocarbon dates was reported by Lepper et al. (2011) to be 10 600±200 and 10 800±200 cal yr BP. Lepper et al. (2011) suggested that the younger age of the optical dates may be due to the samples dating the Lower Campbell strandline, which is indistinguishable from the Upper Campbell strandline at the southern end of the lake. The age of the beach is taken to be the optical date, which is a direct age of the strandline, and overlaps with the maximum age

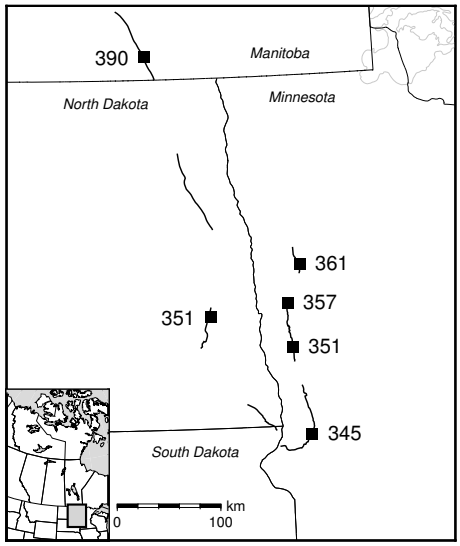

Figure 6.22: Elevation of selected parts of the Norcross strandline. Extent of recently mapped parts of the strandline are shown in the heavy black line.

determined from radiocarbon dates.

Elevation data for the Upper Campbell Strandline was determined from a variety of sources. The elevation data from the United States was primarily derived from LIDAR (Lepper et al., 2011, 2013; Yang and Teller, 2012). For areas north of 51°N, the elevation of the strandline was determined using differential GPS, with a stated error of less than 1.2 m (Rayburn, 1997; Rayburn and Teller, 2007). The average error of these measurements, taking into account the variable height of the strandline above the adjacent topography was stated to be 5.45 m. In areas where there were no previously published elevation measurement, LIDAR and SRTM data were used to determine elevation, using the strandline location map found in Teller et al. (2000) and Fisher and Lowell (2012). Fig. 6.23 shows the extent and elevation measurements of the Upper Campbell Strandline. The minimum elevation (325 m) is slightly northwest of the southernmost point of the lake. The highest elevation at the northern end of the strandline is 479 m. Strandline elevation increases towards the northeast.

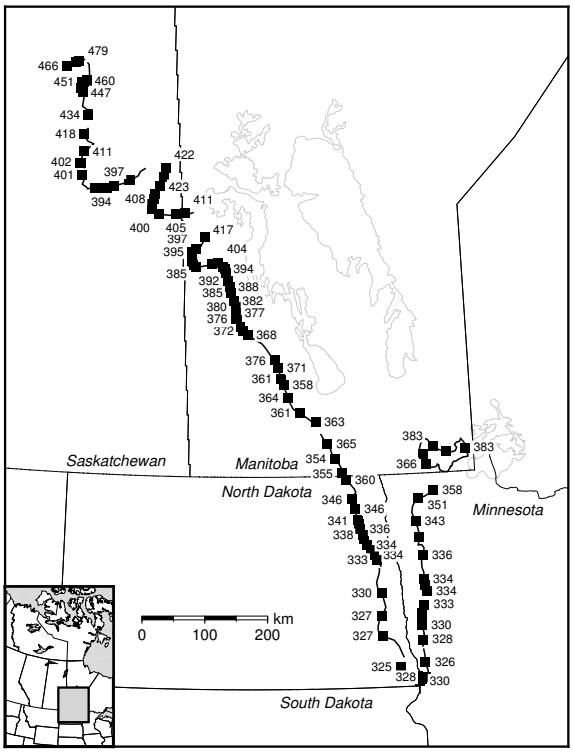

Figure 6.23: Elevation of selected parts of the Upper Campbell strandline. Extent of recently mapped parts of the strandline are shown in the heavy black line.

6.2.6 Summary of paleo-glacial lake tilt

Information on the relative uplift of paleo-glacial lakes has been summarised in this section. The constraints on Glacial Lake McConnell are fairly tenuous, based on the assumption that landforms in different parts of a certain phase of the lake formed at the same time. Nevertheless, they show there is a significant difference in the amount of uplift towards the central parts of the ice sheet. They provide the best information on the amount of GIA in continental Northwest Territories. The relative uplift of Lake Agassiz strandlines are measured using high resolution Lidar, SRTM and GPS data. The age in which these strandlines formed is now well determined through the use of OSL dating. The data from the Upper Campbell strandline indicate that there has been as much as 150 m of relative uplift between the northern and southern end of the strandlines since it formed.

6.3 Summary

This chapter presented an overview of the available constraints of GIA in a paleo-context. Information on relative sea level change exists for much of the northern coast of the study area. Around Hudson Bay, there are fewer data, as a result of fewer studies investigating sea level change in this region. These data provide useful information on the post-glacial uplift during the progressive retreat of the Laurentide Ice Sheet. Several glacial lakes also have information on the relative post-glacial uplift along various strandlines and other lake level indicators within their extent. In particular, high resolution determination of the water level of Lake Agassiz at well dated strandlines provide some of the best information on GIA away from coastal regions. These data are used to constrain the ice sheet model, which is presented in Chapter 7.

Chapter 7

Ice sheet modelling software

7.1 Introduction

Modelling of past ice sheets is complicated, due to the sheer number of factors that can affect their growth and retreat. For example, Tarasov et al. (2012) presented a glacial systems model that contained 39 parameters, which include climatology, Earth rheology, ice physics and chronology. Many of these parameters are poorly constrained, so their final model was an average of thousands of simulations that fit the known constraints reasonably well. Modelling paleo-ice sheets using high order physics (*i.e.* taking into account three-dimensional stress fields) is currently not feasible on the time scale of thousands of years (Kirchner et al., 2011), while the approximate models, such as those used by Tarasov et al. (2012) are not necessarily accurate.

Ultimately, the elevation of an ice sheet is largely controlled by the strength of the interface between the base of the ice sheet and the land underneath it (Cuffey and Paterson, 2010). This interaction is the combination of a variety of factors, such as ice temperature, accumulation rate and the deformability of the bed. Except in rare cases where there are extremely steep slopes, the gradient of the ice surface is proportional to the basal shear stress. Therefore, it is possible to estimate the ice surface topography if the shear stress is known.

In this chapter, I present the software used for ice sheet modelling in this study,

based on the assumption of steady state and perfectly plastic ice conditions. The method was originally established by Reeh (1982) and Fisher et al. (1985) and was successfully applied to model the present day configuration of Greenland Ice Sheet and Last Glacial Maximum Laurentide Ice Sheet. This method requires minimal input parameters (*i.e.* basal shear stress, basal topography and margin location). The basal shear stress parameter balances the driving stress induced by gravitational forces acting on the ice column. This combines many effects and ultimately is estimated in this study. Basal topography changes over time due to the loading of the ice sheet (Cuffey and Paterson, 2010). Since the deformation of the Earth due to the weight of the ice sheet is dependent on the choice of Earth model, it is prudent to determine how much of an effect this has on the equilibrium ice volume and distribution. I conducted tests to determine how many iterations of ice loading are required to reach an equilibrium between Earth deformation and ice distribution (sections 7.6 and 7.7). The ice sheet models produced in this thesis may not conform exactly to the height of the ice sheet if high order physics were included. However, it requires far less computing resources and fewer assumptions, and should still provide a good estimate of the total volume of ice through time.

7.2 Theory

7.2.1 Two-dimensional models

My ice sheet modelling software uses the assumption of ice rheology that adheres to perfectly plastic, steady-state conditions. The two-dimensional form of this theory was developed by Nye (1952), and neglects variability in topography and longitudinal changes in stress. In this equation, the ice surface gradient is directly related to the strength of the ice-bed interface (Fig. 7.1):

$$\frac{dE}{ds} = \frac{\tau_o}{\rho_i g H} \tag{7.1}$$

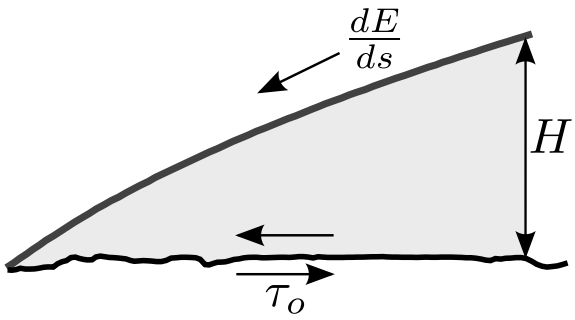

Figure 7.1: Relation between ice surface elevation along a flowline, shear stress and ice thickness (eq. 7.1)

Where E is the ice surface elevation, s is the distance along ice flowline profile, τ_o is the shear stress at the base of the ice sheet, which balances the driving stress, ρ_i is the density of ice, g is the gravity at the Earth's surface, and H is the ice thickness. If the distance from the ice sheet margin to the centre of the ice sheet is known, then the thickness along the profile between the two points can be calculated using the following formula (Cuffey and Paterson, 2010):

$$H^2 = \frac{2\tau_o}{\rho_i g}[L - x] \tag{7.2}$$

Where L is the distance between the margin and centre of the ice sheet, and x is the distance from the centre. Though this equation is simple, it can be used to make a rough estimate the thickness of ice sheets (Cuffey and Paterson, 2010). For example, using a shear stress value of 100 kPa and a distance to the ice sheet centre of 450 km, the thickness of Greenland ice sheet was estimated to be 3.15 km, which is close to the actual thickness of 3.20 km. Fig. 7.2 shows the ice elevation profile calculated from Eq. 7.2 for a variety of shear stress parameters. In the case of a large ice sheet such as the Laurentide Ice Sheet where the ice sheet centre may be in excess of 1000 km from the margin, a high value of shear stress is unlikely to be

representative of average conditions. If it were, the elevation of the ice sheet would be in excess of 5000 m, a value that is higher than the modern day Antarctic Ice Sheet, which is similar in extent.

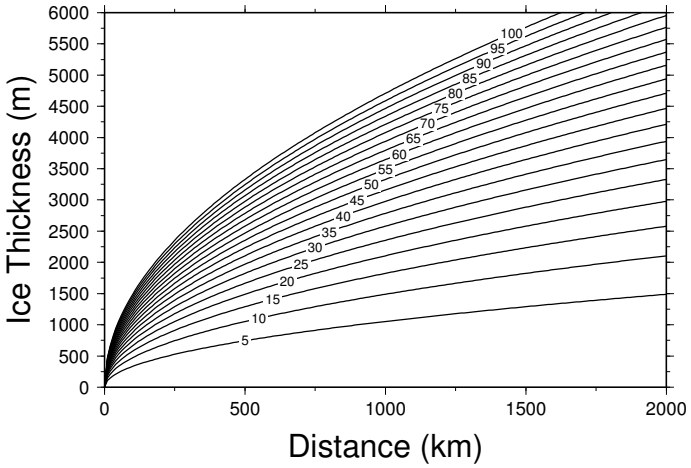

Figure 7.2: Two-dimensional ice sheet models using eq. 7.2. Shear stress values are given in kPa.

Lambeck et al. (1998b, 2010) used Eq. 7.2 to develop models of the Scandinavian ice sheet. They first estimated the maximum thickness of the ice sheet for a given time period, then calculated the ice thickness from a distance s from the centre of the ice sheet, using the following formula:

$$H(s,t) = H_{max}(t)\left\{1 - \left[\frac{s(t)}{s_{max}(t)}\right]^{\frac{3}{2}}\right\}^{0.4} \tag{7.3}$$

In order to produce ice sheet models, they varied the basal shear stress according to the nature of bedrock and topography. After creating initial ice models, they scaled the value of H_{max} to model sea level change in the region. Where needed, the values for the scaling parameters were time and location dependent.

7.2.2 Three-dimensional models

The previous methodology may be inappropriate for the Laurentide ice sheet, where little is known about the thickness of the interior of the ice sheet, due to the relatively

flat underlying topography (Dyke et al., 2002). Another problem is that the central dome of the ice sheet was not static through time (Boulton and Clark, 1990). One way to overcome these uncertainties is to start modelling of the ice sheet at the margin, rather than the centre. Reeh (1982) and Fisher et al. (1985) developed an ice sheet modelling method that made no assumptions about the location of ice domes, and only required inputs of margin location, topography and basal shear stress.

Reeh (1982) used the following partial differential equation to determine the direction of ice flow in three dimensions:

$$\left(\frac{dE}{ds}\right)^2 = \left(\frac{\partial E}{\partial x}\right)^2 + \left(\frac{\partial E}{\partial y}\right)^2 \tag{7.4}$$

Substituting Eq. 7.2 into the left side of Equation 7.4, converting the ice thickness to be in terms of ice surface elevation and basal topography B, and substituting $H_f = \tau_o/\rho_i g$ leads to:

$$\left(\frac{H_f}{E-B}\right)^2 = \left(\frac{\partial E}{\partial x}\right)^2 + \left(\frac{\partial E}{\partial y}\right)^2 \tag{7.5}$$

The above equation describes the change in ice thickness over an arbitrary surface. This partial differential equation can be solved by the method of characteristics. The x and y partial derivatives in Equation 7.5 are substituted by $p = \partial E/\partial x$ and $q = \partial E/\partial y$, then rearranged in terms of p:

$$p = \sqrt{\left(\frac{H_f}{E-B}\right)^2 - q^2} \tag{7.6}$$

The solution to the partial differential equation then becomes three ordinary differential equations that are solved simultaneously:

$$\frac{dy}{dx} = \frac{q}{p} \tag{7.7}$$

$$\frac{dE}{dx} = \frac{p^2 + q^2}{p} = \frac{H_f^2}{(E-B)^2 p} \tag{7.8}$$

$$\frac{dq}{dx} = \frac{(p^2 + q^2)(\partial B/\partial y - q)}{p(E-B)} = \frac{H_f^2}{p(E-B)^3}\left(\frac{\partial B}{\partial y} - q\right) \tag{7.9}$$

Fisher et al. (1985) expanded Equation 7.9 to allow for changes in basal shear stress:

$$\frac{dq}{dx} = \frac{H_f^2}{p(E-B)^3}\left(\frac{\partial B}{\partial y} - q\right) + \left(\frac{H_f}{p(E-B)^2}\right)\frac{\partial H_f}{\partial y} \tag{7.10}$$

These equations can be solved by numerical integration to determine the course and gradient of the ice flowline.

7.3 Ice sheet modelling

The ice sheet models by Reeh (1982) and Fisher et al. (1985) used coarse resolution (50 km) topography. Since many flow features of the Laurentide ice sheet are dependent on relatively narrow and shallow depressions and isolated topographic highs (*i.e.* Evans et al., 2008; Ò Cofaigh et al., 2010), it is desirable to use a higher resolution model of topography. A requirement of automating the construction of ice sheet models using this method is that it must include the ability to find basal topographic highs in order to identify nunatuks. Topography is derived from the ETOPO1 global bedrock relief model (Amante and Eakins, 2009), averaged to a 5 km grid. Elevation is calculated using bicubic interpolation to ensure a continuous surface.

In order to solve the Eqs. 7.7-7.9, initial values for E, y and q are required. Starting model calculation at the margin is convenient from the perspective of reducing a-priori assumptions on ice distribution, though it leads to a singularity because the

ice thickness is zero ($E = B$). Consequently, the value of E at the margin is set to be a nominal value of 0.1 m. Although the actual thickness of ice near the margin may be as high as tens of metres, the choice of starting value will not have a large effect on the final model. For instance, the distance from the margin required in Eq. 7.2 to reach 10 m from a starting value of 0.1 m, and a low basal shear stress value (5000 Pa) is 90 m. The uncertainty in the margin location is much greater than that. For every flowline along the margin, a local coordinate system is defined so that the x-axis points perpendicular to the margin towards the interior of the ice sheet, and the y-axis is parallel to the ice margin. For simplicity, the value of q is defined to be zero at the margin. This can be justified because near the margin the value of term $H_f/(E - B)$ will dominate Eq. 7.6 in the defined coordinate system. A sequential list of the modelling steps are as follows:

- All parameters are converted from geographical coordinates to a distance Cartesian coordinate system, with a central point in Hudson Bay (near the centre of the North America Ice Sheet Complex)

- A time variable basal shear stress model is read into the program (see section 7.4).

- The topography model is read in. For the first iteration of ice sheet development, it uses modern topography. In subsequent iterations, it includes a component of glacial-isostatic adjustment. The modified topography is calculated before running the ice sheet program, using CALSEA (Nakada and Lambeck, 1987; Lambeck et al., 2003).

- The program reads in the margin, and defines locations where the flowline calculation initiates. The interval along the margin polygon is user-defined (see section 7.5). The program defines the initial direction of flow to be perpendicular to the margin, away from the centre of the ice sheet.

- The margin is set to have an initial ice thickness of 0.1 m. If the margin is located where the topography is below sea level, it is assumed that the margin corresponds to the grounding line of the ice sheet. The thickness of ice at this point is $H = -B\rho_{seawater}/\rho_{ice}$, which is the thickness of ice corresponding to the equivalent mass of the water column at that point. CALSEA takes into account that the eustatic contribution of grounded ice is less than the ice thickness. It will equal the difference between the water equivalent ice volume and the water volume if the ice sheet was not there.

- The calculation of ice elevation contours is a recursive process. If the contour crosses over itself (signifying a saddle on the surface of the ice sheet), the contour polygon is split into two, and the calculation is continued in separate polygons.

- The program searches for points on the polygon that are below the current contour elevation. It then calculates the flowline by numerical integration of Eqs. 7.7-7.9.

- If the flowline calculation cannot reach the current contour elevation, which happens when the topography is too steep, the point is flagged and not included in the current contour. A schematic on the determination of flagged points is shown on Fig. 7.3.

- If the flowline direction changes sufficiently so that $q \geq H_f/(E - B)$ (*i.e.* p approaches zero), the local coordinate system is rotated so that p is in the direction of maximum flow.

- If the calculated flowline goes outside the last contour polygon, it is flagged and the point is not included in the current contour. This happens when the ice surface is near its peak height. This can also happen in areas where there is

a sudden change in topography or basal shear stress, which causes a deflection in the flow direction.

- After the flowlines are calculated for each applicable point along the polygon, the program checks to see if any of the calculated flowlines cross over. Offending crossovers are eliminated using a motorcycle algorithm (*e.g.* Vigneron and Yan, 2013). The eliminated flowlines are flagged and not included when determining the elevation contour.

- At this point, an initial polygon of the current elevation contour can be constructed. This must be checked to ensure it is a simple polygon (*i.e.* a polygon that does not cross over itself). If it is not, then the program breaks it into several polygons, and determines whether they represent domes (ice gradient is increasing towards the centre of the polygon) or saddles (the ice gradient is decreasing towards the centre of the polygon). A saddle has reached its peak elevation, and these polygons are eliminated.

- The ice elevation and thickness for all points on a valid polygon (including flagged points) are written to file.

- The polygon is resampled to the user-entered distance interval. This excludes flagged points, and may incorporate basal topographic highs.

The solution of the partial differential equation to calculate flowlines indicates that the flowline should bend when there are changes to basal topography and shear stress. Figs. 7.4 and 7.5 show examples of these transitions. In the model, the flow direction is assumed to be perpendicular to ice surface contours. The modelled ice flow lines go around topographic highs when the resolution is sufficiently high (Fig. 7.4). This allows for the accurate determination the amount of ice in mountainous regions such as the Cordillera, where thick ice existed in valleys, but

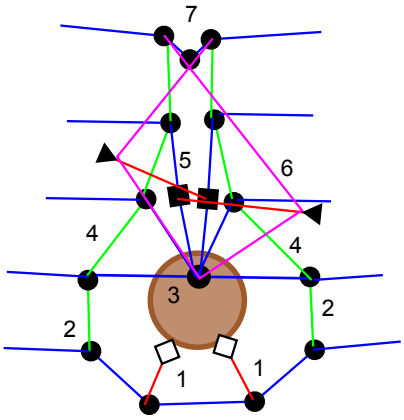

Figure 7.3: Schematic showing how the ice modelling program deals with topographic highs. The blue lines represent the contour. 1) Calculated flowlines are flagged as they do not reach the current contour elevation due to steep topography (represented by the brown circle). 2) Flowline calculation to the current contour is successful. 3) The points where flowline calculation is initiated along the contour polygon are resampled. Flowline calculation is not initiated for the point in the brown circle, as its elevation is too high. 4) Flowline calculation is successful for the points on either side of the topographic high. The point in the topographic high is not eliminated at this step. 5) After another flowline step, the distance along the flowline and the point within the topographic high is sufficient that the resampling puts points at this spot (black squares). 6) The flowline calculation causes the polygon to cross over itself. The polygon is isolated (magenta lines). Since the calculated direction of flow at these points is outside of this isolated polygon, it is eliminated. 7) Final contour polygon includes the crossover point.

mountain peaks likely remained ice free as nunatuks (Clague and James, 2002). Ice flow direction also changes where basal shear stress changes (Fig. 7.5). There was a strong correspondence between ice sheet thickness and velocity and basal geology in the Laurentide ice sheet (Boulton et al., 1985; Fisher et al., 1985; Clark, 1994). The hard-bedded Precambrian Shield provided a more stable ice configuration than areas underlain by weaker sedimentary rocks. For the modelled ice surface in Fig. 7.5 (an area at the transition between the Precambrian Shield and Phanerozoic rocks), the gradient decreases sharply and rotates towards the south when the ice starts flowing over the region with lower shear stress.

After calculating the elevation contours, the final ice sheet model is reduced to a 0.5° longitude by 0.25° latitude grid. The grid is created using a continuous

smoothing algorithm (Smith and Wessel, 1990).

7.4 Shear stress model

The movement of an ice sheet is dependent on many factors, most of which are related to the conditions at the base of the ice sheet. These including the plastic deformation of ice, the sliding of ice over the bed, and the deformability of the sediments below the ice sheet, basal hydrology and basal temperature (Cuffey and Paterson, 2010). Direct observations of basal shear stress in modern glaciers and ice sheets have been limited up to the present, with measured values for land terminating glaciers range between 40 and 130 kPa. Marine terminating glaciers have had measured values ranging between close to zero to over 100 kPa. As an example, the Filchner-Ronne ice streams in Antarctica have basal shear stress of 4-20 kPa (Joughin et al., 2006). The shear stress can locally be highly variable, depending on the roughness of the bed, the presence of water in cavities at the base of the ice sheet, debris carried in the ice, and the temperature at the base. Deformable sediments at the base of the ice sheet can significantly reduce the apparent shear stress. In situ measured values of the shear stress of glacial tills range between 5 and 60 kPa (Cuffey and Paterson, 2010). The strength of till is dependent on local factors, such as water saturation and composition. Ice sheets that terminate in lakes or oceans will have a lower effective shear stress, due to decreased coupling at the base with the buoyant forces acting on the ice.

Reeh (1982) gave an expression for the basal shear stress using Glen's Flow Law:

$$\tau_o = \left[\frac{(n+2)\rho g a}{4B_o \exp(kT)}\right]^{1/(n+1)} \tag{7.11}$$

where ρ is the density of ice, g is the acceleration due to gravity at the surface, T is the ice temperature, a is the accumulation rate, and B_o, n and k are constants.

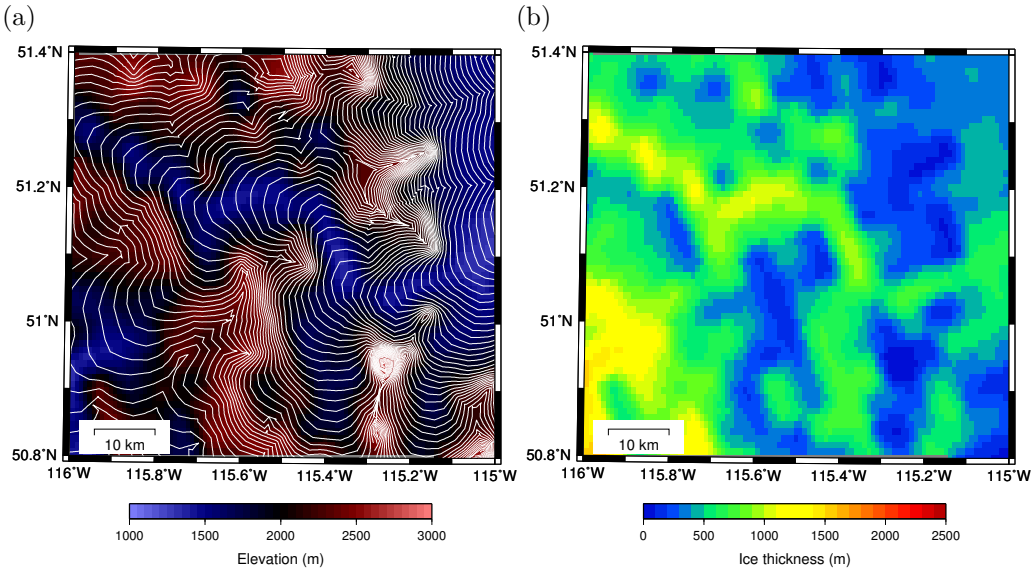

Figure 7.4: Modelled flow around topographic highs. This figure shows an area located in the Rocky Mountains on the border of Alberta and British Columbia. (a) The modelled ice elevation contours (at a 20 m interval) overlying topography. Blue areas are valleys, while red areas are mountains. (b) Modelled ice thickness, with thick ice in valleys and little or no ice on mountains.

Reeh set $B_o = 5 \approx 10^{-7}$ kPa^{-3}yr^{-1}, $k \approx 0.2$ deg^{-1} and $n \approx 3$. The parameter B_o can vary by a factor of 10, while n usually has a value between 3 and 4 (Marshall, 2005). In addition, deformation of sediments beneath the ice sheet is an important parameter in the overall basal shear stress (Clark, 1994). In the Laurentide Ice Sheet model of Licciardi et al. (1998), the shear stress in areas covered in unconsolidated or loosely consolidated sediments was assumed to be wholly due to basal sediment deformation, which is not a factor in Eq. 7.11. The basal shear stress is a complicated parameter, dependent on many factors that are unknown during the last glaciation. It is not the goal of this study to determine what combination of climatic, geological and geophysical processes were involved in changing the basal shear stress through time.

Fisher et al. (1985) produced a map of basal shear stress based on surficial geology. They used values of 5-15 kPa for regions that are dominantly Phanerozoic sedimentary rocks, and higher values (54-81 kPa) for regions that are dominantly

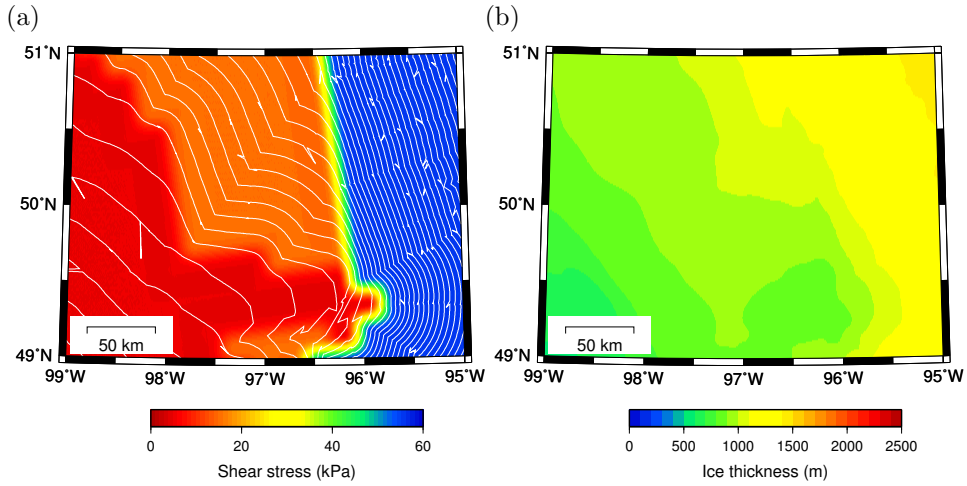

Figure 7.5: Modelled flow at the interface between Phanerozoic sedimentary rocks (where there are deformable beds), and Precambrian shield (which is likely to have a stronger base) in southeastern Manitoba. (a) The modelled ice elevation contours (at a 20 m interval) overlying basal shear stress values. The ice flow direction changes in a counter-clockwise direction when ice flows from a region with high to low basal shear stress. The ice surface topography is also much steeper in hard bedded regions. Note that these are raw contours and include flagged points (b) Modelled ice thickness.

crystalline rocks and mountainous regions. They justified the choice of low stress conditions over sedimentary basins on the ability of loose sediments to deform in those regions. The initial shear stress model used in this chapter is based on the values they used (Fig. 7.6). Boundaries for shear stress domains are based on the bedrock geology map of North America (Reed et al., 2004), along with topographic considerations. Though the map by Fisher et al. (1985) was used as a guide for producing the initial shear stress model, an additional domain of intermediate shear stress was included for Proterozoic sedimentary basins, which may also have deformable sediments (*e.g.* Aylsworth and Shilts, 1989a; Larson and Schaetzl, 2001).

The basal shear stress can be estimated directly from rare topographic highs near the margin of the ice sheet. If a topographic high was not overridden, it can be assumed that the average shear stress between the nunatak and the margin was not sufficiently high to allow ice to get thick enough to flow over the top. Likewise,

if a topographic high was covered in ice, then the minimum shear stress value for that region can be calculated using Eq. 7.2. The Cypress Hills, located in southern Saskatchewan and Alberta, remained ice free during the late Wisconsin, and rise about 430 m above the surrounding area (Kulig, 1996). The Cypress Hills are located approximately 150 km from the closest maximal extent of Laurentide Ice Sheet. From Eq. 7.2, the maximum shear stress for the ice sheet to remain below this elevation is 5.5 kPa. The Melville Hills, located in northern Northwest Territories were considered to be ice free in the late Wisconsin by Dyke (2004). Field studies indicate that ice did reach elevations greater than the summit of the region (876 m), though it is uncertain if it happened during the late Wisconsin (Veillette, 2004). Assuming that the ice sheet terminated at the shelf edge about 400 km to the northwest (*i.e.* Batchelor et al., 2013), the minimum average shear stress required for ice to reach the summit of the Melville Hills is 8.7 kPa. The initial model of shear stress (Fig. 7.6) conforms to both of these estimates.

Another place where basal shear stress can be estimated is where the Laurentide Ice Sheet penetrated into the Cordillera. In northern British Columbia, the ice sheet penetrated at least 17 km into the Rocky Mountains, and reached a thickness of 600 m at the mountain front (Bednarski and Smith, 2007). Using these values, the maximum basal shear stress for this region is 95.5 kPa. Duk-Rodkin and Hughes (1991) determined the highest elevation the Laurentide ice sheet reached in the Mackenzie Mountains in the Yukon and Northwest Territories. The difference in maximum elevation of Canadian Shield lithology erratics was 280-320 m over a 125 km distance between Katherine Creek and Dark Rock Creek. Assuming the source of ice at these locations was from the same ice sheet divide, this slope indicates a minimum basal shear stress of 2.8-3.7 kPa. Beget (1987) calculated basal shear stress values based on the maximum elevation the Laurentide ice sheet reached along the Richardson and British Mountains in northern Yukon and Northwest Territories.

When the ice sheet was at its maximum extent, reaching the edge of the shelf, basal shear stress values were between 1 and 30 kPa, with an average value of 19 kPa. These values serve as an upper limit to the potential shear stress for the northwestern Laurentide ice sheet over deformable sediments, as the average shear stress value when the ice sheet was less extensive was 7 kPa.

Another way to assess basal shear stress is by determining the relative velocity of the ice. For areas where there is low basal shear stress, the velocity of ice can be rapid (Cuffey and Paterson, 2010). Marshall et al. (1996) found that shear stress values would be low in the western Canadian plains and on continental shelves, based on topographic and geological considerations. Evidence of fast flow is evident from landforms in southern Alberta and Saskatchewan (Evans et al., 2008; Ò Cofaigh et al., 2010). At the maximum extent of the ice sheet, the ice was thick enough to flow independent of topographic relief, and ice streams up to 700 km in length may have existed (Ò Cofaigh et al., 2010). Rapid fluctuations of the southwestern margin of the Laurentide ice sheet indicate that subglacial sediments were weak and easily deformed (Clark, 1994). Recent numerical models of the Laurentide Ice Sheet indicate ice sheet velocity in areas underlain by sediments and Phanerozoic sedimentary rocks that were typically high relative to the interior that is underlain by crystalline Precambrian rock (Stokes and Tarasov, 2010; Stokes et al., 2012; Tarasov et al., 2012). Fast flowing ice may have existed in the late stages of deglaciation in the Keewatin sector of the ice sheet, which is speculated to have been caused when the ice margin was in contact with a proglacial lake, with the probable secondary influence of the Proterozoic Thelon sedimentary basin (Stokes and Clark, 2003a,b). This shows that, even though an area may have exhibited hard-bedded conditions for the majority of the history of the ice sheet, the dynamics during retreat may have differed significantly during deglaciation. Changes in hydrology likely played a role, but the effects of hydrology at the base of an ice sheet are not well determined

even in modern ice sheets (*e.g.* Gladstone et al., 2014). Therefore, there has been no attempt to determine the exact cause of basal shear stress variability.

The basal shear stress is the main variable used to adjust ice sheet thickness in the modelling software. The shear stress models used in this chapter are all based on the model in Fig. 7.6. The initial model used to test the program features low shear stress values where soft-bedded conditions are expected to exist, and higher values in areas with crystalline bedrock and mountains. Two other models are also used in the tests, with all shear stress values increased by 10 and 20 kPa, respectively. Increasing the shear stress will increase the slope and thickness of the ice sheet in all areas. Fig. 7.7 shows the calculated ice thickness using these three basal shear stress models at the Last Glacial Maximum. This test is not intended to be diagnositic of the actual ice sheet geometry, but rather to demostrate what happens when the shear stress is changed. The margin corresponds to the LGM margin from Dyke (2004). In northern Alberta, the ice thickness in the initial shear stress model exhibits clear dependence on basal topography. As the shear stress is increased, there is less dependence on basal topography. The location of ice flow centres is close to the same in all models, though the thickness is over 1000 m greater with the highest shear stress model compared to the initial model. Fig. 7.8 shows the ice sheet elevation relative to modern sea level.

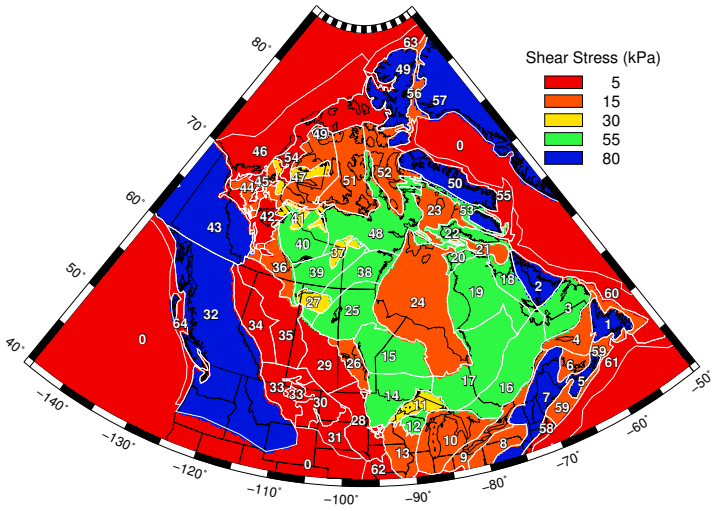

Figure 7.6: Initial shear stress model, based on the values by Fisher et al. (1985) and the surficial bedrock geology of North America (Reed et al., 2004). Parameters are set as follows: 5 kPa – Mesozoic and Cenozoic rocks and sediments; 15 kPa – Paleozoic sedimentary rocks (primarily composed of carbonates (*e.g.* Dineley, 1971; Howell and van der Pluijm, 1999; Kent, 1994; Nelson and Johnson, 1966)); 30 kPa – Proterozoic sedimentary rocks; 55 kPa – Precambrian crystalline rocks; 80 kPa – mountainous regions and Greenland. Domains are divided as follows: 1 - Newfoundland (mountainous); 2 - Torngat Mountains (mountainous); 3 - Southern Labrador (Precambrian); 4 - Strait of Belle Isle / Ile d'Anticosti (Paleozoic); 5 - Nova Scotia (mountainous); 6 - Prince Edward Island and region (Paleozoic); 7 -Appalacian Mountains (mountainous); 8 - South of Lakes Erie and Ontario (Paleozoic); 9 - St. Laurence Valley and Lakes Erie and Ontario (Paleozoic); 10 - Michigan Basin (Paleozoic); 11 - Lake Superior (Proterozoic); 12 - Proterozoic volcanic rocks south of Lake Superior (Precambrian); 13 - Paleozoic rocks south of Lake Superior (Paleozoic); 14 - Superior Province south of the English River subprovince and west of the northern extent of Lake Superior (Precambrian); 15 - northwestern Superior Province (Precambrian); 16 - Grenville Province (Precambrian); 17 - Superior Province southeast of Hudson Bay (Precambrian); 18 - Ungava Bay (Precambrian); 20 - Northern Quebec (Precambrian); 21 - Hudson Strait (Paleozoic); 23 - Foxe Basin (Paleozoic); 24 - Hudson Bay (Paleozoic); 25 - Trans-Hudson Orogen west of Hudson Bay (Precambrian); 26 - Paleozoic rocks in Manitoba; 27 - Athabasca Basin (Proterozoic); 28 - Willison Basin (Mesozoic); 29 - eastern Western Canadian Sedimentary Basin (Mesozoic); 30 - Cenozoic rocks in Montana and North Dakota; 31 - Cretaceous rocks in the Dakotas (Mesozoic); 32 - Cordillera south of 60°N (mountainous); 33 - Cretaceous rocks in southern Alberta, Saskatchewan and Montana; 34 - Cretaceous and Cenozoic Rocks west of the Cordillera; 35 - Cretaceous rocks in Alberta and Saskatchewan; 36 - Paleozoic rocks near Great Slave Lake; 37 - Thelon Basin (Paleozoic); 38 - Hearne Province (Precambrian); 39 - Rae Province (Precambrian); 40 - Slave Craton (Precambrian); 41 - Proterozoic cover over the Slave Craton; 42 - Cretaceous rocks in the Northwest Territories; 43 - Cordillera north of 60°N (mountainous); 44 - Paleozoic rocks in the Mackenzie Lowlands; 45 - Cretaceous rocks in the Mackenzie Lowlands; 46 - Cenozoic sediments offshore of the western Canadian Arctic; 47 - Proterozoic rocks on the Melville Hills and Victoria Island; 48 - northern Rae Province (Precambrian); 49 - Arctic Cordillera (mountainous); 50 - Baffin Mountains (mountainous); 51 - Paleozoic rocks in Arctic Canada; 52 - Gulf of Boothia (Paleozoic); 53 - southern Baffin Island (Precambrian); 54 - northwestern Arctic archipelago (Mesozoic/Cenozoic); 55 - Offshore of Baffin and Devon Islands (Cenozoic); 56 - strait between Ellesmere Island and Greenland (Paleozoic); 57 - Greenland; 58 - Eastern Seaboard of the United States (Cenozoic); 59 - shelf of Atlantic Canada (Paleozoic); 60 - shelf region north of Newfoundland (Mesozoic and Cenozoic); 61 - shelf region south of Newfoundland (Mesozoic and Cenozoic); 62 - midwestern United States (Mesozoic); 63 - shelf north of Ellesmere Island (Cenozoic); 64 - Pacific shelf (Cenozoic); 0 - all other regions (nominally set to 5 kPa).

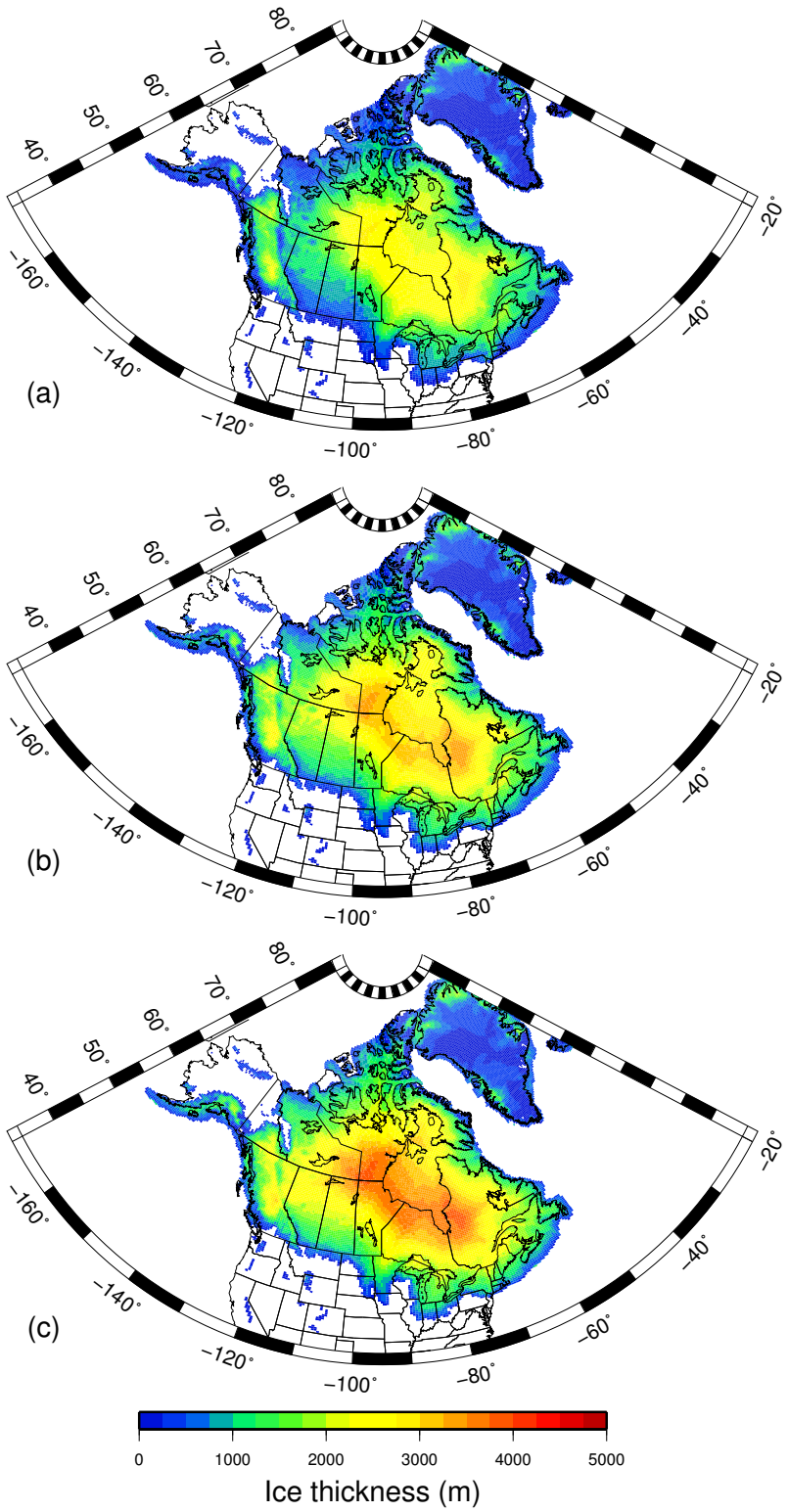

Figure 7.7: Thickness of ice sheet models of the Last Glacial Maximum configuration of the North American ice sheet complex at 18 ^{14}C kyr BP (about 21 500 cal yr BP, Dyke, 2004) relative to present, using different basal shear stress models. No correction for isostatic loading has been made to elevation. Ice thickness is relative to present day values. (a) Using the initial shear stress model (Fig 7.6). (b) Adding 10 kPa to the initial model. (c) Adding 20 kPa to the initial model.

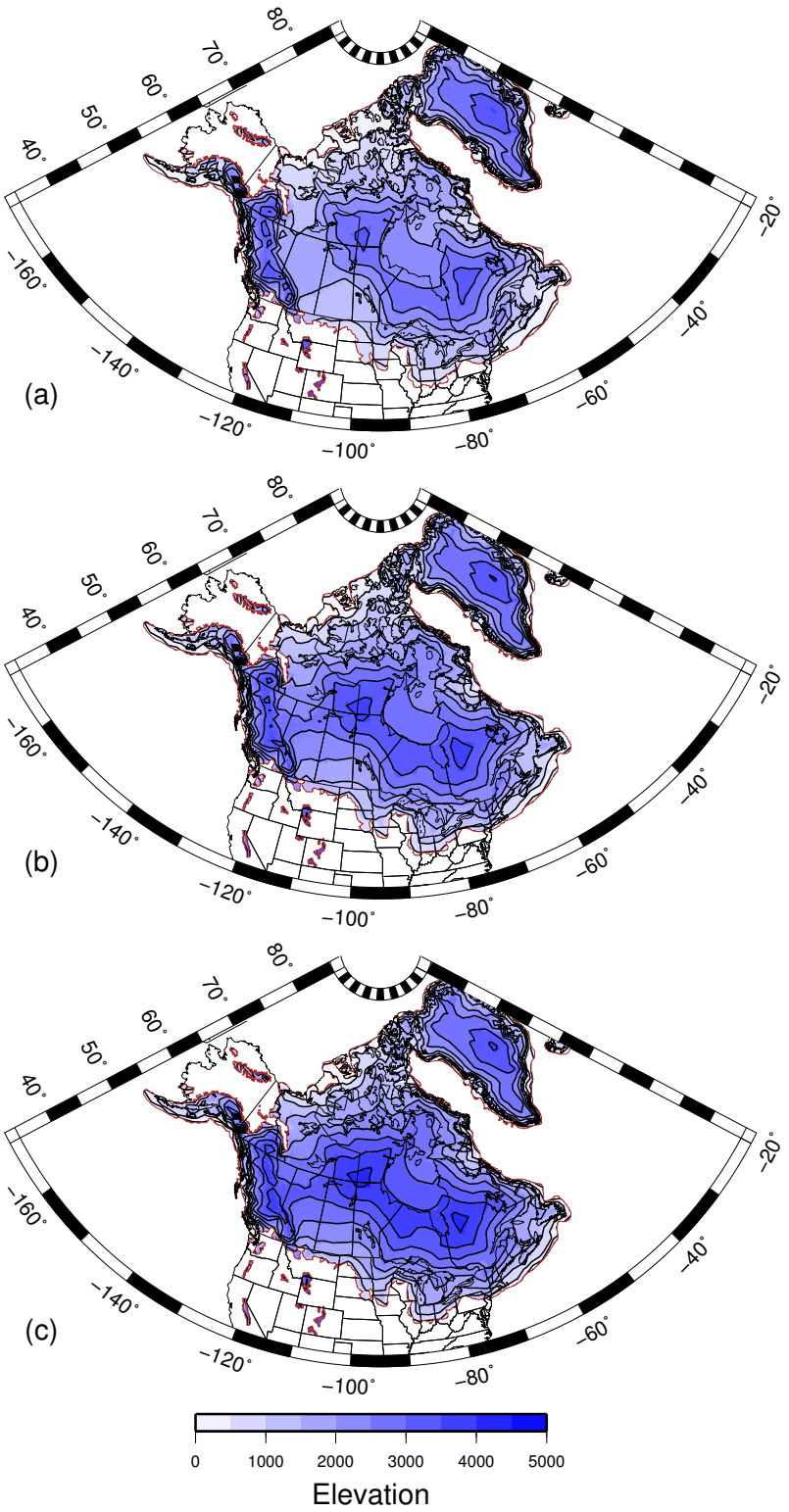

Figure 7.8: Elevation of ice sheet models of the Last Glacial Maximum configuration of the North American ice sheet complex at 18 ^{14}C kyr BP (about 21 500 cal yr BP, Dyke, 2004), using different basal shear stress models. No correction for isostatic loading has been made to the topography, so elevation is relative to modern sea level. (a) Using the initial shear stress model (fig 7.6). (b) Adding 10 kPa to the initial model. (c) Adding 20 kPa to the initial model.

7.5 Resolution test

Two input parameters that may be varied in the software are the elevation contour interval and spacing along the contour from which the flowline calculation is initiated. The shear stress model is on a 20 km grid, while the elevation grid is 5 km. In order to capture the resolution of all topographic changes, it would be necessary to have flowlines calculated less than 5 km apart. Since much of the area occupied by the Laurentide ice sheet has low relief, it may not be necessary to have such high resolution. There are several computationally intensive checks required in the program (section 7.3), so it is desirable to have maximal spacing to decrease execution time. The tests

Table 7.1 shows the results of resolution tests, which involve creating models of the Laurentide ice sheet at the LGM extent. The ice sheet models are averaged onto a 0.5° longitude by 0.25° latitude grid (0.25° corresponds to about 28 km, while the longitude will vary in length depending on latitude) to compare the volume between different ice models. The models use the 18 000 ^{14}C yr BP margin by Dyke (2004) with modern topography and the shear stress model shown in Fig. 7.6. Computations were done on the Terrawulf II beowulf cluster (Sambridge et al., 2009), which has 2.8 GHz processors. The software uses a serial processing approach (/emphi.e. each model was computed with a single processor), with the largest bottleneck being the checking of crossovers of the ice flowlines and elevation contours. The run time refers to the amount of CPU time required to complete the calculation of a single timestep of the ice sheet model. Model comparisons are relative to the highest resolution model (2 km spacing, 10 m contour interval). There are a total of 26 335 grid elements in the final ice sheet models. The percentage of ice thickness elements more than 100 m different from the reference model are displayed in Table 7.1. Unsurprisingly, the 2, 3, 4 and 5 km spacing models give similar results, as they all capture the resolution of the topographic grid. Contour intervals greater

than 20 m produce results that deviate from the reference model, even with small spacing values. This is because in the regions with low basal shear stress, the low ice sheet gradient produces contours that are too far apart to be able to adapt to sudden changes in basal topography. The time it took to calculate the model is strongly dependent on spacing, and shows only a weak relation to contour interval. As a result of these tests, a spacing value of 5 km and contour interval of 20 m is deemed to produce the best balance between matching the reference model and minimising run time. In this test, less than 1% of the elements are different from the reference model, and the run time is nearly 2.5 hours less than the reference.

Table 7.1: Results of the resolution test

Contour interval (m)	Maximum spacing (km)	Percent of elements >100 m	Run time (H:MM:SS)
10	2	–	2:54:43
10	3	0.02	1:30:52
10	4	0.03	0:59:14
10	5	0.19	0:43:23
10	7	1.62	0:27:30
10	10	5.51	0:17:24
10	15	10.55	0:10:38
10	20	14.36	0:07:39
20	2	0.68	1:50:58
20	3	0.19	0:56:49
20	4	0.20	0:37:14
20	5	0.66	0:27:28
20	7	2.35	0:17:52
20	10	6.85	0:11:27
20	15	11.70	0:07:04
20	20	16.20	0:05:09
30	2	3.11	1:31:09
30	3	2.72	0:46:34
30	4	2.63	0:30:12
30	5	2.85	0:22:18
30	7	5.53	0:14:29
30	10	9.64	0:09:30

Table 7.1 - continued

Contour interval (m)	Maximum spacing (km)	Percent of elements >100 m	Run time (H:MM:SS)
30	15	15.30	0:06:00
30	20	20.03	0:04:23
40	2	7.33	1:25:21
40	3	5.41	0:42:16
40	4	6.20	0:27:37
40	5	7.19	0:20:30
40	7	11.03	0:24:34
40	10	13.52	0:16:21
40	15	20.13	0:11:06
40	20	25.46	0:07:54
50	2	12.42	2:13:03
50	3	12.90	1:10:31
50	4	9.99	0:45:26
50	5	12.22	0:37:04
50	7	14.25	0:23:24
50	10	18.58	0:15:52
50	15	26.04	0:10:41
50	20	32.34	0:08:10
100	2	45.01	2:40:47
100	3	45.29	1:19:06
100	4	45.04	0:54:26
100	5	44.88	0:41:32
100	7	45.00	0:26:46
100	10	46.12	0:18:45
100	15	48.06	0:12:35
100	20	50.28	0:08:49

7.6 Dependence on Earth model

The calculation of an ice sheet model requires several iterations to account for the deformation of the Earth caused by the ice sheet, which, in turn, also depends on the rheological properties of the Earth. According to Reeh (1982), a basal trough will cause flowlines to diverge, and thus have a shallower gradient than a flat surface. In areas where the ice sheet causes significant depression, such as in the centre of the Laurentide Ice sheet, there will be a trade-off between the additional volume of ice the depression can accommodate and reduced ice gradient. It is expected that, after several iterations, the ice thickness and the depression caused by the ice sheet will reach equilibrium. The goal of this section is only to see how many iterations are required to produce a balance between Earth deformation and the change in distribution of ice. There is no attempt to relate this to how the Earth response affects the dynamics and stability of the ice sheet, which would require a full dynamic ice sheet modelling technique to assess (*i.e.* Gomez et al., 2010).

To test this, ice sheet models were produced using a variety of three layer, spherical symmetric Earth models. The models included an elastic lithosphere, and viscoelastic upper and lower mantle. Table 7.2 lists the Earth model parameters used in this test. The theoretical framework for calculating Earth deformation can be found in Nakada and Lambeck (1987) and Lambeck et al. (2003). A simple ice sheet model that extends to the beginning of the penultimate glaciation was developed for this test. A more complete description of the pre-Last Glacial Maximum margin reconstructions is described in Chapter 2, but is largely based on the flow patterns described by Kleman et al. (2010) and chronological data summarised by Dyke et al. (2002) and Dyke (2004). Post-Last Glacial Maximum margins for this test are from Dyke (2004). For ease of comparison, a simplistic estimation of ice volume equivalent sea level is done using modern ocean area ($V_i \times 0.9$ kg m^3/(361×10^6 km^2), Licciardi et al., 1998).

Figs. 7.9-7.11 show the results of three iterations of ice sheet calculation at 20 000 cal yr BP (the 17 000 ^{14}C yr BP margin of Dyke, 2004) using the shear stress models described in Section 7.4. In all cases, there is a significant increase in ice volume after the first iteration. Little to no changes in ice volume happen in the third iteration. The results show that the ice sheet volume attained in modelling has a small dependence on mantle viscosity, especially lower mantle viscosity. In general, models with a thin lithosphere and low mantle viscosity produce the largest volume, while models with a thick lithosphere and high mantle viscosity produce the smallest volume. In all cases, the Earth model ehfq produced the smallest ice volumes, while models eb5F and ebAF produced the largest volumes. The absolute difference in volume between the models with the smallest and largest volumes are 0.27×10^6 km^3 for the initial shear stress model, 0.38×10^6 km^3 when increased by 10 kPa, and 0.48×10^6 km^3 when increased by 20 kPa, corresponding to equivalent sea level heights of 0.67 m, 0.95 m, and 1.20 m, respectively.

Figs. 7.12-7.14 show the results of the same analysis at 10 000 cal yr BP (the 9 ^{14}C kyr margin of Dyke, 2004). In this margin configuration, Laurentide ice is restricted to the Canadian Shield, Hudson Bay and Baffin Island. The convergence to equilibrium at this time is often achieved in as little as one iteration. There is a dependence on upper mantle viscosity, though not necessarily in a predictable way, as the models with a viscosity of 3.16×10^{20} Pa s have the lowest volume. The difference between the smallest and largest volume in all cases is less than 0.25×10^6 km^3, or about 0.6 m of equivalent sea level.

Figs. 7.15 shows the change in ice thickness between successive calculations at 20 000 cal yr BP, using an intermediate Earth model, eefk (90 km thick lithosphere, 3.16×10^{20} Pa s upper mantle viscosity, 10^{22} Pa s lower mantle viscosity) and the initial shear stress model. The difference is most stark between the model with modern topography and one iteration of deformed topography. The changes after

two and three iterations are more subtle. In general, the ice increases over much of the ice sheet, though some areas closest to the centre of the ice sheet have less ice. Fig. 7.16 shows the same progression at 10 000 cal yr BP. As with 20,000 cal yr BP model, there is a noticeable difference between the model with modern topography and the first iteration of deformation, and diminished changes after two and three iterations.

Although the ice volume of the models shown in Figs. 7.9-7.11 are similar regardless of the choice of Earth model, the distribution of ice may differ (Fig. 7.17). Ice sheet models calculated using the extreme values found in Fig. 7.9 are compared against each other to show this. Models produced using eefk and ehfq are similar, despite having different lower mantle viscosity and lithospheric thickness. The ice model produced using ebAF differs significantly from the other two models, with less ice in the central area of the ice sheet where there is a longer duration of ice cover, and more ice where cover is for less time. Fig. 7.17 shows the differences at 10 000 cal yr BP. The ice model produced using ebAF shows the most significant difference in the distribution of ice volume, though the absolute difference is never more than 100 m.

The absolute difference of ice element differences and ice volume differences are illustrated on Figs. 7.19-7.21. The ice models produced using the reference Earth model are compared with models created using a 90 km thick lithosphere and different upper and lower mantle viscosity values. Though the ice volume in the models does depend on the Earth model parameters, the difference is generally less than 1%.

The results of these tests show that it is worth calculating at least one iteration of Earth deformation to determine optimal ice sheet models. At an ice sheet configuration close to the Last Glacial Maximum limit, there is a significant increase in ice volume after the first iteration, and a slight increase after two iterations, regardless

of the Earth model used. Though ice volumes are similar regardless of the choice of Earth model, the distribution of ice is different between weak and strong mantle models. This difference is not considered significant enough to justify the additional time required to produce ice models for each Earth model. In the analysis done in this study, ice models are produced using an Earth model with a lithosphere thickness of 120 km, an upper mantle with a viscosity of 4×10^{20} Pa s and lower mantle with a viscosity of 10^{22} Pa s. The reason for the choice of this Earth model is explained further in Chapter 8.

Table 7.2: Earth model parameters. Format is e(L)(UM)(LM).

Lithosphere		Upper Mantle		Lower Mantle	
code	thickness (km)	code	viscosity (Pa s)	code	viscosity (Pa s)
b	60	5	3.16×10^{19}	F	3.16×10^{21}
e	90	a	10^{20}	k	10^{22}
h	120	f	3.16×10^{20}	q	3.16×10^{22}
		A	10^{21}		

7.7 Dependence on temporal resolution of the ice model

The final test displays the effect of model resolution. The program that calculates sea level linearly interpolates the ice thickness between time steps, so if an ice model with a finer time resolution is used, it could affect the calculation of ice volumes. Fig. 7.22 shows an example of the ice volumes calculated using ice models with course and fine temporal resolution. Although the ice volumes at intermediate time steps in the fine resolution model deviate from a linear interpolation of the time steps of the coarse resolution model, the resolution does not have a great impact on the calculated ice volume where the time steps match in both models. This shows that the difference in Earth deformation between the coarse and fine models at 1000

year intervals is not significant enough to produce a different ice surface profile.

7.8 Summary

This chapter contained an overview of the method used to model the Laurentide ice sheet. The variables for determining the model include basal shear stress, basal topography and margin location. The software is able to calculate ice flowlines around areas of steep topography, and determine the change in flow direction and surface gradient when there are changes in basal conditions. Tests were done to evaluate the optimal parameters required to minimise the duration of computation and still capture changes in basal topography and shear stress. A contour interval of 20 m and a flowline spacing of 5 km was deemed to provide the best balance between capturing basal features and computation time. There were two tests on the impact of glacial-isostatic adjustment on the calculated ice volume. Ice distribution was not strongly dependent on the choice of Earth model, but it is necessary to calculate at least one iteration of deformation to capture the true thickness of the ice sheet. For the calculation of my models, two iterations are done to ensure that the model is in equilibrium with adjusted topography.

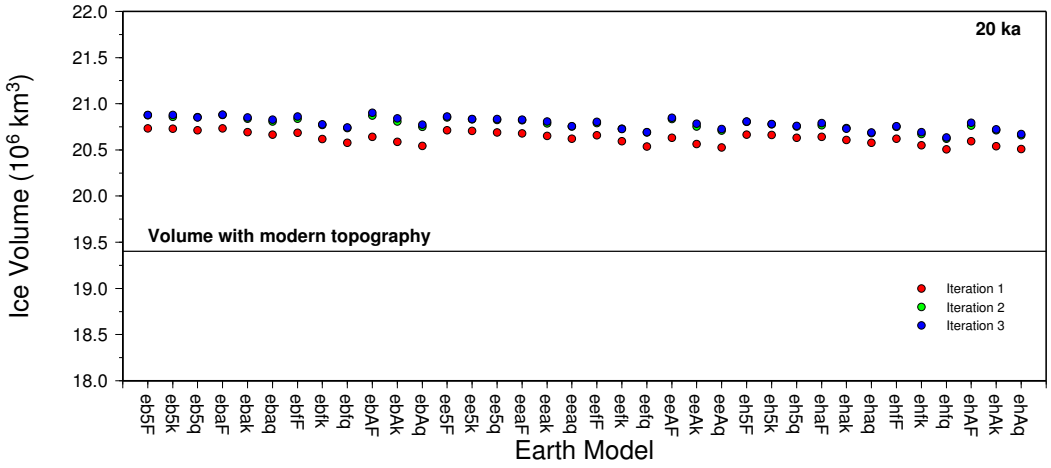

Figure 7.9: Ice volume at 20 000 cal yr BP using using the initial shear stress model (Fig. 7.6) and a variety of Earth models.

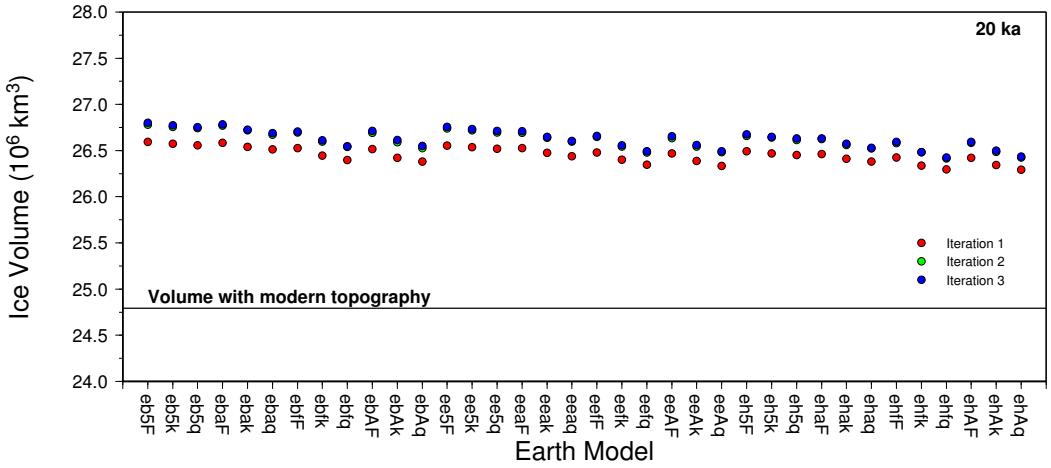

Figure 7.10: Ice volume at 20 000 cal yr BP using using the initial shear stress model (Fig. 7.6) with all values increased by 10 kPa and a variety of Earth models.

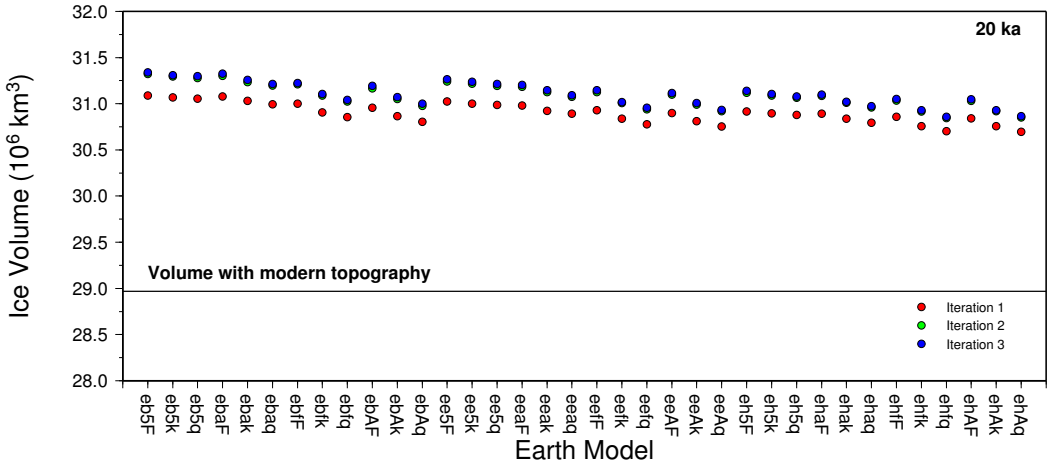

Figure 7.11: Ice volume at 20 000 cal yr BP using using the initial shear stress model (Fig. 7.6) with all values increased by 20 kPa and a variety of Earth models.

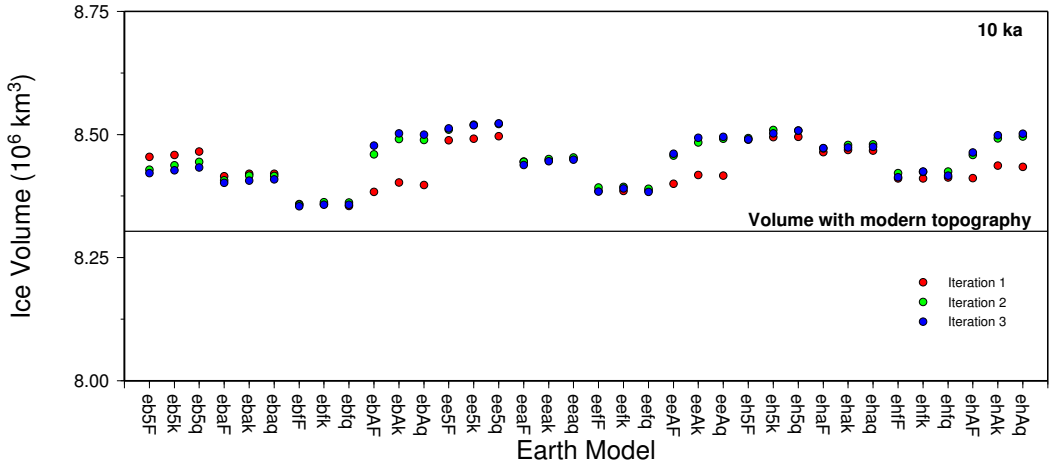

Figure 7.12: Ice volume at 20 000 cal yr BP using using the initial shear stress model (Fig. 7.6) and a variety of Earth models.

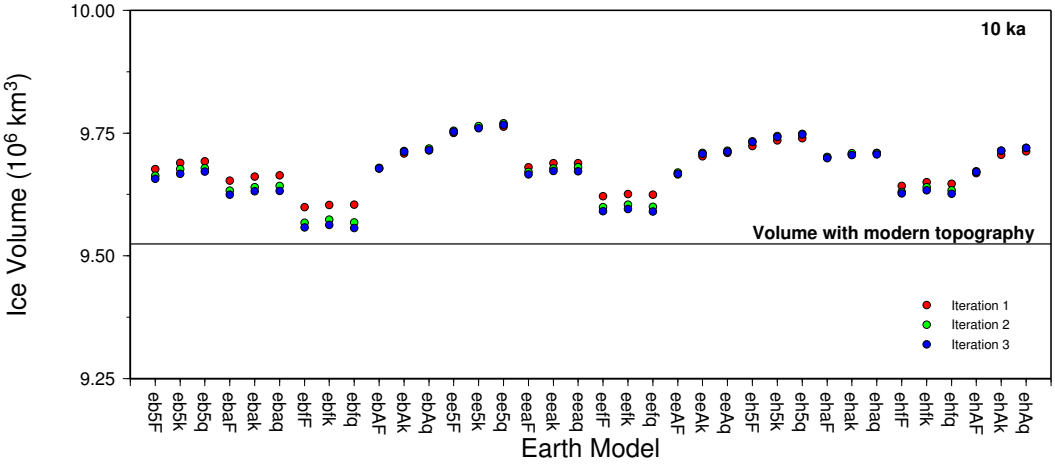

Figure 7.13: Ice volume at 10 000 cal yr BP using using the initial shear stress model (Fig. 7.6) with all values increased by 10 kPa and a variety of Earth models.

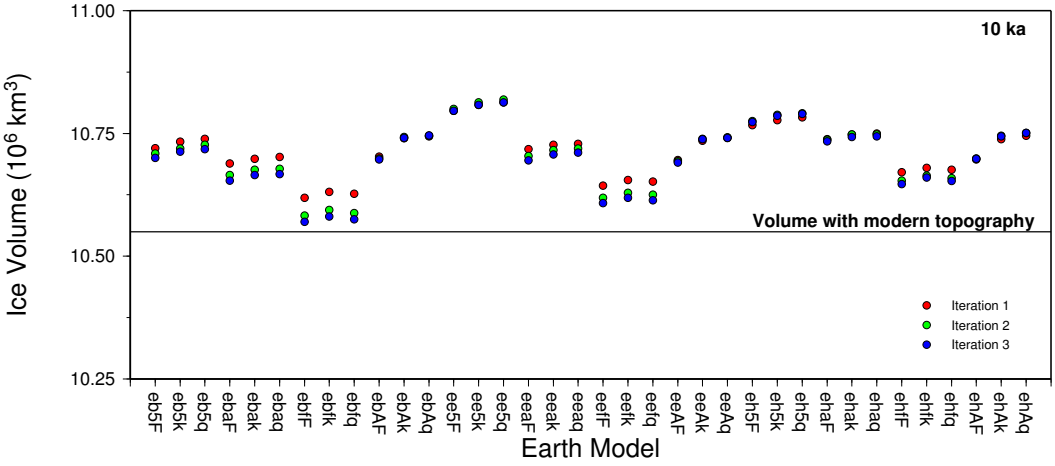

Figure 7.14: Ice volume at 10 000 cal yr BP using using the initial shear stress model (Fig. 7.6) with all values increased by 20 kPa and a variety of Earth models.

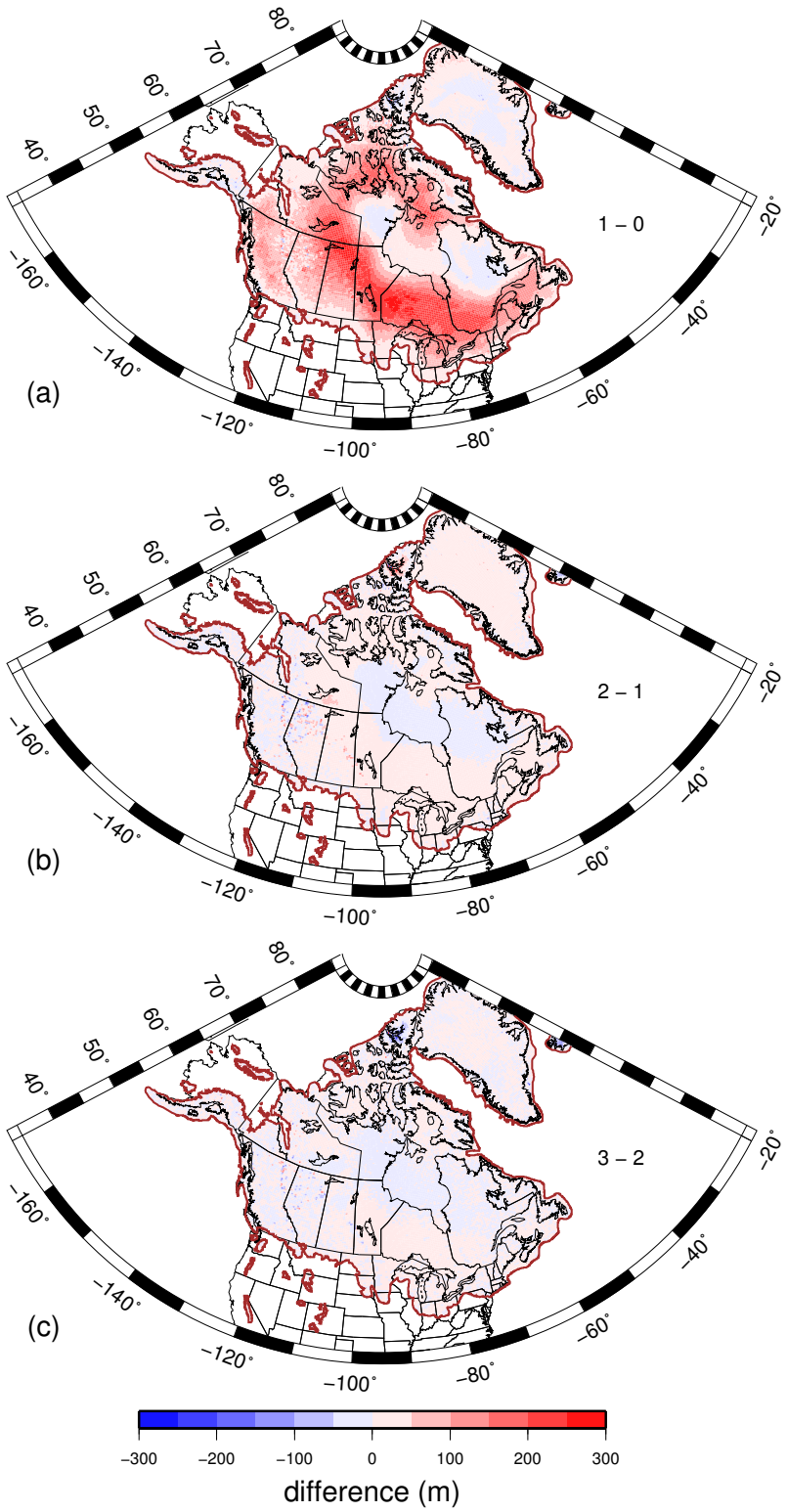

Figure 7.15: Difference between successive iterations of ice sheet model calculation at 20 000 cal yr BP, using Earth model "eefk" to calculate deformation and the initial shear stress model. (a) Difference between the model calculated with modern topography and one iteration of Earth deformation. (b) Difference between one iteration and two iterations. (b) Difference between 3 iterations and 2 iterations.

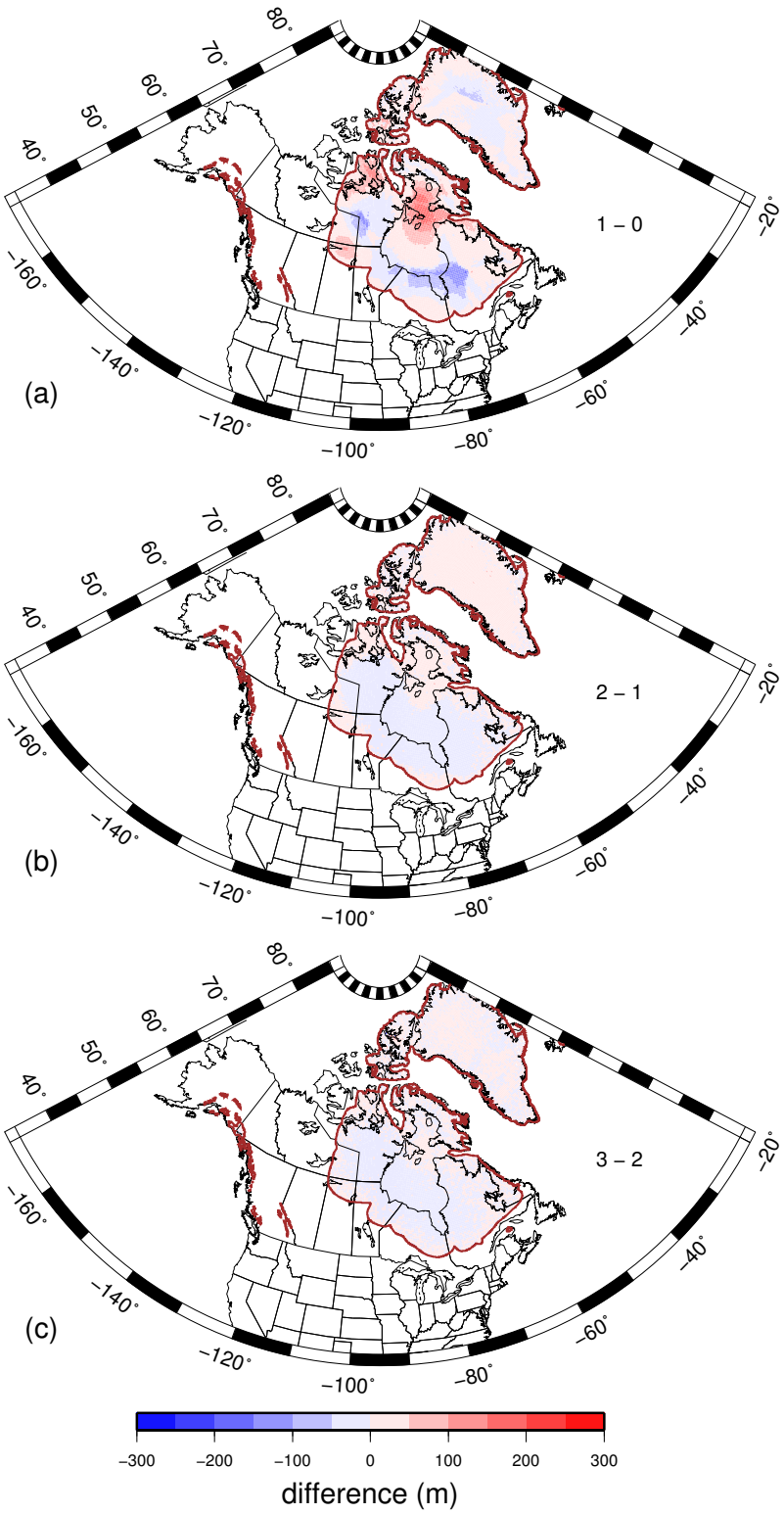

Figure 7.16: Difference between successive iterations of ice sheet model calculation at 10 000 cal yr BP, using Earth model "eefk" to calculate deformation and the initial shear stress model. (a) Difference between the model calculated with modern topography and one iteration of Earth deformation. (b) Difference between one iteration and two iterations. (b) Difference between 3 iterations and 2 iterations.

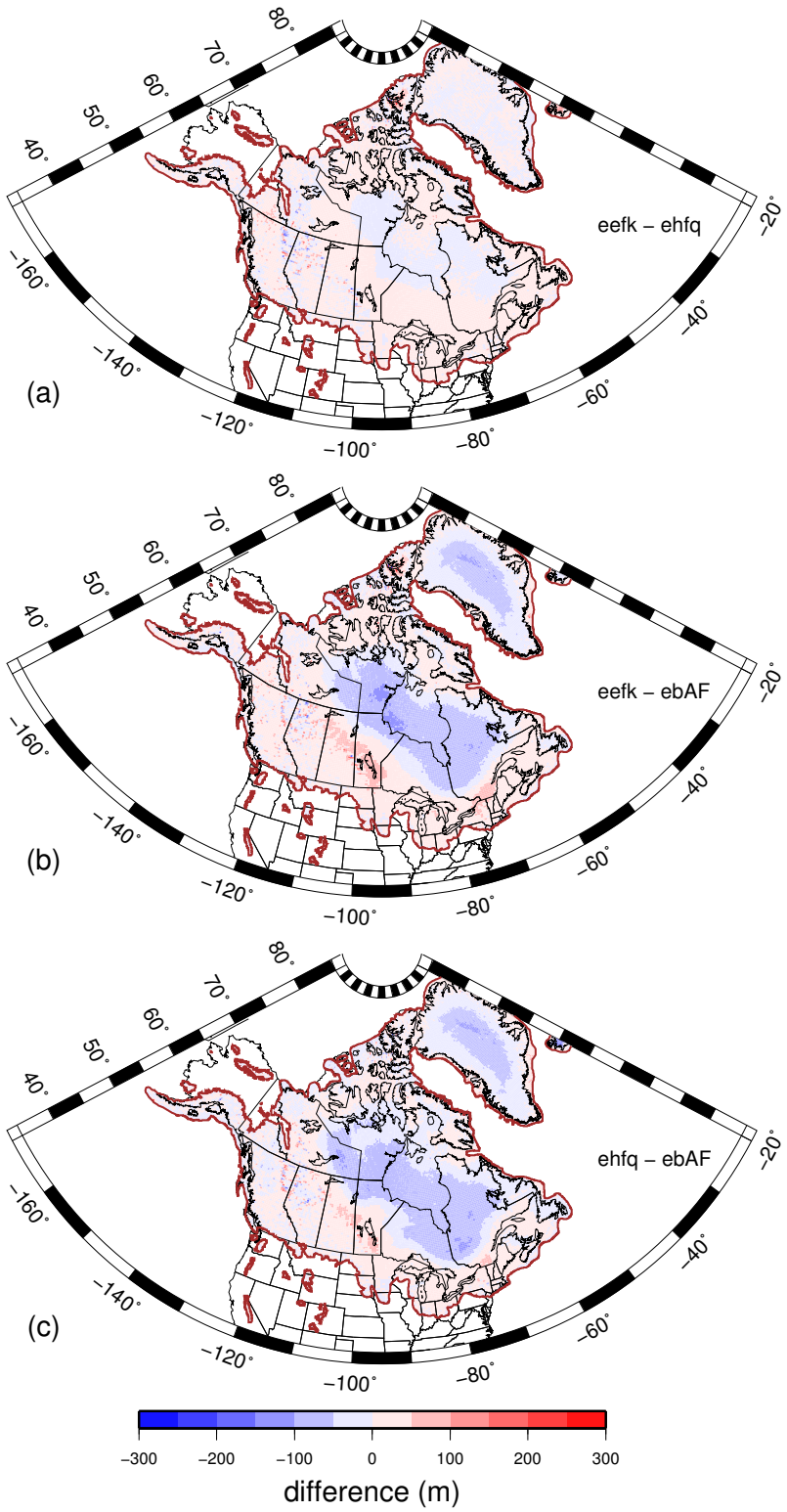

Figure 7.17: Difference ice sheet model volume at 20 000 cal yr BP after two iterations of deformation, using different Earth models and the initial shear stress model. (a) Difference between "eefk" and "ehfq". (b) Difference between "eefk" and "ebAf". (b) Difference between "ehfq" and "ebAf". See Table 7.2 for an explanation of the Earth models.

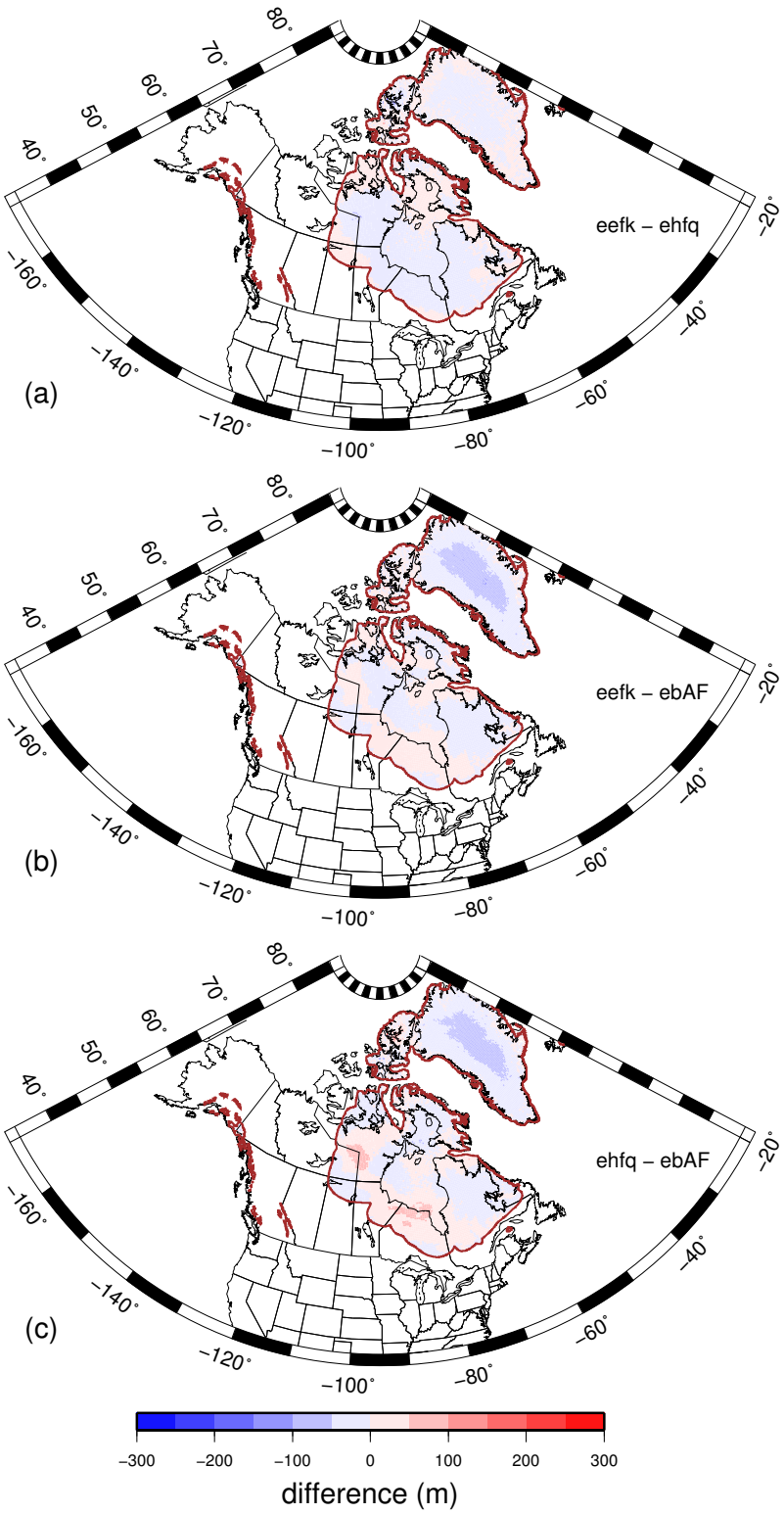

Figure 7.18: Difference ice sheet model volume at 10 000 cal yr BP after two iterations of deformation, using different Earth models and the initial shear stress model. (a) Difference between "eefk" and "ehfq". (b) Difference between "eefk" and "ebAf". (b) Difference between "ehfq" and "ebAf". See Table 7.2 for an explanation of the Earth models.

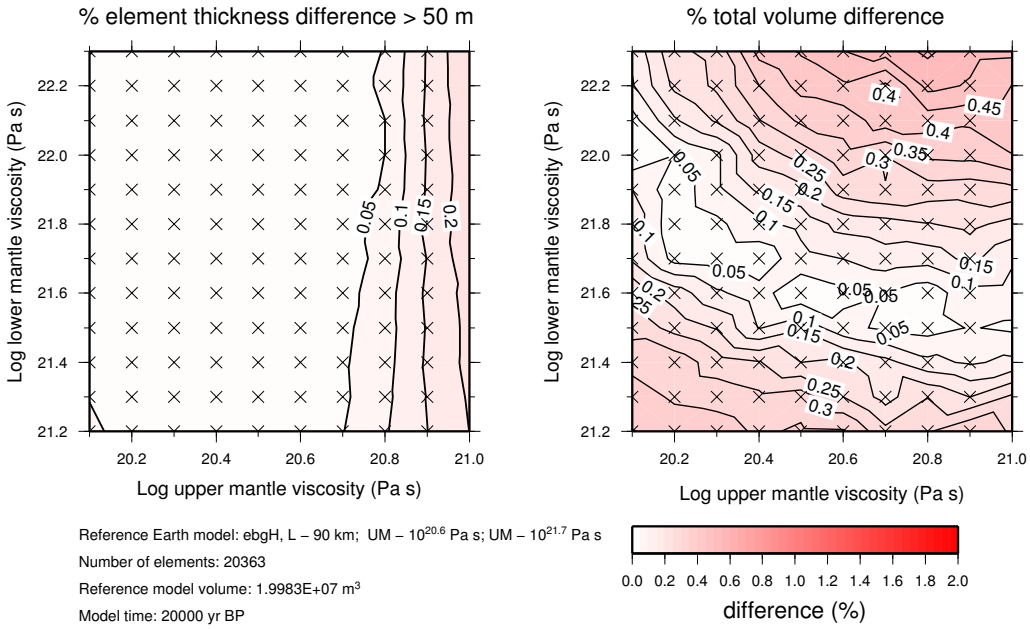

Figure 7.19: Difference in ice thickness between ice models at 20 000 cal yr BP produced using a reference Earth model with a 60 km thick lithosphere, upper mantle with a viscosity of 4×10^{20} Pa s and lower mantle with a viscosity of 5×10^{21} Pa s and models with a 90 km thick lithosphere and variable mantle viscosity.

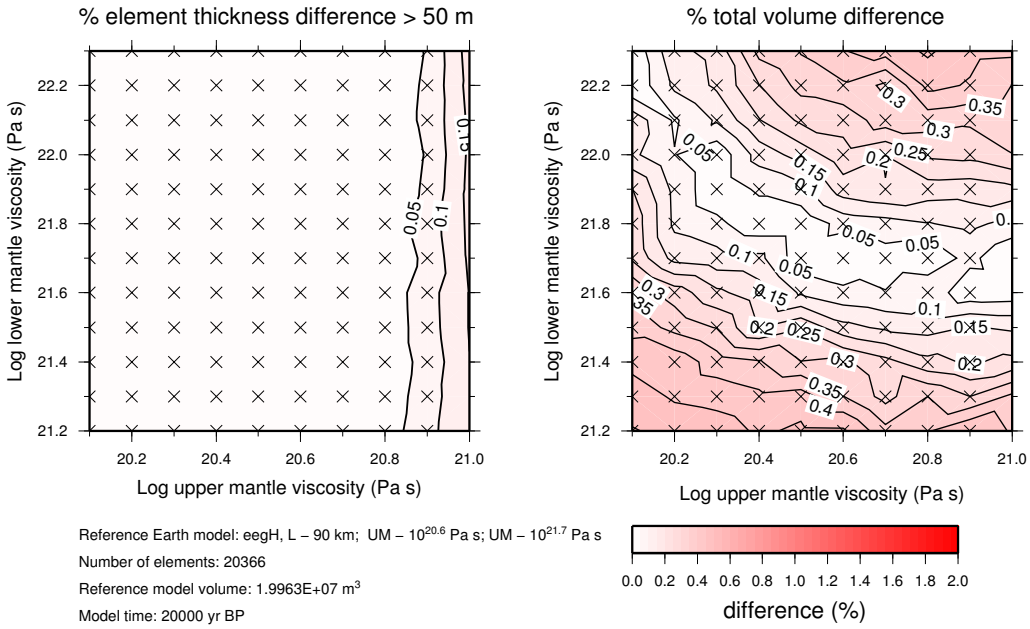

Figure 7.20: Difference in ice thickness between ice models at 20 000 cal yr BP produced using a reference Earth model with a 90 km thick lithosphere, upper mantle with a viscosity of 4×10^{20} Pa s and lower mantle with a viscosity of 5×10^{21} Pa s and models with a 90 km thick lithosphere and variable mantle viscosity. Model comparison is done at 20 000 cal yr BP.

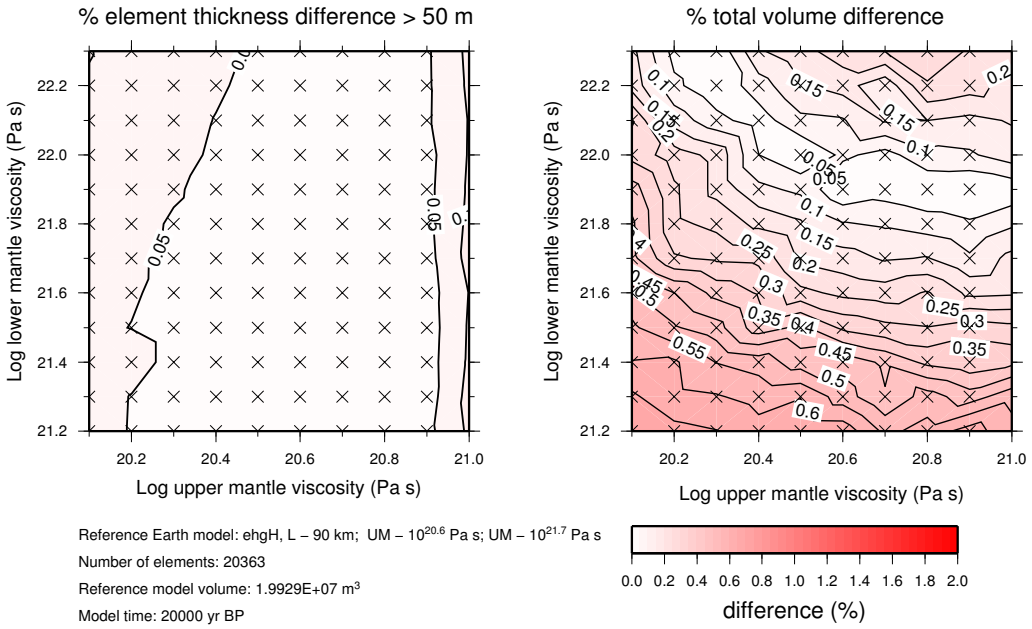

Figure 7.21: Difference between ice models at 20 000 cal yr BP produced using a reference Earth model with a 120 km thick lithosphere, upper mantle with a viscosity of 4×10^{20} Pa s and lower mantle with a viscosity of 5×10^{21} Pa s and models with a 90 km thick lithosphere and variable mantle viscosity.

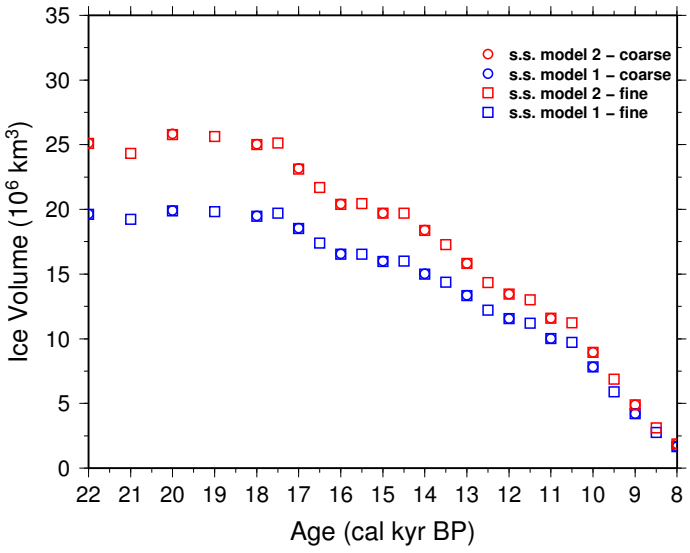

Figure 7.22: Modelled ice volume for margin models at 1000 year (circles) and 500 year (squares) intervals using two different shear stress models. The Earth model used in this example is "eefk". Note, the ice volumes in this example are lower than in previous tests since it does not include Greenland.

Chapter 8

Ice sheet model and modelled glacial-isostatic adjustment

8.1 Introduction

This chapter presents a model of the western Laurentide Ice Sheet model that fits the GIA constraints found in Chapters 4–6. The primary goal was to maximise ice thickness at the Last Glacial Maximum (LGM), while still fitting observations of glacial-isostatic adjustment (GIA) and ensuring that it was geologically and glaciologically realistic. First, I describe the resulting ice sheet model from 20 000 yr BP. The basal shear stress was the primary variable that was used to adjust the ice thickness through time. The margin location was only changed if varying the ice thickness alone was unable to account for the GIA observations. The next section provides an overview of the final shear stress parameters that were used to produce the ice model. Finally, the modelled GIA response is compared with observations of relative sea level change, glacial lake strandline tilt, modern lake tilt and GPS vertical velocity. These results are compared with two other models that were developed using GIA observations: ICE-5G and the ANU ice sheet model.

8.2 Ice sheet model

8.2.1 Introduction

This section provides an overview of my final ice sheet model (figures showing the model for all times is shown in Appendix A). The primary focus of the modelling was the time period between 20 000 yr BP and the present. The entire North American ice sheet complex was reconstructed in this study (Fig. 8.1), as it is not possible to model small parts in isolation. The ice sheet model outside of the study area was not adjusted to fit any constraints, and the shear stress values were based on similar geographic areas in the western Laurentide ice sheet. Nevertheless, the ice sheet model in the eastern Laurentide ice sheet has a large dome centred over northern Quebec and Labrador, as is expected based on geological constraints (Prest, 1990). It is possible that errors in the ice sheet outside of the study area could affect the calculated GIA. Future studies that include adjustments to the whole ice sheet may cause these reconstructions to be revised in future studies.

In order to properly calculate sea level, it is necessary to include far-field ice sheets in the calculation. The model for the Fennoscandian and northern European ice sheet complex used in the modelling is described in Lambeck et al. (1998a), Lambeck et al. (1998b), Lambeck et al. (2006) and Lambeck et al. (2010). The model for the British Ice Sheet is described in Lambeck (1993a), Lambeck (1993b) and Lambeck et al. (1996). Details of the Greenland Ice Sheet model can be found in Fleming and Lambeck (2004). The Antarctic ice sheet model is based on the reconstruction by Denton and Hughes (1981), scaled to fit the far-field relative sea level curve inferred from deep sea oxygen isotope records (Waelbroeck et al., 2002).

The ice sheet model was calculated using an iterative process to incorporate changing topography due to GIA, as described in Chapter 7. The final model incorporates an Earth model with a 120 km thick lithosphere, an upper mantle viscosity

of 4×10^{20} Pa s and a lower mantle viscosity of 10^{22} Pa s. The paleotopographic reconstructions shown in the figures in this section are based on this Earth model. Due to uncertainties in the Earth model parameters, it was considered sufficient if the modelled optimal fit to the data fell within a range of mantle viscosity values, with an upper mantle viscosity of 3–5$\times 10^{20}$ Pa s, and a lower mantle viscosity of 6.3$\times 10^{21}$–2.5$\times 10^{22}$ Pa s. This is discussed in further detail in section 8.4.2.

8.2.2 Ice model adjustment

The ice sheet model was developed by adjusting the basal shear stress values up or down, depending on whether a region needed more or less ice to fit observations on glacial-isostatic adjustment. The initial modelling used constant shear stress through time. This proved to be inadequate, so it was allowed to be time-varying. This was a forward modelling exercise, though different datasets were incorporated incrementally as the model improved. Initially, the ice model was adjusted purely on the basis of matching vertical velocities at four GPS stations with the highest uplift rates (Baker Lake, Churchill, Yellowknife and Pickle Lake), and contemporary lake tilts within the prescribed Earth model range. The reason for this is that these observations are unlikely to be heavily influenced by far-field ice sheets, or even the adjacent Cordilleran and eastern Laurentide Ice Sheet. The next dataset incorporated was glacial lake strandline tilt. The reason that this dataset was incorporated before relative sea level is that it is not influenced by uncertainties in global ice volume that sea level indicators would be subject to. Finally, relative sea level data were included. The initial focus was to try to fit post-glacial sea level (< 6000 yr BP), when global ice volume was close to present.

Occasionally, the ice margin position was adjusted if changing the basal shear stress alone was insufficient to explain the observations. The initial ice margin was based on the results of Gowan (2013) (chapter 3). The initial margin was set to be

at the 50% probability threshold of the minimum timing of retreat for each time step. There were two primary areas where this was adjusted. The margin had to be adjusted to account for the glacial lake level indicators, particularly for Lake McConnell. This meant placing the margin behind the indicator locations for the inferred age of them. The margin was also adjusted in the Keewatin sector after 10 000 yr BP so that the margin matched the radiating pattern of eskers from the inferred centre of the late Laurentide Ice Sheet, since there were few radiocarbon dates in this region. In general, the margin of the late stage of the Laurentide Ice Sheet was kept as extensive as possible to try to match early-post glacial sea level indicators in northwestern Hudson Bay. The margin in the final ice sheet model is more extensive than the reconstructions by Dyke (2004). Overall, the GIA constraints were less sensitive to margin location changes than to changes in basal shear stress (since basal shear stress could be adjusted downwards to make a very thin ice sheet), so the margin was not adjusted from the initial model except in those two cases. Another change to margin chonology was that the temporal resolution was increased as the model was refined. Initially, it was set to 2000 year intervals, but the final model had 500 year inverals.

8.2.3 Last Glacial Maximum – 20 000-17 000 yr BP

The margin of the western Laurentide ice sheet is reaches its maximum extent at 18 000 yr BP. Ice sheet topography and thickness is near maximum at 20 000 yr BP, and remains that way at 17 000 yr BP. The ice dome (Keewatin Dome) reaches peak elevation of about 3500 m east of Great Slave Lake. The corresponding maximum thickness is about 4000 m in this region. There is an ice divide that extends from the centre of the dome location to the Cordillera in northeastern British Columbia. Less prominent ice ridges surround Hudson Bay, with small peaks of about 2000 m located over the Melville Peninsula and northwestern Ontario. Ice thickness is less

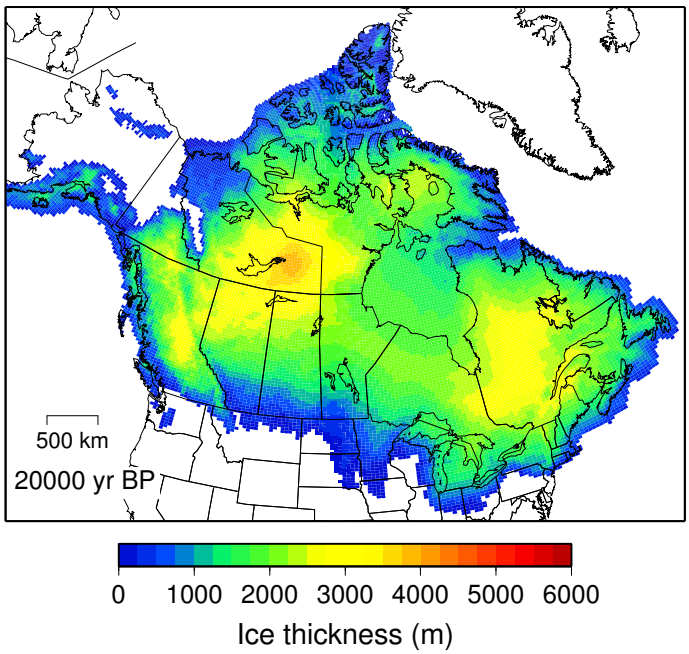

Figure 8.1: Resulting North American Ice Sheet complex model at 20 000 yr BP

than 1000 m south of the Canada-US border, and the topography is subdued. The ice elevation contours are consistent with southward oriented ice flow in southern Saskatchewan and southeastern Alberta at the LGM (Evans et al., 2008; Ò Cofaigh et al., 2010; Ross et al., 2012). The ice sheet was also thin in the Mackenzie Lowlands. The ice surface contours are consistent with the "early Wisconsin" elevation profile determined by Beget (1987) from the maximum elevation of Laurentian drift on adjacent mountain ranges. This ice model has relatively thin ice cover within Hudson Bay, with a maximum thickness less than 2000 m, and maximum elevation of 1500 m.

8.2.4 Early deglaciation – 16 000-13 000 yr BP

By 16 000 yr BP, ice margin retreat had commenced. The margin was north of Montana, and the confluence with the Cordilleran Ice Sheet was significantly reduced. The domes and ridges were located in the same positions as at the LGM, with a ridges surrounding Hudson Bay, and a dome centred east of Great Slave Lake. The peak thickness of the dome was between 3000 and 3500 m, and a peak elevation of

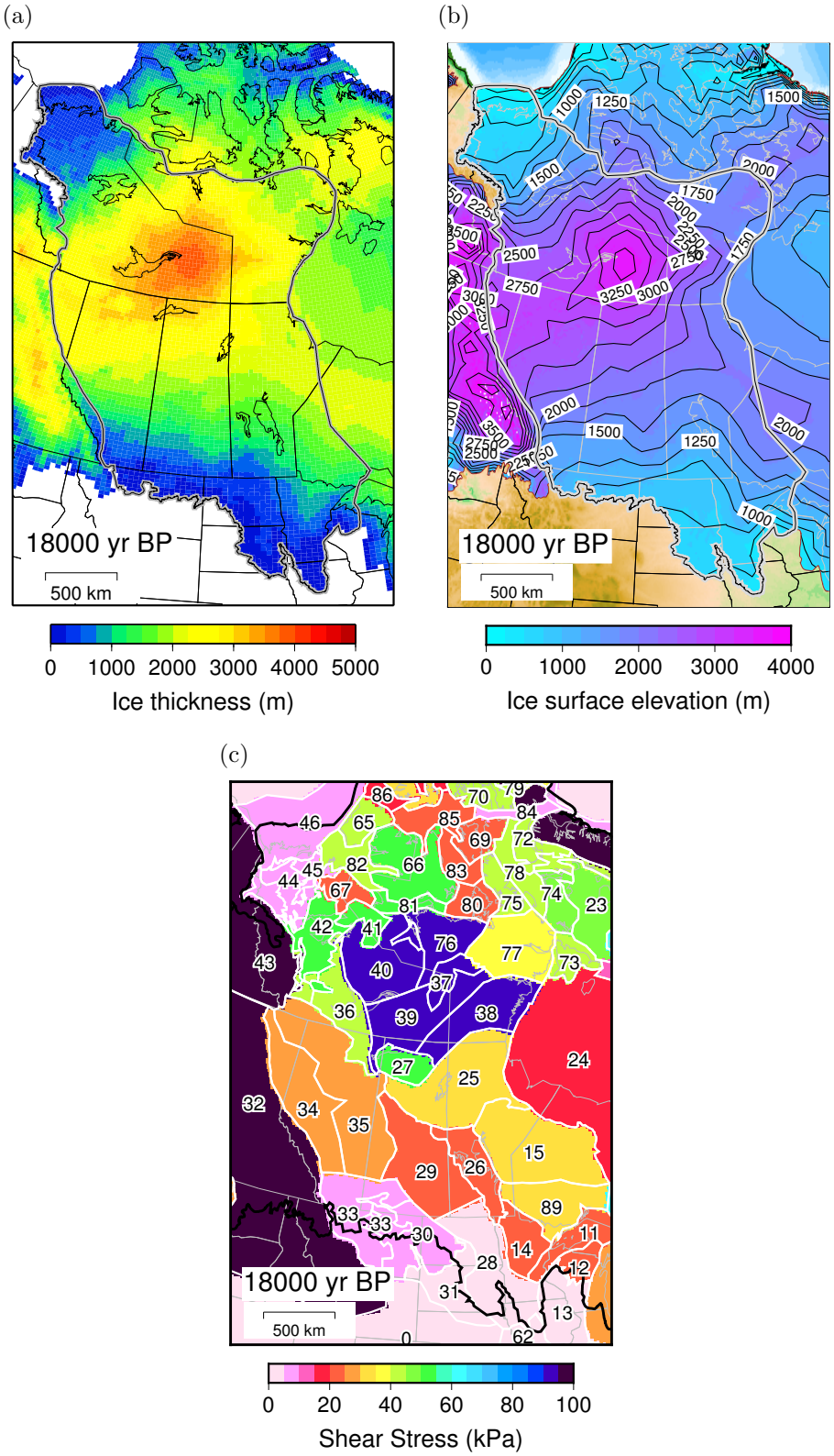

Figure 8.2: Ice sheet reconstruction at 18 000 yr BP. The grey and black line is the study area. (a) Ice thickness. (b) Paleotopography. The contour interval is 250 m.(b) Paleotopography. The contour interval is 250 m. (c) Shear stress values used to produce the ice model at this time step. For an explanation on the domain numbers, see Fig. 8.7.

3000 m.

At 15 000 yr BP, the margin was in central Alberta, and straddled the Canada-US border in eastern Saskatchewan and Manitoba. The Mackenzie Lowlands were also ice free at this time. The ice dome had a peak elevation of over 2500 m and thickness over 3000 m. The majority of ice volume lost by 16 000 yr BP was due to margin retreat.

At 14 000 yr BP, there was further retreat in northern Alberta and British Columbia, and Great Bear Lake was partially ice free (Fig. 8.3). At this point, the ice sheet was likely not pushing into the Cordillera, though the margin in my model is located in the vicinity of the mountains. The ice thickness was reduced greatly along the western fringe of the ice sheet, and the topography was shallow. The peak elevation at the ice dome was less than 2500 m. This time is significant because it marks the approximate timing of the start of Lake Agassiz (and the oldest constraints on GIA) (*e.g.* Lepper et al., 2013), and happened after a rapid sea level rise event, Meltwater Pulse 1A (*e.g.* Hanebuth et al., 2000). The implications of this will be discussed later in this chapter.

After 14 000 yr BP, the model resolution was increased to 500 year intervals to accommodate the fine tuning required to fit GIA constraints. Ice volume loss continued periodically between 14 000 yr BP and 13 000 yr BP, but with slowed margin retreat. Peak ice elevation was between 2000 and 2500 m, while the maximum ice thickness was less than 2500 m. The ice dome centre had shifted eastward to be located at the Northwest Territories-Nunavut border.

8.2.5 Younger Dryas – 12 500-11 500 yr BP

The Younger Dryas, which began shortly after 13 000 yr BP, was dominated by a return to cold conditions in the study area, which caused ice retreat to slow down (Dyke, 2004). The largest change in the model between 13 000 and 12 500 yr BP is

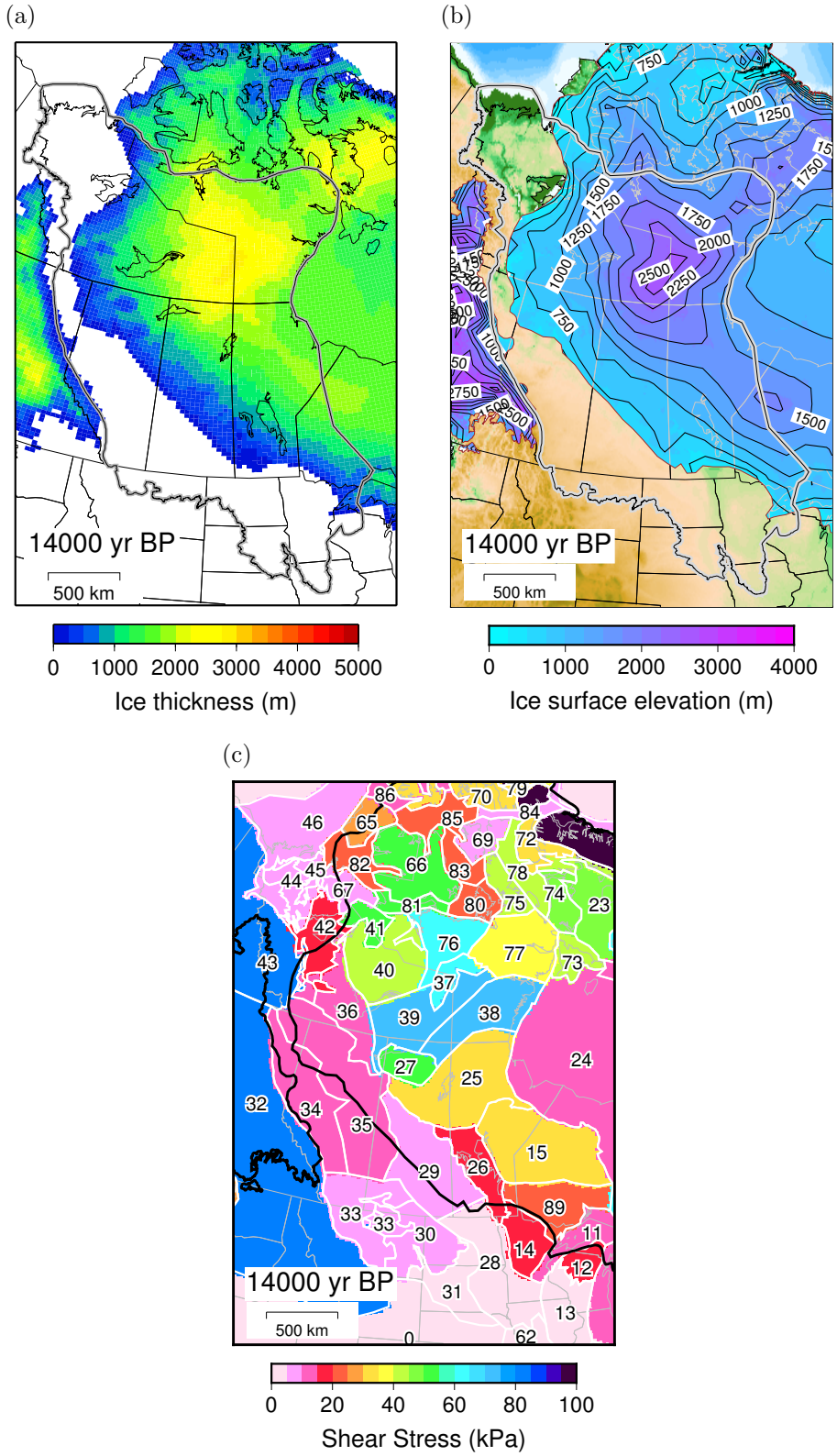

Figure 8.3: Ice sheet reconstruction at 14 000 yr BP, after Meltwater Pulse 1A. The grey and black line is the study area. (a) Ice thickness. (b) Paleotopography. The contour interval is 250 m. (c) Shear stress values used to produce the ice model at this time step. For an explanation on the domain numbers, see Fig. 8.7.

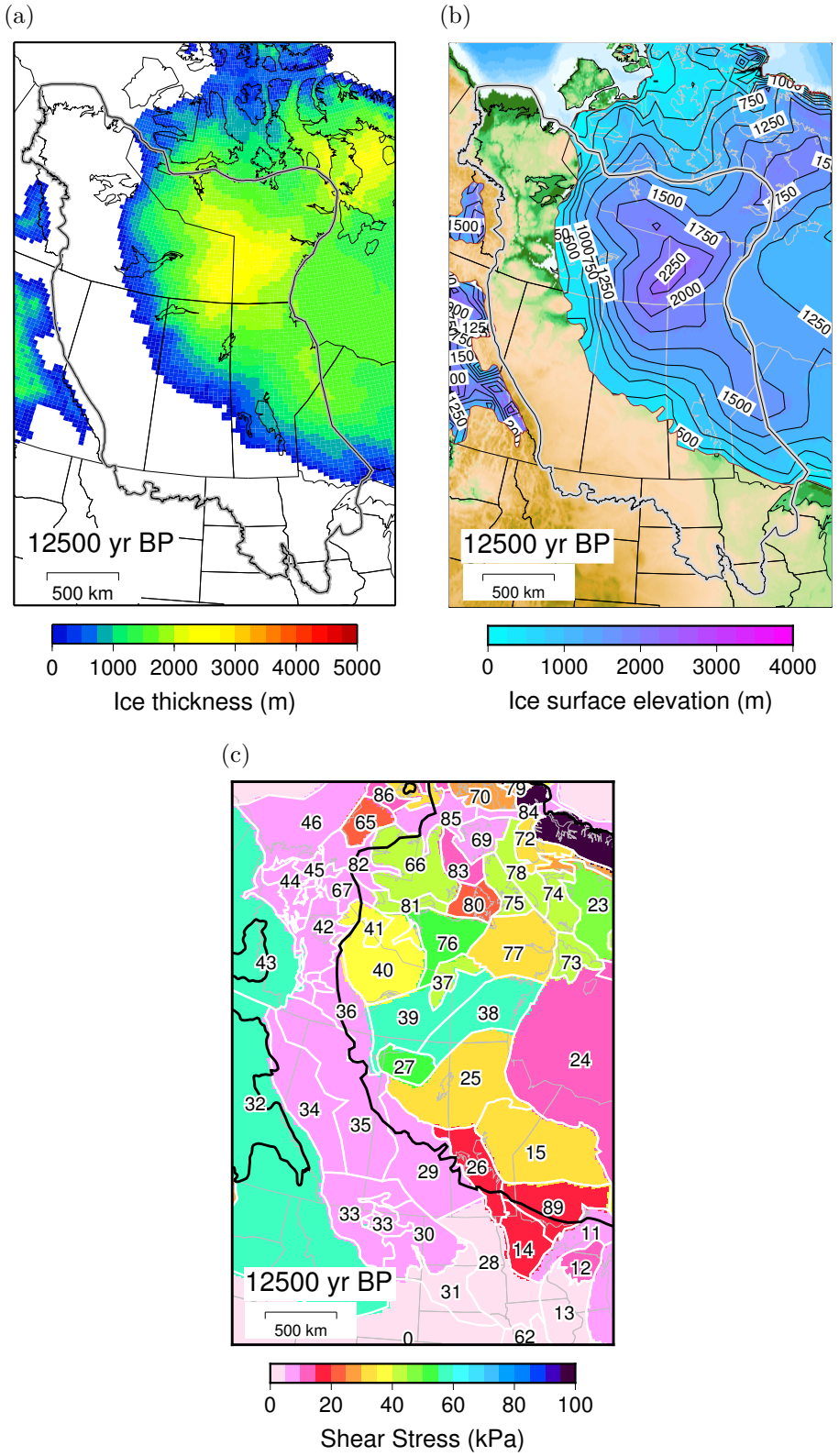

Figure 8.4: Ice sheet reconstruction at 12 500 yr BP, during the Younger Dryas. The grey and black line is the study area. (a) Ice thickness. (b) Paleotopography. The contour interval is 250 m. (c) Shear stress values used to produce the ice model at this time step. For an explanation on the domain numbers, see Fig. 8.7.

the retreat of the margin from the Mackenzie Mountains to the eastern side of Great Slave Lake (Fig. 8.4). The ridge that surrounded Hudson Bay had begun to break apart, and a small dome existed in northern Ontario. The margin did not migrate much along the western Laurentide Ice Sheet, and the ice thickness was generally close to the values at 13 000 yr BP. The model at 12 000 yr BP is almost identical to 12 500, with small amounts of margin retreat in the Great Slave Lake Region.

Between 12 000 yr BP and 11 500 yr BP, thinning of the western Laurentide Ice Sheet resumed. Though there was little margin retreat at 11 500 yr BP, the main dome was shrinking, and had a maximum elevation of 2000 m. The topography in northern Ontario was reduced, reaching 1500 m.

8.2.6 Early Holocene – 11 000-9000 yr BP

The early Holocene was the time when the remaining part of the ice sheet lost the majority of its volume. At 11 000 yr BP, most of the margin was retreating. The main ice dome was centred almost entirely in mainland Nunavut, with elevation less than 2000 m. Depression in the vicinity of Great Slave Lake caused the land to be below sea level. Ice margin retreat in Manitoba was rapid between 11 000 and 10 500 yr BP. The ice thickness was rapidly diminishing, no longer exceeding 2000 m. By 10 000 yr BP the ice dome that existed over northern Ontario had almost completely diminished (Fig. 8.5), though it was still over 1000 m thick within Hudson Bay. The ice dome that existed over Nunavut became a broad region with ice elevation between 1000 and 1500 m. At 9500 yr BP, the ice still remained over 1000 m thick in the southern part of Hudson Bay, but the ice sheet topography dropped further north. Ice margin retreat in mainland parts of Nunavut and Northwest Territories was minimal between 10 000 yr BP and 9500 yr BP, but retreat in the Arctic Archipelago caused a decrease in volume of the northern part of the ice sheet in the study area. At 9000 yr BP, very little of the ice sheet still had thickness in

excess of 1000 m, and peak elevation rarely exceeded 1000 m.

8.2.7 Final retreat – 8500-5000 yr BP

By 8500 yr BP, most of Hudson Bay was likely ice free (Dyke, 2004). There is still extensive ice cover over much of mainland Nunavut, extending into northern Manitoba, Saskatchewan and eastern Northwest Territories, however, ice thickness was below 1000 m over the entire area. There was little ice left at 8000 yr BP, and Hudson Bay was entirely ice free (Fig. 8.6). Though ice covered most of eastern mainland Nunavut, peak thickness was not more than 500 m, and the elevation was less than 500 m. Calculated paleo-topography indicates that the ocean extended far from the modern shoreline along much of the northern and southeastern parts of the ice sheet at this time, which would likely hasten retreat. After 8000 yr BP, the western Laurentide Ice Sheet remained as a fragment that extended from the northern Manitoba border to the remnants of the Foxe Dome at the Melville Peninsula. In my model, the remaining ice in mainland Nunavut is completely gone at 6500 yr BP, except for a small ice cap on the Melville Peninsula.

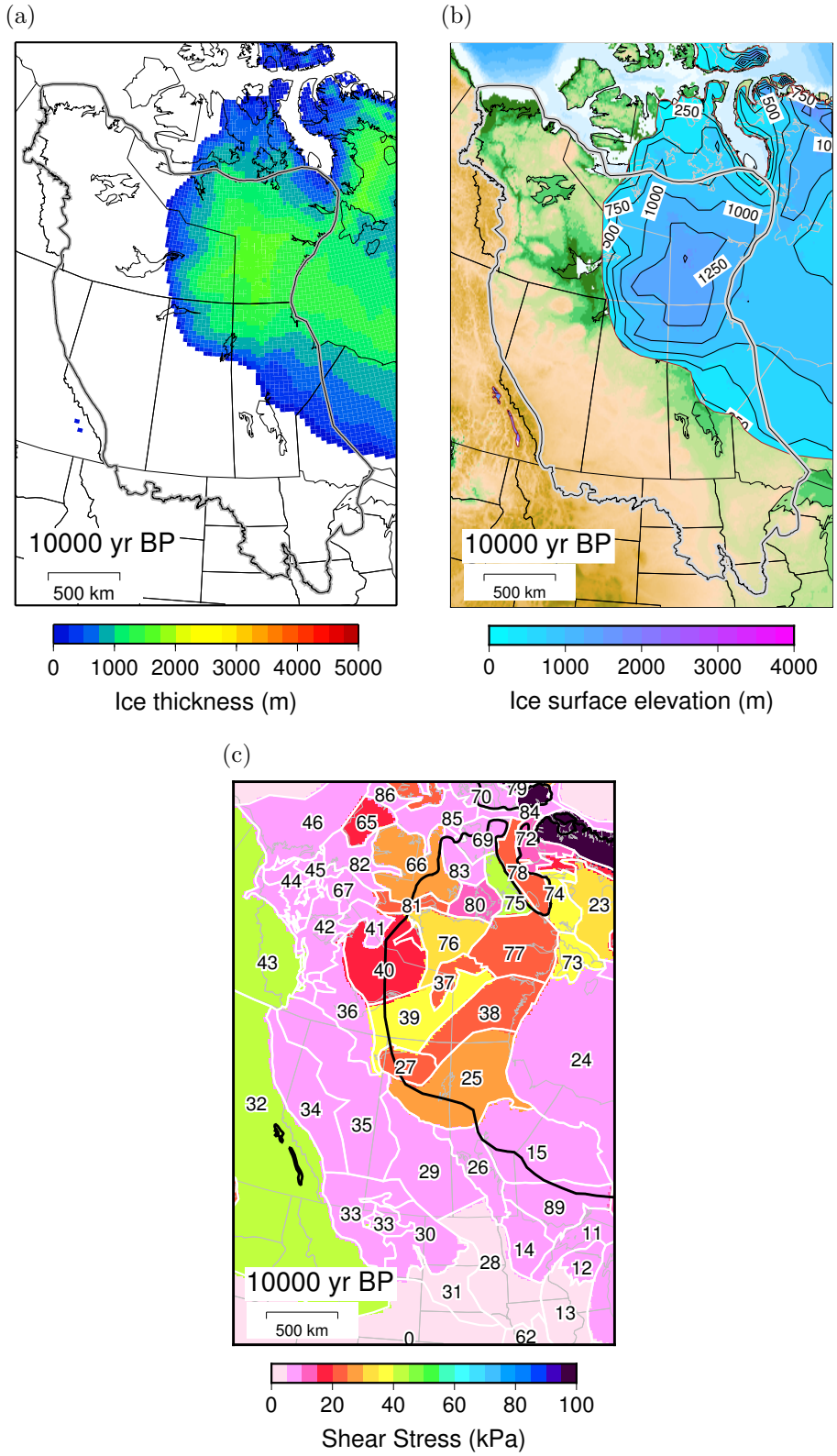

Figure 8.5: Ice sheet reconstruction at 10 000 yr BP. (a) Ice thickness. (b) Paleotopography. The contour interval is 250 m. (c) Shear stress values used to produce the ice model at this time step. For an explanation on the domain numbers, see Fig. 8.7.

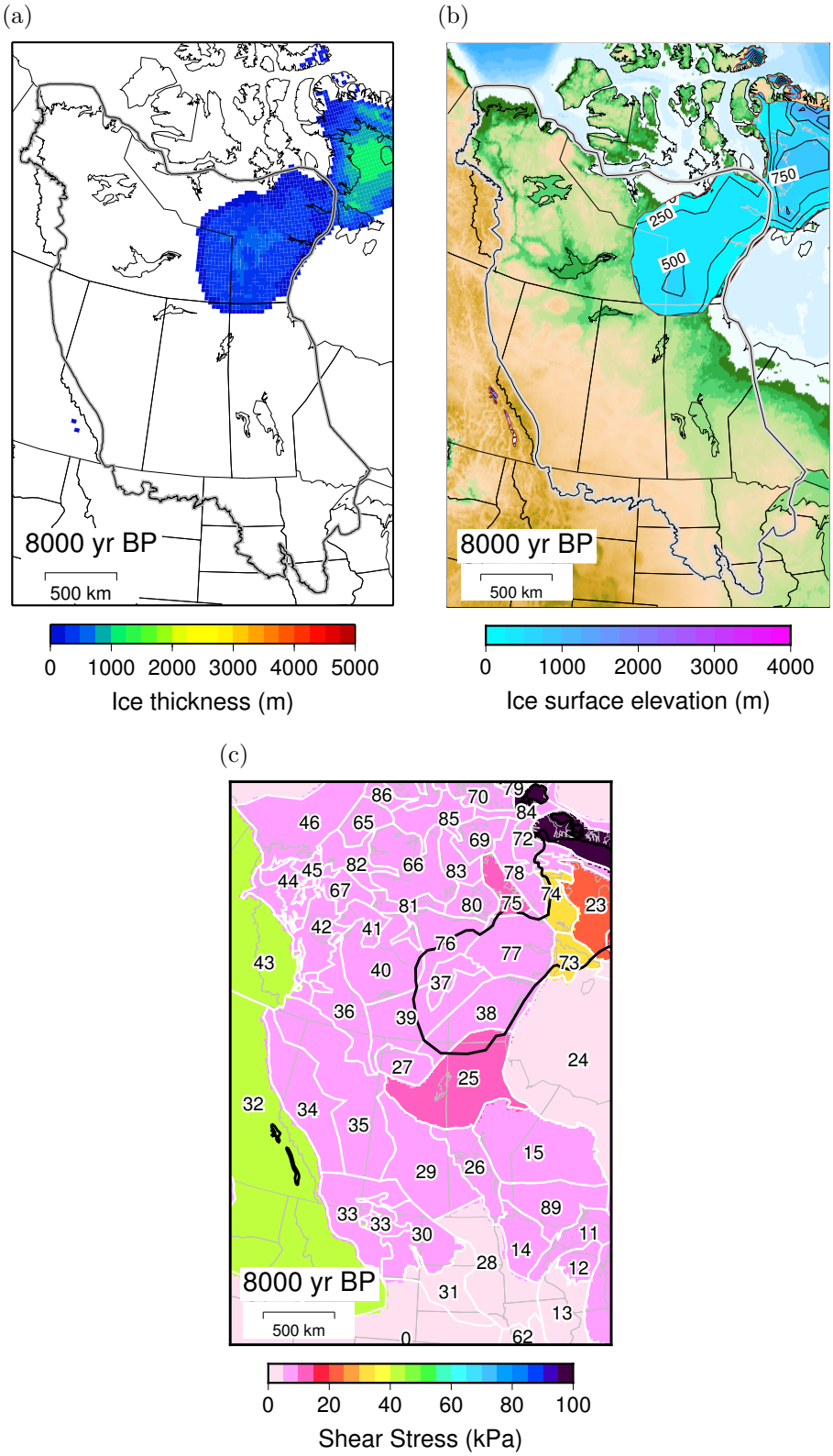

Figure 8.6: Ice sheet reconstruction at 8000 yr BP. (a) Ice thickness. (b) Paleotopography. The contour interval is 250 m. (c) Shear stress values used to produce the ice model at this time step. For an explanation on the domain numbers, see Fig. 8.7.

8.3 Basal shear stress

8.3.1 Introduction

The basal shear stress was the primary parameter that was varied through the modelling exercise. The shear stress controls the steepness of the ice profile, thus increased values causes the ice sheet to attain greater thickness. No attempt was made to identify the cause of changes in the basal shear stress through time, though the domains were defined based on geological and geographical considerations. The shear stress values were changed to increase or decrease the amount of ice for specific regions. The observations of GIA were used to constrain ice volume (Section 8.4), and the basal shear stress was adjusted to reach the required amount. The shear stress domains are described in detail on Fig. 8.7.

There is a strong time dependence on the shear stress, and the shear stress generally decreased as the ice sheet retreated. If the shear stress values were too high near the margin, it would cause the ice to become excessively thick towards the centre of the ice sheet. My model is consistent with models of Fisher et al. (1985) and Licciardi et al. (1998), with a contrast between areas inferred to be soft bedded (low shear stress due to the presence of deformable sediments) regions in the southwestern Laurentide Ice Sheet and inferred to be hard-bedded (high shear stress due to hard crystalline bedrock at the surface) on the Canadian Shield, which is mostly crystalline bedrock at the surface. The shear stress on the Canadian Shield is not uniform, and is much higher in the north than in the south. Borehole temperature profiles from central Manitoba and northern Ontario indicate that the temperature beneath the southwestern part of the ice sheet was unlikely to have dropped below freezing during the LGM (Rolandone et al., 2003). If basal temperatures were low, it may have prevented regions in southwestern Canadian Shield from attaining high values. Hudson Bay has low shear stress values for the entire duration of

the glaciation in my model, while Fisher et al. (1985) and Licciardi et al. (1998) presented scenarios with high and low values. The following section highlights the basal shear stress models at selected time periods. The remaining models are shown in appendix B.

8.3.2 Last Glacial Maximum configuration – 20 000 yr BP

The shear stress model at 20 000 yr BP is shown on Fig. 8.2, and the values at this time were at a maximum. The shear stress in the Precambrian region north of 60°N reached a peak level of about 90 kPa. The southern Canadian Prairies have values between 25 and 35 kPa. In southern Alberta and Saskatchewan, there were relatively high stress conditions, which is required to account for the ice flow direction that was in a nearly southwards direction, independent of topography (Ross et al., 2009). Hudson Bay has low shear stress (15 kPa) relative to other areas covered by the ice sheet.

As a comparison, the shear stress values used by Fisher et al. (1985) is shown on Fig 8.8. They justified their choice of shear stress values based purely on geological considerations, as there are few locations where the shear stress could be directly estimated. They used a low shear stress in the southwestern portion of the area covered by the Laurentide ice sheet, based on the surface profile reconstructions by Mathews (1974). The value used in this study is the same in southern Alberta, Saskatchewan and Montana. The shear stress in this study is lower in the area covered by the Des Moines and James Lobe, which was required to fit glacial lake strandline tilt values. Within the Canadian Shield region, the shear stress values are higher in the areas north of 60°N, and lower south of Hudson Bay. The value used in Hudson Bay in my model was about the same as Fisher *et al.*'s "soft bedded" reconstruction. They suggested that Hudson Bay may have alternated between soft and hard bedded situations, depending on the temperature at the base of the

ice sheet. The observations on GIA surrounding Hudson Bay indicate that a high shear stress scenario was unlikely to have dominated during the last glaciation, as increasing the value during the LGM causes the modelled modern day uplift rates to be too high. The model in this study has higher elevation in the Keewatin ice dome (by about 700 m) and lower elevation in northern Ontario (about 400 m) than Fisher *et al.*'s minimum reconstruction (Fig. 8.9). It also has a significantly higher ice elevation profile at the convergence between the Laurentide ice sheet and the Cordillera (>2500 m, versus 1200-1600 m), though Fisher *et al.* did not explicitly model this confluence. The location and ice thickness of these domes were required to fit GPS uplift rates, modern lake tilt and paleo-lake levels of glacial Lake McConnell.

8.3.3 Conditions during the Younger Dryas – 13 000–11 500 yr BP

By the Younger Dryas, the ice margin was located several hundred km from its maximum position (Fig. 8.4). The basal shear stress, especially in the northern Canadian Shield region, was significantly lower (by 30-50 kPa) than at the LGM. The shear stress in the Prairie provinces (Manitoba, Saskatchewan and Alberta) was minimal. The shear stress in Hudson Bay is also lower during the Younger Dryas than at the LGM. Observations of glacial lake tilt by this time period indicate that ice volume must have diminished considerably from the LGM maximum. To account for this, shear stress values had to be reduced throughout the entire area covered by the ice sheet.

8.3.4 Early Holocene – 10 000 yr BP

By 10 000 yr BP, the ice margin was largely confined to the Canadian Shield (Fig. 8.5). At this point, the ice thickness south of Hudson Bay had to be low, and therefore shear stress had to be low, in order to match observations of GPS

uplift and lake tilt. The northwestern Canadian Shield continued to have relatively high shear stress values, between 30 and 40 kPa. These values are lower than at 13 000 yr BP, with Hudson Bay reduced to 5 kPa, and the northern Canadian Shield less than 40 kPa.

8.3.5 Late glacial – 8000 yr BP

At 8000 yr BP, Hudson Bay was largely ice free, and ice was restricted to the Foxe Basin, Keewatin and Labrador (Fig. 8.6). High shear stress values only persisted in the Foxe Basin. The ice in Keewatin was likely stagnant at this time, and the incursion of ocean water from the north and east likely contributed to low shear stress conditions.

8.3.6 Comments on basal shear stress and ice dynamics

As stated in Chapter 7, the basal shear stress is dependent on many poorly understood and unconstrained factors. The steady state ice model used in this study is also a very simplistic representation of the true Laurentide Ice Sheet, which likely was never in steady state (Fisher et al., 1985). For instance, this model will not be able to determine the location of fast flowing regions such as ice streams, which certainly existed in the western Laurentide Ice Sheet (De Angelis and Kleman, 2005; Evans et al., 2008). In addition, this method prescribes the margin at fixed positions through time, and does not allow for variability based on the response of ice sheet on various forcing mechanisms (*e.g.* climate change, formation of lakes, basal temperature change). Finally, when modelling GIA, the response is not very sensitive to the difference between having a very thin ice sheet over a large area or no ice at all. In this situation, the basal shear stress will be set to a very low value, when it might be more appropriate to move the margin. Additional chronological information on margin history may cause this model to be revised in the future, and

this may also cause the shear stress values to be increased (if the margin location is not as extensive).

Although the model may not truly represent a fully dynamic ice sheet, it is useful to obtain a general pattern of the evolution of basal conditions through time. The conditions at the base were generally weaker over Western Canadian Sedimentary Basin than they were over the Precambrian Shield, as expected from the difference in deformability of the bed (Clark, 1994). The shear stress in the southern parts of the ice sheet is generally lower than in areas that cover the Northwest Territories. The shear stress is predicted to have been low within Hudson Bay. The shear stress also decreases with time. This would be expected due to the increased supply of water to the base as the ice sheet retreated, due to melting and ponding of water at the margin by proglacial lakes. Since this model does not explicitly model ice velocity, it is not possible to comment directly on the location of fast flowing ice features, such as those described by Evans et al. (2008) and De Angelis and Kleman (2005). This model is more applicable for determining the general evolution of topography of the ice sheet through time. From that, estimates of the parameters regarding ice dynamics may be possible.

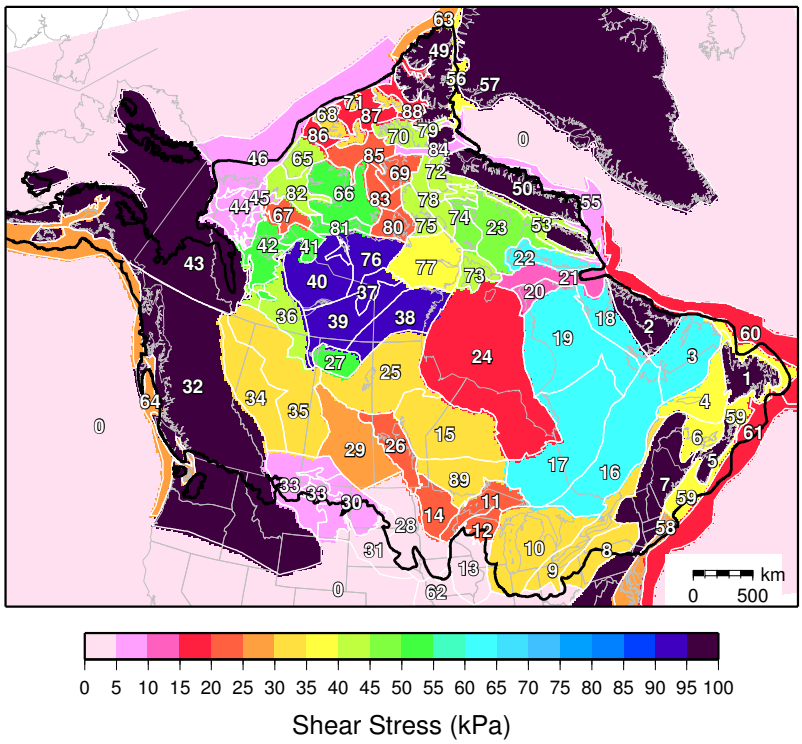

Figure 8.7: Shear stress model at 20 000 yr BP. The black line is the margin reconstruction at this time. Domains are divided as follows: 1 - Newfoundland; 2 - Torngat Mountains; 3 - Southern Labrador; 4 - Strait of Belle Isle / Ile d'Anticosti; 5 - Nova Scotia; 6 - Prince Edward Island and region; 7 - Appalachian Mountains; 8 - South of Lakes Erie and Ontario; 9 - St. Laurence Valley and Lakes Erie and Ontario; 10 - Michigan Basin; 11 - Lake Superior; 12 - Proterozoic volcanic rocks south of Lake Superior; 13 - Paleozoic rocks south of Lake Superior; 14 - Superior Province located primarily in Minnesota; 15 - northwestern Superior Province; 16 - Grenville Province; 17 - Superior Province southeast of Hudson Bay; 18 - Ungava Bay; 20 - Northern Quebec; 21 - Hudson Strait; 23 - Foxe Basin; 24 - Hudson Bay; 25 - Trans-Hudson Orogen west of Hudson Bay; 26 - Paleozoic rocks in Manitoba; 27 - Athabasca Basin; 28 - Williston Basin; 29 - eastern Western Canadian Sedimentary Basin; 30 - Cenozoic rocks in Montana and North Dakota; 31 - Cretaceous rocks in the Dakotas; 32 - Cordillera south of 60°N; 33 - Cretaceous rocks in southern Alberta, Saskatchewan and Montana; 34 - Cretaceous and Cenozoic Rocks west of the Cordillera; 35 - Cretaceous rocks in Alberta and Saskatchewan; 36 - Paleozoic rocks near Great Slave Lake; 37 - Thelon Basin; 38 - Hearne Province; 39 - Rae Province; 40 - Slave Craton; 41 - Proterozoic cover over the Slave Craton; 42 - Cretaceous rocks in the Northwest Territories; 43 - Cordillera north of 60°N; 44 - Paleozoic rocks in the Mackenzie Lowlands; 45 - Cretaceous rocks in the Mackenzie Lowlands; 46 - Cenozoic sediments offshore of the western Canadian Arctic; 47 - Proterozoic rocks on the Melville Hills and Victoria Island; 48 - northern Rae Province; 49 - Arctic Cordillera; 50 - Baffin Mountains; 53 - southern Baffin Island; 55 - Offshore of Baffin and Devon Islands; 56 - strait between Ellesmere Island and Greenland; 57 - Greenland; 58 - Eastern Seaboard of the United States; 59 - shelf of Atlantic Canada; 60 - shelf region north of Newfoundland; 61 - shelf region south of Newfoundland; 62 - midwestern United States; 63 - shelf north of Ellesmere Island; 64 - Pacific shelf; 65 - Banks Island; 66 - Victoria Island; 67 - Northwest mainland Nunavut sedimentary rocks; 68 - Melville Island; 69 - Prince of Wales/Sommerset Island; 70 - Bathurst/western Devon Island; 71 - Mackenzie King Island; 72 - Northwest Baffin Island; 73 - Southampton Island; 74 - Melville Peninsula; 75 - Boothia Peninsula; 76 - northwest Rae Province; 77 - northeast Rae Province; 78 - Gulf of Boothia; 79 - Jones Sound; 80 - King William Island; 81 - Coronation Gulf; 82 - Amundsen Gulf; 83 - McClintock Channel; 84 - Lancaster Sound; 85 - Viscount Melville Sound; 86 - McClure Strait; 87 - Hazen Strait; 88 - Norwegian Bay; 0 - all other regions.

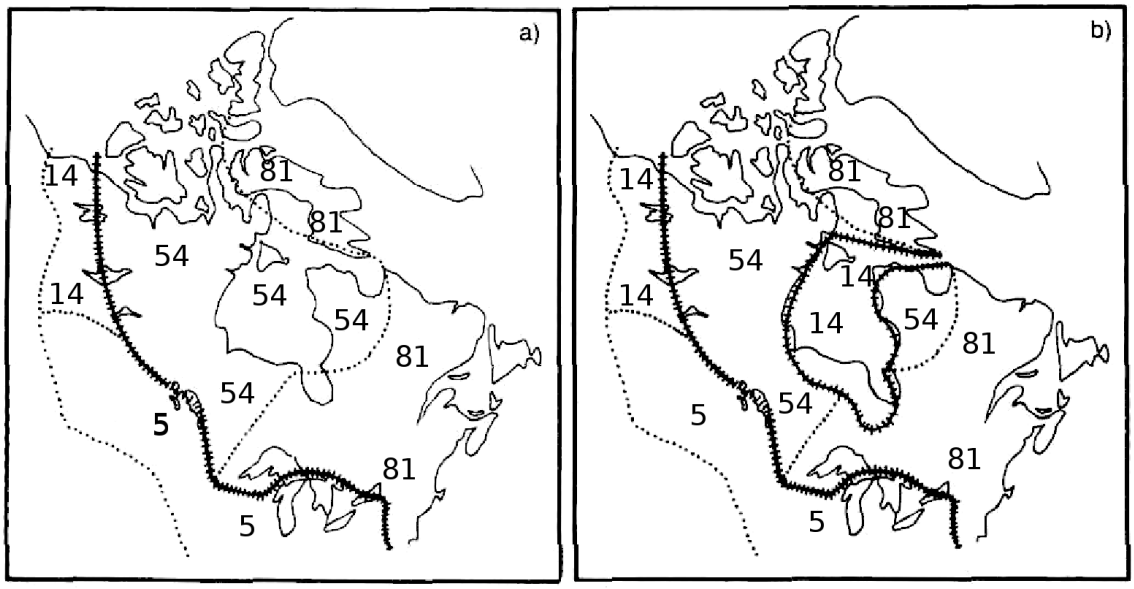

Figure 8.8: Shear stress values used by Fisher et al. (1985). All values are in kPa. The thick hashed line is the boundary between Phanerozoic sedimentary rocks and the Canadian Shield. (a) Hard bedded Hudson Bay. (b) Soft bedded Hudson Bay

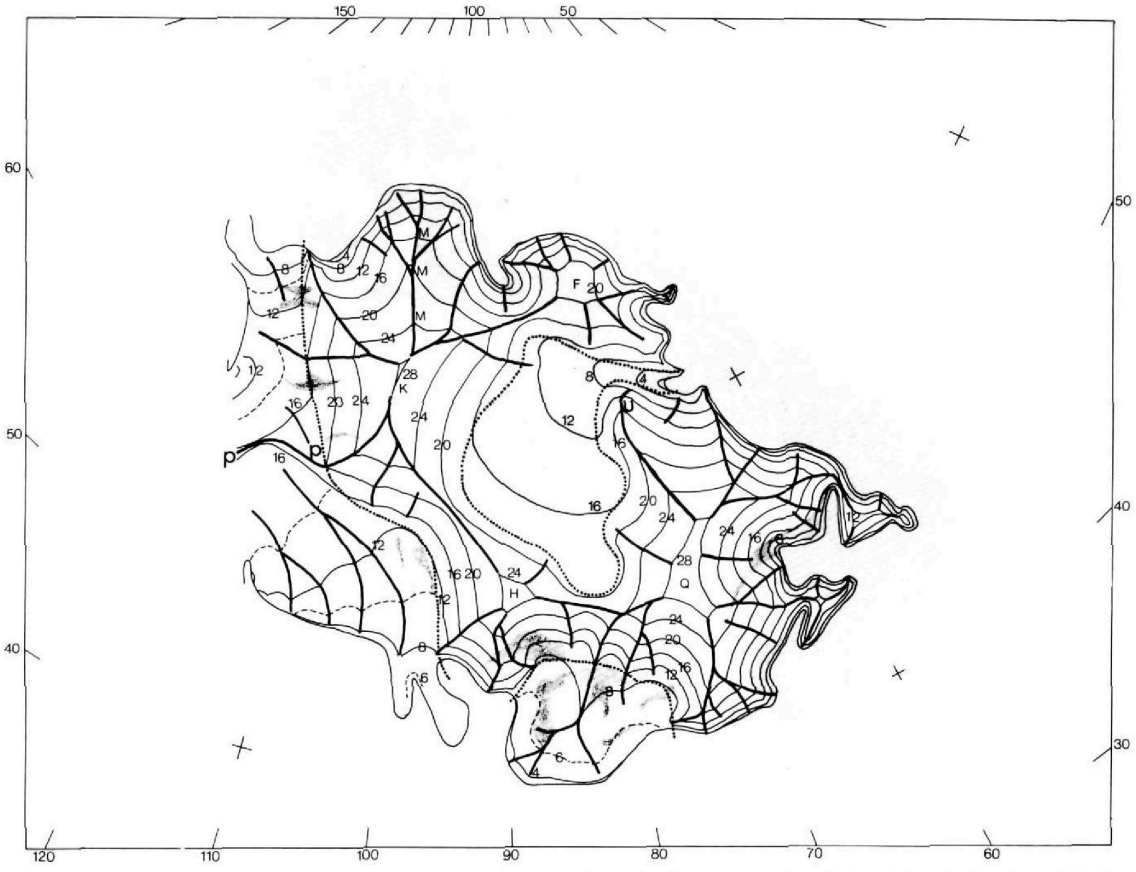

Figure 8.9: "Minimum" ice sheet model of Fisher et al. (1985), using assuming a soft bedded Hudson Bay. Elevation values are in hundreds of m above sea level.

8.4 Comparison of modelled GIA and observations

8.4.1 Introduction

The ice sheet model in this study was constrained predominantly from observations of glacial-isostatic adjustment and relative sea level. This consists of vertical velocity rates from GPS, modern lake tilts, relative sea level and glacial lake strandline tilts. Ice thickness in the model was adjusted so that the amount of GIA calculated matched the observations An overview of the data is covered in Chapters 4–6. This section presents a comparison of the modelled GIA with the observations. Calculation of Earth deformation and sea level was done using CALSEA (Nakada and Lambeck, 1987; Lambeck et al., 2003).

8.4.2 Earth model parameters

The magnitude of GIA caused by ice loading is strongly dependent on the choice of Earth model parameters. This study uses a three-layer Earth model, with an elastic lithosphere of variable thickness, and a division between the upper and lower mantle at 660 km depth. The target mantle viscosity values used to determine the optimal modelled fit to the GIA constraints are 3-5$\times 10^{20}$ Pa s for the upper mantle, and $> 5 \times 10^{21}$ Pa s for the lower mantle, following the methodology of Lambeck et al. (2010). Further justification of this range is provided below.

Peltier (1996) determined an Earth viscosity model (called VM2) by inverting the relaxation of sea level at locations in Fennoscandia and North America and changes in Earth rotation. This inversion was weakly dependent on the loading history of the Laurentide Ice Sheet. VM2 has a complex relationship of mantle viscosity with depth, but the upper mantle averages to 4×10^{20} Pa s, and the lower mantle has an average value of 2–2.5$\times 10^{21}$ Pa s. Peltier (2004) used a lithospheric thickness of

90 km in his development of ICE-5G, to account for relative sea level observations in Scotland. He argued that the higher lower mantle viscosity determined in the modelling by Lambeck *et al.* (*e.g.* Lambeck et al., 1996, 1998a) was the result of modelling the British ice sheet, which was too small to sufficiently perturb the lower mantle. Recently, Peltier introduced the VM5 model (*i.e.* Peltier and Drummond, 2008). VM5 is essentially a simplified version of VM2, except that the lithosphere is reduced to 60 km, and a 40 km thick layer with a viscosity of 10^{22} Pa s is added below the lithosphere. This change largely affected horizontal deformation.

It is desirable to make inferences on the viscosity structure of the Earth that are not dependent on the response of GIA. One issue is that these inferences are based on specific locations, such as beneath North America and Fennoscandia. Another issue is that depth of the mantle that is perturbed by the ice sheet will be dependent on the size of the ice sheet, and the duration of ice cover. This could cause smoothing of the estimated viscosity if there is strong stratification in the mantle, as is suspected for the difference between the upper and lower mantle. The resulting ice sheet model from GIA modelling is strongly dependent on the choice of Earth rheology (Kaufmann and Lambeck, 2002), so the inferred rheology used in this study comes from sources independent of GIA.

The viscosity of the mantle can be independently inferred from seismic, gravity, topography and mineral physics data. Forte and Mitrovica (2001) determined the viscosity structure of the Earth by using constraints from seismic data and mantle flow. The results of their inversion yielded a jump in viscosity at 670 km depth by a factor of 50. The two-layer upper and lower mantle viscosity values in their modelling were 4×10^{20} and 2×10^{22} Pa s, respectively. Panasyuk and Hager (2000) determined the relative viscosity structure of the mantle based on dynamic topography and geoid observations. Their results showed that the upper mantle structure is uncertain, but that the lower mantle viscosity was generally about 1-2 orders of magnitude higher

than the upper mantle. King and Masters (1992) determined the viscosity structure of the mantle by inverting seismic topography data. They found a factor of 30-100 increase in viscosity at 670 km. Steinberger and Calderwood (2006) used models derived from mineral physics to determine viscosity, with optimisations using geoid, GIA and radiative heat flux observations. Their results suggested that there is likely a jump in viscosity by at least an order of magnitude at 670 km depth. Their model showed that the upper mantle has a viscosity between 10^{20} and 10^{21} Pa s, while the lower mantle is between 7×10^{21} and 4×10^{23} Pa s, increasing with depth.

The preceding studies showed that there is likely a significant increase (at least an order of magnitude) in viscosity between the upper and lower mantle. The viscosity in the upper mantle is complicated, and assuming a constant value is certainly a simplification. However, at present there is no consensus on a structure that would justify a the use of a highly stratified model. The density of observations of GIA in North America is also unlikely to be sufficient to resolve stratification unless the contrast was large. The structure of the lithosphere in the Hudson Bay region is known to have lateral variability from seismic tomography (Bastow et al., 2013). The lower part of the seismic lithosphere corresponds to the upper part of what is defined as "upper mantle" in this study, and probably also would correspond to variability in the viscous properties. Therefore the target mantle viscosity range of 3-5$\times 10^{20}$ Pa s used in this study may be too narrow. This range includes upper mantle viscosity values used in previous GIA studies, such as Peltier (2004) and Lambeck et al. (2010), and independent joint inversion of GIA relaxation and mantle convection (Mitrovica and Forte, 2004). Most of the GIA observations used in this study are highly sensitive to the choice of upper mantle viscosity, so increasing this range would lead to greater variability in possible ice sheet configurations (so if the assumed upper mantle viscosity is different, it would lead to an ice sheet model that is different from that presented here). The lower mantle is set to have viscosity

values that are least an order of magnitude higher than the upper mantle ($> 5 \times 10^{21}$ Pa s). This ensures the minimum one order of magnitude increase in viscosity at the transition between the two layers. The exact depth where the jump in viscosity occurs may not be resolvable with GIA, and indeed might be a gradual increase with depth (*i.e.* Mitrovica and Forte, 2004). Setting it at 670 km is convenient from a geochemical and geophysical point of view, as described above.

8.4.3 Vertical velocity at GPS sites

The vertical velocity from GPS sites was discussed in detail in chapter 4. Vertical velocity was calculated at all of the GPS sites located within the study area using a wide range of Earth model parameters (Fig. 8.10). The weighed RMS of all 11 GPS sites was calculated for each Earth model in order to assess how well the modelled uplift rates from the final ice sheet model matched the observed uplift rates. The RMS was calculated by:

$$\sqrt{\frac{\sum_{i=1}^{n} r_i/\sigma_i}{\sum_{i=1}^{n} 1/\sigma_i}} \tag{8.1}$$

In this equation, r_i is the residual (the difference between the modelled value and observed value) for station i, and σ_i is the uncertainty of the measured uplift rate. The calculated uplift rate is computed for the year 2000 C.E.. The target range of best fit was for an upper mantle viscosity between 3×10^{20} and 5×10^{20} Pa s and for lower mantle viscosity was between 5×10^{21} and 2.5×10^{22} Pa s. Lithospheric thickness values between 90 km and 140 km were investigated, though there was not a strong dependence on this parameter. If lithospheric thickness is increased, the optimal fit requires a slightly higher lower mantle viscosity if upper mantle viscosity is held constant. Modelled velocity values using an Earth model with a lithospheric thickness of 120 km, upper mantle viscosity of 4×10^{20} Pa s and lower mantle viscosity of 10^{22} Pa s is shown on Table 8.1. From Fig. 8.10, the fit

to the GPS data are good over a wide range of possible Earth model parameters, including the prefered Earth model range.

Table 8.1: Modelled vertical velocity at GPS sites (mm.yr^{-}1)

Location	Station	Observed rate	This study	ICE-5G	ANU
Baker Lake, Nunavut	BAKE	12.56±0.43	12.48	11.99	14.52
Churchill, Manitoba	CHUR	10.33±0.26	10.94	13.73	10.37
Lac Du Bonnet, Manitoba	DUBO	1.17±0.31	1.38	6.99	5.45
Flin Flon, Manitoba	FLIN	4.25±0.42	4.30	8.94	10.93
Ulukhaktok, Northwest Territories	HOLM	2.70±0.33	1.98	−0.15	1.86
Inuvik, Northwest Territories	INVK	-1.28±0.46	−0.83	−0.88	−1.30
North Liberty, Iowa	NLIB	-2.24±0.30	−1.26	−1.48	−1.41
Pickle Lake, Ontario	PICL	5.68±0.62	5.08	6.38	12.33
Calgary, Alberta	PRDS	-0.46±0.34	0.19	0.70	1.49
Saskatoon, Saskatchewan	SASK	-0.32±0.31	0.72	2.98	2.77
Yellowknife, Northwest Territories	YELL	6.45±0.25	6.96	8.31	9.53
Weighted RMS			0.65	3.04	2.98

The four stations with the highest uplift rates were (Baker Lake, Churchill, Pickle Lake and Yellowknife), served as highly weighted during the initial stages ice sheet modelling (by finding the difference between the observed and modelled rate), as they were most sensitive to changes in the ice sheet model (Fig. 8.11). In all cases, the modelled rates are within 0.5 mm.yr^{-1} of the observed rate (which would match observations within two-sigma of all the sites) within the target mantle viscosity range. With the exception of Baker Lake, the uplift rates seem more sensitive to lower mantle viscosity than upper mantle viscosity. In Baker Lake, an upper mantle viscosity that is lower than the 3×10^{20} Pa s does not provide a good fit with this ice sheet model.

The uplift rates for other the other sites were less sensitive to changes in ice sheet

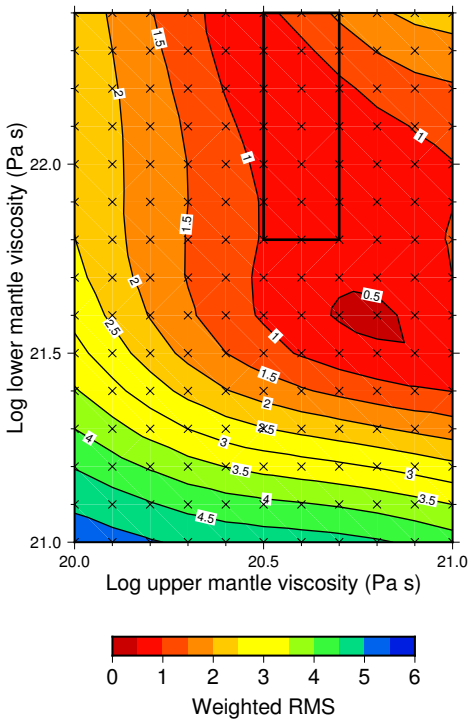

Figure 8.10: Weighted RMS of the 11 GPS uplift rates used in this study using variable mantle viscosity, and a lithospheric thickness of 120 km.

model, which is consistent with the tests of Wu et al. (2010). This is also reflected in the calculated uplift rates, which do not vary as much when the mantle viscosity is changed (Figs. 8.12 and 8.13). Like the other four sites, the calculated uplift rate is within 0.5 mm.yr^{-1} of the observed rate in the target viscosity range, with the exception of Ulukhaktok. The calculated rates at North Liberty, Inuvik and Calgary are relatively incentive to the choice of lower mantle viscosity.

The velocity at the four highly weighted sites had a strong impact on the ice model. The calculated rates at Churchill, Baker Lake and Pickle Lake matched the observed rate if ice thickness was limited in Hudson Bay. Increasing the ice thickness significantly increases the contemporary vertical velocity at these sites, especially at Churchill. The rate at Yellowknife provided limits on the maximum thickness of ice near the Keewatin dome. The rate at Baker Lake indicated that in northeastern mainland Nunavut, the ice was thinner than the Keewatin Dome to the southwest, and Foxe Dome to the northeast. The station at Pickle Lake indicates that the ice

thickness south of Hudson Bay could not have been as much as the Keewatin Dome.

The calculated vertical velocity at the sites located in Saskatchewan and Manitoba were not highly sensitive to small changes to the ice model. Changing the calculated rates within the target viscosity range would require either substantial increases in ice thickness or significant changes to the deglaciation history. Significant changes in the deglaciation history in the southern Laurentide Ice Sheet is unlikely (see Chapter 3). This gives confidence for the estimates of ice volume in this model at the southern part of the study area.

The modelled rates at Ulukhaktok, Calgary and North Liberty also fall within the target mantle viscosity. It is more difficult to make statements on the ice sheet model for these stations, as they will be affected by the Cordillera Ice Sheet (in the case of Calgary), the eastern Laurentide Ice Sheet (in the case of North Liberty), and the Innuitian Ice Sheet and northern Laurentide Ice Sheet (in the case of Ulukhaktok). The modelled rates are consistent with the observations, indicating that the ice model at the periphery of the study area is sound.

Overall, the modeled fit (weighted RMS) of the model from this study is much better than the ANU model and ICE-5G. This is not entirely surprising, since those models did not incorporate the GPS observations as a tuning parameter. As a result, the model from this study is more appropriate for assessments of modern day GIA uplift.

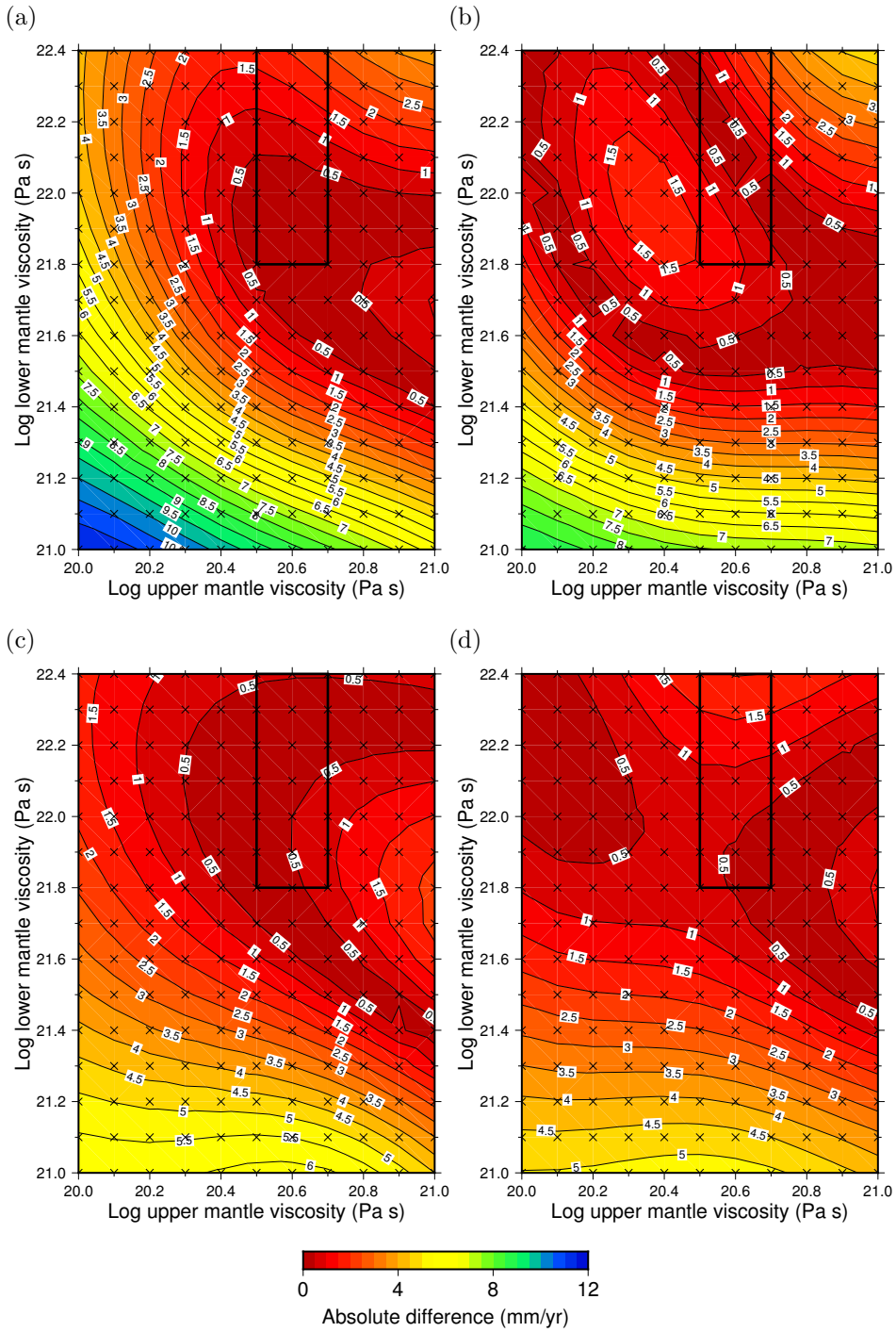

Figure 8.11: Absolute difference between observed and calculated vertical velocity at (a) Baker Lake, Nunavut, (b) Churchill, Manitoba, (c) Yellowknife, Northwest Territories and (d) Pickle Lake, Ontario using a lithospheric thickness of 120 km, and variable upper and lower mantle viscosity. The black box indicates the target viscosity range for best fit.

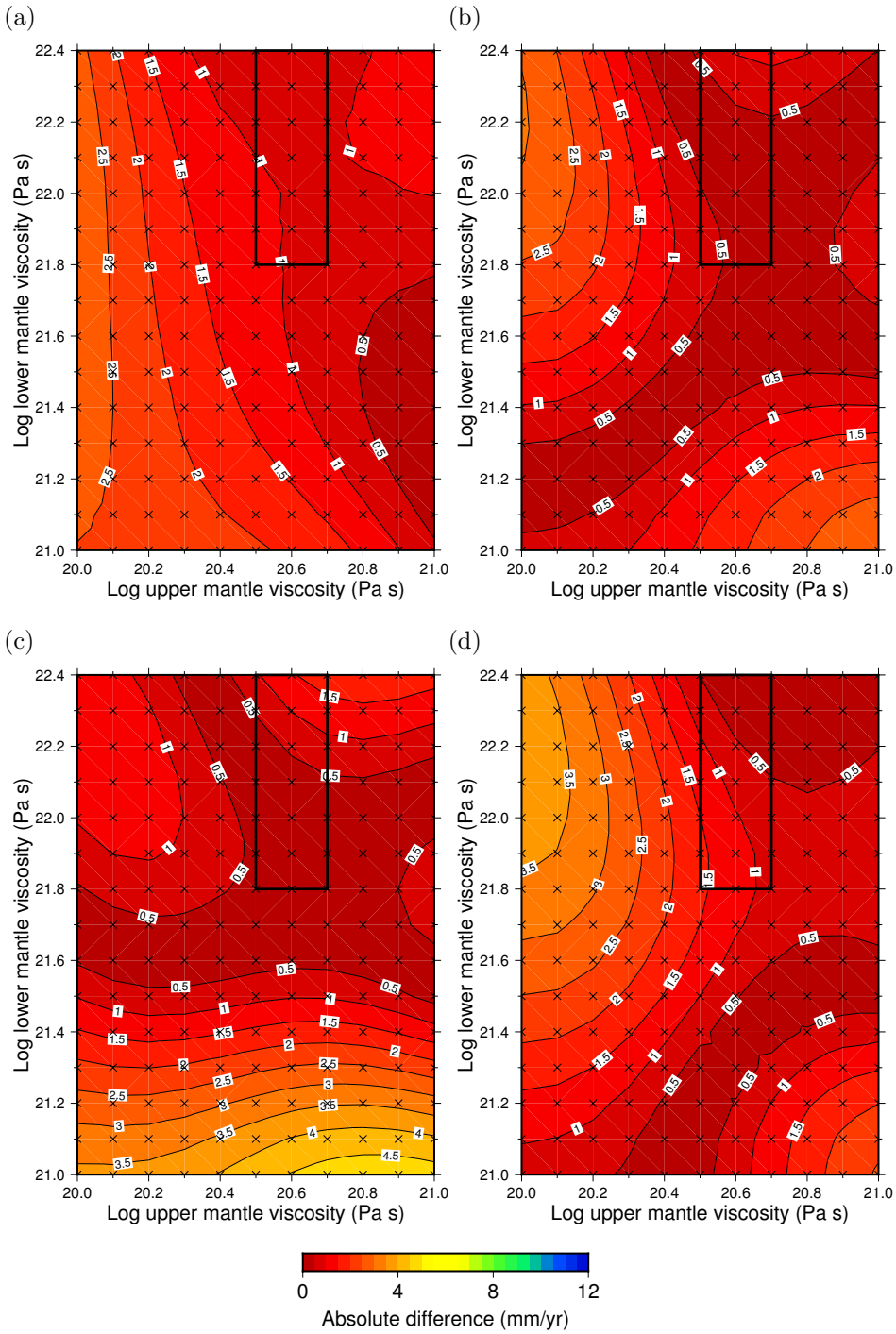

Figure 8.12: Difference between observed and calculated vertical velocity at (a) North Liberty, Iowa, (b) Lac Du Bonnet, Manitoba, (c) Flin Flon, Manitoba and (d) Saskatoon, Saskatchewan using a lithospheric thickness of 120 km, and variable upper and lower mantle viscosity. The black box indicates the target viscosity range for best fit.

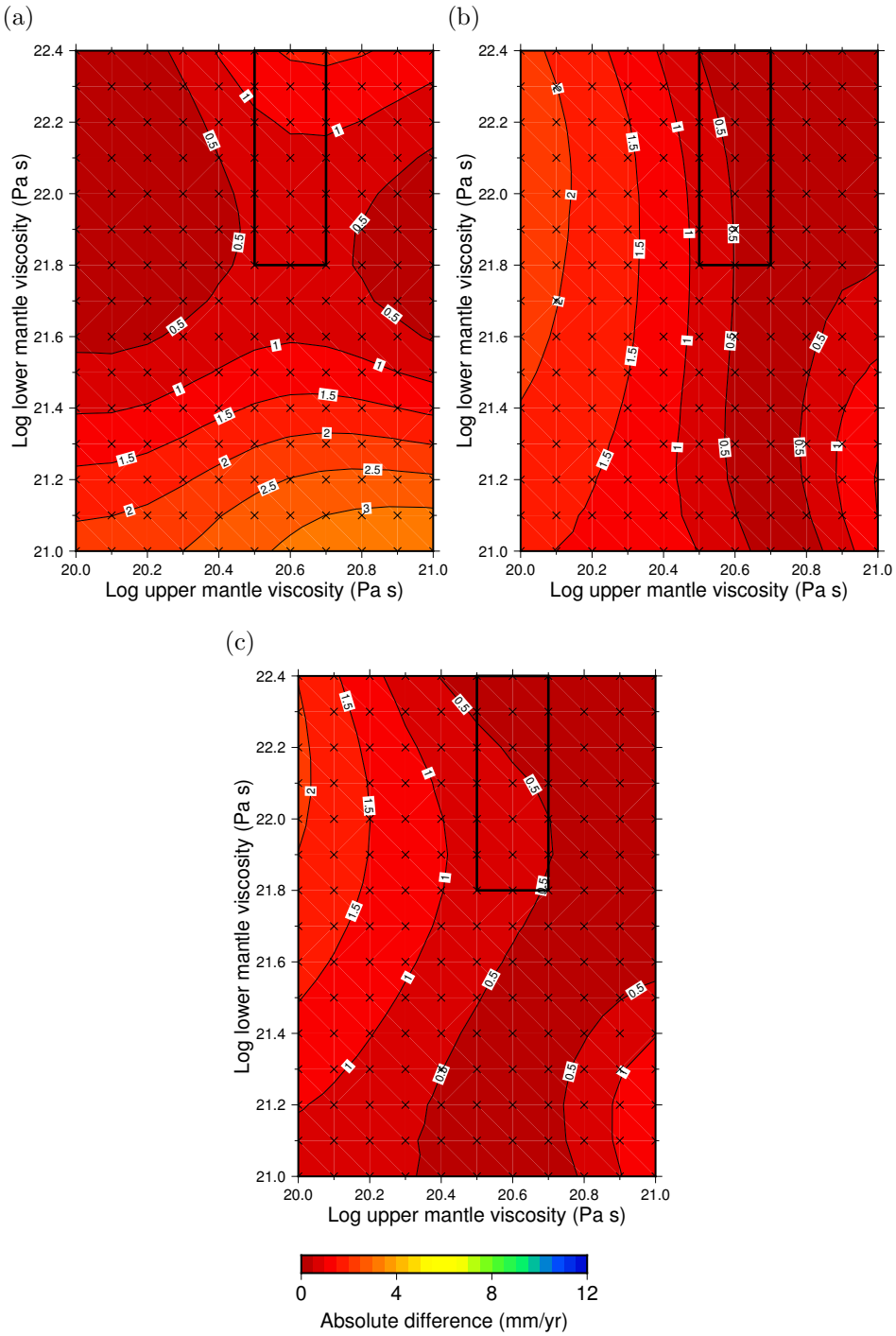

Figure 8.13: Absolute difference between observed and calculated vertical velocity at (a) Ulukhaktok, Northwest Territories, (b) Inuvik, Northwest Territories, and (c) Calgary, Alberta using a lithospheric thickness of 120 km, and variable upper and lower mantle viscosity. The black box indicates the target viscosity range for best fit.

8.4.4 Lake Tilt

A comparison of the measured and calculated lake level change rates due to differential GIA of lakes as measured by differenced lake gauges is shown in Table 8.2. As stated in Chapter 5, the rates from the method proposed by Mainville and Craymer (2005) were considered to be the most reliable, as they took into account the measurements of all gauges within the lake simultaneously. The GIA tilt rate can be taken as the negative of these values. There are tilt rates in ten lakes within the study area, with a total of 29 pairs. When the weighted RMS is determined incorporating all gauge pairs, there is a slight dependence on mantle viscosity, with the best fit falling within the preferred Earth model range (Fig. 8.14). It is better to assess the fit for individual lakes, rather than for the sum of the gauges for all of the lakes. Confidence in the measured rates is dependent on factors like the duration of overlapping measurements of the gauges, and the number of gauges within the lake. The results from individual lakes are discussed in further detail in this section. Overall, the weighted RMS from the model in this study provides a slightly better fit than ICE-5G, and a much better fit than the ANU model.

Table 8.2: Comparison of measured and calculated lake level change rate ($mm.yr^{-1}$)

Gauge	Reference gauge	Measured rate	This Study	ICE-5G	ANU
Cedar Lake					
Oleson Point	Easterville	1.45±0.19	−0.09	0.04	−0.07
Weighted RMS			1.48	1.41	1.51
Dauphin Lake					
Outlet	Ochre Beach	-0.14±0.06	−0.24	−0.20	−0.56
Weighted RMS			0.04	0.07	0.42
Great Slave Lake					
Fort Resolution	Yellowknife Bay	-0.77±0.30	−0.06	0.10	0.15
Hay River	Yellowknife Bay	0.16±0.09	1.29	2.21	1.96
Reliance	Yellowknife Bay	-0.20±1.07	−4.01	−4.69	−6.27
Snowdrift	Yellowknife Bay	-2.67±0.42	−2.72	−3.30	−4.05
Weighted RMS			1.46	1.98	1.79
Lac Seul					
Hudson	Lac Seul	-0.10±0.12	0.20	0.14	0.53

Table 8.2 continued

Gauge	Reference gauge	Measured rate	This Study	ICE-5G	ANU
Weighted RMS			0.29	0.25	0.63
Lake Athabasca					
Fort Chipewyan	Crackingstone Point	1.69±0.07	2.16	2.79	3.61
Bustard Island	Crackingstone Point	0.77±0.30	1.87	2.37	3.14
Weighted RMS			0.71	1.14	1.95
Lake Manitoba					
The Narrows	Steep Rock	-0.01±0.16	0.34	0.31	0.85
Toutes Aides	Steep Rock	0.67±0.17	0.15	0.24	0.47
Delta	Steep Rock	1.21±0.06	0.98	1.05	2.40
Westbourne	Steep Rock	0.45±0.08	1.00	1.08	2.46
Meadow Portage	Steep Rock	0.83±0.94	0.07	0.18	0.26
Weighted RMS			0.41	0.40	1.45
Lake of the Woods					
Clearwater Bay	Warroad	-0.98±0.01	−0.85	−0.84	−1.89
Cyclone Island	Warroad	-0.60±0.03	−0.49	−0.47	−1.05
Hanson Bay	Warroad	-0.75±0.02	−0.52	−0.19	−1.01
Keewatin	Warroad	-0.928±0.004	−0.99	−0.84	−2.19
Kenora	Warroad	-0.61±0.03	−1.02	−0.84	−2.26
Weighted RMS			0.12	0.14	1.21
Lake Winnipeg					
Berens River	Victoria Beach	-1.47±0.23	−1.58	−1.16	−3.98
George Island	Victoria Beach	-1.02±0.69	−1.87	−1.49	−4.58
Matheson Island Landing	Victoria Beach	-1.64±0.49	−0.93	−0.75	−2.42
Mission Point	Victoria Beach	-1.66±0.3	−1.70	−1.48	−3.96
Montreal Point	Victoria Beach	-2.50±0.53	−2.73	−2.08	−6.09
Pine Dock	Victoria Beach	-1.36±0.38	−0.88	−0.69	−2.29
Weighted RMS			0.49	0.45	2.36
Lake Winnipegosis					
Dawson Bay	Winnipegosis	-3.77±0.67	−1.05	−0.51	−2.24
Weighted RMS			3.03	3.26	1.52
Southern Indian Lake					
Missi Falls	Opachuanau Lake	-1.44±0.16	−1.02	−0.77	0.87
South Bay	Opachuanau Lake	-0.84±0.08	0.04	−0.05	0.29
South Indian Lake	Opachuanau Lake	-0.73±0.13	−0.11	−0.14	0.31
Weighted RMS			0.89	0.73	1.37
Weighted RMS	all pairs		0.13	0.18	1.21

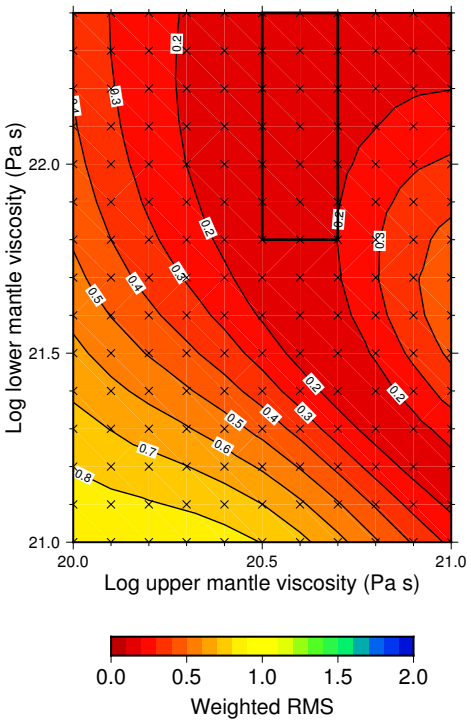

Figure 8.14: Weighted RMS of all lake gauge pairs (29 in total) in this study using variable mantle viscosity, and a lithospheric thickness of 120 km

Cedar Lake

The calculated tilt rate of the single gauge pair at Cedar Lake is very small, compared with the observed rate of 1.45±0.19 mm.yr^{-1}. Varying the Earth model has little effect on the calculated tilt rate (Fig. 8.15). It is suspected that the measured rate is too high. This could be the result of the small duration of overlapping measurement between the gauges (16 years), which may not be long enough to determine a reliable rate. It could also be a result of the effects of damming the lake, which was completed prior the beginning of recording (Chapter 5).

Lake Dauphin

There is one gauge pair in Lake Dauphin, and the calculated rate matches the observed rate (Fig. 8.16). The calculated rate is nearly the same for the suite of Earth models investigated, which indicates that the gauges are too close together to

provide strong constraints on Earth rheology.

Great Slave Lake

There are four gauge pairs in Great Slave Lake, relative to Yellowknife Bay. The weighted RMS indicates that the best fit would require a very low lower mantle viscosity with the ice sheet model here (Fig. 8.17). From the comparison of individual pairs (Table 8.2), the only modelled tilt that matches observations was with respect to Snowdrift. With the exception of Yellowknife Bay, the time series in Great Slave Lake discontinuous, and not always at measured at the same datum. The most suspect pair is with respect to Reliance, which is located east of Snowdrift, and would be expected to have a larger rate given the pattern of GIA in Northwest Territories. If the gauge pair with respect to Snowdrift is reliable, the modelled tilt is consistent with the measured lake level change.

Lac Seul

Lac Seul has a single gauge pair, and the modelled rate does not match the measured rate within two-sigma (Fig. 8.18). The rate is very small and based on a single gauge pair, so it is not considered an important and trustworthy observation to constrain the ice sheet model.

Lake Athabasca

There are two gauge pairs in Lake Athabasca, relative to Crackingstone Point. The optimal fit to the lake tilt falls just below the target upper mantle viscosity (Fig. 8.19). The fit of the model is better with respect to Fort Chipewyan than Bustard Island, which may not be surprising considering that it has a much longer time series. The modelled tilt is consistent with the observation of a larger uplift rate towards the northeast.

Lake Manitoba

There are five gauge pairs in Lake Manitoba, with lake level measured with relative to Steep Rock. The optimal weighted RMS falls within the target viscosity range (Fig. 8.20). Of the individual pairs, the calculated rate with respect to Delta fits best with observations (Table 8.2). The calculated rate at the nearby gauge in Westbourne is nearly the same, but the measured rate is less than half. One possible reason for this discrepancy is that the regulation of the level Lake Manitoba, which began in 1961, may have affected the measurements (the majority of the time series at Delta was prior to regulation). The calculated rates of the other gauge pairs are relatively insensitive to changes in Earth model.

Lake of the Woods

There are five gauge pairs in Lake of the Woods, relative to the southernmost gauge at Warroad. The optimal weighted RMS falls in the target viscosity range (Fig. 8.21). Lake of the Woods has some of the longest duration and best quality lake level observations of all the lakes used in this study, and the close fit of the modelled tilt to the observations gives confidence that the ice model in northwestern Ontario has the right distribution of ice.

Lake Winnipeg

Lake Winnipeg has the most gauge pairs of any of the lakes investigated in this study, with six gauges, measured relative to Victoria Beach at the southern end of the lake. Despite having six gauges, the modelled WRMS is not as tight as with Lake of the Woods (Fig. 8.22), which may not be surprising considering that the uncertainties are generally higher. The optimal RMS values do fall in the target viscosity range, regardless. The calculated rates do match all observations within two-sigma (Table 8.2). The calculated rates are consistent with increasing GIA rates

towards the north. Throughout the modelling exercise, it was determined that the ice thickness in the region north of Lake Winnipeg had to be limited to match the rates in Lake Winnipeg.

Lake Winnipegosis

The gauge pair in Lake Winnipegosis had the highest measured tilt of all of the sites in the study area (Table 8.2). The calculated rate of this pair shows a strong dependence on upper mantle viscosity (Fig. 8.23). Regardless of changes to the ice sheet model, it was not possible to match the observed lake level change within two-sigma. This gauge pair is considered to be anomalous.

Southern Indian Lake

There are three gauge pairs in Southern Indian Lake, relative to Opachuanau Lake. The weighted RMS is not strongly dependent on the Earth model (Fig. 8.24). It appears that the main cause of this is that the measured rates with respect South Bay and South Indian Lake are much larger in magnitude than the calculated rates (Table 8.2). As noted in Chapter 5, these two gauges are suspected to be in a part of the lake that may be periodically affected by conditions that do not affect the other two gauges, and these rates are not considered to be a reliable indicators of GIA. The calculated rate with respect to Missi Falls is closer to the measured value, though slightly to low to fit at the two-sigma level. The modelled value is consistent with increasing GIA uplift velocity towards the northeast in northern Manitoba.

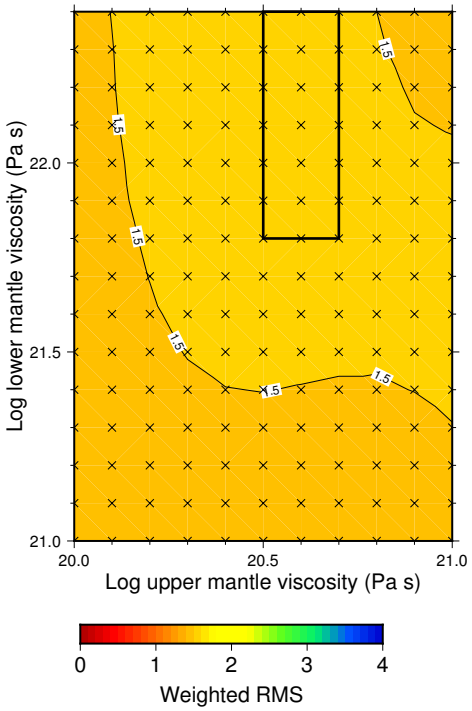

Figure 8.15: Weighted RMS of the gauges pairs in Cedar Lake (one pair) using a lithospheric thickness of 120 km, and variable upper and lower mantle viscosity. The black box indicates the target viscosity range for best fit.

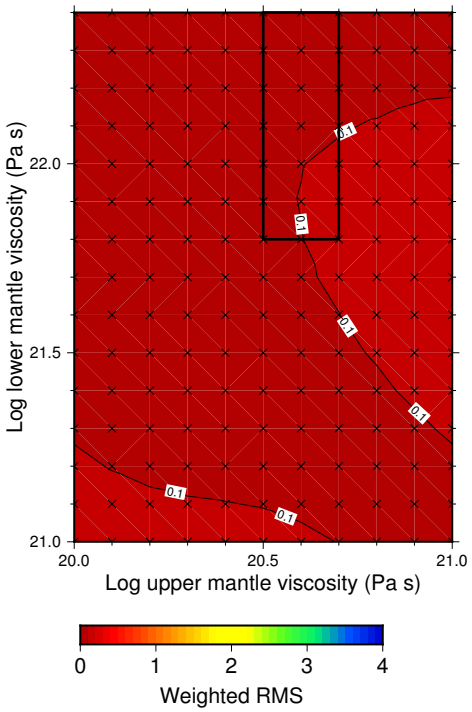

Figure 8.16: Weighted RMS of the gauges pairs in Dauphin Lake (one pair) using a lithospheric thickness of 120 km, and variable upper and lower mantle viscosity. The black box indicates the target viscosity range for best fit.

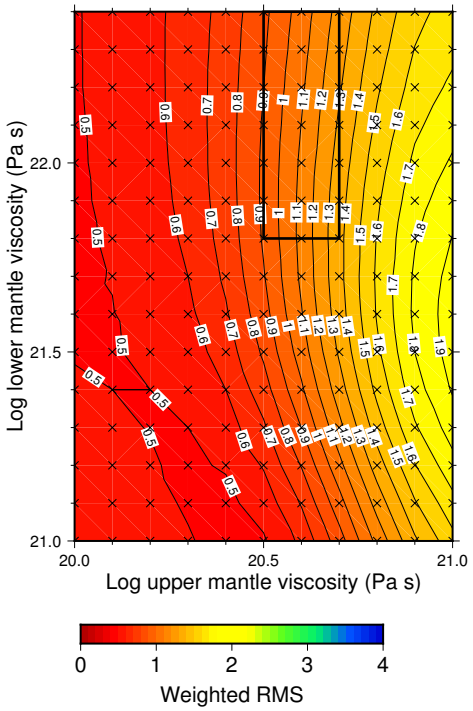

Figure 8.17: Weighted RMS of the gauges pairs in Great Slave Lake (four pairs) using a lithospheric thickness of 120 km, and variable upper and lower mantle viscosity. The black box indicates the target viscosity range for best fit.

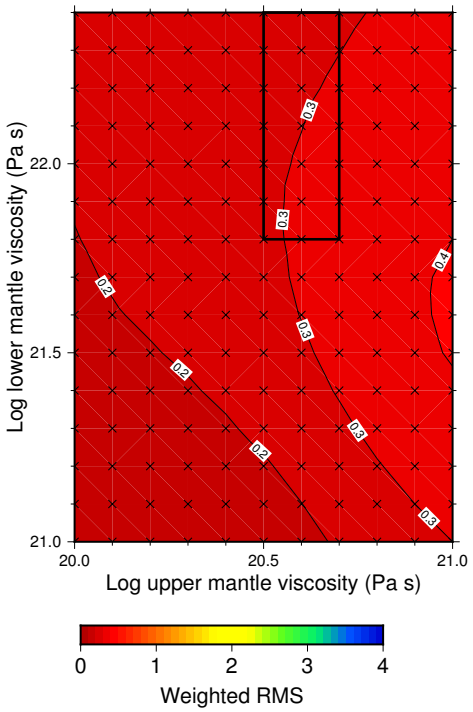

Figure 8.18: Weighted RMS of the gauges pairs in Lac Seul (one pair) using a lithospheric thickness of 120 km, and variable upper and lower mantle viscosity. The black box indicates the target viscosity range for best fit.

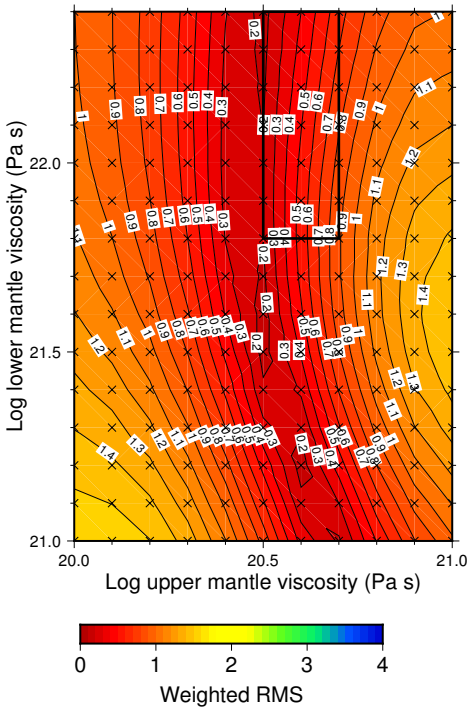

Figure 8.19: Weighted RMS of the gauges pairs in Lake Athabasca (two pairs) using a lithospheric thickness of 120 km, and variable upper and lower mantle viscosity. The black box indicates the target viscosity range for best fit.

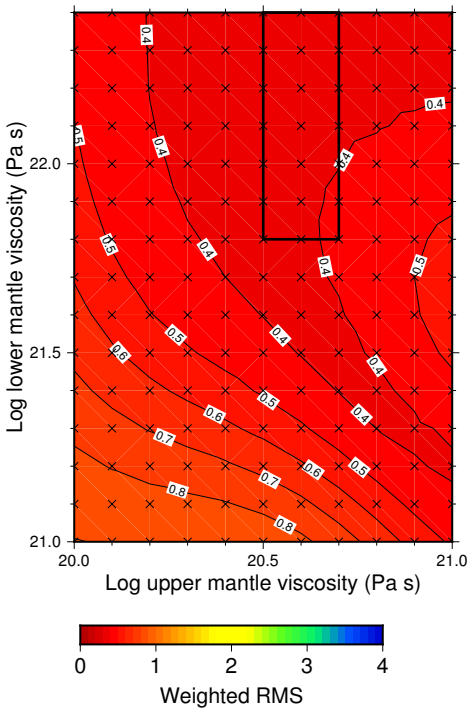

Figure 8.20: Weighted RMS of the gauges pairs in Lake Manitoba (five pairs) using a lithospheric thickness of 120 km, and variable upper and lower mantle viscosity. The black box indicates the target viscosity range for best fit.

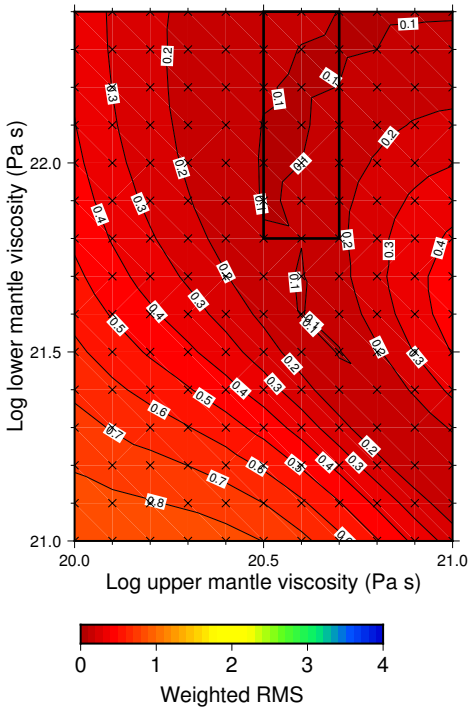

Figure 8.21: Weighted RMS of the gauges pairs in Lake of the Woods (five pairs) using a lithospheric thickness of 120 km, and variable upper and lower mantle viscosity. The black box indicates the target viscosity range for best fit.

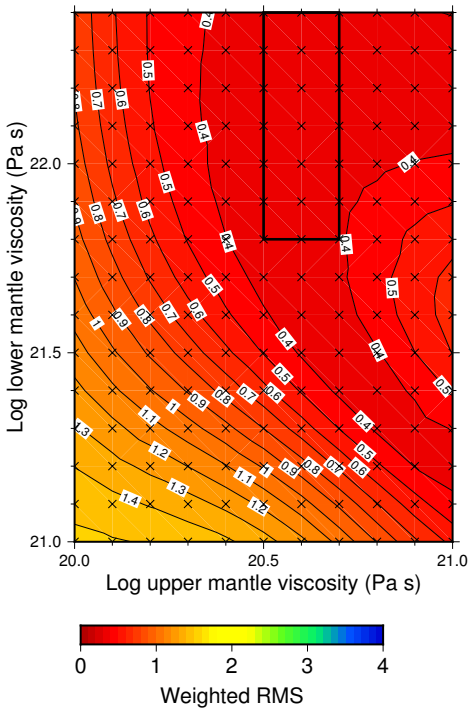

Figure 8.22: Weighted RMS of the gauges pairs in Lake Winnipeg (six pairs) using a lithospheric thickness of 120 km, and variable upper and lower mantle viscosity. The black box indicates the target viscosity range for best fit.

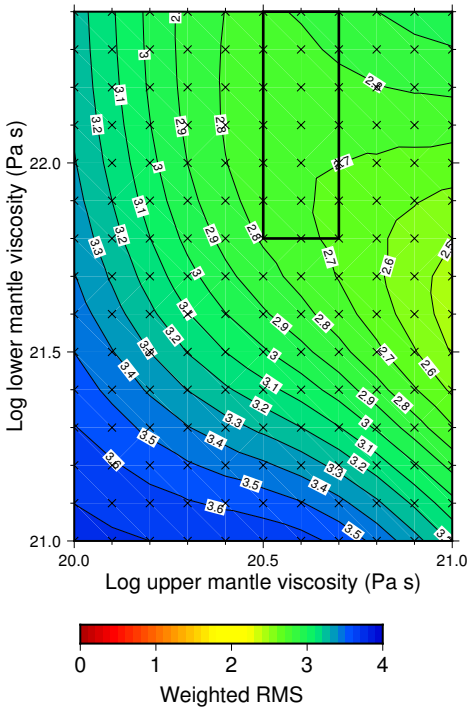

Figure 8.23: Weighted RMS of the gauges pairs in Lake Winnipegosis (one pair) using a lithospheric thickness of 120 km, and variable upper and lower mantle viscosity. The black box indicates the target viscosity range for best fit.

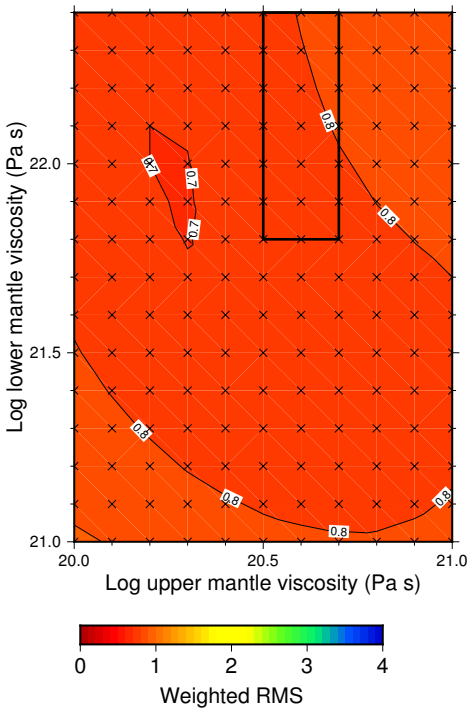

Figure 8.24: Weighted RMS of the gauges pairs in Southern Indian Lake (three pairs) using a lithospheric thickness of 120 km, and variable upper and lower mantle viscosity. The black box indicates the target viscosity range for best fit.

8.4.5 Glacial lake strandline tilts

Introduction

The glacial lake strandline elevation values were determined by calculating the difference in GIA between the present-day and the inferred age of the features. Glacial lake strandline tilt is highly sensitive to ice sheet volume and history (Clark et al., 2008), and should give a good indication that the ice model is robust. Loading due to the water in the lakes was not included (as the lakes were not explicitly modelled). This likely will cause an small error in the ice model, as the lakes may have had substantial amounts of water in them (*i.e.* Lemmen et al., 1994; Teller and Leverington, 2004). Clark et al. (2007) determined the effect of changing water loads for the Great Lakes. They found that lake loading accounted for up to 10% of the observed tilting of paleo-shorelines. One reason to expect that the value is less than that for Lake Agassiz and Lake McConnell is that they existed for a short period of time compared to the Great Lakes, which are still present.

As a test of the magnitude of lake loading, the GIA was calculated using a simple model of Lake Agassiz from volume reconstructions by Leverington et al. (2000, 2002). This model is not used to correct for lake loading, as the volume of the lake is highly dependent on the location of the ice margin. This model has volume estimates for the following lake stages: Herman (set to have an age of 14 100 yr BP), early Moorhead (set to have an age of 12 700 yr BP), Upper Campbell (set to have an age of 10 600 yr BP), Burnside (set to have an age of 9500 yr BP) and The Pas (set to have an age of 8800 yr BP). The ages of the Burnside and The Pas stages are based on the estimates of Teller and Leverington (2004). The GIA calculation was the same as the rest of this study, though the water volume was converted to an equivalent ice volume by dividing the water height by 0.92. The lake loading causes net uplift relative to present along the strandlines, because they

were located at the edge of the lake, and some distance from the deepest parts of the basin. The GIA was calculated at locations along the Herman and Upper Campbell strandlines. For the Herman Strandline, the water load caused uplift 0.6 m at the south end of the lake, and 2.3 m at the north end of the lake. Along the Upper Campbell strandline, the amount of uplift caused by the water loading varied between 0.5 and 7 m. These values are small compared to the total amount of tilt along the entire strandlines, though it will introduce a small error in the ice volume. There are no a-priori estimates of the volume of Lake McConnell, so there was no calulcation done there.

Northern Glacial Lake McConnell

Northern Glacial Lake McConnell has tilt measurements between two strandlines located northeast of Great Bear Lake with respect to the early outlet of the glacial lake. The comparison of modelled and calculated tilt is shown on Fig. 8.25. The ice model presented in this study has a better fit to the observed tilt at a time closer to the younger age limit of the features. Though the tilt fit within the target viscosity range for all tested Earth models with lithospheric thickness values of 90 km-140 km.

To use these data, the margin had to be adjusted from the limits of the minimum timing of retreat model. The margin was set to be located east of the strandlines at 14 000 yr BP, and relatively stable between 14 000 and 13 000 yr BP. In order for the calculated tilt to match observations, the LGM ice thickness northwest of Great Bear Lake could not exceed 1200 m in the ice model. The tilt rate of northern Glacial Lake McConnell supports the inference that there was substantial thinning of the entire northwestern Laurentide Ice Sheet between 18 000 and 14 000 yr BP.

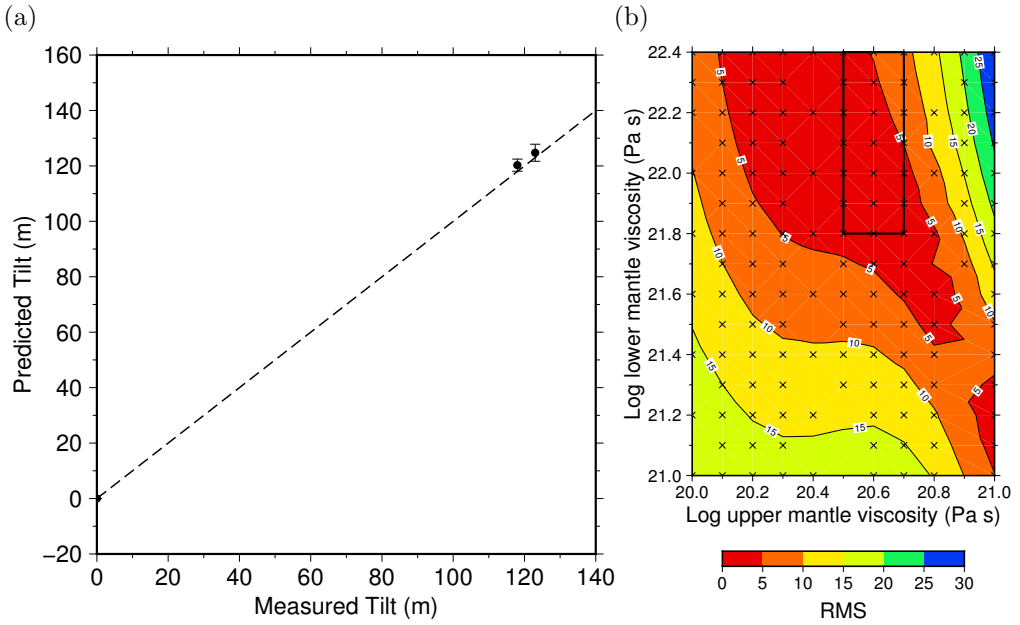

Figure 8.25: Tilt of northern glacial Lake McConnell. (a) Observed versus predicted tilt of northern glacial Lake McConnell using a lithospheric thickness of 120 km, upper mantle viscosity of 4×10^{20} Pa s and lower mantle viscosity of 10^{22} Pa s. The error bars represent the calculated change in elevation between 13 800 yr BP and 13 100 yr BP. The dashed line is the one-to-one line. (b) Contours showing the root mean square (RMS) error of the observed versus calculated tilt at 13 100 yr BP using a variety of Earth models. The black box indicates the target viscosity range for best fit. The dashed line is the one-to-one line.

Southern Glacial Lake McConnell

Southern Glacial Lake McConnell has four features that indicate the amount of tilt relative to the outlet since their formation. The age of these features was assumed to be 11 200-10 800 yr BP. In order to model these lake level indicators, the margin had to be moved several hundred km to the east of the minimum timing limit, to a location that is similar to the reconstruction by Dyke (2004). The modelled tilt at the two eastern-most locations fits the observations fairly closely, and the third location is only underpredicted by about 20 metres (Fig. 8.26). A southernmost fourth observation is underpredicted by over 50 m. The ice sheet margin chronology is reasonably well established in this region (*i.e* Fisher et al., 2009). Adjustments to the ice thickness through time had a relatively equal effect on the modelled

elevation of each feature. The most likely explanation for the discrepancies is that these features formed at slightly different times, therefore when the lake level was different. There were no age or elevation uncertainties estimated for these features, which were only indirectly dated.

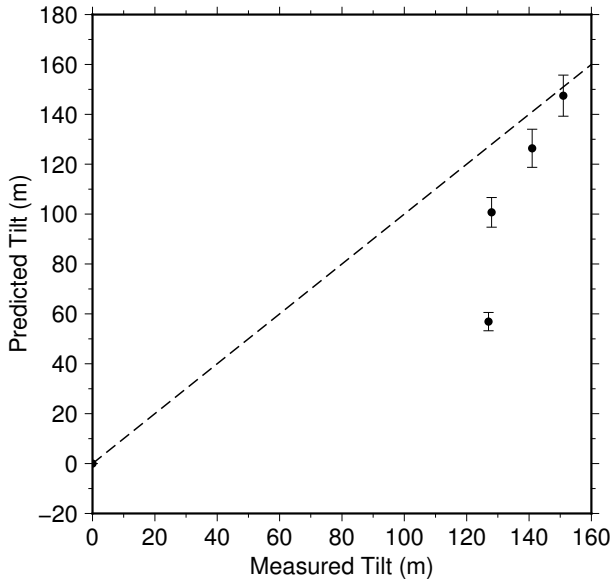

Figure 8.26: Observed versus predicted tilt of southern glacial Lake McConnell using a lithospheric thickness of 120 km, upper mantle viscosity of 4×10^{20} Pa s and lower mantle viscosity of 10^{22} Pa s. The error bars represent the calculated change in elevation between 11 200 yr BP and 10 800 yr BP relative to the reference location. The dashed line is the one-to-one line.

Glacial Lake Agassiz – Herman strandline

The Herman strandline is the oldest of the extensive strandlines in the Lake Agassiz Basin, with an age of 14 400-13 800 yr BP. Fig. 8.27 shows tilt of the strandline relative to the lowest elevation point, near the southern end of the basin. The modelled tilt of the strandline generally comes within a few metres of the observed tilt, though the amount of tilt is overpredicted at some of the locations. Since the elevation of the paleo-lake level has an uncertainty of at least a few metres (McMillan and Teller, 2012), the modelled tilts still fall within the observed range. The best fits to the strandline are at a younger age. In order to attain these tilt values, the

ice lobe that occupied this part of the Lake Agassiz basin had to be very thin and transient. The ice margin at 15 000 yr BP was placed at the Canada-US border, which may be too old to account for the Big Stone Moraine, which was located 400 km to the south (Lepper et al., 2007). The sensitivity of the calculated tilt on local ice cover implies that the moraine may be caused by a short-lived re-advance. The ice surface slope in the southern Lake Agassiz basin had to be shallow, even at the LGM. Higher slopes (*i.e.* increasing the shear stress values) caused the calculated tilt to increase, as the volume of ice became too great in the northern part of the basin.

Glacial Lake Agassiz – Norcross strandline

The Norcross strandline is the second oldest strandline in Lake Agassiz, with an age of 13 800-13 400 yr BP. Like the Herman Strandline, the best fit happens at the younger end of the age range, though the modelled tilt comes within a few metres of the observed tilt throughout the age range (Fig. 8.28).

Glacial Lake Agassiz – Upper Campbell strandline

The Upper Campbell strandline is the most extensive in the Lake Agassiz basin, with an age of 10 800-10 200 yr BP. Due to the continuity of the strandline over a distance in excess of 1000 km, it provides an opportunity to assess the lithospheric thickness in the study area. Fig. 8.29 shows the modelled fit of the tilt of the strandline relative to the location with the lowest elevation, near the southern end of the basin, using lithospheric thickness values of 90 km and 120 km. For most of the strandline, the choice of lithospheric thickness has little impact on the modelled tilt values, except near the southern end of the basin. With a 90 km thick lithosphere, the tilt at the southern end of the basin is underpredicted. Increasing the thickness to 120 km increases the amount of tilt in that region, supporting the use of thicker

lithosphere. Overall, the predicted tilt matches the observations along the entire strandline. At the northern end of the basin, there is a much higher rebound rate, and the modelled tilt is best fit at 10 800 yr BP. The Upper Campbell strandline provides strong support for thin ice (and low shear stress) in the southern part of the study area. The location of the margin is consistent with the reconstruction of Teller and Leverington (2004) during this phase of the lake. The calculated tilt was relatively insensitive to changes in ice thickness in northern Ontario and Manitoba, possibly because the strandline is roughly parallel to the gradient of increasing ice thickness.

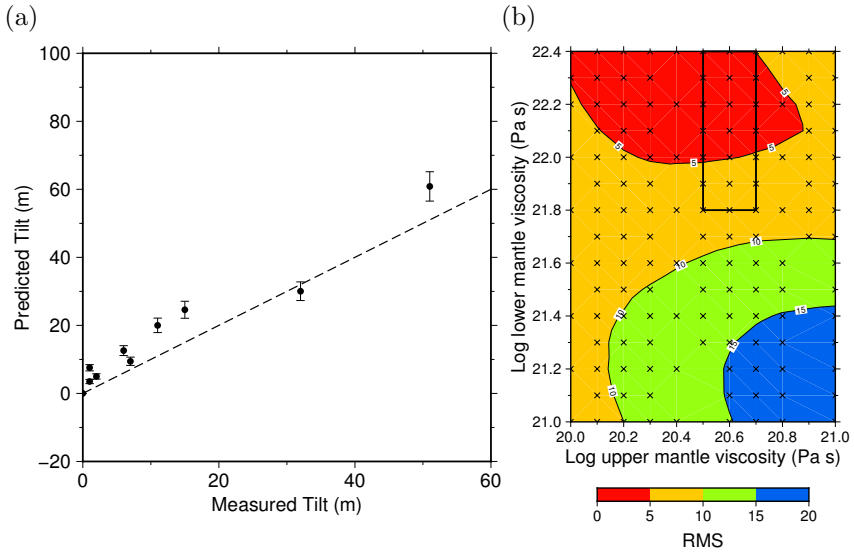

Figure 8.27: Tilt of the Herman strandline of glacial Lake Agassiz, relative to the location with the lowest elevation. (a) Observed versus predicted tilt of the Herman Strandline using a lithospheric thickness of 120 km, upper mantle viscosity of 4×10^{20} Pa s and lower mantle viscosity of 10^{22} Pa s. The error bars represent the calculated change in elevation between 14 400 yr BP and 13 800 yr BP relative to the reference location. The dashed line is the one-to-one line. (b) Contours showing the root mean square (RMS) error of the observed versus calculated tilt at 13 800 yr BP using a variety of Earth models. The black box indicates the target viscosity range for best fit.

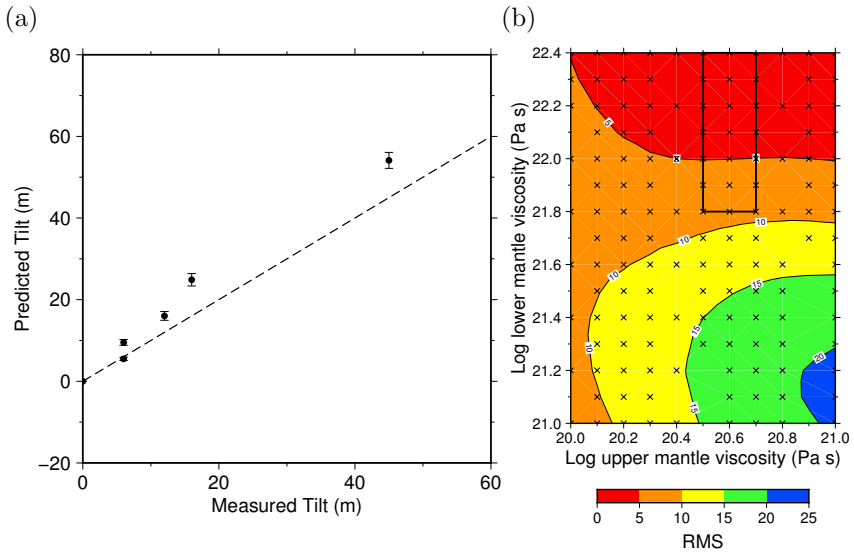

Figure 8.28: Tilt of the Norcross strandline of glacial Lake Agassiz, relative to the location with the lowest elevation. (a) Observed versus predicted tilt of the strandline using a lithospheric thickness of 120 km, upper mantle viscosity of 4×10^{20} Pa s and lower mantle viscosity of 10^{22} Pa s. The error bars represent the calculated change in elevation between 13 800 yr BP and 13 400 yr BP relative to the reference location. (b) Contours showing the root mean square error (RMS) of the observed versus calculated tilt at 13 400 yr BP using a variety of Earth models. The black box indicates the target viscosity range for best fit.

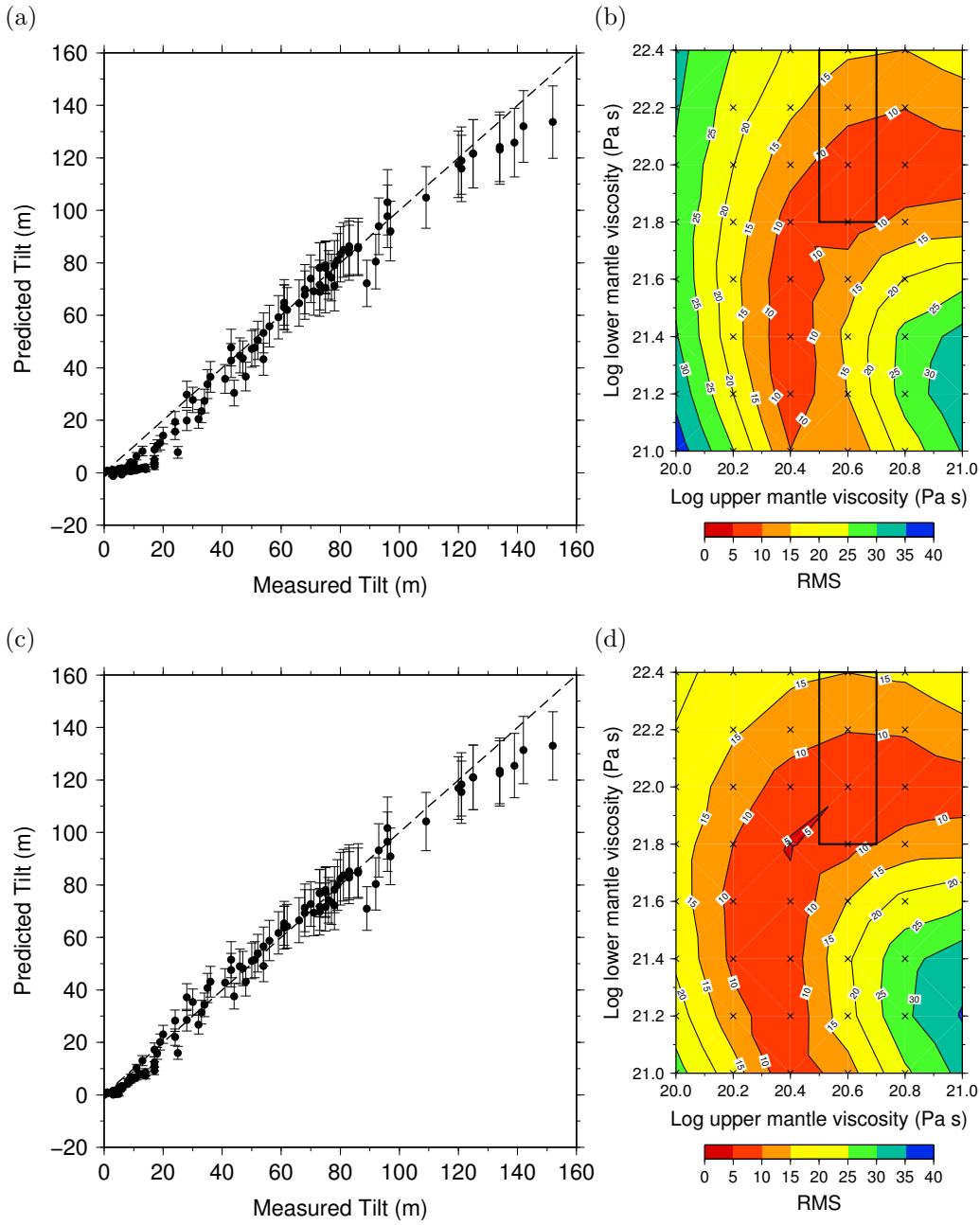

Figure 8.29: Tilt of the Upper Campbell strandline of glacial Lake Agassiz, relative to the location with the lowest elevation. (a) Observed versus predicted tilt of the strandline using a lithospheric thickness of 90 km, upper mantle viscosity of 4×10^{20} Pa s and lower mantle viscosity of 10^{22} Pa s. The error bars represent the calculated change in elevation between 10 800 yr BP and 10 200 yr BP relative to the reference location. The dashed line is the one-to-one line. (b) Contours showing the root mean square (RMS) error of the observed versus calculated tilt at 10 500 yr BP using a variety of Earth models and a 90 km thick lithosphere. The black box indicates the target viscosity range for best fit. (c) Same as (a) but with a lithospheric thickness of 120 km. (d) same as (b) but with a lithospheric thickness of 120 km.

8.4.6 Relative sea level

Introduction

The sea level indicator data are split into 17 regions, though sea level is calculated for each individual sample location. Modelled relative sea level is assessed based on the fit to the observed elevation, and the age of the sample. No attempt was made to model the true relative sea level through time, as most of the data only provide estimates of minimum or maximum sea level. More weight was placed on recently dated samples, which are not as affected by uncertainties in eustatic sea level. For the plots with respect to time, the error bars are the combined uncertainty of observed elevation plus the calculated error for the entire age range of the sample (quadrature sum). For the plots in this section, sea level was calculated using a 120 km thick lithosphere, an upper mantle viscosity of 4×10^{20} Pa s and a lower mantle viscosity of 10^{22} Pa s. As with the previous sections, the modelled sea level was fit to the observations using Earth models with an upper mantle viscosity of $3 - 5 \times 10^{20}$ Pa s and lower mantle viscosity of $> 5 \times 10^{21}$ Pa s.

Effect of reservoir correction uncertainty

In Chapter 6, it was mentioned that using the modern reservoir correction based on the apparent age of shells collected from live specimens prior to atomic bomb testing may be inappropriate for late-glacial shells (*i.e.* Vickers et al., 2010). How much of an effect will this have on the calculated sea level values? An error of several hundred years could result in a large change in the results. In part, this is because of the calibration step, where the calendar age uncertainty of the calibrated radiocarbon age increases during the deglacial period. As an example, the calculated relative sea level change of a sample in the Boothia Peninsula (sample GSC-2093, with an uncalibrated age of 9830±105 yr BP) was determined for a variety of reservoir cor-

rections (Fig. 8.30). The Earth model used for this test had a lithosphere thickness of 120 km, an upper mantle viscosity of 4×10^{20} Pa s and a lower mantle viscosity of 10^{22} Pa s. In this region, the reservoir correction was 335±85. The uncertainty of 85 years was applied equally to all of the reservoir corrections. If the reservoir age of the sample was 0 years rather than 335 years (*i.e.* the average ocean value), the maximum calculated sea level would be between 268-295 m, rather than 218-281 m. If the reservoir correction is increased by 200 years (535 years), the calculated range is 190-270 m. As can be seen, even a small change (on the order of 200-300 years) of the reservoir correction can have a substantial effect on the resulting range of calculated sea level. This is the main reason why the younger samples are favoured over the older ones, because the uncertainty in the reservoir age will have less of an impact on the resulting modelled sea level range, when calculated sea level was not falling as rapidly.

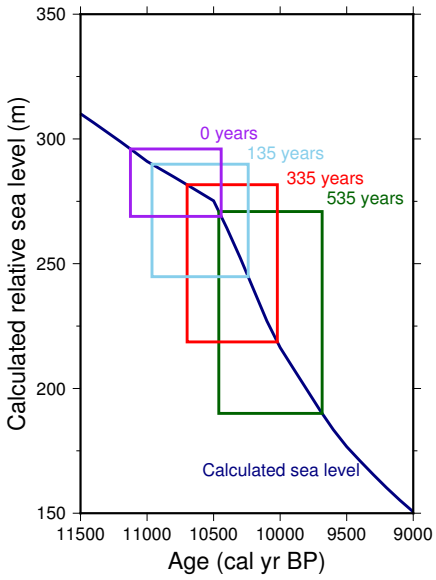

Figure 8.30: Age (at two-sigma) and calculated sea level of GSC-2093 using a variety of reservoir corrections.

Southwestern Hudson Bay

Fig. 8.31 shows the results for southwestern Hudson Bay. This region became ice free after 8500 years ago, with maximum relative sea level in excess of 140 m. Modelled sea level falls within the range of most of the observations. Decreasing the lower mantle viscosity to 6×10^{21} Pa s raises late glacial sea level by about 20-25 m, bringing it up to the higher range of the bounded constraints.

Northwestern Hudson Bay

Northwestern Hudson Bay was the last place to be deglaciated in the study area, and all data are younger than 8000 yr BP (Fig. 8.32). The modelled sea level is consistent with the observations, except for a couple of samples with an age of about 800 yr BP, where sea level is overpredicted by a few metres.

Southampton Island

Southampton Island is located in northwestern Hudson Bay, just outside of the area where the margin history was altered from Dyke (2004). The modelled sea level of several of the samples that have bounded elevation ranges are underpredicted (Fig. 8.33). Most of these were considered by Ross et al. (2012) to be anomalously young. No combination of change to the ice sheet model and Earth model was able to attain calculated sea level that was able to fit the anomalous data and other data simultaneously. The other data reported by Ross *et al.* fit better when a lower mantle viscosity of $4 - 6 \times 10^{21}$ Pa s, which is at the low end of the target viscosity range. Increasing ice thickness was not effective in increasing early deglacial sea level without affecting younger constraints.

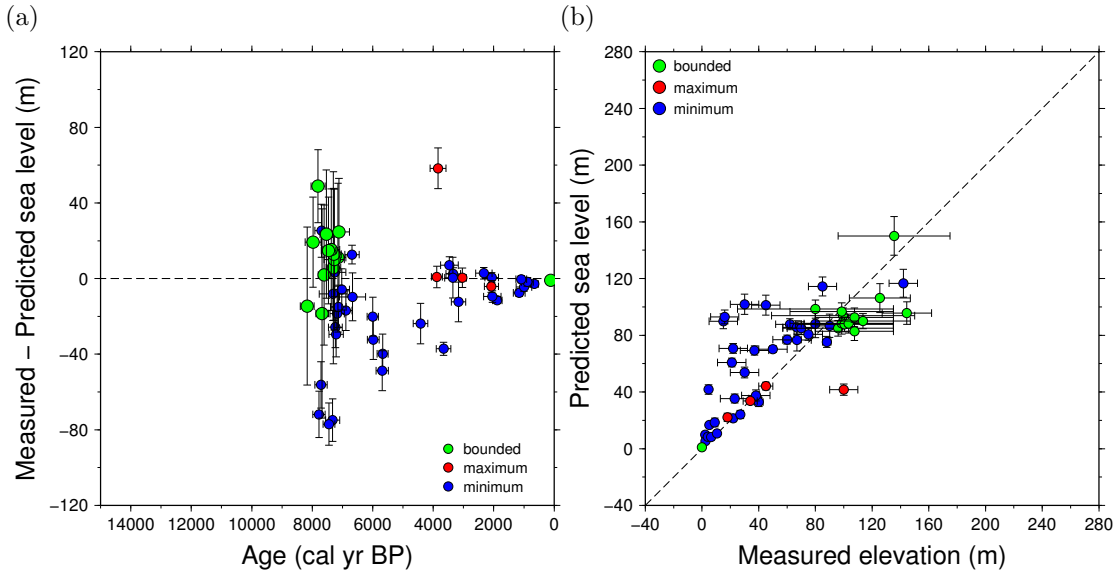

Figure 8.31: Comparison of calculated and observed relative sea level indicators for southwestern Hudson Bay. (a) Difference between sample elevation and calculated sea level. Maximum constraints should fall above the 0 m line, minimum constraints should fall below. (b) Comparison of sample elevation versus calculated sea level. Maximum constraints should be on the bottom right portion of the plot, while minimum constraints should be on the top left side.

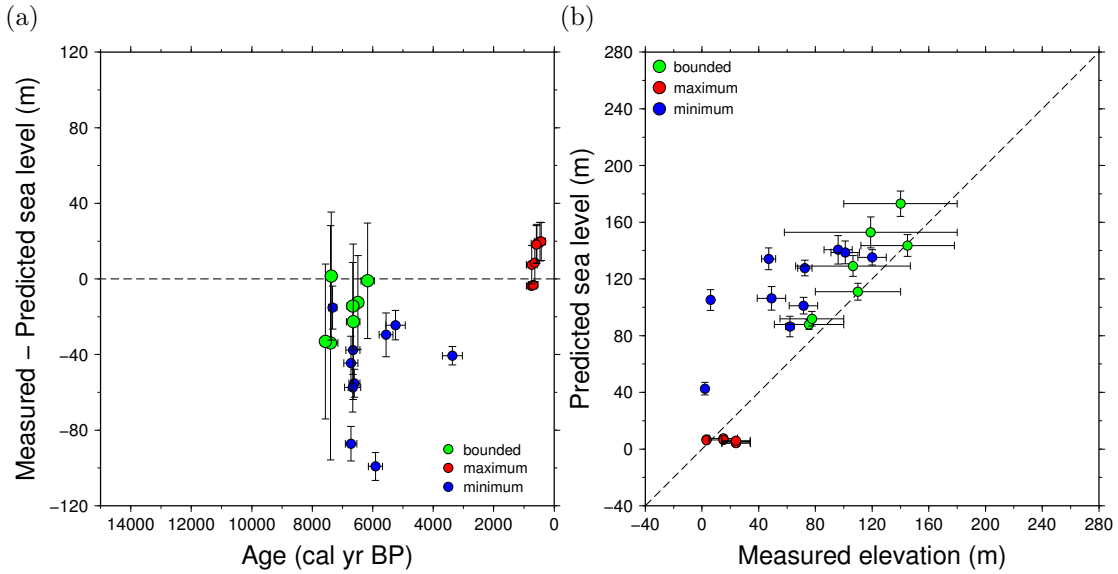

Figure 8.32: Comparison of calculated and observed relative sea level indicators for northwestern Hudson Bay. (a) Difference between sample elevation and calculated sea level. Maximum constraints should fall above the 0 m line, minimum constraints should fall below. (b) Comparison of sample elevation versus calculated sea level. Maximum constraints should be on the bottom right portion of the plot, while minimum constraints should be on the top left side.

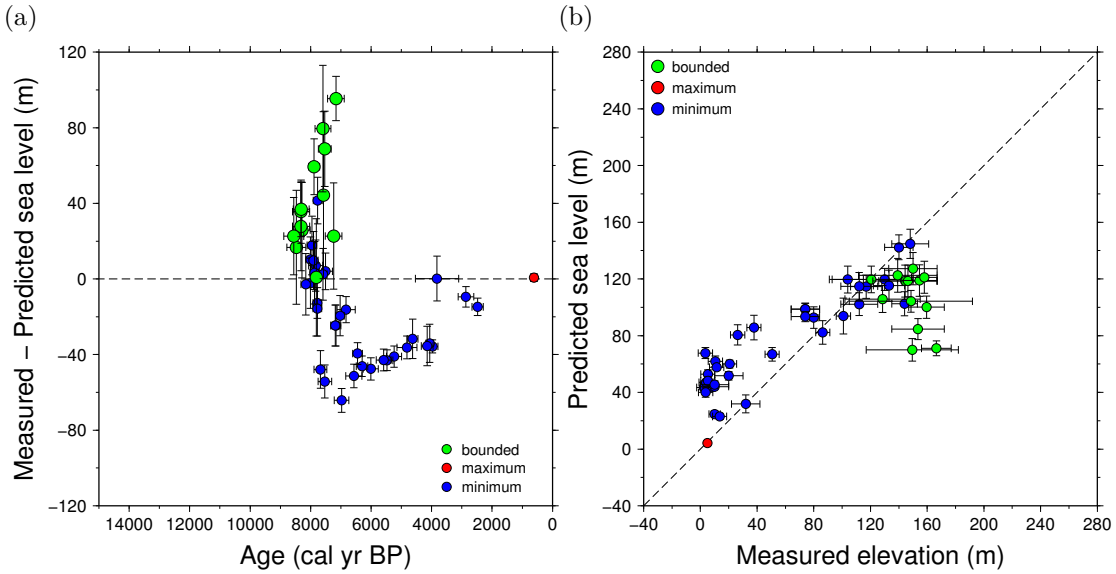

Figure 8.33: Comparison of calculated and observed relative sea level indicators for Southampton Island. (a) Difference between sample elevation and calculated sea level. Maximum constraints should fall above the 0 m line, minimum constraints should fall below. (b) Comparison of sample elevation versus calculated sea level. Maximum constraints should be on the bottom right portion of the plot, while minimum constraints should be on the top left side.

Melville Peninsula

The indicators from the Melville Peninsula were split into two regions, as only the southern portion lay within the study area (Fig. 8.34). Modelled sea level in southern Melville Peninsula match the observations, while predicted sea level matches the majority of the indicators in the northern Melville Peninsula. These results give confidence that the amount of ice covering the Foxe Basin is properly modelled, even without detailed analysis.

Boothia Peninsula

Similar to the Melville Peninsula, Boothia Peninsula was split into two regions, as only the southern portion lay within the study area (Fig. 8.35). Modelled sea level is consistent with the constraints for the southern part of the peninsula. There is one minimum constraint that is underpredicted by over 60 m, which may indicate it

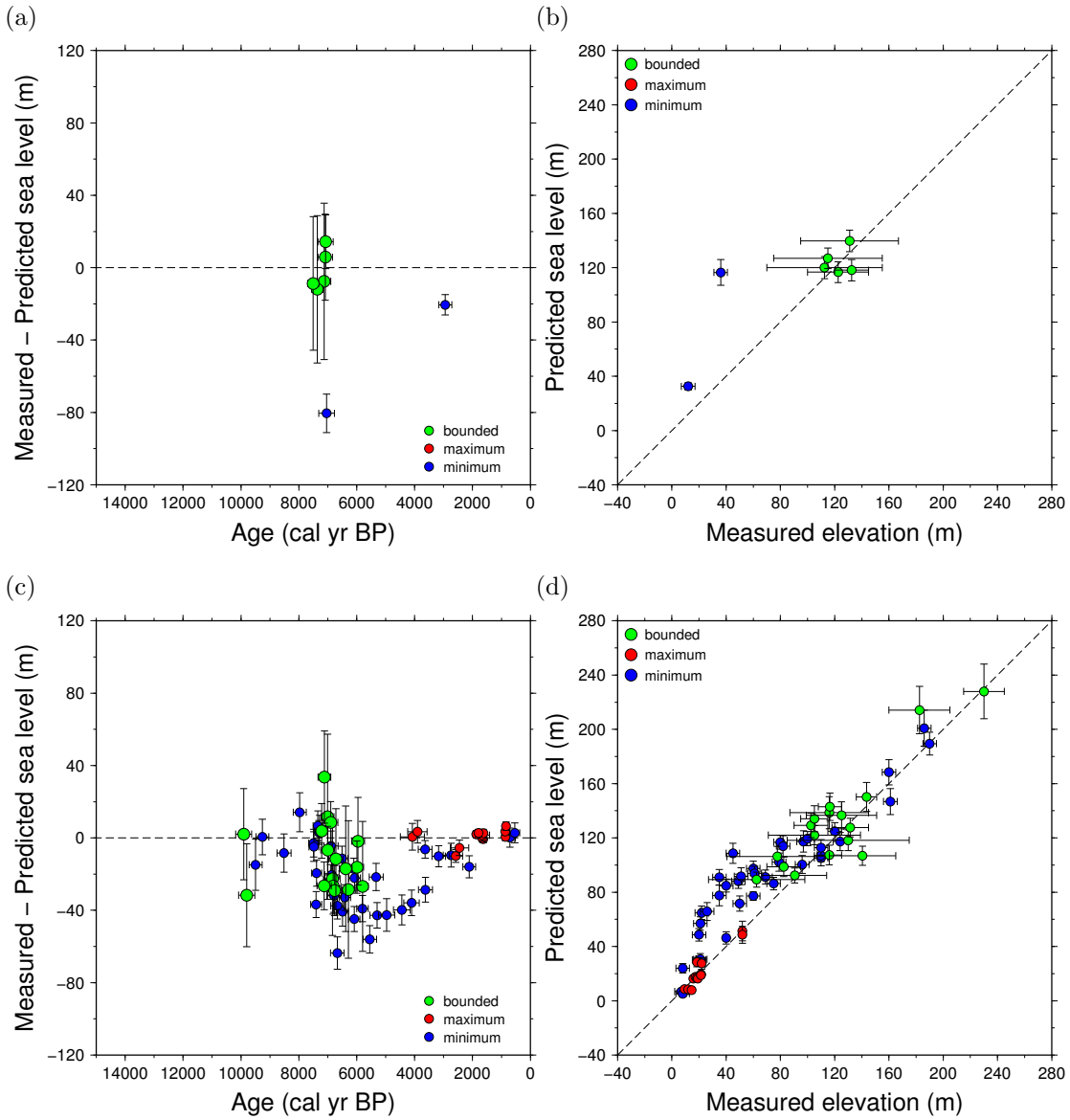

Figure 8.34: Comparison of calculated and observed relative sea level indicators for the Melville Peninsula. (a) Difference between sample elevation and calculated sea level for southern Melville Peninsula. Maximum constraints should fall above the 0 m line, minimum constraints should fall below. (b) Comparison of sample elevation versus calculated sea level for southern Melville Peninsula. Maximum constraints should be on the bottom right portion of the plot, while minimum constraints should be on the top left side. (c) Difference between sample elevation and calculated sea level for northern Melville Peninsula. (b) Comparison of sample elevation versus calculated sea level for northern Melville Peninsula.

is anomalously young. In the northern part of the peninsula, the relative sea level history after 6000 yr BP is well determined by minimum and maximum constraints, suggesting that the ice thickness in my model is adequate in this region. Increasing ice thickness in this region during the LGM causes calculated sea level after 6000 yr BP to be too high. These data are also not highly sensitive to the choice of Earth model. Modelled sea level for samples with ages between 11 000 and 8000 yr BP is too low. In order to fit these data, a lower mantle viscosity of about 2.5×10^{21} Pa s would be required, though this is below the target viscosity range. The misfit could be due to deficiencies in the ice margin history for this region, as it was not adjusted from the Dyke (2004) reconstruction. Alternatively, the data could be anomalously young. If the late-glacial reservoir age was less than the present value (335±85 years, Coulthard et al., 2010), this would cause the calibrated radiocarbon age of these samples to be too young.

King William Island

The modelled sea level of King William Island is generally consistent with observations (Fig. 8.36). There are some maximum constraints where sea level is overpredicted. Dyke and Savelle (2009) noted that several samples from their survey of King William Island appeared to be too old given their elevation. This is the likely reason for the misfit. Increasing the lower mantle viscosity slightly causes the calculated mid-lake Holocene sea level to decrease, but it causes a misfit to the early Holocene minimum sea level indicators.

Northwestern mainland Nunavut

Northwestern mainland Nunavut was split into three regions (Figs. 8.37 and 8.38). The maximum elevation of sea level increases towards the east in this area (Kerr, 1996). Predicted sea level is generally consistent with the observations. Calculated

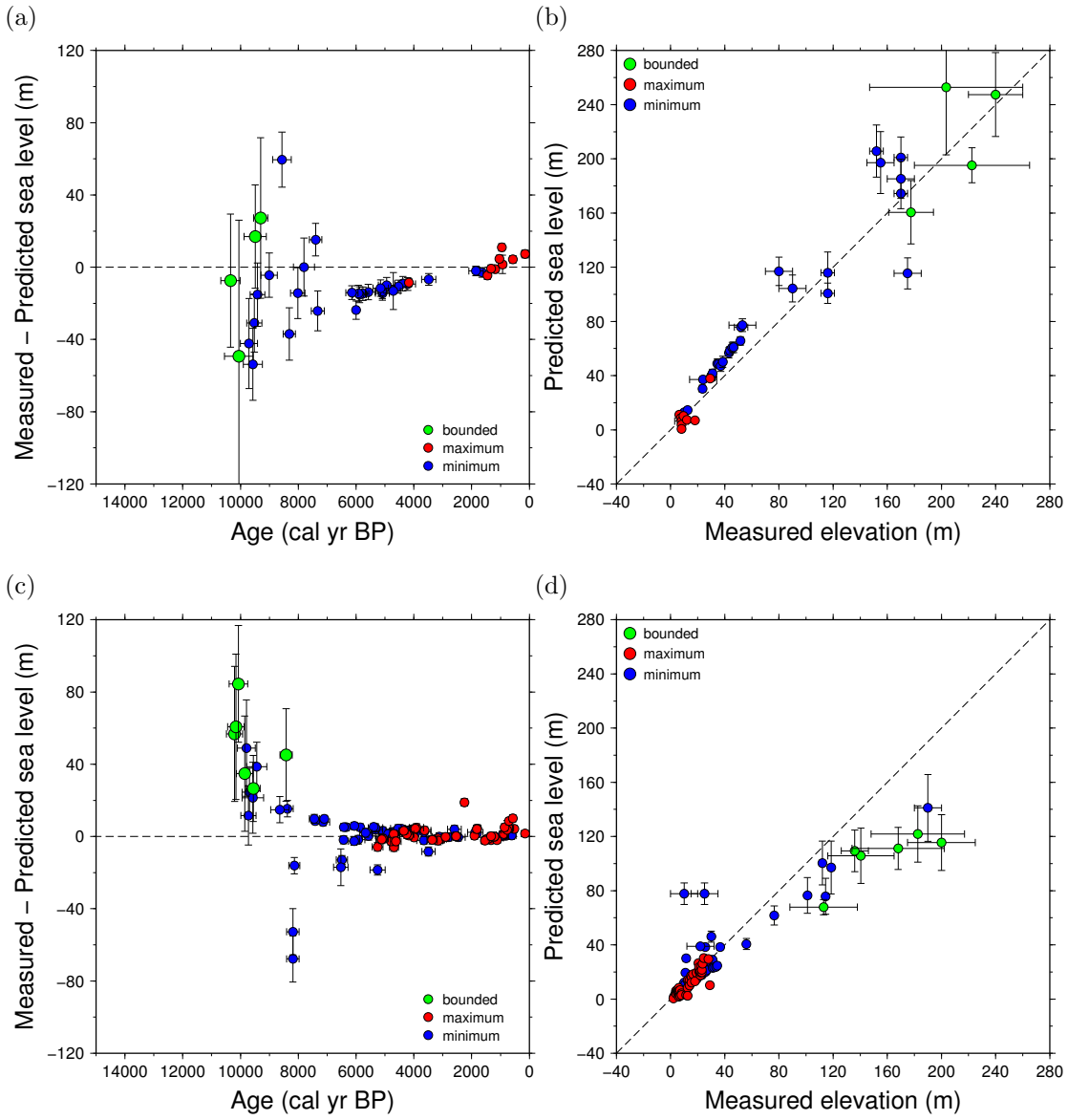

Figure 8.35: Comparison of calculated and observed relative sea level indicators for the Boothia Peninsula. (a) Difference between sample elevation and calculated sea level for southern Boothia Peninsula. Maximum constraints should fall above the 0 m line, minimum constraints should fall below. (b) Comparison of sample elevation versus calculated sea level for southern Boothia Peninsula. Maximum constraints should be on the bottom right portion of the plot, while minimum constraints should be on the top left side. (c) Difference between sample elevation and calculated sea level for northern Boothia Peninsula. (d) Comparison of sample elevation versus calculated sea level for northern Boothia Peninsula.

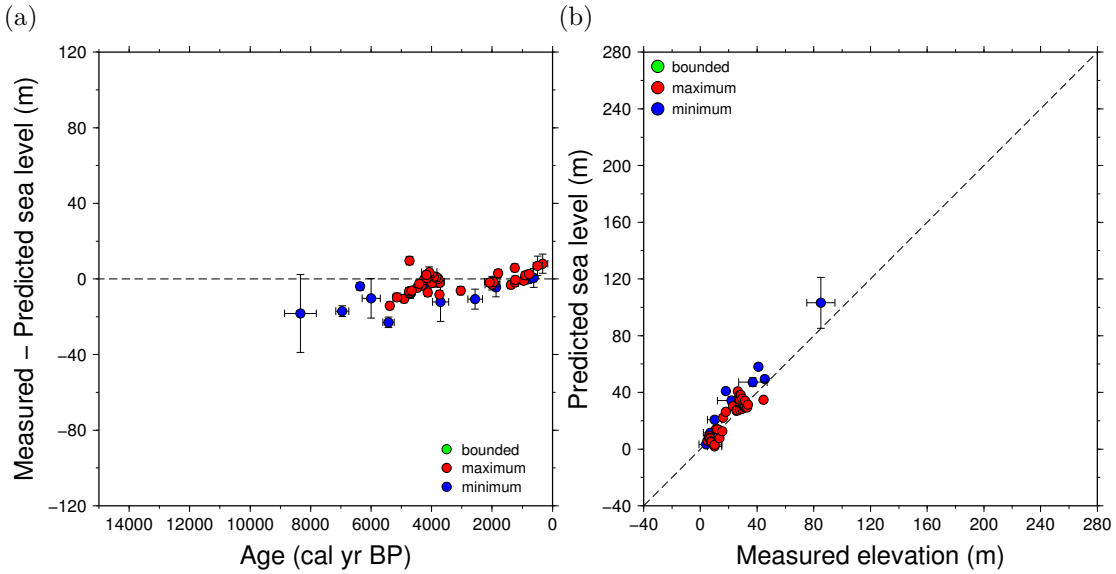

Figure 8.36: Comparison of calculated and observed relative sea level indicators for King William Island. (a) Difference between sample elevation and calculated sea level. Maximum constraints should fall above the 0 m line, minimum constraints should fall below. (b) Comparison of sample elevation versus calculated sea level. Maximum constraints should be on the bottom right portion of the plot, while minimum constraints should be on the top left side.

sea level is underestimated during the period between 10 000 and 12 000 yr BP. Despite efforts to adjust the ice model within the study area, an improved fit was not found. This could be due to deficiencies in the ice margin reconstructions in the Arctic Archipelago. Decreasing lower mantle viscosity improves the fit of the data in this time range, but causes sea level to be too high to fit the data older than 12 000 yr BP.

Mackenzie Delta

The majority of the sea level indicators for the Mackenzie Delta region are maximum constraints, as relative sea level remained below present after deglaciation (Fig. 8.39). Modelled sea level is consistent with the observations in this region. This indicates that the amount of ice in my model is not excessive in this area.

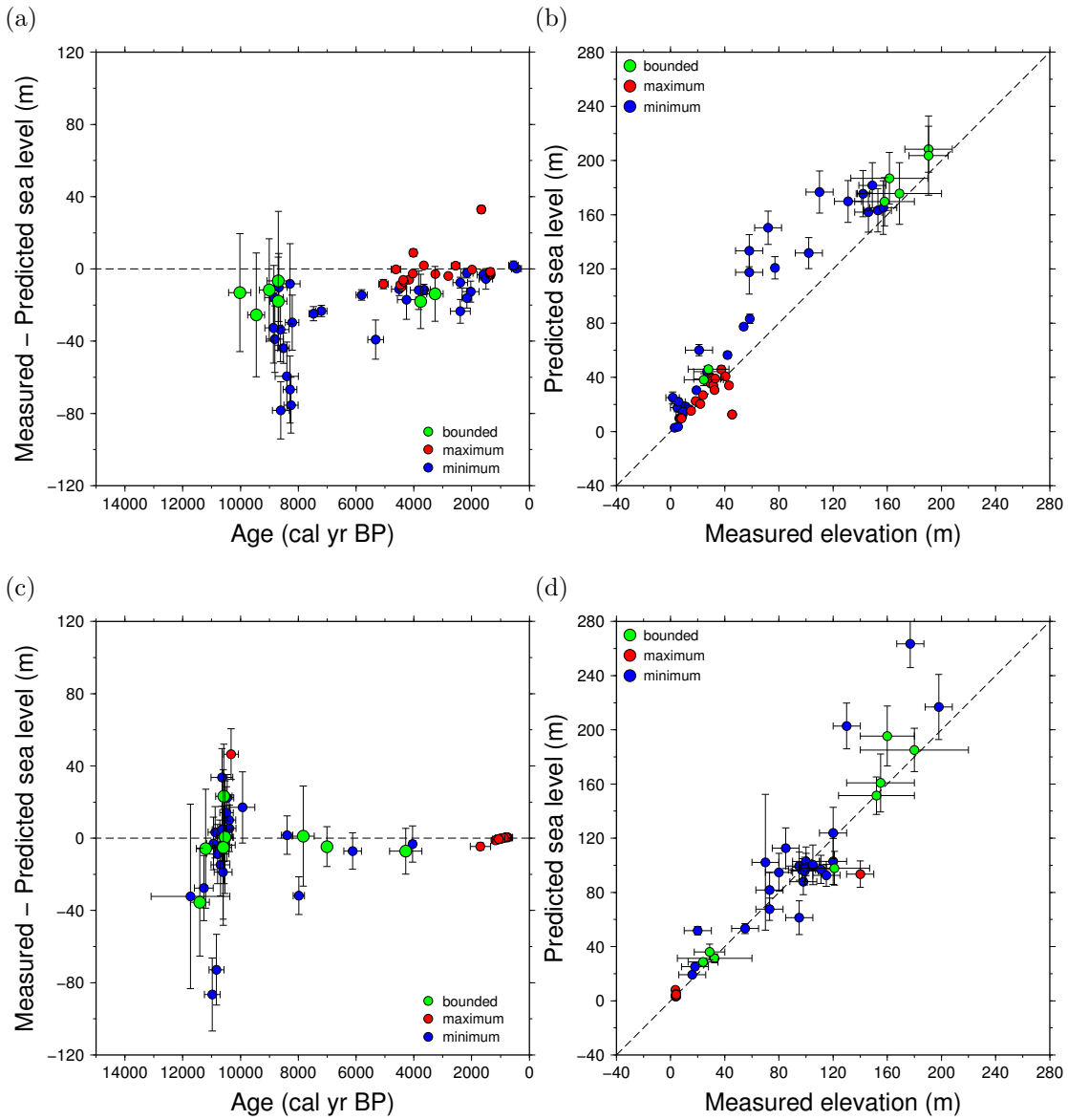

Figure 8.37: Comparison of calculated and observed relative sea level indicators for the northwestern mainland Nunavut. (a) Difference between sample elevation and calculated sea level for Bathurst Inlet and Kent Peninsula. Maximum constraints should fall above the 0 m line, minimum constraints should fall below. (b) Comparison of sample elevation versus calculated sea level for Bathurst Inlet and Kent Peninsula. Maximum constraints should be on the bottom right portion of the plot, while minimum constraints should be on the top left side. (c) Difference between sample elevation and calculated sea level for the mainland Coronation Gulf. (d) Comparison of sample elevation versus calculated sea level for mainland Coronation Gulf.

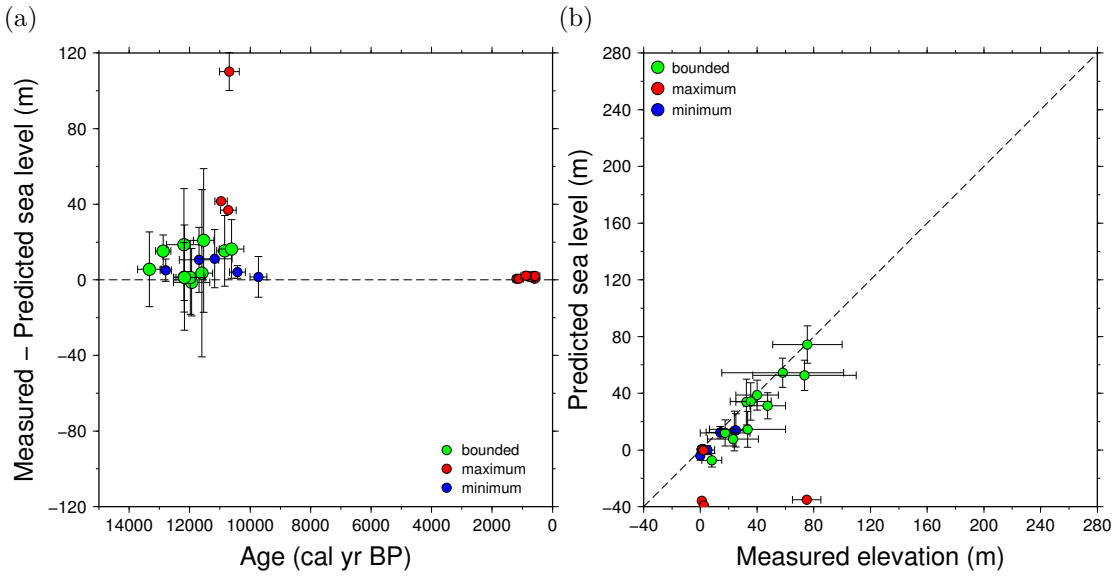

Figure 8.38: Comparison of calculated and observed relative sea level indicators for mainland Amundsen Gulf. (a) Difference between sample elevation and calculated sea level. Maximum constraints should fall above the 0 m line, minimum constraints should fall below. (b) Comparison of sample elevation versus calculated sea level. Maximum constraints should be on the bottom right portion of the plot, while minimum constraints should be on the top left side.

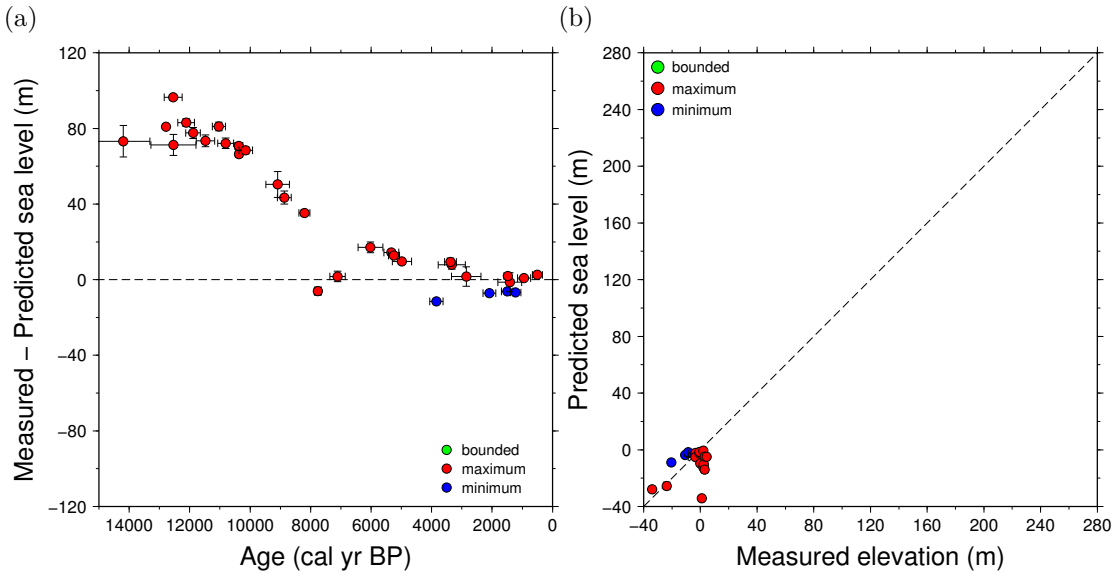

Figure 8.39: Comparison of calculated and observed relative sea level indicators for the Mackenzie Delta. (a) Difference between sample elevation and calculated sea level. Maximum constraints should fall above the 0 m line, minimum constraints should fall below. (b) Comparison of sample elevation versus calculated sea level. Maximum constraints should be on the bottom right portion of the plot, while minimum constraints should be on the top left side.

Victoria and Banks Islands

The Victoria and Banks Islands lie to the north of the study area, but samples located in the southern portions of these islands were included in the analysis to ensure that the amount of ice in that region was correct. The results of modelling sea level on Victoria Island are shown on Figs. 8.40 and 8.41 and Banks Island on Fig. 8.42. As in the adjacent regions on mainland Nunavut, modelled sea level between 10 000 and 12 000 yr BP is underestimated, indicating that there may be a problem with the margin chronology at this time. The tight fit of modelled mid-late Holocene sea level indicates that the long term ice volume estimates in the model are likely correct.

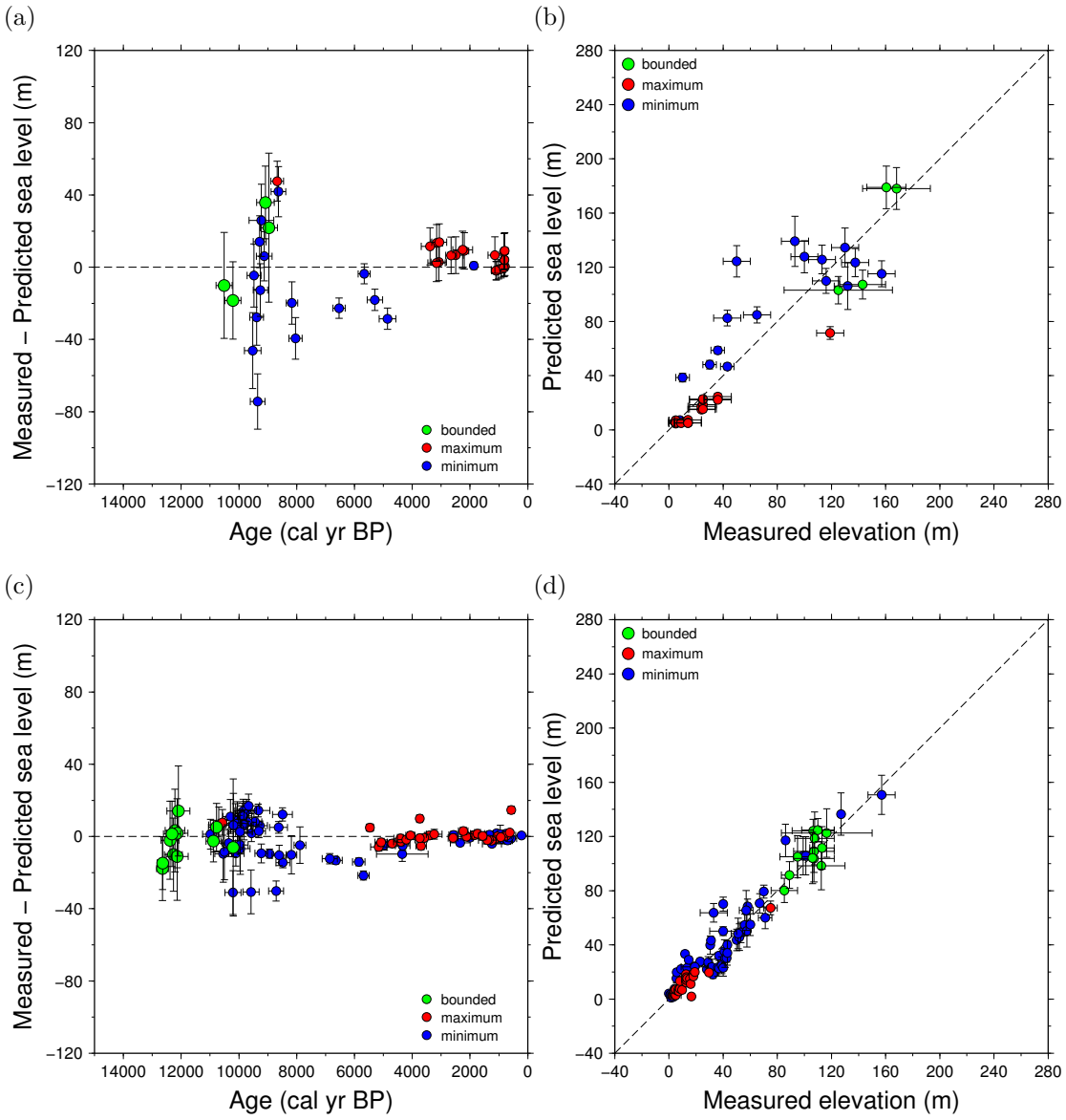

Figure 8.40: Comparison of calculated and observed relative sea level indicators for Victoria Island. (a) Difference between sample elevation and calculated sea level for southeastern Victoria Island. Maximum constraints should fall above the 0 m line, minimum constraints should fall below. (b) Comparison of sample elevation versus calculated sea level for southeastern Victoria Island. Maximum constraints should be on the bottom right portion of the plot, while minimum constraints should be on the top left side. (c) Difference between sample elevation and calculated sea level for the southwestern Victoria Island. (d) Comparison of sample elevation versus calculated sea level for southwestern Victoria Island.

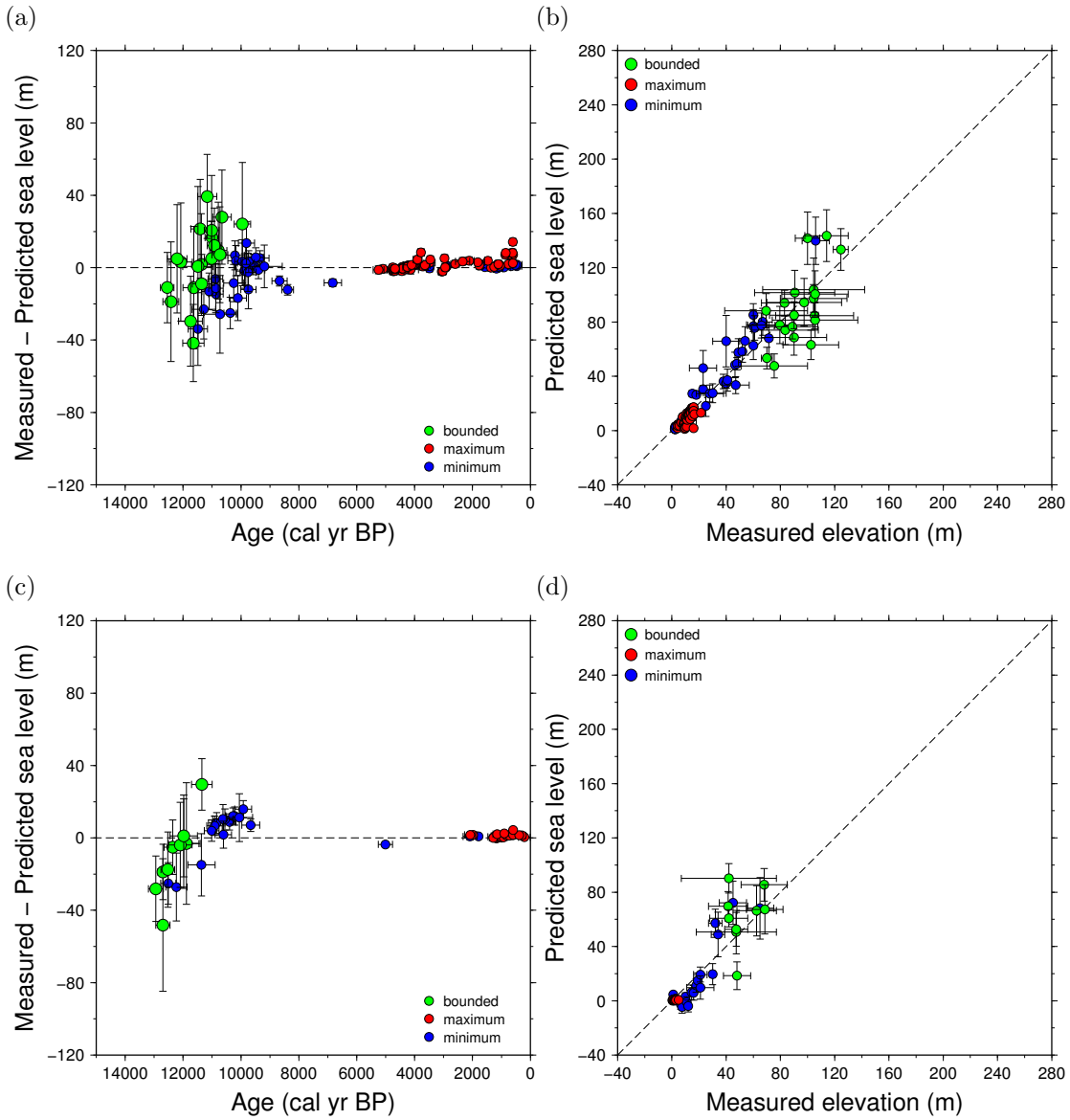

Figure 8.41: Comparison of calculated and observed relative sea level indicators for Victoria Island. (a) Difference between sample elevation and calculated sea level for Prince Albert Sound. Maximum constraints should fall above the 0 m line, minimum constraints should fall below. (b) Comparison of sample elevation versus calculated sea level for Prince Albert Sound. Maximum constraints should be on the bottom right portion of the plot, while minimum constraints should be on the top left side. (c) Difference between sample elevation and calculated sea level for northwestern Victoria Island. (d) Comparison of sample elevation versus calculated sea level for northwestern Victoria Island.

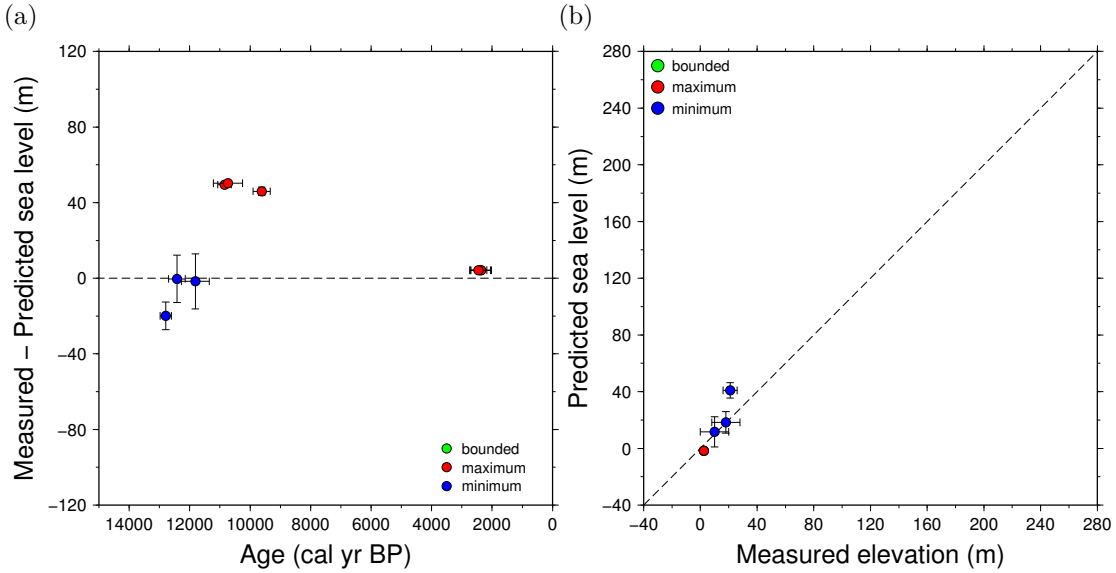

Figure 8.42: Comparison of calculated and observed relative sea level indicators for southern Banks Island. (a) Difference between sample elevation and calculated sea level. Maximum constraints should fall above the 0 m line, minimum constraints should fall below. (b) Comparison of sample elevation versus calculated sea level. Maximum constraints should be on the bottom right portion of the plot, while minimum constraints should be on the top left side.

8.5 Comparison with other ice models

8.5.1 Introduction

There are two other ice sheet models of the Laurentide Ice Sheet that were developed based on observations of GIA, which can be compared with the model in this study. ICE-5G (Peltier, 2004) was developed with the primary goal of fitting relative and eustatic sea level since the LGM. The Earth model used to calculate GIA and sea level to compare the model from this study with the others has a lithospheric thickness of 120 km, an upper mantle viscosity of 4×10^{20} and a lower mantle viscosity of 10^{22} Pa s. The ANU model has a lithospheric thickness of 100 km, an upper mantle viscosity of 4.5×10^{20} Pa s, and a lower mantle viscosity of 10^{22} Pa s. The rheology model for ICE-5G is based on VM2, which is described in section 8.4.2. As demonstrated in the previous section, most of the GIA data can be fit with a higher viscosity. Any estimate of lower mantle viscosity based purely on GIA observations is ambiguous. The ANU Laurentide ice sheet model has yet to be published (K. Lambeck and A. Purcell, *pers. comm.*, 2011). The methodology used to develop this model is similar to the present study (Lambeck et al., 2010), though the ANU model did not include the glacial lake strandline tilt observations or GPS vertical velocities. Figures showing the predicted sea level and glacial lake tilt from these two models is shown in Appendix C.

8.5.2 Ice volume estimates

Table 8.3 shows the ice volume and sea level equivalent (*i.e.* how much the volume of ice would decrease global sea level) for the three models. The ice volume is only compared for the study area, and does not include other parts of the Laurentide Ice Sheet that were not adjusted to fit observations. The sea level equivalent is calculated based on modern ocean area, and therefore will be underestimated during

times when global ice sheets were extensive, as ocean area decreased when sea level was lower. At 21 000 yr BP, the modelled volume of ice in my model is about 46% lower than ICE-5G and 23% lower than the ANU model in the study area. The primary reason for this difference is that the model in this study has far less ice in the region southwest of Hudson Bay (Fig. 8.43). The other two models did not incorporate the strandline tilt data from Lake Agassiz, which may explain why they included more ice there. ICE-5G has a large (about 30% or 3.8×10^6 km^3) drop in ice volume between 14 500 and 14 000 yr BP, to simulate Meltwater Pulse 1A. The model in this study has a decrease in ice volume of 1.8×10^6 km^3 between 15 000 and 14 000 yr BP. The ANU model has a much more gradual decrease in ice volume, with the largest decrease between 14 000 and 13 000 yr BP. By 12 000 yr BP, the ANU model has the same ice volume as the model in this study. The volume of ICE-5G becomes similar to the model in this study at 10 000 yr BP.

Table 8.3: Ice volume and sea level equivalent (SLE) of ICE-5G, the ANU model and this study for the study area

Time (kyr BP)	ICE-5G volume (10^6 km^3)	ICE-5G SLE (m)*	ANU volume (10^6 km^3)	ANU SLE (m)*	This study volume (10^6 km^3)	This study SLE (m)*
21	15.08	37.60	10.66	26.58	8.20	20.45
20	14.99	37.38	10.43	26.00	8.34	20.80
19	14.91	37.18	9.74	24.29	8.40	20.93
18	14.77	36.82	9.45	23.57	8.45	21.06
17	14.71	36.68	9.11	22.72	8.31	20.73
16.5	14.64	36.50	8.91	22.21	7.64	19.04
16	14.57	36.32	8.65	21.56	6.96	17.35
15.5	13.91	34.68	8.35	20.83	6.17	15.39
15	13.25	33.04	8.07	20.13	5.39	13.44
14.5	12.79	31.88	7.85	19.58	4.75	11.85
14	8.97	22.35	6.93	17.28	4.11	10.25
13.5	7.69	19.18	5.62	14.00	3.85	9.61
13	6.35	15.82	4.53	11.31	3.58	8.93
12.5	5.31	13.24	3.74	9.31	3.21	8.01
12	4.05	10.10	3.06	7.63	3.01	7.50
11.5	3.80	9.48	2.98	7.44	2.77	6.91
11	3.06	7.63	2.57	6.42	2.27	5.66

continued...

... continued

Time (kyr BP)	ICE-5G volume (10^6 km^3)	ICE-5G SLE (m)*	ANU volume (10^6 km^3)	ANU SLE (m)*	This study volume (10^6 km^3)	This study SLE (m)*
10.5	2.29	5.72	2.19	5.46	1.83	4.56
10	1.36	3.39	1.77	4.40	1.44	3.59
9.5	1.05	2.61	1.28	3.20	1.13	2.81
9	0.66	1.65	0.80	1.98	0.90	2.23
8.5	0.42	1.04	0.61	1.53	0.57	1.42
8	0.10	0.26	0.43	1.08	0.22	0.54
7.5	0.06	0.14	0.25	0.63	0.05	0.14
7	0.00	0.00	0.07	0.18	0.02	0.04

* Sea level equivalent was calculated by multiplying the volume of ice by 0.9 and dividing by the area of the area of the modern ocean (361×10^6 km^3) (following Licciardi et al., 1998).

Fig. 8.43 shows a comparison of the ice thickness of the three models at 20 000 yr BP. The peak ice thickness for the other models is in excess of 5000 m, while it is about 4000 m in the model from this study. The ice thickness is substantially thinner in central Manitoba and northern Ontario in the model from this study. The ice thickness in the southern part of the ice sheet in the model from this study is similar to the ANU model. ICE-5G has similar ice volume in the northern coastal regions. the model from this study has minimal ice volume in Hudson Bay compared with the other models. Fig. 8.44 shows the comparison at about 13 000 yr BP, after Meltwater Pulse 1A. The ice margin location in ICE-5G is similar to the model from this study, though it has a far larger ice volume. Peak ice thickness is located in the same area in the ANU model, but it has much lower ice thickness in northwestern Manitoba than the model from this study.

8.5.3 GPS vertical velocity rates

The vertical velocity rates for all three models are on (Table 8.1). ICE-5G and the model from this study both fit the station at Baker Lake within two-sigma, while the ANU model significantly overpredicts the rate. The ANU model has the closest to the rate at Churchill, while ICE-5G overestimates it by over 3 mm.yr^{-1}. The

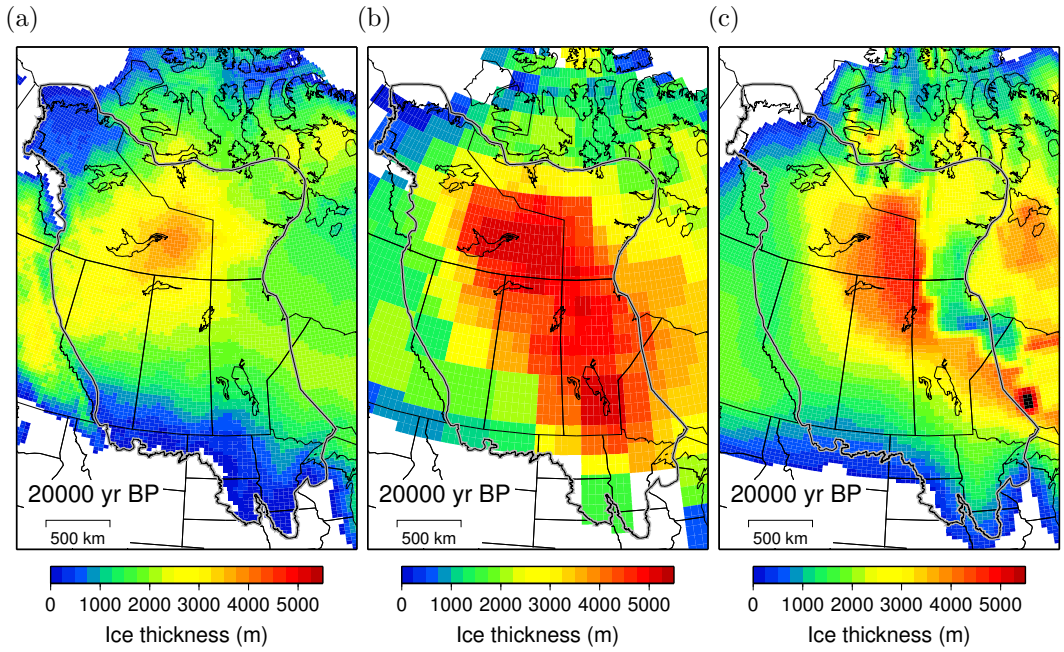

Figure 8.43: Comparison of the three ice sheet models at 20 000 yr BP. (a) This Study. (b) ICE-5G (c) ANU Model.

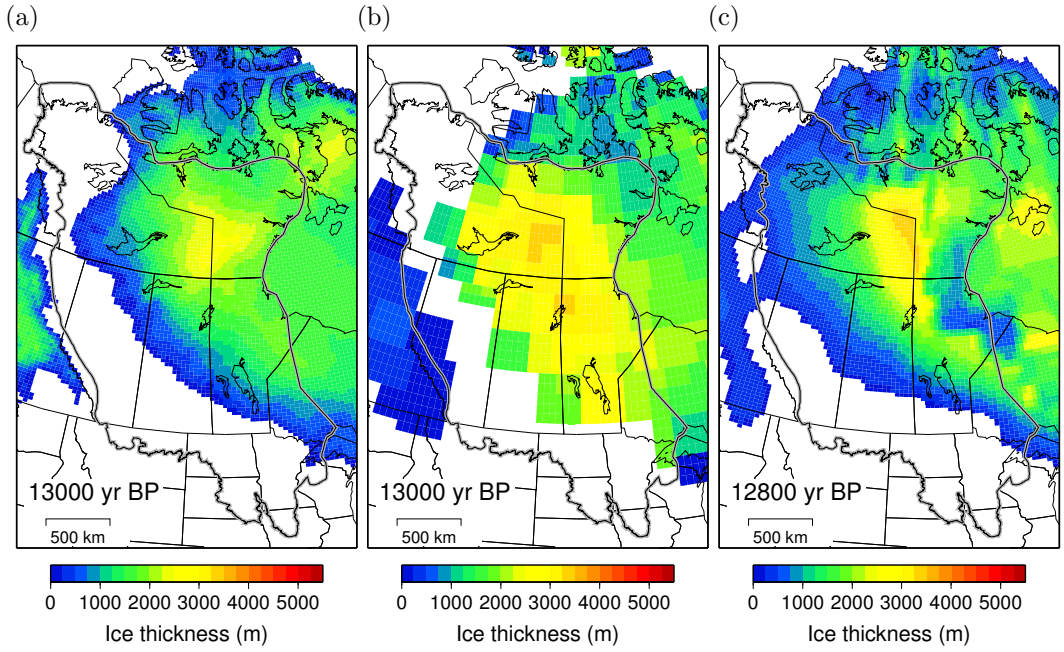

Figure 8.44: Comparison of the three ice sheet models at around 13 000 yr BP. (a) This Study. (b) ICE-5G (c) ANU Model (note, this is at 12 800 yr BP).

model from this study and ICE-5G fit the rate at Pickle Lake equally, while the ANU model performs the worst, overestimating the uplift rate by over 6 mm.yr^{-1}. The model from this study is closest to matching the observed rate at Yellowknife, while ICE-5G and the ANU both overpredict the rate. The velocity calculated from the other two other models have a velocity that is over 2 mm.yr^{-1} larger than the observed rate. The observed rates at Calgary, Flin Flon, Lac Du Bonnet and Saskatoon are overpredicted by all three models, but the model from this study is the only one that fits the observed rates within two sigma. The calculated rates at these locations from the ANU model and ICE-5G are significantly higher than the model from this study. All three models are able to fit the observed uplift rate and Inuvik within one-sigma. None of the models are able to match the rate at North Liberty within two-sigma.

8.5.4 Contemporary lake tilt

Table 8.2 shows a comparison of the tilt values calculated from the three ice sheet models. In Great Slave Lake and Lake Athabasca, the magnitude of the modelled tilt is lower in the model from this study than in ICE-5G and the ANU model. If the gauge data is reliable, then the model from this study is closer to the true values. The modelled tilt values in Southern Indian Lake show the greatest uplift towards the east with the model from this study, and is most consistent with the observations. The ANU model provides the closest to the tilt rate observed in Lake Winnipegosis, but still underestimates it by over 1 mm.yr^{-1}. ICE-5G and the model from this study have rates that are close to the observed rate in Dauphin Lake. The modelled tilt rates in Lake Manitoba are also similar between the model from this study and ICE-5G. The calculated rates from the ANU model are much higher. The gauge pairs in Lake Winnipeg relative to Victoria Beach were deemed to be the among most robust of all the lakes considered in this study. The tilt

rates determined from the model from this study match the observations, and ICE-5G slightly underestimates the tilt gradient, though is still within two-sigma for most pairs. The ANU model significantly overestimates the amount of tilt in Lake Winnipeg. The calculated tilt of Lake of the Woods is similar with ICE-5G and this study, and provide a good fit the observed tilt. The ANU model significantly overestimates it. There are considerable differences between the model from this study and ICE-5G in southern Manitoba and northern Ontario (Fig. 8.43). Since they provide similar modelled lake tilt rates, it is not possible to discriminate which model is best based on these data. The ANU model has calculated tilt rates that are the furthest from the observations.

8.5.5 Glacial lake strandline tilt

Glacial Lake McConnell had strandline tilt observations for two different stages of the lake (Fig. 8.45). The tilt of strandlines in the northern part of the basin are underestimated by at least 40-60 m in the ANU model, though it should be noted that this model still has ice cover over the basin when these strandlines formed. ICE-5G overpredicts the tilt at one feature, while underpredicting it at the other. Only the model from this study is able to match the observed tilt. ICE-5G significantly overestimates the tilt of the southern part of the basin, by up to 200 m (Fig. 8.45). The calculated tilt from the ANU model is much less, and is similar to the results of the model from this study.

There are three dated strandlines for Glacial Lake Agassiz (Fig. 8.45). The Herman strandline is the oldest of the three. The ANU model fits the observations about as well as this study. ICE-5G overpredicts the tilt by several hundred metres. The results for the Norcross strandline are similar, with the model from this study and the ANU model producing relatively good fit to the observations, while ICE-5G significantly overpredicts the tilt. The tilt Upper Campbell strandline is overpre-

dicted in the ANU model by about 100 m at the northern end of the basin. ICE-5G overpredicts the tilt by at least 150 m for most of the strandline.

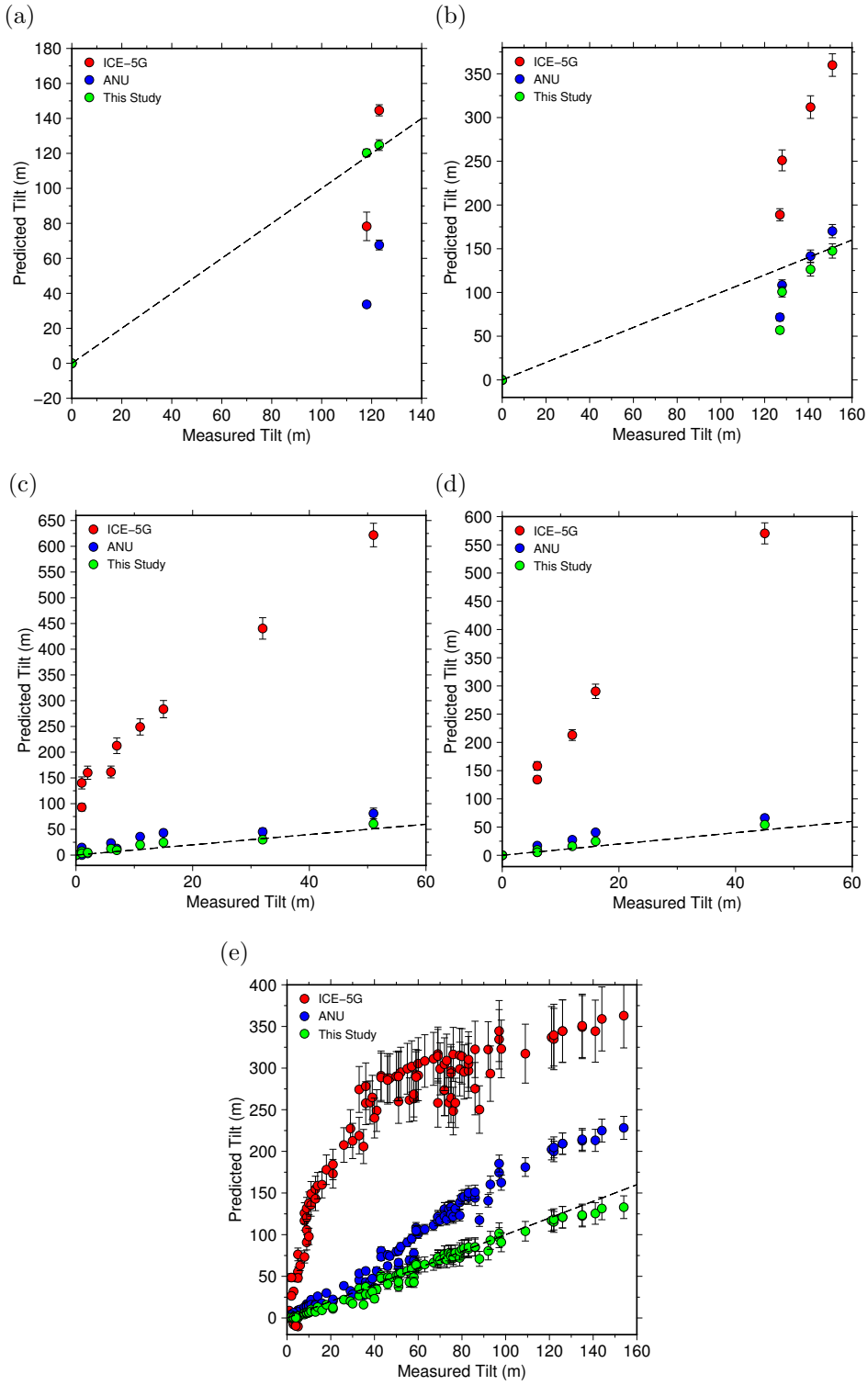

Figure 8.45: Comparison of calculated and observed tilt of the glacial lakes for ICE-5G, the ANU model and the model from this study. The dashed line is the one-to-one line (*i.e.* if the modelled and observed tilt were the same, they would fall on this line). The error bars represent the relative change in elevation compared to the reference location for the inferred age of the feature. (a) Northern Glacial Lake McConnell. (b) Southern Glacial Lake McConnell. For Glacial Lake Agassiz: (c) Herman strandline, (d) Norcross strandline, (e) Upper Campbell strandline

8.5.6 Relative Sea Level

The misfit of relative sea level in the ANU model relative to the model from this study should be somewhat less than with the glacial lake tilts, as the same data were used. ICE-5G may not fit all the data as it was developed before many of the samples used in this study were published. These models also used different reservoir corrections for marine organisms and different calibration curves to convert the radiocarbon ages to calendar ages. This likely contributes to some of the difference in fit between the models.

In southwestern Hudson Bay, ICE-5G overpredicts relative sea level by 20-80 m shortly after deglaciation. The ANU model has a similar fit as the model from this study, though both may underestimate the relative sea level highstand position. For northwestern Hudson Bay, ICE-5G overpredicts relative sea level at the location of some of the bounded constraints, while the ANU model has similar results to this study. At Southampton Island, ICE-5G has similar modelled sea level as the model from this study, while the ANU model overpredicts relative sea level for many constraints. In southern Melville Peninsula, the ANU model and the model from this study have roughly the same modelled sea level, while ICE-5G slightly underpredicts relative sea level. For northern Melville Peninsula, calculated sea level from the model from this study is consistent with more observations than the other two models, which underpredict relative sea level during the early Holocene. In the Boothia Peninsula, the ANU model slightly overpredicts the tightly constrained mid-Late Holocene relative sea level fall, while ICE-5G underpredicts it. None of the models are able to account for the observed high relative sea level between 11 000 and 9000 yr BP in the northern Boothia Peninsula, though the model from this study is successful in modelling it in the southern part of the Peninsula. In King William Island, ICE-5G is the only model to fit all of the maximum constraints, though it underpredicts relative sea level between 9000 and 7000 yr BP. the model

from this study and the ANU model have similar predicted relative sea level in northwestern mainland Nunavut and the Mackenzie Delta. ICE-5G overpredicts late glacial relative sea level in the Coronation Gulf and Bathurst Inlet. All of the models underpredict late glacial relative sea level on Victoria Island, though the model from this study has the highest modelled relative sea level of the three, and fits mid-late Holocene relative sea level the best. Modelled relative sea level at Banks Island has the largest discrepancy between this study and the other models, as they did not have extensive ice cover of the island and therefore underestimate relative sea level.

Table 8.4 shows a summary of how well each model fits the observations. the model from this study fits 84% of the observations, compared with 73% for the ANU model and 68% for ICE-5G. Calculated relative sea level from the model from this study fits more of the bounded and minimum relative sea level constraints than the other sites, but fits fewer of the maximum relative sea level constraints than ICE-5G. Since ICE-5G fits far fewer minimum constraints, it likely systematically underpredicts sea-level throughout the study area (*i.e* it does not cause enough subsidence of the Earth's surface in the coastal regions of the study area). The number of constraints that are modelled correctly in the model from this study indicates that it provides an improved estimate of GIA throughout the study area.

Table 8.4: Number of relative sea level indicators modelled correctly within the prescribed height uncertainty and two-sigma calibrated age of the samples with the three models

Constraint type	Number of observations	This Study	ICE-5G	ANU
minimum	434	377	227	325
maximum	330	284	326	255
bounded	137	98	57	82
total	901	759	610	662

8.6 Summary

This chapter showed the details of this study's reconstruction of the western Laurentide Ice Sheet. The model was constrained using observations of GIA from GPS vertical velocity rates, contemporary lake tilting, glacial lake strandline tilt and relative sea level indicators. This model was developed using an Earth model with a lithospheric thickness of 120 km, an upper mantle viscosity of about 4×10^{20} Pa s, and a lower mantle viscosity of about 10^{22} Pa s. The peak ice thickness in this model is about 4000 m, and the peak elevation is about 3500 m. The resulting model has much less ice volume than ICE-5G and the ANU model within the study area at the LGM. Predicted GIA is more consistent with observations than the other two models, especially in the Lake Agassiz basin. This is the result of additional constraints that were not available during the development of those models.

Chapter 9

Conclusions

9.1 Minimum timing of retreat

A model of the minimum timing of retreat was developed to serve as the starting point of post-LGM margin reconstruction. Carefully scrutinised radiocarbon and optical dates, along with an inferred direction of margin retreat determined from geomorphic features, were used to determine the area covered by the western Laurentide Ice Sheet that was certain to be ice free. In many areas, the timing of deglaciation is highly uncertain, especially on the Canadian Shield and north of 60°N. The earliest time it is certain that retreat had commenced was about 17 500 yr BP. By 14 000 yr BP, it is certain that much of southern Alberta was ice free, and that the ice margin was located in Manitoba. Most of the Canadian Prairies and the Mackenzie Lowlands were certain to be ice free by 13 000 yr BP. Full retreat of the margin away from the Cordillera is not certain until after 11 000 yr BP. Ice free conditions at northern Manitoba are certain at 8000 yr BP. There are few radiocarbon dates in mainland Nunavut, and it is not certain that most of this region was ice free until after 7000 yr BP.

9.2 Observations of GIA in the area covered by the western Laurentide Ice Sheet

There are four sources of information on GIA that are used in this study: GPS uplift rates, contemporary tilting of lakes, tilts of glacial lake strandlines and relative sea level indicators. GPS uplift rates were checked to ensure they were reliable. There were eleven stations in the study area, which after correction for offsets, and calculated with a coloured noise model, gave reliable estimates of vertical velocity. Contemporary lake tilts were determined by finding the difference in lake level at gauges in different parts of ten lakes in the study area. Using a joint inversion of all gauges within a lake basin, reliable estimates of tilt were determined for all lakes. Glacial Lake McConnell has two stages where strandlines and deltas could be correlated to lake outlets. Glacial Lake Agassiz has three strandlines that could be continuously traced for several hundred km, and have recently been dated by optical methods. The modern elevation of these strandlines were determined from LIDAR and SRTM data in places where there were not previously published elevation values. The amount of tilt of these strandlines since their formation is in excess of 100 m. These three sets of data provide information on the amount of GIA in areas away from the coast. Relative sea level indicators have been the traditional dataset that has been used to infer ice sheet volume. There are 901 radiocarbon dates from the northern coastal parts of the study area. These data were scrutinised based on the reliability of the material dated, assigned uncertainties in elevation and calibrated using the most recent assessment of reservoir age.

9.3 Ice sheet model

A new numerical ice sheet model of the western Laurentide Ice Sheet was developed in this study. This model was created using simple glaciological principles, using

two variables: ice margin location and basal shear stress. The initial ice margin was place at the maximum possible extent allowed for by the minimum timing of retreat models presented in Chapter 3. The basal shear stress was initially set to values based on geological and geographical considerations, then adjusted to change ice thickness in order to fit constraints on GIA. The ice model was adjusted fit the observations of GIA in the following order: GPS vertical velocity, contemporary lake tilt, glacial lake strandline tilt, late Holocene relative sea level, and finally early Holocene and late Pleistocene relative sea level.

My ice sheet model has less ice volume at the LGM than both ICE-5G and the ANU model. This is not surprising, as the creation of these models happened prior to the publication of many of the observations used in this study. The model in this study was developed by using observations of lake tilt, glacial strandline tilt and GPS vertical velocity to assess the ice volume in areas away from the coast. This set of observations indicates that the ice sheet in southern part of the study area had to be relative thin, and more closely matches models based purely on surficial geological constraints such as Fisher et al. (1985) and Licciardi et al. (1998). The ice sheet model from this study is similar to the maximum reconstruction of Licciardi et al. (1998), which has an ice dome located west of Hudson Bay with a maximum elevation in 3000 m though the model in this study has a slightly higher peak elevation (3500 m). The ice thickness of northern Ontario is less than the Licciardi et al. (1998) model, which suggests that the basal conditions were not the same in all parts of the Canadian Shield. The ice sheet in southern areas of the Canadian Shield needed to be thin to fit observations, in particular the contemporary tilt rate of Lake Winnipeg and Lake of the Woods and GPS vertical velocities in Pickle Lake and Lac Du Bonnet. The total volume of ice at the LGM in the study area is 8.2×10^6 km^3, which is 6.9×10^6 km^3 less than ICE-5G and 2.5×10^6 km^3 less than the ANU Model.

Retreat of the western Laurentide ice sheet was rapid between 17 000 yr BP and 14 000 yr BP. By 14 000 yr BP, the volume of the study area in the model from this study had decreased by 50% from the LGM maximum. Meltwater Pulse 1A was a large increase in sea level that happened between 15 000 and 14 000 yr BP (Carlson and Clark, 2012). Peltier (2004) suggested that the source of most of this sea level rise was from the sudden retreat of the northern hemisphere ice sheets, with a large portion of that from the western Laurentide Ice Sheet. However, Carlson and Clark (2012) suggested that a large portion of the water was sourced from the southern hemisphere. In the model from this study, there is a loss of 1.3×10^6 km^3 between 15 000 and 14 000 yr BP, or about 3.2 m of sea level equivalent. This is about three times less than the ice loss at that time in the ICE-5G model. The model from this study does not show a distinctive acceleration of volume loss at this time in the study area, a conclusion that is supported by glacial lake strandline tilts that formed between 14 000 to 13 000 yr BP, which do not support delayed deglaciation.

The rate of ice volume loss in the model from this study decreases significantly between 14 000 and 11 500 yr BP. This is consistent with cooling during the Younger Dryas event, which happened between 13 000 and 11 500 yr BP. By 11 000 yr BP, the volume of the ice sheet in the model from this study was less than 30% of the LGM total. Volume loss accelerated at after 11 500 yr BP and the rate is steady between that time and 8000 yr BP, at which time there was little ice left in the area covered by the western Laurentide Ice Sheet.

9.4 Modelled GIA

Calculated deformation and relative sea level from the model from this study is consistent with the majority of the observations and matches better than the ICE-5G and ANU models. The calculated tilt glacial lakes matched observed tilt, and provided strong control on ice volume on the western and southern parts of the study

area. GPS uplift rates provided control on the duration and volume of ice cover in areas close to where the location of ice flow centres during the LGM. Contemporary lake tilt rates were instrumental on determining the ice volume in northern Ontario and Manitoba. The calculate tilt rates of Lake Winnipeg and Lake of the Woods were matched when volume in that region was relatively low compared to ICE-5G and the ANU model. Calculated sea level from the model from this study was able to fit 84% of the relative sea level indicators from the study area and areas adjacent to the study area, compared with 68% for the ICE-5G model and 73% for the ANU model.

9.5 Earth rheology

Calculated GIA from the model from this study was best able to match observations using an Earth model with a lithospheric thickness of 120 km, an upper mantle viscosity of $3 - 5 \times 10^{20}$ Pa s and a lower mantle viscosity of $> 5 \times 10^{21}$ Pa s. The fit of the model to most observations was not highly sensitive to the choice of lithospheric thickness, though the tilt at the southern end of the Upper Campbell strandline of Lake Agassiz provides evidence that this thickness is more appropriate than a lower value of 90 km. The density of observations of GIA is not sufficient to uniquely determine mantle viscosity. Since the model from this study is similar to previous models that were developed purely on geological considerations, it leads to confidence that the target mantle viscosity values are correct.

9.6 Suggestions for future work

One of the most powerful datasets that made modelling the western Laurentide Ice Sheet possible was the determination of the age and extent of strandlines in Glacial Lake Agassiz. Finding the age and mapping of additional strandlines in this and

other glacial lakes would provide information on magnitude of GIA in continental areas. Additional permanent GPS stations would be useful to attain better spatial resolution of contemporary uplift. In order to make best use of this data, more work needs to be done to assess water storage in the study area and determine what component of the vertical velocity is related to hydrological loading. Doing so would allow space gravity measurements from GRACE to be used. Acquiring more relative sea level data would also be beneficial. One area that is most deficient in samples is western Hudson Bay. This area was one of the last places to be deglaciated, and has some of the most rapid GIA rates in the world. Acquiring more data in this area would help characterise the GIA and reduce the uncertainties in the timing of deglaciation in this area. There needs to be more work to determine the late glacial reservoir age in the study area. If the modern correction in the Arctic (335±85 years) is larger than it was in the past, it could explain why it was not possible to correctly model some of the observations. The ice volume in the model from this study is less than in other reconstructions that were constrained predominantly on relative sea level data. Though the Maxwell mantle rheology used in this study was able to match observations of GIA, alternative rheology types (*e.g* non-linear rheology, Karato and Wu, 1993) may allow for more ice volume at the LGM, while still matching the GIA observations. Finally, this study only focused on the western part of the Laurentide ice sheet. Completing this analysis for the eastern Laurentide Ice Sheet, Innuitian Ice Sheet and Cordilleran Ice Sheet are required to improve our understanding of the glacial history of North America.

Chapter 10

References

Abbott, M.B., Stafford, T.W., 1996. Radiocarbon geochemistry of modern and ancient Arctic lake systems, Baffin Island, Canada. Quaternary Research 45, 300–311.

Abe-Ouchi, A., Saito, F., Kawamura, K., Raymo, M.E., Okuno, J., Takahashi, K., Blatter, H., 2013. Insolation-driven 100,000-year glacial cycles and hysteresis of ice-sheet volume. Nature 500, 190–193.

Allard, G., Roy, M., Ghaleb, B., Richard, P., Larouche, A., Veillette, J., Parent, M., 2012. Constraining the age of the last interglacial–glacial transition in the Hudson Bay lowlands (Canada) using U–Th dating of buried wood. Quaternary Geochronology 7, 37–47.

Altamimi, Z., Collilieux, X., Métivier, L., 2011. ITRF2008: an improved solution of the international terrestrial reference frame. Journal of Geodesy 85, 457–473.

Amante, C., Eakins, B.W., 2009. ETOPO1 1 arc-minute global relief model: procedures, data sources and analysis. NOAA Technical Memorandum NESDIS NGDC-24. US Department of Commerce, National Oceanic and Atmospheric Administration, National Environmental Satellite, Data, and Information Service, National Geophysical Data Center, Marine Geology and Geophysics Division.

Anderson, T., 2012. Evidence from Nipawin Bay in Frobisher Lake, Saskatchewan, for three highstand and three lowstand lake phases between 9 and 10 (10.1 and 11.5 cal) ka BP. Quaternary International 260, 66–75.

Andrews, J., 1970. Present and postglacial rates of uplift for glaciated northern and eastern North America derived from postglacial uplift curves. Canadian Journal of Earth Sciences 7, 703–715.

Argus, D.F., Peltier, W.R., 2010. Constraining models of postglacial rebound using space geodesy: a detailed assessment of model ICE-5G (VM2) and its relatives. Geophysical Journal International 181, 697–723.

Arnold, T.G., 2002. Radiocarbon dates from the ice-free corridor. Radiocarbon 44, 437–454.

Aylsworth, J.M., Shilts, W.W., 1989a. Bedforms of the Keewatin ice sheet, Canada. Sedimentary Geology 62, 407–428.

Aylsworth, J.M., Shilts, W.W., 1989b. Glacial features around the Keewatin Ice Divide, Northwest Territories Scale 1:1 000 000.

Baird & Associates, 2000. Review of Lake Winnipeg water level reporting procedures. Final Report. W.F. Baird & Associates Coastal Engineers LTD.

Bajc, A., Schwert, D., Warner, B., Williams, N., 2000. A reconstruction of Moorhead and Emerson Phase environments along the eastern margin of glacial Lake Agassiz, Rainy River basin, northwestern Ontario. Canadian Journal of Earth Sciences 37, 1335–1353.

Barber, D.C., Dyke, A., Hillaire-Marcel, C., Jennings, A.E., Andrews, J.T., Kerwin, M.W., Bilodeau, G., McNeely, R., Southon, J., Morehead, M.D., Gagnon, J.M., 1999. Forcing of the cold event of 8,200 years ago by catastrophic drainage of Laurentide lakes. Nature 400, 344–348.

Bastow, I.D., Eaton, D.W., Kendall, J.M., Helffrich, G., Snyder, D.B., Thompson, D.A., Wookey, J., Darbyshire, F.A., Pawlak, A.E., 2013. The Hudson Bay Lithospheric Experiment (HuBLE): insights into Precambrian plate tectonics and the development of mantle keels. Geological Society, London, Special Publications 389, SP389–7.

Batchelor, C.L., Dowdeswell, J.A., Pietras, J.T., 2013. Seismic stratigraphy, sedimentary architecture and palaeo-glaciology of the Mackenzie Trough: evidence for two Quaternary ice advances and limited fan development on the western Canadian Beaufort Sea margin. Quaternary Science Reviews 65, 73–87.

Bateman, M.D., Murton, J.B., 2006. The chronostratigraphy of Late Pleistocene glacial and periglacial aeolian activity in the Tuktoyaktuk Coastlands, NWT, Canada. Quaternary Science Reviews 25, 2552–2568.

Bayrock, L.A., Reimchen, T.H.F., 1980. Surficial Geology Alberta Foothills and Rocky Mountains. Map 150. Alberta Research Council. Scale 1:250 000.

Bednarski, J.M., 2008. Landform assemblages produced by the Laurentide Ice Sheet in northeastern British Columbia and adjacent Northwest Territories – constraints on glacial lakes and patterns of ice retreat. Canadian Journal of Earth Sciences 45, 593–610.

Bednarski, J.M., Smith, I.R., 2007. Laurentide and montane glaciation along the Rocky Mountain foothills of northeastern British Columbia. Canadian Journal of Earth Sciences 44, 445–457.

Beget, J., 1987. Low profile of the northwest Laurentide ice sheet. Arctic and Alpine Research 19, 81–88.

Beierle, B., Smith, D.G., 1998. Severe drought in the early Holocene (10,000–6800 BP) interpreted from lake sediment cores, southwestern Alberta, Canada. Palaeogeography, Palaeoclimatology, Palaeoecology 140, 75–83.

Bélanger, N., Carcaillet, C., Padbury, G.A., Harvey-Schafer, A.N., Van Rees, K.J.C., 2014. Periglacial fires and trees in a continental setting of Central Canada, Upper Pleistocene. Geobiology 12, 109–118.

Berger, G.W., Nielsen, E., 1991. Evidence from thermoluminescence dating for Middle Wisconsinan deglaciation in the Hudson Bay Lowland of Manitoba. Canadian Journal of Earth Sciences 28, 240–249.

Bertrand, S., Araneda, A., Vargas, P., Jana, P., Fagel, N., Urrutia, R., 2012. Using the N/C ratio to correct bulk radiocarbon ages from lake sediments: Insights from Chilean Patagonia. Quaternary Geochronology 12, 23–29.

Bindoff, N.L., Willebrand, J., Artale, V., Cazenave, A., Gregory, J.M., Gulev, S., Hanawa, K., Quéré, C.L., Levitus, S., Nojiri, Y., Shum, C.K., Talley, L.D., Unnikrishnan, A.S., 2007. Observations: oceanic climate change and sea level, in: Solomon, S., Qin, D., Manning, M., Chen, Z., Marquis, M., Averyt, K.B., Tignor, M., Miller, H. (Eds.), Climate Change 2007: The Physical Science Basis. Contribution of Working Group I to the Fourth Assessment Report of the Intergovernmental Panel on Climate Change. Cambridge University Press, Cambridge, United Kingdom and New York, NY, USA. chapter 5.

Blewitt, G., Lavallée, D., 2002. Effect of annual signals on geodetic velocity. Journal of Geophysical Research: Solid Earth (1978–2012) 107, ETG–9.

Borsa, A.A., Agnew, D.C., Cayan, D.R., 2014. Ongoing drought-induced uplift in the western United States. Science 345, 1587–1590.

Bos, M.S., Fernandes, R.M.S., Williams, S.D.P., Bastos, L., 2013. Fast error analysis of continuous GNSS observations with missing data. Journal of Geodesy 87, 351–360.

Boulton, G.S., Clark, C.D., 1990. A highly mobile Laurentide ice sheet revealed by satellite images of glacial lineations. Nature 346, 813–817.

Boulton, G.S., Smith, G.D., Jones, A.S., Newsome, J., 1985. Glacial geology and glaciology of the last mid-latitude ice sheets. Journal of the Geological Society of London 142, 447–474.

Boyd, M., 2007. Early postglacial history of the southeastern Assiniboine Delta, glacial Lake Agassiz basin. Journal of Paleolimnology 37, 313–329.

Breckenridge, A., Lowell, T.V., Fisher, T.G., Yu, S., 2012. A late Lake Minong transgression in the Lake Superior basin as documented by sediments from Fenton Lake, Ontario. Journal of Paleolimnology 47, 1–14.

Briner, J.P., Davis, T., Miller, G.H., 2009. Latest Pleistocene and Holocene glaciation of Baffin Island, Arctic Canada: key patterns and chronologies. Quaternary Science Reviews 28, 2075–2087.

Brock, F., Froese, D.G., Roberts, R.G., 2010. Low temperature (LT) combustion of sediments does not necessarily provide accurate radiocarbon ages for site chronology. Quaternary Geochronology 5, 625–630.

Brock, F., Lee, S., Housley, R.A., Bronk Ramsey, C., 2011. Variation in the radiocarbon age of different fractions of peat: A case study from Ahrenshöft, northern Germany. Quaternary Geochronology 6, 550–555.

Broecker, W.S., 2006. Was the Younger Dryas Triggered by a flood? Science 312, 1146–1148.

Bronk Ramsey, C., 2009. Bayesian analysis of radiocarbon dates. Radiocarbon 51, 337–360.

Brown, V.H., 2012. Ice stream dynamics and pro-glacial lake evolution along the north-western margin of the Laurentide Ice Sheet. Ph.D. thesis. Durham University.

Brown, V.H., Stokes, C.R., Ò Cofaigh, C., 2011. The glacial geomorphology of the north-west sector of the Laurentide Ice Sheet. Journal of Maps 7, 409–428.

Bryson, R.A., Wendland, W.M., Ives, J.D., Andrews, J.T., 1969. Radiocarbon isochrones on the disintegration of the Laurentide Ice Sheet. Arctic and Alpine Research , 1–13.

Burns, J.A., 1996. Vertebrate paleontology and the alleged ice-free corridor: the meat of the matter. Quaternary International 32, 107–112.

Burns, J.A., 2010. Mammalian faunal dynamics in Late Pleistocene Alberta, Canada. Quaternary International 217, 37–42.

Calais, E., Han, J.Y., DeMets, C., Nocquet, J.M., 2006. Deformation of the North American plate interior from a decade of continuous GPS measurements. Journal of Geophysical Research: Solid Earth 111, B06402.

Camill, P., Umbanhowar, C.E., Geiss, C., Hobbs, W.O., Edlund, M.B., Shinneman, A.C., Dorale, J.A., Lynch, J., 2012. Holocene climate change and landscape development from a low-Arctic tundra lake in the western Hudson Bay region of Manitoba, Canada. Journal of Paleolimnology 48, 1–18.

Carlson, A.E., Clark, P.U., 2012. Ice sheet sources of sea level rise and freshwater discharge during the last deglaciation. Reviews of Geophysics 50, RG4007.

Carlson, A.E., Clark, P.U., Raisbeck, G.M., Brook, E.J., 2007. Rapid Holocene deglaciation of the Labrador Sector of the Laurentide Ice Sheet. Journal of Climate 20, 5126–5133.

Carlson, A.E., Ullman, D.J., Anslow, F.S., He, F., Clark, P.U., Liu, Z., Otto-Bliesner, B.L., 2012. Modeling the surface mass-balance response of the laurentide ice sheet to bølling warming and its contribution to meltwater pulse 1a. Earth and Planetary Science Letters 315, 24–29.

Carlson, A.E., Winsor, K., 2012. Northern Hemisphere ice-sheet responses to past climate warming. Nature Geoscience 5, 607–613.

Carrera, G.H., Vaníček, P., Craymer, M.R., 1991. The compilation of a map of recent vertical crustal movements in Canada. Department of Surveying Engineering Technical Report 153.

Catto, N., Liverman, D.G., Bobrowsky, P.T., Rutter, N., 1996. Laurentide, Cordilleran, and montane glaciation in the western Peace River–Grande Prairie region, Alberta and British Columbia, Canada. Quaternary International 32, 21–32.

Chanard, K., Avouac, J., Ramillien, G., Genrich, J., 2014. Modeling deformation induced by seasonal variations of continental water in the Himalaya region: Sensitivity to earth elastic structure. Journal of Geophysical Research: Solid Earth 119, 5097–5113.

Christiansen, E.A., 1979. The Wisconsinan deglaciation, of southern Saskatchewan and adjacent areas. Canadian Journal of Earth Sciences 16, 913–938.

Christiansen, E.A., Sauer, E.K., Schreiner, B.T., 1995. Glacial Lake Saskatchewan and Lake Agassiz deltas in east-central Saskatchewan with special emphasis on the Nipawin delta. Canadian Journal of Earth Sciences 32, 334–348.

Church, J.A., White, N.J., 2011. Sea-level rise from the late 19th to the early 21st century. Surveys in Geophysics 32, 585–602.

Church, J.A., White, N.J., Coleman, R., Lambeck, K., Mitrovica, J.X., 2004. Estimates of the regional distribution of sea level rise over the 1950-2000 period. Journal of Climate 17, 2609–2625.

Clague, J.J., 1989. Quaternary geology of the Canadian Cordillera, in: Fulton, R.J. (Ed.), Quaternary Geology of Canada and Greenland. Geological Survey of Canada. number 1 in Geology of Canada. chapter 1, pp. 17–96.

Clague, J.J., Froese, D., Hutchinson, I., James, T.S., Simon, K.M., 2005. Early growth of the last Cordilleran ice sheet deduced from glacio-isostatic depression in southwest British Columbia, Canada. Quaternary Research 63, 53–59.

Clague, J.J., James, T.S., 2002. History and isostatic effects of the last ice sheet in southern British Columbia. Quaternary Science Reviews 21, 71–87.

Clague, J.J., Ward, B., 2011. Pleistocene Glaciation of British Columbia, in: Ehlers, J., Gibbard, P.L., Hughes, P.D. (Eds.), Quaternary Glaciations - Extent and Chronology A Closer Look. Elsevier. volume 15 of *Developments in Quaternary Sciences*. chapter 44, pp. 563 – 573.

Clark, J.A., Befus, K.M., Hooyer, T.S., Stewart, P.W., Shipman, T.D., Gregory, C.T., Zylstra, D.J., 2008. Numerical simulation of the paleohydrology of glacial lake oshkosh, eastern wisconsin, usa. Quaternary Research 69, 117–129.

Clark, J.A., Zylstra, D.J., Befus, K.M., 2007. Effects of Great Lakes water loading upon glacial isostatic adjustment and lake history. Journal of Great Lakes Research 33, 627–641.

Clark, P.U., 1994. Unstable behavior of the Laurentide Ice Sheet over deforming sediment and its implications for climate change. Quaternary Research 41, 19–25.

Clark, P.U., Alley, R.B., Pollard, D., 1999. Northern Hemisphere ice-sheet influences on global climate change. Science 286, 1104–1111.

Clark, P.U., Dyke, A.S., Shakun, J.D., Carlson, A.E., Clark, J., Wohlfarth, B., Mitrovica, J.X., Hostetler, S.W., McCabe, A.M., 2009. The Last Glacial Maximum. Science 325, 710–714.

Clark, P.U., Licciardi, J.M., MacAyeal, D.R., Jenson, J.W., 1996. Numerical reconstruction of a soft-bedded Laurentide Ice Sheet during the last glacial maximum. Geology 24, 679–682.

Clark, P.U., Walder, J.S., 1994. Subglacial drainage, eskers, and deforming beds beneath the Laurentide and Eurasian ice sheets. Geological Society of America Bulletin 106, 304–314.

Clayton, L., Moran, S.R., 1982. Chronology of late Wisconsinan glaciation in middle North America. Quaternary Science Reviews 1, 55–82.

Condron, A., Winsor, P., 2012. Meltwater routing and the Younger Dryas. Proceedings of the National Academy of Sciences 109, 19928–19933.

Couch, A.G., Eyles, N., 2008. Sedimentary record of glacial Lake Mackenzie, Northwest Territories, Canada: Implications for Arctic freshwater forcing. Palaeogeography, Palaeoclimatology, Palaeoecology 268, 26–38.

Coulthard, R.D., Furze, M.F., Pieńkowski, A.J., Nixon, C., England, J.H., 2010. New marine ΔR values for Arctic Canada. Quaternary Geochronology 5, 419–434.

Craig, B.G., 1961. Surficial Geology, northern District of Keewatin. Preliminary Map 7-1961A. Geological Survey of Canada. Scale 1:1 013 760.

Cuffey, K.M., Paterson, W.S.B., 2010. The physics of glaciers. Elsevier.

Curry, B., Petras, J., 2011. Chronological framework for the deglaciation of the Lake Michigan lobe of the Laurentide Ice Sheet from ice-walled lake deposits. Journal of Quaternary Science 26, 402–410.

Curry, B.B., Grimley, D.A., McKay, E.D., 2011. Quaternary glaciations in illinois, in: Ehlers, J., Gibbard, P.L., Hughes, P.D. (Eds.), Quaternary Glaciations - Extent and Chronology A Closer Look. Elsevier. volume 15 of *Developments in Quaternary Sciences*. chapter 36, pp. 467–487.

Darbeheshti, N., Zhou, L., Tregoning, P., McClusky, S., Purcell, A., 2013. The ANU GRACE visualisation web portal. Computers & Geosciences 52, 227–233.

Davis, N.K., Locke III, W.W., Pierce, K.L., Finkel, R.C., 2006. Glacial Lake Musselshell: Late Wisconsin slackwater on the Laurentide ice margin in central Montana, USA. Geomorphology 75, 330–345.

De Angelis, H., Kleman, J., 2005. Palaeo-ice streams in the northern keewatin sector of the laurentide ice sheet. Annals of Glaciology 42, 135–144.

Deevey, E.S., Gross, M.S., Hutchinson, G.E., Kraybill, H.L., 1954. The natural C14 contents of materials from hard-water lakes. Proceedings of the National Academy of Sciences of the United States of America 40, 285.

Demuro, M., Froese, D.G., Arnold, L.J., Roberts, R.G., 2012. Single-grain OSL dating of glaciofluvial quartz constrains Reid glaciation in NW Canada to MIS 6. Quaternary Research 77, 305–316.

Denton, G., Hughes, T., 1981. The last great ice sheets. John Wiley & Sons.

Dineley, D., 1971. Arches and basins of the southern Arctic Islands of Canada. Proceedings of the Geologists' Association 82, 411–443.

Dredge, L.A., 1983. Character and development of northern Lake Agassiz and its relation to Keewatin and Hudsonian ice regimes. Geological Association of Canada. Special Paper 26, pp. 117–131.

Dredge, L.A., 1995. Quaternary geology of northern Melville Peninsula, District of Franklin, Northwest Territories: surface deposits, glacial history, environmental geology, and till geochemistry. Geological Survey of Canada Bulletin 484.

Dredge, L.A., 2002. Quaternary geology of southern Melville Peninsula, Nunavut. Geological Survey of Canada Bulletin 561.

Dredge, L.A., Cowan, W.R., 1989. Quaternary geology of the southwestern Canadian Shield, in: Fulton, R.J. (Ed.), Quaternary Geology of Canada and Greenland. Geological Survey of Canada. 1. chapter 3, pp. 214–235.

Dredge, L.A., Kerr, D.E., Wolfe, S.A., 1999. Surficial materials and related ground ice conditions, Slave Province, NWT, Canada. Canadian Journal of Earth Sciences 36, 1227–1238.

Dredge, L.A., McMartin, I., 2005. Postglacial marine deposits and marine limit determinations, inner Wager Bay area, Kivalliq region, Nunavut. Current Research 2005-B3.

Dubé-Loubert, H., Roy, M., Allard, G., Lamothe, M., Veillette, J.J., Gajewski, K., 2012. Glacial and nonglacial events in the eastern James Bay lowlands, Canada. Canadian Journal of Earth Sciences 50, 379–396.

Duk-Rodkin, A., Barendregt, R.W., Tarnocai, C., Phillips, F.M., 1996. Late Tertiary to late Quaternary record in the Mackenzie Mountains, Northwest Territories, Canada: stratigraphy, paleosols, paleomagnetism, and chlorine-36. Canadian Journal of Earth Sciences 33, 875–895.

Duk-Rodkin, A., Hughes, O.L., 1991. Age relationships of Laurentide and montane glaciations, Mackenzie Mountains, Northwest Territories. Géographie physique et Quaternaire 45, 79–90.

Dutton, A., Lambeck, K., 2012. Ice volume and sea level during the last interglacial. Science 337, 216–219.

Dyke, A., Morris, T.F., Green, D.E.C., 1991. Postglacial tectonic and sea level history of the central Canadian Arctic. Bulletin 397. Geological Survey of Canada.

Dyke, A.S., 1984. Quaternary geology of Boothia Peninsula and northern district of Keewatin, central Canadian Arctic. Memoir 407. Geological Survey of Canada.

Dyke, A.S., 2004. An outline of North American deglaciation with emphasis on central and northern Canada, in: Ehlers, J., Gibbard, P.L., Hughes, P.D. (Eds.), Quaternary Glaciations–Extent and Chronology - Part II: North America. Elsevier. Developments in Quaternary Science, pp. 373–424.

Dyke, A.S., Andrews, J.T., Clark, P.U., England, J.H., Miller, G.H., Shaw, J., Villette, J.J., 2002. The Laurentide and Innuitian ice sheets during the Last Glacial Maximum. Quaternary Science Reviews 21, 9–31.

Dyke, A.S., Dredge, L.A., 1989. Quaternary geology of the northwestern Canadian Shield, in: Quaternary Geology of Canada and Greenland. Geological Survey of Canada. volume 1. chapter 3, pp. 189–214.

Dyke, A.S., Giroux, D., Robertson, L., 2004. Paleovegetation maps of northern North America, 18 000 to 1000 BP. Open File 4682. Geological Survey of Canada.

Dyke, A.S., Moore, A., Robertson, L., 2003. Deglaciation of North America. Open File 1574. Geological Survey of Canada.

Dyke, A.S., Prest, V.K., 1987. Late Wisconsinan and Holocene history of the Laurentide ice sheet. Géographie physique et Quaternaire 41, 237–263.

Dyke, A.S., Savelle, J.M., 2000a. Holocene driftwood incursion to southwestern Victoria Island, Canadian Arctic Archipelago, and its significance to paleoceanography and archaeology. Quaternary Research 54, 113–120.

Dyke, A.S., Savelle, J.M., 2000b. Major end moraines of Younger Dryas age on Wollaston Peninsula, Victoria Island, Canadian Arctic: implications for paleoclimate and for formation of hummocky moraine. Canadian Journal of Earth Sciences 37, 601–619.

Dyke, A.S., Savelle, J.M., 2001. Holocene history of the Bering Sea bowhead whale (*Balaena mysticetus*) in its Beaufort Sea summer grounds off southwestern Victoria Island, Western Canadian Arctic. Quaternary Research 55, 371–379.

Dyke, A.S., Savelle, J.M., 2009. Paleoeskimo demography and sea-level history, Kent Peninsula and King William Island, central Northwest Passage, Arctic Canada. Arctic , 371–392.

Dyke, A.S., Savelle, J.M., Johnson, D.S., 2011. Paleoeskimo Demography and Holocene Sea-level History, Gulf of Boothia, Arctic Canada. Arctic 64, 151–168.

Dziewonski, A.M., Anderson, D.L., 1981. Preliminary reference earth model. Physics of the Earth and Planetary Interiors 25, 297–356.

Elson, J.A., 1967. Geology of glacial Lake Agassiz, in: Life, land and water. University of Manitoba Press Manitoba, Canada, pp. 36–95.

England, J., Atkinson, N., Bednarski, J., Dyke, A., Hodgson, D., Ò Cofaigh, C., 2006. The Innuitian Ice Sheet: configuration, dynamics and chronology. Quaternary Science Reviews 25, 689–703.

England, J., Dyke, A.S., Coulthard, R.D., Mcneely, R., Aitken, A., 2013. The exaggerated radiocarbon age of deposit-feeding molluscs in calcareous environments. Boreas 42.

England, J.H., Furze, M.F., Doupé, J.P., 2009. Revision of the NW Laurentide Ice Sheet: implications for paleoclimate, the northeast extremity of Beringia, and Arctic Ocean sedimentation. Quaternary Science Reviews 28, 1573–1596.

Evans, D.J.A., Clark, C.D., Rea, B.R., 2008. Landform and sediment imprints of fast glacier flow in the southwest Laurentide Ice Sheet. Journal of Quaternary Science 23, 249–272.

Fairbanks, R.G., 1989. A 17,000-year glacio-eustatic sea level record: influence of glacial melting rates on the Younger Dryas event and deep-ocean circulation. Nature 342, 637–642.

Farr, T.G., Rosen, P.A., Caro, E., Crippen, R., Duren, R., Hensley, S., Kobrick, M., Paller, M., Rodriguez, E., Roth, L., Seal, D., Shaffer, S., Shimada, J., Umland, J., Werner, M., Oskin, M., Burbank, D., Alsdorf, D., 2007. The Shuttle Radar Topography Mission. Reviews of Geophysics 45, RG2004.

Farrell, W.E., Clark, J.A., 1976. On postglacial sea level. Geophysical Journal of the Royal Astronomical Society 46, 647–667.

Fisher, D., Reeh, N., Langley, K., 1985. Objective reconstructions of the Late Wisconsinan Laurentide Ice Sheet and the significance of deformable beds. Géographie Physique et Quaternaire 39, 229–238.

Fisher, T.G., 2005. Strandline analysis in the southern basin of glacial Lake Agassiz, Minnesota and North and South Dakota, USA. Geological Society of America Bulletin 117, 1481–1496.

Fisher, T.G., 2007. Abandonment chronology of glacial Lake Agassiz's northwestern outlet. Palaeogeography, Palaeoclimatology, Palaeoecology 246, 31–44.

Fisher, T.G., Lepper, K., Ashworth, A.C., Hobbs, H.C., 2011. Southern outlet and basin of glacial Lake Agassiz. Field Guides 24, 379–400.

Fisher, T.G., Lowell, T.V., 2012. Testing northwest drainage from Lake Agassiz using extant ice margin and strandline data. Quaternary International 260, 106–114.

Fisher, T.G., Smith, D.G., Andrews, J.T., 2002. Preboreal oscillation caused by a glacial Lake Agassiz flood. Quaternary Science Reviews 21, 873–878.

Fisher, T.G., Waterson, N., Lowell, T.V., Hajdas, I., 2009. Deglaciation ages and meltwater routing in the Fort McMurray region, northeastern Alberta and northwestern Saskatchewan, Canada. Quaternary Science Reviews 28, 1608–1624.

Fisher, T.G., Yansa, C.H., Lowell, T.V., Lepper, K., Hajdas, I., Ashworth, A., 2008. The chronology, climate, and confusion of the Moorhead Phase of glacial Lake Agassiz: new results from the Ojata Beach, North Dakota, USA. Quaternary Science Reviews 27, 1124–1135.

Fleming, K., Lambeck, K., 2004. Constraints on the Greenland Ice Sheet since the Last Glacial Maximum from sea-level observations and glacial-rebound models. Quaternary Science Reviews 23, 1053–1077.

Forman, S.L., Pierson, J., Lepper, K., 2000. Luminescence geochronology, in: Quaternary geochronology: methods and applications. American Geophysical Union, Washington, pp. 157–176.

Forte, A.M., Mitrovica, J.X., 2001. Deep-mantle high-viscosity flow and thermochemical structure inferred from seismic and geodynamic data. Nature 410, 1049–1056.

Friesen, T.M., 2004. Contemporaneity of Dorset and Thule Cultures in the North American Arctic: New Radiocarbon Dates from Victoria Island, Nunavut. Current Anthropology 45, 685–691.

Fullerton, D.S., Bluemle, J.P., Clayton, L., Steece, F.V., Tipton, M.J., Bretz, R., Goebel, J.E., 1995. Quaternary geologic map of the Dakotas 4 degrees x 6 degrees quadrangle, United States. USGS Numbered Series I-1420(NL-14). U.S. Geological Survey. Scale 1:1,000,000.

Fullerton, D.S., Christiansen, E.A., Schreiner, B.T., Colton, R.B., Clayton, L., 2007. Quaternary Geologic Map of the Regina 4 Degrees x 6 Degrees Quadrangle, United States and Canada. USGS Numbered Series I-1420(NM-13). U.S. Geological Survey. Scale 1:1,000,000.

Fullerton, D.S., Colton, R.B., Bush, C.A., Straub, A.W., 2004. Map showing spatial and temporal relations of mountain and continental glaciations on the northern plains, primarily in northern Montana and northwestern North Dakota. Scientific Investigations Map 2843. United States Geological Survey. 1 map.

Fullerton, D.S., Ringrose, S.M., Clayton, L., Schreiner, B.T., Goebel, J.E., 2000. Quaternary geologic map of the Winnipeg 4 degrees x 6 degrees quadrangle, United States and Canada. USGS Numbered Series I-1420(NM-14). U.S. Geological Survey. Scale 1:1,000,000.

Fulton, R.J., 1995. Surficial materials of Canada. Map 1880A. Geological Survey of Canada. Scale 1:5 000 000.

Fulton, R.J., Blais-Stevens, A., Sun, C., Eilers, R.G., Betcher, R., Elson, J.A., Veldhuis, H., Fraser, W.R., 2004. Surficial materials of the Virden area, Manitoba and Saskatchewan. Geological Survey of Canada, Bulletin 546, 104.

Furze, M.F., Pieńkowski, A.J., Coulthard, R.D., in press. New cetacean ΔR values for Arctic North America and their implications for marine-mammal-based palaeoenvironmental reconstructions. Quaternary Science Reviews .

Giangioppi, M., Little, E.C., Ferbey, T., Ozyer, C.A., Utting, D.J., 2003. Quaternary glaciomarine environments west of Committee Bay, central mainland Nunavut. Current Research 2003-C5. Geological Survey of Canada.

Gladstone, R., Schafer, M., Zwinger, T., Gong, Y., Strozzi, T., Mottram, R., Boberg, F., Moore, J.C., 2014. Importance of basal processes in simulations of a surging svalbard outlet glacier. The Cryosphere 8, 1393–1405.

Glover, K.C., Lowell, T.V., Wiles, G.C., Pair, D., Applegate, P., Hajdas, I., 2011. Deglaciation, basin formation and post-glacial climate change from a regional network of sediment core sites in Ohio and eastern Indiana. Quaternary Research 76, 401–410.

Goebel, J.E., Mickelson, D.M., Farrand, W.R., Clayton, L., Knox, J.C., Cahow, A., C.Hobbs, H., Walton Jr., M.S., 1983. Quaternary geologic map of the Minneapolis 4 degrees x 6 degrees quadrangle, United States. USGS Numbered Series I-1420(NL-15). U.S. Geological Survey. Scale 1:1,000,000.

Gomez, N., Mitrovica, J.X., Huybers, P., Clark, P.U., 2010. Sea level as a stabilizing factor for marine-ice-sheet grounding lines. Nature Geoscience 3, 850–853.

Gosse, J.C., Phillips, F.M., 2001. Terrestrial in situ cosmogenic nuclides: theory and application. Quaternary Science Reviews 20, 1475–1560.

Gough, W.A., Robinson, C.A., 2000. Sea-level variation in Hudson Bay, Canada, from tide-gauge data. Arctic, Antarctic, and Alpine Research 32, 331–335.

Government of Manitoba, 2013. 2011 flood: technical review of Lake Manitoba, Lake St. Martin and Assiniboine River water levels. Technical Report.

Gowan, E.J., 2013. An assessment of the minimum timing of ice free conditions of the western Laurentide Ice Sheet. Quaternary Science Reviews 75, 100–113.

Gregoire, L.J., Payne, A.J., Valdes, P.J., 2012. Deglacial rapid sea level rises caused by ice-sheet saddle collapses. Nature 487, 219–222.

Grimm, E.C., Maher Jr., L.J., Nelson, D.M., 2009. The magnitude of error in conventional bulk-sediment radiocarbon dates from central North America. Quaternary Research 72, 301–308.

Hallberg, G.R., Lineback, J.A., Mickelson, D.M., Knox, J.C., Goebel, J.E., Hobbs, H.C., Whitfield, J.W., Ward, R.A., Boellstorff, J.D., Swinehart, J.B., Dreeszen, V.H., 1994. Quaternary Geologic Map of the Des Moines 4 Degrees x 6 Degrees Quadrangle, United States. USGS Numbered Series I-1420(NK-15). U.S. Geological Survey. Scale 1:1,000,000.

Hanebuth, T., Stattegger, K., Grootes, P.M., 2000. Rapid flooding of the Sunda Shelf: a late-glacial sea-level record. Science 288, 1033–1035.

Hanesiak, J.M., Stewart, R.E., Bonsal, B.R., Harder, P., Lawford, R., Aider, R., Amiro, B.D., Atallah, E., Barr, A.G., Black, T.A., Bullock, P., Brimelow, J.C., Brown, R., Carmichael, H., Derksen, C., Flanagan, L.B., Gachon, P., Greene, H., Gyakum, J., Henson, W., Hogg, E.H., Kochtubajda, B., Leighton, H., Lin, C., Luo, Y., McCaughey, J.H., Meinert, A., Shabbar, A., Snelgrove, K., Szeto, K., Trishchenko, A., van der Kamp, G., Wang, S., Wen, L., Wheaton, E., Wielki, C., Yang, Y., Yirdaw, S., Zha, T., 2011. Characterization and summary of the 1999–2005 Canadian Prairie drought. Atmosphere-Ocean 49, 421–452.

Hanson, M., Campbell, J.E., Smith, J.S., Slimmon, W.L., 2011. Saskatchewan ice-flow indicator mapping project: preliminary report. Miscellaneous Report 2011-4.2, Paper A-11. Saskatchewan Geological Survey, Saskatchewan Ministry of Energy and Resources.

Harington, C., 2003. Annotated Bibliography of Quaternary Vertebrates of Northern North America – With Radiocarbon Dates. University of Toronto Press.

Harington, C., Cinq-Mars, J., 1995. Radiocarbon dates on saiga antelope (Saiga tatarica) fossils from Yukon and the Northwest Territories. Arctic 48, 1–7.

He, F., Shakun, J.D., Clark, P.U., Carlson, A.E., Liu, Z., Otto-Bliesner, B.L., Kutzbach, J.E., 2013. Northern Hemisphere forcing of Southern Hemisphere climate during the last deglaciation. Nature 494, 81–85.

Herring, T.A., King, R.W., McClusky, S.C., 2008. Introduction to GAMIT/GLOBK. Technical Report Release 10.3. Massachussetts Institute of Technology.

Hill, C.L., Feathers, J.K., 2002. Glacial Lake Great Falls and the Late-Wisconsin-episode Laurentide ice margin. Current Research in the Pleistocene 19, 119–121.

Hill, P.R., Héquette, A., Ruz, M.H., 1993. Holocene sea-level history of the Canadian Beaufort shelf. Canadian Journal of Earth Sciences 30, 103–108.

Holgate, S.J., Matthews, A., Woodworth, P.L., Rickards, L.J., Tamisiea, M.E., Bradshaw, E., Foden, P.R., Gordon, K.M., Jevrejeva, S., Pugh, J., 2012. New data systems and products at the permanent service for mean sea level. Journal of Coastal Research 29, 493–504.

Howell, P.D., van der Pluijm, B.A., 1999. Structural sequences and styles of subsidence in the michigan basin. Geological Society of America Bulletin 111, 974–991.

Huntley, D., Mills, A., Paulen, R., 2008. Surficial deposits, landforms, glacial history, and reconnaissance drift sampling in the Trout Lake map area, Northwest Territories. Current Research 2008-14. Geological Survey of Canada.

Hutchinson, I., James, T.S., Reimer, P.J., Bornhold, B.D., Clague, J.J., 2004. Marine and limnic radiocarbon reservoir corrections for studies of late- and postglacial environments in Georgia Basin and Puget Lowland, British Columbia, Canada and Washington, USA. Quaternary Research 61, 193–203.

Imbrie, J., Boyle, E.A., Clemens, S.C., Duffy, A., Howard, W.R., Kukla, G., Kutzbach, J., Martinson, D.G., McIntyre, A., Mix, A.C., Molfino, B., Morley, J.J., Peterson, L.C., Pisias, N.G., Prell, W.L., Raymo, M.E., Shackleton, N.J., Toggweiler, J.R., 1992. On the structure and origin of major glaciation cycles 1. Linear responses to Milankovitch forcing. Paleoceanography 7, 701–738.

IOC-UNESCO, 2006. Manual on Sea-level Measurements and Interpretation, Volume IV : An update to 2006. Manual 14. Intergovernmental Oceanographic Commission of UNESCO. JCOMM Technical Report No.31; WMO/TD. No. 1339.

Jackson, L.E., Andriashek, L.D., Phillips, F.M., 2011. Limits of successive middle and late Pleistocene continental ice sheets, interior plains of southern and central Alberta and adjacent areas, in: Ehlers, J., Gibbard, P.L., Hughes, P.D. (Eds.), Quaternary Glaciations - Extent and Chronology A Closer Look. Elsevier. volume 15 of *Developments in Quaternary Sciences*. chapter 45, pp. 575–589.

Jackson, L.E., Phillips, F.M., Little, E.C., 1999. Cosmogenic ^{36}Cl dating of the maximum limit of the Laurentide Ice Sheet in southwestern Alberta. Canadian Journal of Earth Sciences 36, 1347–1356.

Jackson, L.E., Phillips, F.M., Shimamura, K., Little, E.C., 1997. Cosmogenic ^{36}Cl dating of the Foothills erratics train, Alberta, Canada. Geology 25, 195–198.

Jansen, E., Overpeck, J., Briffa, K.R., Duplessy, J.C., Joos, F., Masson-Delmotte, V., Olago, D., Otto-Bliesner, B., Peltier, W.R., Rahmstorf, S., Ramesh, R., Raynaud, D., Rind, D., Solomina, O., Villalba, R., Zhang, D., 2007. Paleoclimate, in: Solomon, S., Qin, D., Manning, M., Chen, Z., Marquis, M., Averyt, K.B., Tignor, M., Miller, H. (Eds.), Climate Change 2007: The Physical Science Basis. Contribution of Working Group I to the Fourth Assessment Report of the Intergovernmental Panel on Climate Change. Cambridge University Press, Cambridge, United Kingdom and New York, NY, USA. chapter 6, pp. 435–497.

Jenson, J.W., Clark, P.U., MacAyeal, D.R., Ho, C., Vela, J.C., 1995. Numerical modeling of advective transport of saturated deforming sediment beneath the Lake Michigan Lobe, Laurentide Ice Sheet. Geomorphology 14, 157–166.

Jenson, J.W., MacAyeal, D.R., Clark, P.U., Ho, C.L., Vela, J.C., 1996. Numerical modeling of subglacial sediment deformation: implications for the behavior of the Lake Michigan Lobe, Laurentide Ice Sheet. Journal of Geophysical Research 101, 8717–8728.

Johnsen, S.J., Dahl-Jensen, D., Gundestrup, N., Steffensen, J.P., Clausen, H.B., Miller, H., Masson-Delmotte, V., Sveinbjörnsdottir, A.E., White, J., 2001. Oxygen isotope and palaeotemperature records from six Greenland ice-core stations: Camp Century, Dye-3, GRIP, GISP2, Renland and NorthGRIP. Journal of Quaternary Science 16, 299–307.

Johnson, G.D., McCormick, K.A., 2005. Geology of Yankton County, South Dakota. Bulletin 34. United States Geological Survey.

Johnston, W.A., 1942. Glacial Lake Agassiz, with special reference to the mode of deformation of the beaches. Bulletin 7. Geological Survey of Canada.

Joughin, I., Bamber, J.L., Scambos, T., Tulaczyk, S., Fahnestock, M., MacAyeal, D.R., 2006. Integrating satellite observations with modelling: basal shear stress of the Filcher-Ronne ice streams, Antarctica. Philosophical Transactions of the Royal Society A: Mathematical, Physical and Engineering Sciences 364, 1795–1814.

Karato, S.I., Wu, P., 1993. Rheology of the upper mantle- a synthesis. Science 260, 771–778.

Kaufmann, G., Lambeck, K., 2002. Glacial isostatic adjustment and the radial viscosity profile from inverse modeling. Journal of Geophysical Research: Solid Earth 107, ETG–5.

Kennedy, K., Froese, D., Zazula, G., Lauriol, B., 2010. Last Glacial Maximum age for the northwest Laurentide maximum from the Eagle River spillway and delta complex, northern Yukon. Quaternary Science Reviews 29, 1288–1300.

Kent, D.M., 1994. Paleogeographic evolution of the cratonic platform – Cambrian to Triassic, in: Mossop, G.D., Shetsen, I. (Eds.), Geological Atlas of the Western Canada Sedimentary Basin, pp. 69–86.

Kerr, D.E., 1996. Late Quaternary sea level history in the Paulatuk to Bathurst Inlet area, Northwest Territories. Canadian Journal of Earth Sciences 33, 389–403.

King, S.D., Masters, G., 1992. An inversion for radial viscosity structure using seismic tomography. Geophysical research letters 19, 1551–1554.

Kirby, M.E., Andrews, J.T., 1999. Mid-Wisconsin Laurentide ice sheet growth and decay: Implications for Heinrich events 3 and 4. Paleoceanography 14, 211–223.

Kirchner, N., Hutter, K., Jakobsson, M., Gyllencreutz, R., 2011. Capabilities and limitations of numerical ice sheet models: a discussion for earth-scientists and modelers. Quaternary Science Reviews 30, 3691–3704.

Kleman, J., Borgström, I., 1996. Reconstruction of palaeo-ice sheets: the use of geomorphological data. Earth Surface Processes and Landforms 21, 893–909.

Kleman, J., Fastook, J., Ebert, K., Nilsson, J., Caballero, R., 2013. Pre-LGM Northern Hemisphere ice sheet topography. Climate of the Past 9, 2365–2378.

Kleman, J., Jansson, K., De Angelis, H., Stroeven, A.P., Hättestrand, C., Alm, G., Glasser, N., 2010. North American Ice Sheet build-up during the last glacial cycle, 115–21kyr. Quaternary Science Reviews 29, 2036–2051.

Kovanen, D.J., Easterbrook, D.J., 2002. Paleodeviations of radiocarbon marine reservoir values for the northeast Pacific. Geology 30, 243–246.

Kulig, J.J., 1996. The glaciation of the Cypress Hills of Alberta and Saskatchewan and its regional implications. Quaternary International 32, 53–77.

Lacelle, D., Lauriol, B., Zazula, G., Ghaleb, B., Utting, N., Clark, I.D., 2013. Timing of advance and basal condition of the Laurentide Ice Sheet during the last glacial maximum in the Richardson Mountains, NWT. Quaternary Research 80, 274–283.

Lajeunesse, P., St-Onge, G., 2008. The subglacial origin of the Lake Agassiz–Ojibway final outburst flood. Nature Geoscience 1, 184–188.

Lake of the Woods Control Board, 2013. Annual Report, 2013. Technical Report.

Lakeman, T.R., England, J.H., 2012. Paleoglaciological insights from the age and morphology of the Jesse moraine belt, western Canadian Arctic. Quaternary Science Reviews 47, 82–100.

Lakeman, T.R., England, J.H., 2013. Late Wisconsinan glaciation and postglacial relative sea-level change on western Banks Island, Canadian Arctic Archipelago. Quaternary Research 80, 99–112.

Lambeck, K., 1993a. Glacial rebound of the British Isles–I. preliminary model results. Geophysical Journal International 115, 941–959.

Lambeck, K., 1993b. Glacial rebound of the British Isles–II. A high-resolution, high-precision model. Geophysical Journal International 115, 960–990.

Lambeck, K., 1995. Constraints on the Late Weichselian ice sheet over the Barents Sea from observations of raised shorelines. Quaternary Science Reviews 14, 1–16.

Lambeck, K., 1996. Limits on the areal extent of the Barents Sea ice sheet in Late Weichselian time. Global and Planetary Change 12, 41–51.

Lambeck, K., Chappell, J., 2001. Sea level change through the last glacial cycle. Science 292, 679–686.

Lambeck, K., Esat, T.M., Potter, E.K., 2002. Links between climate and sea levels for the past three million years. Nature 419, 199–206.

Lambeck, K., Johnston, P., Smither, C., Nakada, M., 1996. Glacial rebound of the British Isles–III. constraints on mantle viscosity. Geophysical Journal International 125, 340–354.

Lambeck, K., Purcell, A., Funder, S., Kjær, K.H., Larsen, E., Moller, P., 2006. Constraints on the Late Saalian to early Middle Weichselian ice sheet of Eurasia from field data and rebound modelling. Boreas 35, 539–575.

Lambeck, K., Purcell, A., Johnston, P., Nakada, M., Yokoyama, Y., 2003. Water-load definition in the glacio-hydro-isostatic sea-level equation. Quaternary Science Reviews 22, 309–318.

Lambeck, K., Purcell, A., Zhao, J., Svensson, N.O., 2010. The Scandinavian Ice Sheet: from MIS 4 to the end of the Last Glacial Maximum. Boreas 39, 410–435.

Lambeck, K., Smither, C., Ekman, M., 1998a. Tests of glacial rebound models for Fennoscandinavia based on instrumented sea-and lake-level records. Geophysical Journal International 135, 375–387.

Lambeck, K., Smither, C., Johnston, P., 1998b. Sea-level change, glacial rebound and mantle viscosity for northern Europe. Geophysical Journal International 134, 102–144.

Lambert, A., Courtier, N., Sasagawa, G.S., Klopping, F., Winester, D., James, T.S., Liard, J.O., 2001. New constraints on Laurentide postglacial rebound from absolute gravity measurements. Geophysical Research Letters 28, 2109–2112.

Lambert, A., Huang, J., Kamp, G., Henton, J., Mazzotti, S., James, T.S., Courtier, N., Barr, A.G., 2013. Measuring water accumulation rates using GRACE data in areas experiencing glacial isostatic adjustment: The Nelson River basin. Geophysical Research Letters 40, 6118–6122.

Larson, G., Schaetzl, R., 2001. Origin and evolution of the great lakes. Journal of Great Lakes Research 27, 518–546.

Leaman, D., 1984. Notes on microbarometer elevation determinations. Exploration Geophysics 15, 53–59.

Lemmen, D.S., Duk-Rodkin, A., Bednarski, J.M., 1994. Late glacial drainage systems along the northwestern margin of the Laurentide Ice Sheet. Quaternary Science Reviews 13, 805–828.

Lepper, K., Buell, A.W., Fisher, T.G., Lowell, T.V., 2013. A chronology for glacial Lake Agassiz shorelines along Upham's namesake transect. Quaternary Research 80, 88–98.

Lepper, K., Fisher, T.G., Hajdas, I., Lowell, T.V., 2007. Ages for the Big Stone Moraine and the oldest beaches of glacial Lake Agassiz: Implications for deglaciation chronology. Geology 35, 667–670.

Lepper, K., Gorz, K.L., Fisher, T.G., Lowell, T.V., 2011. Age determinations for glacial Lake Agassiz shorelines west of Fargo, North Dakota, USA. Canadian Journal of Earth Sciences 48, 1199–1207.

Lepper, K., Sager, L., 2000. A revised age determination for the Embden, North Dakota, mammoth using optically stimulated luminescence dating. Current Research in the Pleistocene 27, 171–173.

Leverington, D.W., Mann, J.D., Teller, J.T., 2000. Changes in the bathymetry and volume of glacial Lake Agassiz between 11,000 and 9300 14C yr B.P. Quaternary Research 54, 174–181.

Leverington, D.W., Mann, J.D., Teller, J.T., 2002. Changes in the bathymetry and volume of glacial Lake Agassiz between 9200 and 7700 14 C yr BP. Quaternary Research 57, 244–252.

Leverington, D.W., Teller, J.T., 2003. Paleotopographic reconstructions of the eastern outlets of glacial Lake Agassiz. Canadian Journal of Earth Sciences 40, 1259–1278.

Lewis, C.F.M., Miller, A.A.L., Levacc, E., Piper, D.J.W., Sonnichsen, G.V., 2012. Lake Agassiz outburst age and routing by Labrador Current and the 8.2 cal ka cold event. Quaternary International 260, 83–97.

Licciardi, J., Clark, P., Jenson, J., Macayeal, D., 1998. Deglaciation of a soft-bedded Laurentide Ice Sheet. Quaternary Science Reviews 17, 427–448.

Little, E.C., 2006. Surficial geology, Ellice Hills (north), Nunavut. Open File 5016. Geological Survey of Canada. Scale 1:50 000.

Little, E.C., Ferbey, T., 2003. Surficial geology, Laughland Lake south, Nunavut. Open File 4278. Geological Survey of Canada. Scale 1:100 000.

Lowdon, J., Blake, W., 1968. Geological Survey of Canada radiocarbon dates VII. Radiocarbon 10, 207–245.

Lowdon, J.A., Robertson, I.M., Blake, W., 1971. Geological Survey of Canada radiocarbon dates XI. Radiocarbon 13, 255–324.

Lowell, T., Fisher, T., Comer, G., Haidas, I., Waterson, N., Glover, K., Loope, H., Schaffer, J., Rinterknecht, V., Broecker, W., Denton, G., Teller, J., 2005. Testing the Lake Agassiz meltwater trigger for the Younger Dryas. EOS Transactions 86, 365–373.

Lowell, T.V., Fisher, T.G., Hajdas, I., Glover, K., Loope, H., Henry, T., 2009. Radiocarbon deglaciation chronology of the Thunder Bay, Ontario area and implications for ice sheet retreat patterns. Quaternary Science Reviews 28, 1597–1607.

MacAyeal, D., 1993. Binge/purge oscillations of the Laurentide ice sheet as a cause of the North Atlantic's Heinrich events. Paleoceanography 8, 775–784.

MacDonald, G.M., 1987. Postglacial vegetation history of the Mackenzie River basin. Quaternary Research 28, 245–262.

MacDonald, G.M., Beukens, R.P., Kieser, W.E., 1991. Radiocarbon dating of limnic sediments: a comparative analysis and discussion. Ecology 72, 1150–1155.

Mainville, A., Craymer, M.R., 2005. Present-day tilting of the Great Lakes region based on water level gauges. Geological Society of America Bulletin 117, 1070.

Manitoba Hydro, 2010. Water power act licenses, Churchill River diversion final licence request. Supporting documentation PS&O - 10/11. Manitoba Hydro.

Manitoba Hydro, 2014. Grand Rapids Generating Station. `https://www.hydro.mb.ca/corporate/facilities/gs_grand_rapids.shtml`, Accessed December 29, 2014.

Marshall, S., James, T., Clarke, G., 2002. North American ice sheet reconstructions at the last glacial maximum. Quaternary Science Reviews 21, 175–192.

Marshall, S.J., 2005. Recent advances in understanding ice sheet dynamics. Earth and Planetary Science Letters 240, 191–204.

Marshall, S.J., Clarke, G.K., Dyke, A.S., Fisher, D.A., 1996. Geologic and topographic controls on fast flow in the Laurentide and Cordilleran Ice Sheets. Journal of Geophysical Research: Solid Earth (1978–2012) 101, 17827–17839.

Mathews, W.H., 1974. Surface profiles of the Laurentide ice sheet in its marginal areas. Journal of Glaciology 13.

Mazzotti, S., Lambert, A., Henton, J., James, T.S., Courtier, N., 2011. Absolute gravity calibration of GPS velocities and glacial isostatic adjustment in mid-continent North America. Geophysical Research Letters 38.

McMartin, I., Campbell, E, J., Dredge, L.A., 2013. Pre-Late Wisconsinan shells in Rae Isthmus Ice Stream tills: implications for LIS dynamics and deglaciation of northwestern Hudson Bay, in: CANQUA-CGRG biannual meeting, abstracts, CANQUA. p. 167.

McMartin, I., Campbell, J.E., Dredge, L.A., Robertson, L., 2010. A digital compilation of ice-flow indicators for central Manitoba and Saskatchewan: datasets, digital scalable maps and 1:500 000 scale generalized map. Scale 1:500 000.

McMartin, I., Campbell, J.E., Dredge, L.A., Robertson, L., 2011. A digital compilation of ice-flow indicators for central Manitoba and Saskatchewan: datasets, digital scalable maps and 1:500 000 scale generalized map. Open File 6405. Geological Survey of Canada.

McMartin, I., Dredge, L.A., 2005. History of ice flow in the Schultz Lake and Wager Bay areas, Kivalliq region, Nunavut. Current Research 2005-B2. Geological Survey of Canada.

McMartin, I., Dredge, L.A., Ford, K.L., Kjarsgaard, I.M., 2006. Till composition, provenance and stratigraphy beneath the Keewatin Ice Divide, Schultz Lake area (NTS 66A), mainland Nunavut. Open File 5312. Geological Survey of Canada.

McMillan, K., Teller, J.T., 2012. Origin of the Herman–Norcross–Tintah sequence of Lake Agassiz beaches in Manitoba, Canada. Geomorphology .

McNeely, R., 1989. Geological Survey of Canada radiocarbon dates XXVIII. Paper 88-7. Geological Survey of Canada.

McNeely, R., 2006. Geological Survey of Canada radiocarbon dates XXXV. Current Research 2006-G. Geological Survey of Canada.

McNeely, R., Atkinson, D.E., 1995. Geological Survey of Canada radiocarbon dates XXXII. Current Research 1995-G. Geological Survey of Canada.

McNeely, R., Brennan, J., 2005. Geological Survey of Canada radiocarbon dates XXXV. Open File 5019. Geological Survey of Canada.

McNeely, R., Dyke, A., Southon, J., 2006. Canadian marine reservoir ages, preliminary data assessment. Open File 5049. Geological Survey of Canada.

McNeely, R., Jorgensen, P.K., 1992. Geological Survey of Canada radiocarbon dates XXX. Paper 90-7. Geological Survey of Canada.

Mekis, É., Vincent, L.A., 2011. An overview of the second generation adjusted daily precipitation dataset for trend analysis in Canada. Atmosphere-Ocean 49, 163–177.

Meltzer, D.J., 2003. Peopling of North America, in: Gillespie, A., Porter, S., Atwater, B. (Eds.), The Quaternary Period in the United States. Elsevier. volume 1 of *Developments in Quaternary Sciences*, pp. 539–563.

Menounos, B., Osborn, G., Clague, J.J., Luckman, B.H., 2009. Latest Pleistocene and Holocene glacier fluctuations in western Canada. Quaternary Science Reviews 28, 2049–2074.

Meyer, G.N., Stefanova, I., 2009. Dating the onset of the last glaciation in eastern Minnesota, in: Geological Society of America Abstracts with Programs, p. 5.

Mitrovica, J.X., Forte, A.M., 2004. A new inference of mantle viscosity based upon joint inversion of convection and glacial isostatic adjustment data. Earth and Planetary Science Letters 225, 177–189.

Mitrovica, J.X., Milne, G.A., 2002. On the origin of late Holocene sea-level highstands within equatorial ocean basins. Quaternary Science Reviews 21, 2179–2190.

Mitrovica, J.X., Peltier, W.R., 1991. On postglacial geoid subsidence over the equatorial oceans. Journal of Geophysical Research 96, 20053–20071.

Montillet, J.P., Williams, S.D.P., Koulali, A., McClusky, S.C., 2015. Estimation of offsets in GPS time-series and application to the detection of earthquake deformation in the far-field. Geophysical Journal International 200, 1207–1221.

Montillet, J.P., Yu, K., 2014. Modeling geodetic processes with Levy α-stable distribution and FARIMA. Mathematical Geosciences , 1–20.

Morlan, R., McNeely, R., Nielsen, E., 2000. Manitoba radiocarbon dates. Open File Report OF2000-1. Manitoba Industry, Trade and Mines, Geological Survey.

Munyikwa, K., Feathers, J.K., Rittenour, T.M., Shrimpton, H.K., 2011. Constraining the Late Wisconsinan retreat of the Laurentide ice sheet from western Canada using luminescence ages from postglacial aeolian dunes. Quaternary Geochronology 6, 407–422.

Murton, J.B., 2009. Stratigraphy and palaeoenvironments of Richards Island and the eastern Beaufort Continental Shelf during the last glacial-interglacial cycle. Permafrost and Periglacial Processes 20, 107–125.

Murton, J.B., Bateman, M.D., Dallimore, S.R., Teller, J.T., Yang, Z., 2010. Identification of Younger Dryas outburst flood path from Lake Agassiz to the Arctic Ocean. Nature 464, 740–743.

Murton, J.B., Frechen, M., Maddy, D., 2007. Luminescence dating of mid-to Late Wisconsinan aeolian sand as a constraint on the last advance of the Laurentide Ice Sheet across the Tuktoyaktuk Coastlands, western Arctic Canada. Canadian Journal of Earth Sciences 44, 857–869.

Nakada, M., Lambeck, K., 1987. Glacial rebound and relative sea-level variations: a new appraisal. Geophysical Journal International 90, 171–224.

Nambudiri, E.M.V., Teller, J.T., Last, W.M., 1980. Pre-Quaternary microfossils–a guide to errors in radiocarbon dating. Geology 8, 123–126.

Nelson, S.J., Johnson, R.D., 1966. Geology of Hudson Bay Basin. Bulletin of Canadian Petroleum Geology 14, 520–578.

Nielsen, E., Gryba, E.M., Wilson, M.C., 1984. Bison remains from a Lake Agassiz spit complex in the Swan River valley, Manitoba: depositional environment and paleoecological implications. Canadian Journal of Earth Sciences 21, 829–842.

Nielsen, E., Morgan, A.V., Morgan, A., Mott, R.J., Rutter, N.W., Causse, C., 1986. Stratigraphy, paleoecology, and glacial history of the Gillam area, Manitoba. Canadian Journal of Earth Sciences 23, 1641–1661.

Nilsson, M., Klarqvist, M., Bohlin, E., Possnert, G., 2001. Variation in ^{14}C age of macrofossils and different fractions of minute peat samples dated by AMS. The Holocene 11, 579–586.

Not, C., Hillaire-Marcel, C., 2012. Enhanced sea-ice export from the Arctic during the Younger Dryas. Nature Communications 3, 647.

Nye, J., 1952. A method of calculating the thicknesses of the ice-sheets. Nature 169, 529–530.

Occhietti, S., Parent, M., Lajeunesse, P., Robert, F., Govare, E., 2011. Late Pleistocene-early Holocene decay of the Laurentide ice sheet in Québec-Labrador. Developments in Quaternary Science 15, 601–630.

Ò Cofaigh, C., Evans, D.J., Smith, I.R., 2010. Large-scale reorganization and sedimentation of terrestrial ice streams during late Wisconsinan Laurentide ice sheet deglaciation. Geological Society of America Bulletin 122, 743–756.

Ogden, J.G., 1977. The use and abuse of radiocarbon dating. Annals of the New York Academy Of Sciences 288, 167–173.

Olivares, G., Teferle, F.N., 2013. A Bayesian Monte Carlo Markov chain method for parameter estimation of fractional differenced Gaussian processes. Signal Processing, IEEE Transactions on 61, 2405–2412.

Panasyuk, S.V., Hager, B.H., 2000. Inversion for mantle viscosity profiles constrained by dynamic topography and the geoid, and their estimated errors. Geophysical Journal International 143, 821–836.

Patterson, C.J., Johnson, M., 2004. The status of glacial mapping in Minnesota, in Ehlers, J., and Gibbard, PL, in: Ehlers, J., Gibbard, P.L. (Eds.), Quaternary Glaciations–Extent and Chronology - Part II: North America. Elsevier. Developments in Quaternary Science, pp. 119–123.

Peltier, W., 1974. The impulse response of a maxwell earth. Reviews of Geophysics 12, 649–669.

Peltier, W., 1994. Ice age paleotopography. Science 265, 195–201.

Peltier, W., 2004. Global glacial isostasy and the surface of the ice-age Earth: the ICE-5G (VM2) model and GRACE. Annual Review of Earth and Planetary Sciences 32, 111–149.

Peltier, W., Drummond, R., 2008. Rheological stratification of the lithosphere: A direct inference based upon the geodetically observed pattern of the glacial isostatic adjustment of the North American continent. Geophysical Research Letters 35.

Peltier, W.R., 1996. Mantle viscosity and ice-age ice sheet topography. Science 273, 1359.

Peltier, W.R., 2002. Global glacial isostatic adjustment: palaeogeodetic and space-geodetic tests of the ICE-4G (VM2) model. Journal of Quaternary Science 17, 491–510.

Peltier, W.R., Andrews, J.T., 1976. Glacial-isostatic adjustment–I. The forward problem. Geophysical Journal of the Royal Astronomical Society 46, 605–646.

Peltier, W.R., Argus, D.F., Drummond, R., 2015. Space geodesy constrains ice age terminal deglaciation: The global ICE-6G_C (VM5a) model. Journal of Geophysical Research: Solid Earth 120.

Permanent Service for Mean Sea Level, 2014. Tide gauge data. `http://www.psmsl.org/data/obtaining/`.

Peters, D.L., 2014. Comment on "Streamflow input to Lake Athabasca, Canada" by Rasouli et al.(2013). Hydrology and Earth System Sciences Discussions 11, 3137–3153.

Prest, V., 1990. Laurentide ice-flow patterns: A historical review, and implications of the dispersal of belcher island erratics. Géographie Physique et Quaternaire 44, 113–136.

Prest, V., Grant, D., Rampton, V., 1968. Glacial map of Canada. Map 1253A. Geological Survey of Canada. Scale 1:5,000,000.

Prest, V.K., 1969. Retreat of Wisconsin and recent ice in North America. Map 1257A. Geological Survey of Canada. Scale 1:5,000,000.

Purcell, A., Dehecq, A., Tregoning, P., Potter, E.K., McClusky, S., Lambeck, K., 2011. Relationship between glacial isostatic adjustment and gravity perturbations observed by GRACE. Geophysical Research Letters 38.

Rampton, V.N., 1988. Quaternary geology of the Tuktoyaktuk coastlands, Northwest Territories. Memoir 423. Energy, Mines and Resources Canada.

Rapp, R., 1997. Use of potential coefficient models for geoid undulation determinations using a spherical harmonic representation of the height anomaly/geoid undulation difference. Journal of Geodesy 71, 282–289.

Rayburn, J.A., 1997. Correlation of the Campbell strandlines along the northwestern margin of glacial Lake Agassiz. Master's thesis. University of Manitoba.

Rayburn, J.A., Teller, J.T., 2007. Isostatic rebound in the northwestern part of the Lake Agassiz basin: Isobase changes and overflow. Palaeogeography, Palaeoclimatology, Palaeoecology 246, 23–30.

Reed, J.C., Wheeler, J.O., Tucholke, B.E., 2004. Geologic Map of North America: Decade of North American Geology. Map 001. Geological Society of America. Scale 1:5 00 000.

Reeh, N., 1982. A plasticity theory approach to the steady-state shape of a three-dimensional ice sheet. Journal of Glaciology 28, 431–455.

Reimer, P.J., Baillie, M.G.L., Bard, E., Bayliss, A., Beck, J.W., Blackwell, P.G., Bronk Ramsey, C., Buck, C.E., Burr, G.S., Edwards, R.L., Friedrich, M., Grootes, P.M., Guilderson, T.P., Hajdas, I., Heaton, T.J., Hogg, A.G., Hughen, K.A., Kaiser, K.F., Kromer, B., McCormac, F.G., Manning, S.W., Reimer, R.W., Richards, D.A., Southon, J.R., Talamo, S., Turney, C.S.M., van der Plicht, J., Weyhenmeyer, C.E., 2009. IntCal09 and Marine09 radiocarbon age calibration curves, 0–50,000 years cal BP. Radiocarbon 51, 1111–1150.

Reimer, P.J., Bard, E., Bayliss, A., Beck, J.W., Blackwell, P.G., Bronk Ramsey, C., Buck, C.E., Cheng, H., Edwards, R.L., Friedrich, M., Grootes, P.M., Guilderson, T.P., Haflidason, H., Hajdas, I., Hatté, C., Heaton, T.J., Hoffmann, D.L., Hogg, A.G., Hughen, K.A., Kaiser, K.F., Kromer, B., Manning, S.W., Niu, M., Reimer, R.W., Richards, D.A., Scott, E.M., Southon, J.R., Staff, R.A., Turney, C.S.M., van der Plicht, J., 2013. IntCal13 and Marine13 radiocarbon age calibration curves 0–50,000 years cal BP. Radiocarbon 55, 1869–1887.

Risberg, J., Sandgren, P., Teller, J.T., Last, W.M., 1999. Siliceous microfossils and mineral magnetic characteristics in a sediment core from Lake Manitoba, Canada: a remnant of glacial Lake Agassiz. Canadian Journal of Earth Sciences 36, 1299–1314.

Rolandone, F., Mareschal, J.C., Jaupart, C., 2003. Temperatures at the base of the Laurentide Ice Sheet inferred from borehole temperature data. Geophysical Research Letters 30.

Ross, M., Campbell, J.E., Parent, M., Adams, R.S., 2009. Palaeo-ice streams and the subglacial landscape mosaic of the North American mid-continental prairies. Boreas 38, 421–439.

Ross, M., Utting, D.J., Lajeunesse, P., Kosar, K.G.A., 2012. Early Holocene deglaciation of northern Hudson Bay and Foxe Channel constrained by new radiocarbon ages and marine reservoir correction. Quaternary Research 78, 82–94.

Roy, M., Dell'Oste, F., Veillette, J.J., de Vernal, A., Hélie, J., Parent, M., 2011. Insights on the events surrounding the final drainage of Lake Ojibway based on James Bay stratigraphic sequences. Quaternary Science Reviews 30, 682–692.

Ruhe, R.V., 1969. Quaternary landscapes in Iowa. Iowa State University Press.

Sado, E.V., Fullerton, D.S., Goebel, J.E., Ringrose, S.M., 1995. Quaternary Geologic Map of the Lake of the Woods 4 Degrees x 6 Degrees Quadrangle, United States and Canada. USGS Numbered Series I-1420(NM-15). U.S. Geological Survey. Scale 1:1 000 000.

Sambridge, M., Bodin, T., McQueen, H., Tregoning, P., Bonnefoy, S., Watson, C., 2009. TerraWulf II: Many hands make light work of data analysis. Research School of Earth Sciences Annual Report 2009. The Australian National University.

Savelle, J.M., Dyke, A.S., 2002. Variability in Palaeoeskimo occupation on southwestern Victoria Island, Arctic Canada: causes and consequences. World Archaeology 33, 508–522.

Savelle, J.M., Dyke, A.S., 2009. Palaeoeskimo Demography on Western Boothia Peninsula, Arctic Canada. Journal of Field Archaeology 34, 267–283.

Savelle, J.M., Dyke, A.S., Whitridge, P.J., Poupart, M., 2012. Paleoeskimo Demography on Western Victoria Island, Arctic Canada: Implications for Social Organization and Longhouse Development. Arctic 65, 167–181.

Schaetzl, R.J., Forman, S.L., Attig, J.W., 2014. Optical ages on loess derived from outwash surfaces constrain the advance of the Laurentide Ice Sheet out of the Lake Superior Basin, USA. Quaternary Research 81, 318–329.

Sella, G.F., Stein, S., Dixon, T.H., Craymer, M., James, T.S., Mazzotti, S., Dokka, R.K., 2007. Observation of glacial isostatic adjustment in "stable" North America with GPS. Geophysical Research Letters 34, L02306.

Seppä, H., Cwynar, L.C., MacDonald, G.M., 2003. Post-glacial vegetation reconstruction and a possible 8200 cal. yr BP event from the low arctic of continental Nunavut, Canada. Journal of Quaternary Science 18, 621–629.

Shore, J.S., Bartley, D.D., Harkness, D.D., 1995. Problems encountered with the ^{14}C dating of peat. Quaternary Science Reviews 14, 373–383.

Slimmon, W.L., 2011. Geological Atlas of Saskatchewan. Miscellaneous Report 2011-7. Saskatchewan Ministry of Energy and Resources.

Smith, D.G., 1992. Glacial Lake Mackenzie, Mackenzie Valley, Northwest Territories, Canada. Canadian Journal of Earth Sciences 29, 1756–1766.

Smith, D.G., 1994. Glacial Lake McConnell: paleogeography, age, duration, and associated river deltas, Mackenzie River basin, western Canada. Quaternary Science Reviews 13, 829–843.

Smith, I.R., Paulen, R.C., Plouffe, A., 2007. Surficial geology, Mega River, Alberta. Open File 5237. Geological Survey of Canada. Scale 1:100 000.

Smith, W., Wessel, P., 1990. Gridding with continuous curvature splines in tension. Geophysics 55, 293–305.

Stea, R.R., Seaman, A.A., Pronk, T., Parkhill, M.A., Allard, S., Utting, D., 2011. The Appalachian Glacier Complex in Maritime Canada, in: Ehlers, J., Gibbard, P.L., Hughes, P.D. (Eds.), Quaternary Glaciations - Extent and Chronology A Closer Look. Elsevier. volume 15 of *Developments in Quaternary Sciences*. chapter 48, pp. 631 – 659.

Steinberger, B., Calderwood, A.R., 2006. Models of large-scale viscous flow in the Earth's mantle with constraints from mineral physics and surface observations. Geophysical Journal International 167, 1461–1481.

Stokes, C.R., Clark, C.D., 2003a. Laurentide ice streaming on the Canadian Shield: A conflict with the soft-bedded ice stream paradigm? Geology 31, 347–350.

Stokes, C.R., Clark, C.D., 2003b. The Dubawnt Lake palaeo-ice stream: evidence for dynamic ice sheet behaviour on the Canadian Shield and insights regarding the controls on ice-stream location and vigour. Boreas 32, 263–279.

Stokes, C.R., Tarasov, L., 2010. Ice streaming in the Laurentide Ice Sheet: A first comparison between data-calibrated numerical model output and geological evidence. Geophysical Research Letters 37, L01501.

Stokes, C.R., Tarasov, L., Dyke, A.S., 2012. Dynamics of the North American Ice Sheet Complex during its inception and build-up to the Last Glacial Maximum. Quaternary Science Reviews 50, 86–104.

Swinehart, J.B., Dreeszen, V.H., Richmond, G.M., Tipton, M.J., Bretz, R., Steece, F.V., Hallberg, G.R., Goebel, J.E., 1994. Quaternary Geologic Map of the Platte River 4 Degrees x 6 Degrees Quadrangle, United States. USGS Numbered Series I-1420(NK-14). U.S. Geological Survey. Scale 1:1 000 000.

Syverson, K.M., Colgan, P.M., 2011. The Quaternary of Wisconsin: an updated review of stratigraphy, glacial history and landforms, in: Ehlers, J., Gibbard, P.L., Hughes, P.D. (Eds.), Quaternary Glaciations - Extent and Chronology A Closer

Look. Elsevier. volume 15 of *Developments in Quaternary Sciences*. chapter 42, pp. 537–552.

Tackman, G.E., Bills, B.G., James, T.S., Currey, D.R., 1999. Lake-gauge evidence for regional postglacial tilting in southern Manitoba. Geological Society of America Bulletin 111, 1684–1699.

Tarasov, L., Dyke, A.S., Neal, R.M., Peltier, W., 2012. A data-calibrated distribution of deglacial chronologies for the North American ice complex from glaciological modeling. Earth and Planetary Science Letters 315–316, 30–40.

Tarasov, L., Peltier, W., 2004. A geophysically constrained large ensemble analysis of the deglacial history of the North American ice-sheet complex. Quaternary Science Reviews 23, 359–388.

Tarasov, L., Peltier, W., 2005. Arctic freshwater forcing of the Younger Dryas cold reversal. Nature 435, 662–665.

Tarasov, L., Peltier, W.R., 1997. Terminating the 100 kyr ice age cycle. Journal of Geophysical Research 102, 21665–21693.

Tarasov, L., Peltier, W.R., 1999. Impact of thermomechanical ice sheet coupling on a model of the 100 kyr ice age cycle. Journal of Geophysical Research 104, 9517–9545.

Tarasov, L., Peltier, W.R., 2000. Laurentide ice sheet aspect ratio in models based on Glen's flow law. Annals of Glaciology 30, 177–186.

Taylor, K.E., Stouffer, R.J., Meehl, G.A., 2012. An overview of CMIP5 and the experiment design. Bulletin of the American Meteorological Society 93, 485–498.

Teller, J., Clayton, L. (Eds.), 1983. Glacial Lake Agassiz. Special Paper 26, The Geological Association of Canada.

Teller, J.T., 1989. Importance of the Rossendale site in establishing a deglacial chronology along the southwestern margin of the Laurentide ice sheet. Quaternary Research 32, 12–23.

Teller, J.T., Boyd, M., 2006. Two possible routings for overflow from Lake Agassiz during the Younger Dryas, A Reply to Comment by T. Fisher, T. Lowell, H. Loope on "Alternative routing of Lake Agassiz overflow during the Younger Dryas: new dates, paleotopography, a re-evaluation". Quaternary Science Reviews 25, 1142–1145.

Teller, J.T., Boyd, M., Yang, Z., Kor, P.S., Fard, A.M., 2005. Alternative routing of Lake Agassiz overflow during the Younger Dryas: new dates, paleotopography, and a re-evaluation. Quaternary Science Reviews 24, 1890–1905.

Teller, J.T., Leverington, D.W., 2004. Glacial Lake Agassiz: A 5000 yr history of change and its relationship to the $\delta^{18}O$ record of Greenland. GSA Bulletin 116, 729–742.

Teller, J.T., Leverington, D.W., Mann, J.D., 2002. Freshwater outbursts to the oceans from glacial Lake Agassiz and their role in climate change during the last deglaciation. Quaternary Science Reviews 21, 879–887.

Teller, J.T., Risberg, J., Matile, G., Zoltai, S., 2000. Postglacial history and paleoecology of Wampum, Manitoba, a former lagoon in the Lake Agassiz basin. Geological Society of America Bulletin 112, 943–958.

Thomas, A.L., Henderson, G.M., Deschamps, P., Yokoyama, Y., Mason, A.J., Bard, E., Hamelin, B., Durand, N., Camoin, G., 2009. Penultimate deglacial sea-level timing from uranium/thorium dating of Tahitian corals. Science 324, 1186–1189.

Thorleifson, L., Wyatt, P., Shilts, W., Nielsen, E., 1992. Evidence for early Wisconsinan glaciation centered in Quebec, in: Clark, P.U., Lea, P.D. (Eds.), The Last Interglacial–Glacial Transition in North America. Geological Society of America. volume 270 of *Special Paper*, pp. 207–221.

Tregoning, P., Morgan, P.J., Coleman, R., 2004. The effect of receiver firmware upgrades on GPS vertical timeseries. Cahiers du Centre Européen de Géodynamique et de Séismologie 23, 37–46.

Tregoning, P., Ramillien, G., McQueen, H., Zwartz, D., 2009a. Glacial isostatic adjustment and nonstationary signals observed by GRACE. Journal of Geophysical Research: Solid Earth (1978–2012) 114.

Tregoning, P., Watson, C., Ramillien, G., McQueen, H., Zhang, J., 2009b. Detecting hydrologic deformation using GRACE and GPS. Geophysical Research Letters 36, L15401.

Trommelen, M., Ross, M., 2010. Subglacial landforms in northern Manitoba, Canada, based on remote sensing data. Journal of Maps 6, 618–638.

Trommelen, M.S., Ross, M., Campbell, J.E., 2012. Glacial terrain zone analysis of a fragmented paleoglaciologic record, southeast Keewatin sector of the Laurentide Ice Sheet. Quaternary Science Reviews 40, 1–20.

Trommelen, M.S., Ross, M., Campbell, J.E., 2013. Inherited clast dispersal patterns: Implications for palaeoglaciology of the se keewatin sector of the laurentide ice sheet. Boreas 42, 693–713.

Tushingham, A.M., 1992. A compilation of Canadian relative sea-level data for use in constraining glacial isostatic adjustment models. Open File 2454. Geological Survey of Canada.

Tushingham, A.M., Peltier, W.R., 1991. ICE-3G: a new global model of Late Pleistocene deglaciation based upon geophysical predictions of post-glacial relative sea level change. Journal of Geophysical Research 96, 4497–4523.

Tyrrell, J.B., 1894. Notes on the Pleistocene of the North-West Territories of Canada, North-West and West of Hudson Bay. Geological Magazine (Decade IV) 1, 394–399.

Upham, W., 1895. The Glacial Lake Agassiz. volume 25 of *Monographs of the United States Geological Survey*.

van Dam, T., Wahr, J., Milly, P., Shmakin, A., Blewitt, G., Lavallée, D., Larson, K., 2001. Crustal displacements due to continental water loading. Geophysical Research Letters 28, 651–654.

Veillette, J.J., 2004. Surficial geology and glacial history of Tuktut Nogait National Park, District of Mackenzie, N.W.T. Technical Report 04-01. Parks Canada.

Vickers, K., Ward, B., Utting, D., Telka, A., 2010. Deglacial reservoir age and implications, Foxe Peninsula, Baffin Island. Journal of Quaternary Science 25, 1338–1346.

Vigneron, A., Yan, L., 2013. A faster algorithm for computing motorcycle graphs, in: Proceedings of the 29th annual symposium on Symposuim on computational geometry, ACM. pp. 17–26.

Vincent, J.S., 1989. Quaternary geology of the northern Canadian Interior Plains, in: Fulton, R.J. (Ed.), Quaternary Geology of Canada and Greenland. Geological Survey of Canada. number 1 in Geology of Canada. chapter 2, pp. 100–137.

Waelbroeck, C., Labeyrie, L., Michel, E., Duplessy, J.C., McManus, J., Lambeck, K., Balbon, E., Labracherie, M., 2002. Sea-level and deep water temperature changes derived from benthic foraminifera isotopic records. Quaternary Science Reviews 21, 295–305.

Wahr, J., Dazhong, H., Trupin, A., 1995. Predictions of vertical uplift caused by changing polar ice volumes on a viscoelastic earth. Geophysical Research Letters 22, 977–980.

Walcott, R., 1972. Late Quaternary vertical movements in eastern North America: Quantitative evidence of glacio-isostatic rebound. Reviews of Geophysics 10, 849–884.

Wang, H., Jia, L., Steffen, H., Wu, P., Jiang, L., Hsu, H., Xiang, L., Wang, Z., Hu, B., 2013. Increased water storage in north america and scandinavia from grace gravity data. Nature Geoscience 6, 38–42.

Weller, M.B., Fisher, T.G., 2009. Feasibility study of mapping continuous water planes along the southeast Lake Agassiz basin. Journal of Maps 5, 152–165.

Werth, S., Güntner, A., Schmidt, R., Kusche, J., 2009. Evaluation of GRACE filter tools from a hydrological perspective. Geophysical Journal International 179, 1499–1515.

Williams, S.D., 2003. Offsets in global positioning system time series. Journal of Geophysical Research: Solid Earth (1978–2012) 108.

Williams, S.D., 2008. CATS: GPS coordinate time series analysis software. GPS solutions 12, 147–153.

Wolfe, S., Paulen, R., Smith, I., Lamothe, M., 2007. Age and paleoenvironmental significance of Late Wisconsinan dune fields in the Mount Watt and Fontas River map areas, northern Alberta and British Columbia. Current Research 2007-B4. Geological Survey of Canada.

Wolfe, S.A., Huntley, D.J., Ollerhead, J., 2004. Relict late Wisconsinan dune fields of the northern great plains, Canada. Géographie Physique et Quaternaire 58, 323–336.

Wolfe, S.A., Ollerhead, J., Huntley, D.J., Lian, O.B., 2006. Holocene dune activity and environmental change in the prairie parkland and and boreal forest, central Saskatchewan, Canada. The Holocene 16, 17–29.

Wright, H., Watts, W.A., 1969. Glacial and Vegetational History of Northeastern Minnesota. Special Publications Series 11. Minnesota Geological Survey.

Wu, P., Peltier, W., 1983. Glacial isostatic adjustment and the free air gravity anomaly as a constraint on deep mantle viscosity. Geophysical Journal of the Royal Astronomical Society 74, 377–449.

Wu, P., Steffen, H., Wang, H., 2010. Optimal locations for GPS measurements in North America and northern Europe for constraining glacial isostatic adjustment. Geophysical Journal International 181, 653–664.

Yang, Z., Teller, J.T., 2012. Using LiDAR Digital Elevation Model data to map Lake Agassiz beaches, measure their isostatically-induced gradients, and estimate their ages. Quaternary International 260, 32–42.

Yansa, C.H., Ashworth, A.C., 2005. Late Pleistocene palaeoenvironments of the southern Lake Agassiz basin, USA. Journal of Quaternary Science 20, 255–267.

Yokoyama, Y., Lambeck, K., De Deckker, P., Johnston, P., Fifield, L.K., 2000. Timing of the Last Glacial Maximum from observed sea-level minima. Nature 406, 713–716.

Young, R.R., Burns, J.A., Smith, D.G., Arnold, L.D., Rains, R.B., 1994. A single, late Wisconsin, Laurentide glaciation, Edmonton area and southwestern Alberta. Geology 22, 683–686.

Yu, S.Y., Colman, S.M., Lowell, T.V., Milne, G.A., Fisher, T.G., Breckenridge, A., Boyd, M., Teller, J.T., 2010. Freshwater outburst from Lake Superior as a trigger for the cold event 9300 years ago. Science 328, 1262–1266.

Zazula, G.D., MacKay, G., Andrews, T.D., Shapiro, B., Letts, B., Brock, F., 2009. A late Pleistocene steppe bison (Bison priscus) partial carcass from Tsiigehtchic, Northwest Territories, Canada. Quaternary Science Reviews 28, 2734–2742.

Zhao, S., 2013. Lithosphere thickness and mantle viscosity estimated from joint inversion of GPS and GRACE-derived radial deformation and gravity rates in North America. Geophysical Journal International 194, 1455–1472.

Zou, R., Freymueller, J.T., Ding, K., Yang, S., Wang, Q., 2014. Evaluating seasonal loading models and their impact on global and regional reference frame alignment. Journal of Geophysical Research: Solid Earth 119, 1337–1358.

Zreda, M.G., Phillips, F.M., 2000. Cosmogenic nuclide buildup in surficial materials, in: Quaternary geochronology: methods and applications. American Geophysical Union, Washington, pp. 61–76.

Appendix A

Western Laurentide Ice Sheet model

This appendix shows plots of my final ice sheet model. There are 40 time steps in the model from 200 000 yr BP to present. This appendix can be found on the CD-ROM that is attached with this thesis.

Appendix B

Shear stress models

This appendix shows the final shear stress parameters used as input for the ice sheet modelling program. This appendix can be found on the CD-ROM that is attached with this thesis.

Appendix C

Modelled GIA of other models

This appendix presents a comparison of the relative sea level and observed values for my model, ICE-5G and the ANU model. This appendix can be found on the CD-ROM that is attached with this thesis.